Designing Functional Nanocomposites towards Energy Applications: Examining the Performance of Hierarchical Nanostructures as a Function of Composition, Morphology, and Structure for Fuel Cell and Photovoltaic Device Applications

A Dissertation Presented

By

Haiqing Liu

To

The Graduate School

in Partial Fulfillment of the

Requirements

for the Degree of

Doctor of Philosophy

in

Chemistry

Stony Brook University

August 2016

Stony Brook University

The Graduate School

Haiqing Liu

We, the dissertation committee for the above candidate for the

Doctor of Philosophy degree, hereby recommend

acceptance of this dissertation.

Dr. Stanislaus S. Wong – Dissertation Advisor
Professor, Department of Chemistry

Dr. Andreas Mayr – Chairperson of Defense
Professor, Department of Chemistry

Dr. Joseph Lauher – Third Member of Academic Committee
Professor, Department of Chemistry

Dr. Jingguang Chen – Outside Member
Thayer Lindsley Professor of Chemical Engineering, Columbia University

This dissertation is accepted by the Graduate School

Nancy Goroff

Interim Dean of the Graduate School

Abstract of the Dissertation

Designing Functional Nanocomposites towards Energy Applications: Examining the Performance of Hierarchical Nanostructures as a Function of Composition, Morphology, and Structure for Fuel Cell and Photovoltaic Device Applications

By

Haiqing Liu

Doctor of Philosophy

in

Chemistry

Stony Brook University

2016

The inherently finite quantity of fossil fuels has triggered the search for alternative renewable energy sources. Therefore, in this thesis, we have synthesized various types of high quality nanomaterials, including metal alloys, noble-metal-based core-shell structures, and lanthanum-doped fluorides with well-defined shapes as well as controlled chemical compositions, to demonstrate both morphology-dependent and composition-dependent relationships between nanostructures and their resulting electrochemical and/or photo-physical properties, with potential applications for fuel cell and solar cell configurations.

In terms of exploring plausible electrocatalysts to replace expensive and scarce platinum (Pt), a series of one-dimensional (1D) ultrathin (d ~ 2 nm) $Pd_{1-x}Ni_x$ and $Pd_{1-x}Cu_x$ nanowires with controllable chemical compositions have been synthesized. These nanowires have exhibited a volcano-shaped relationship between their compositions and corresponding electrocatalytic activities towards the oxygen reduction reaction (ORR) and the formic acid oxidation reaction (FAOR), respectively. Moreover, after deposition of a Pt monolayer (Pt_{ML}), these $Pt\sim Pd_{1-x}M_x$ (M = Ni or Cu) nanowires evinced outstanding catalytic performance towards various reactions, including the oxygen reduction reaction (ORR), the methanol oxidation reaction (MOR) and the ethanol oxidation reaction (EOR), thereby proving the feasibility, promise, and viability of such hierarchical 1D ultrathin motifs. As a follow-up topic, we have probed the exact structure of $Pt_{ML}\sim Pd_9Au$ ultrathin nanowires, a key ORR catalyst candidate, by combining theoretical calculations, spectroscopic techniques, and electrochemical results. Through X-ray absorption spectroscopy (XAS), an Au surface segregation phenomenon was successfully demonstrated, a finding also suggested by the collective results from both DFT modelling and electrochemical results.

In terms of solar cells, the incorporation of upconversion materials such as lanthanum-doped $NaYF_4$ has become one of the key approaches to harnessing a broader range of the solar spectrum, thereby improving the overall efficiency. Herein, we report on a straightforward hydrothermal synthesis, in the absence of any surfactant, to readily synthesize $NaYF_4$ nanocrystals with various shapes, including 0D (nanoparticles), 1D (nanorods), and 3D (nanowire-bundles). Upon formation of a class of $NaYF_4$-CdSe quantum dot (QD, utilized as a light absorber) heterostructures, incorporating all of these distinctive constituent nanomaterials, we have observed tunable, structure-dependent energy transfer behavior.

This dissertation is dedicated to my family and all that supported me during my period of study.

Table of Contents

Chapter 1: Introduction to Energy-Related Nanomaterials..1

Chapter 2: Experimental Methods for Synthesis and Characterization of Materials......…45

List of Figures

List of Tables

List of Abbreviations and Symbols

°C	degree Celsius
0D	zero-dimensional
1D	one-dimensional
2D	two-dimensional
2θ	two theta
3D	three-dimensional
A	Ampere
Å	Angstrom
Ag/AgCl	silver/silver chloride reference electrode
BA	n-Butylamine
bcc	body-centered cubic
BE-O	Oxygen binding energy
BET	Brunauer-Emmett-Teller
C	Coulombs
CA	chronoamperometry
cm	centimeter
cm^2	Centimeter squared
CO	carbon monoxide
CV	cyclic voltammetry
d	diameter
DAFC	direct alcohol fuel cell
DEFC	direct ethanol fuel cell
DFT	density functional theory
DMFC	direct methanol fuel cell
DOE	U.S. Department of Energy
DTAB	dodecyltrimethylammonium bromide
E	potential
e^-	electron
ECSA	electrochemically accessible surface area
EDAX	energy dispersive X-ray spectroscopy
EELS	Electron energy loss spectroscopy
EOR	ethanol oxidation reaction
EtOH	ethanol
FAOR	formic acid oxidation reaction
FCC	face centered cubic
g	gram
GCE	glassy carbon electrode
h	hours
IR	Infrared Spectroscopy
HAADF	high-angle annular dark field detector
H_{ads}	hydrogen adsorption

H_{des}	hydrogen desorption
HRTEM	high resolution transmission electron microscopy
I	current
I_D	diffusion limited current
I_K	kinetic current
IPA	isopropyl alcohol
J	current density
JCPDS	Joint Committee on Powder Diffraction Standards
J_K	kinetic current density
JK [MeOH]	specific activity in the presence of methanol
kg	kilogram
K-L	Koutecky - Levich
kV	kilovolts
kW	kilowatt
L	liter
LSV	linear sweep voltammogram
M	molar
MCFC	molten carbonate fuel cell
MEA	membrane electrode assembly
MeOH	methanol
mg	milligram
mg_{Pt}	milligrams of platinum
min	minute
mL	milliliter
mM	millimolar
MOR	methanol oxidation reaction
mV	millivolts
$NaBH_4$	Sodium Borohydride
nm	nanometer
NP	nanoparticle
NP/C	carbon supported nanoparticles
NR	nanorod
NT	nanotube
NW	nanowire
NW/C	carbon supported nanowires
O_{ads}	Adsorbed oxygen
ODA	octadecylamine
ORR	oxygen reduction reaction
PEMFC	polymer electrolyte membrane fuel cells
Pt_{ML}	platinum monolayer
RDE	rotating disk electrode
RHE	reversible hydrogen electrode
rpm	revolutions per minute

s	seconds
SAED	selected area electron diffraction
SEM	scanning electron microscopy
SI	international system of units
SOFC	solid oxide fuel cell
STEM	scanning transmission electron microscopy
T	temperature
TEM	transmission electron microscopy
UPD	under potential deposition
UV	ultraviolet
UV/vis	ultraviolet/visible
V	volts
W	watt
XRD	X-ray powder diffraction
α	lattice parameter
λ	X-ray wavelength
μC	micro-Coulombs
μm	micrometer

Acknowledgments

First and foremost, I would like to thank Dr. Stanislaus Wong for his persistent effort and support as a research advisor, over the course of my doctoral course work and research. His guidance, expertise, and support over the past five years have greatly enhanced my Ph.D. career. I would also like to express genuine gratitude to my committee chair, Dr. Andreas Mayr, and my third member, Dr. Joseph Lauher, for their challenging questions and insightful discussions on my research projects. I would also like to thank Dr. Jingguang Chen for taking the time to serve as the outside member of my committee. Additionally, I would also like to thank Dr. Radoslav Adzic for his mentorship. His expertise and commitment to training me in the fields of electrochemistry and catalysis have provided me with both extremely useful and indispensable experience that will be helpful to me throughout my career. I would also like to thank him for providing access to his research facilities over the course of my Ph.D.

I would like to acknowledge my fellow group members, Lei Wang, Crystal Lewis, Coray McBean, Dominic Moronta, Shiyu Yue, and Luyao Li, for their support and help during my research career. In addition, I would like to extend my deepest gratitude to a previous group member, Dr. Christopher Koenigsmann, for his expert guidance in the initial stages of my research career, and for providing me with the fundamental knowledge concerning electrochemical characterization and analysis. Additionally, I would like to thank Dr. James Quinn and Susan Van Horn, in addition to a number of collaborators including Dr. Anatoly Frenkel, Dr. Ping Liu, Dr. Mircea Cotlet, and Dr. Dong Su, for their assistance with various spectroscopy and microscopy techniques as well as their help in the data interpretation; Dr. Yuanyuan Li for enabling me to properly collect X-ray Absorption Spectroscopy data; as well as

Dr. Prahlad Kumar Routh and Dr. Jinkyu Han for their contribution to the collection and interpretation of optical Upconversion data.

I am very grateful for the assistance and support of the faculty and staff in the Chemistry Department at Stony Brook University as well as the Condensed Matter Physics and Materials Sciences Division, the Chemistry Department, and the Center for Functional Nanomaterials at Brookhaven National Lab.

Finally, I would like to sincerely thank my family and friends, especially my parents, Heping Liu and Jing Xi, along with my friends for their unconditional love and support during the past 5 years. I could not have succeeded during my PhD career without their positive reinforcement and encouragement.

List of Publications

1. **Haiqing Liu**, Radoslav R. Adzic, and Stanislaus S. Wong, "Multi-functional ultrathin Pd_xCu_{1-x} and Pt~Pd_xCu_{1-x} one-dimensional nanowire motifs for various small molecule oxidation reactions", *ACS Appl. Mater. Interf.*, **7(47)**, 26145-26157 (2015).
2. **Haiqing Liu**, Wei An, Yuanyuan Li, Anatoly I. Frenkel, Kotaro Sasaki, Christopher Koenigsmann, Dong Su, Rachel M. Anderson, Richard M. Crooks, Radoslav R. Adzic, Ping Liu, and Stanislaus S. Wong, "In situ Probing of the Active Site Geometry of Ultrathin Nanowires for the Oxygen Reduction Reaction", *J. Am. Chem. Soc.*, **137(39)**, 12597-12609 (2015).
3. **Haiqing Liu**, Luyao Li, Megan E. Scofield, and Stanislaus S. Wong, "Synthesis, Properties, and Applications of Ultrathin Metallic Nanowires and Associated Heterostructures", invited contribution, *APL Materials*, **3(8)**, 080701/1-15 (2015).
4. **Haiqing Liu**, Christopher Koenigsmann, Radoslav R. Adzic, and Stanislaus S. Wong, "Probing Ultrathin One-dimensional Pd-Ni Nanostructures as Oxygen Reduction Reaction Catalysts", *ACS Catalysis*, **4(8)**, 2544-2555 (2014).
5. Crystal S. Lewis, **Haiqing Liu**, Jinkyu Han, Lei Wang, Shiyu Yue, Nicholas A. Brennan, and Stanislaus S. Wong, "Probing Charge Transfer in a Novel Class of Luminescent Perovskite-Based Heterostructures Composed of Quantum Dots Bound to RE-Activated $CaTiO_3$ Phosphors", invited contribution, *Nanoscale*, **8**, 2129-2142 (2016).
6. Lei Wang, Jinkyu Han, Yuqi Zhu, Ruiping Zhou, Cherno Jaye, **Haiqing Liu**, Zhuo-Qun Li, Gordon T. Taylor, Daniel A. Fischer, Joerg Appenzeller, and Stanislaus S. Wong, "Probing the Dependence of Electron Transfer on Size and Coverage in Carbon Nanotube-Quantum Dot Heterostructures", *J. Phys. Chem. C*, **119(47)**, 26327-26338 (2015).
7. Megan E. Scofield, **Haiqing Liu**, and Stanislaus S. Wong, "A Concise Guide to Sustainable PEMFCs: Recent Advances in Improving both Oxygen Reduction Catalysts and Proton Exchange Membranes", invited contribution, *Chem. Soc. Rev.* (inside cover), **44(16)**, 5836-5860 (2015).
8. Jinkyu Han, Coray McBean, Lei Wang, Cherno Jaye, **Haiqing Liu**, Daniel A. Fischer, and Stanislaus S. Wong, "Synthesis of Compositionally-Defined Single-Crystalline Eu^{3+}-Activated Molybdate-Tungstate Solid Solution Composite Nanowires and Observation of Charge Transfer in a Novel Class of 1D $CaMoO_4$-$CaWO_4$: Eu^{3+} – 0D CdS/CdSe QD Nanoscale Heterostructures", *J. Phys. Chem. C*, **119(7),** 3826-3842 (2015).
9. Jinkyu Han, Coray McBean, Lei Wang, Jessica Hoy, Cherno Jaye, **Haiqing Liu**, Zhuo-Qun Li, Matthew Y. Sfeir, Daniel A. Fischer, Gordon T. Taylor, James A. Misewich, and Stanislaus S. Wong, "Probing structure-induced optical behavior in a new class of self-activated luminescent 0D/1D $CaWO_4$ metal oxide – CdSe nanocrystal composite heterostructures", *Chem. Mater.*, **27(3)**, 778-792 (2015).
10. Megan E. Scofield, Christopher Koenigsmann, Lei Wang, **Haiqing Liu**, and Stanislaus S. Wong, "Tailoring the Composition of Ultrathin, Ternary Alloy PtRuFe Nanowires for the Methanol Oxidation Reaction and Formic Acid Oxidation Reaction", *Energy & Environmental Sciences*, **8(1)**, 350-363 (2015).

11. Jonathan M. Patete, Jinkyu Han, Amanda L. Tiano, **Haiqing Liu**, Myung-Geun Han, J. W. Simonson, Yuanyuan Li, Alexander C. Santulli, M.C. Aronson, Anatoly I. Frenkel, Yimei Zhu, and Stanislaus S. Wong, "Observation of Ferroelectricity and Structure-Dependent Magnetic Behavior in Novel One-Dimensional Motifs of Pure, Crystalline Yttrium Manganese Oxides", *J. Phys. Chem. C*, **118 (37)**, 21695-21705 (2014).
12. Crystal S. Lewis, Lei Wang, **Haiqing Liu**, Jinkyu Han, and Stanislaus S. Wong, "Synthesis, Characterization, and Formation Mechanism of Crystalline Cu and Ni Metallic Nanowires under Ambient, Seedless, Surfactantless Conditions", *Crystal Growth and Design*, **14(8)**, 3825-3838 (2014).
13. Lei Wang, Jinkyu Han, Jessica Hoy, Fang Hu, **Haiqing Liu**, Molly M. Gentleman, Matthew Y. Sfeir, James A. Misewich, and Stanislaus S. Wong,"Probing Differential Optical and Coverage Behavior in Nanotube-Nanocrystal Heterostructures Synthesized by Covalent versus Non-covalent Approaches", invited contribution, 'Organometallic and Coordination Derivatives of Nanocarbons' special issue, *Dalton Transactions*, **43(20)**, 7480-7490 (2014).
14. Lei Wang, **Haiqing Liu**, Robert M. Konik, James A. Misewich, and Stanislaus S. Wong, "Carbon Nanotube-based Heterostructures for Solar Energy Applications", invited contribution, *Chem. Soc. Rev.*, **42(20)**, 8134-8156 (2013).
15. Christopher Koenigsmann, Megan E. Scofield, **Haiqing Liu**, and Stanislaus S. Wong, "Designing Enhanced One-Dimensional Electrocatalysts for the Oxygen Reduction Reaction: Probing Size-and Composition-Dependent Electrocatalytic Behavior in Noble Metal Nanowires", invited Perspective, *J. Phys. Chem. Lett.*, **3(22)**, 3385-3398 (2012).

Chapter 1. Introduction to Energy-Related Nanomaterials

1.1. Brief introduction to "Nano", Nanomaterials and Nanotechnologies

According to the international system of units (SI), nano- (symbol n) is a unit prefix meaning one billionth (i.e., 10^{-9}). In order to place the nanometer length scale in perspective, the diameter of a human hair is about 80,000 nm wide. Conversely, it is becoming popular that the term nanomaterials (NMs) includes natural or manmade particles with at least one dimension of 100 nm or less, while nanoparticles (NPs) encompasses those materials with at least two dimensions between 1 and 100 nm.[1] The term "nanotechnology" is generally associated with the study and control of phenomenon and materials at length scales of tens or hundreds of nanometers. The fundamental motivation for the development of nanotechnology as well as for the expansion of the nanomaterials' market are the ever increasing range of possible applications, for example by their increasing use in the health care and the energy storage industry.[2] Also, a decrease in the price of nanomaterials is expected, due to advanced production techniques which drive the market. Specifically, nanomaterials have great potential in electrical and electronics applications, because of their extraordinary electrical conductivity. In upcoming years, the advance of energy-related nanotechnology is expected to maintain a pace of growth of 10% or more.[3] Statistically, world demand for nanomaterials has risen to $5.5 billion in 2016, while nanotubes, nanoclays, and quantum dots represent the fastest growing types of nanomaterials that can be commercialized.[4]

Nanomaterials differ from micron-sized and bulk materials not only in the scale of their characteristic dimensions but also in the fact that they may possess new physical properties and offer diverse possibilities for various technical applications. For instance, when the characteristic dimensions of semiconductors are reduced to below a certain size, quantum confinement leads to specific changes in their electronic structures, i.e. their bandgaps.[5] By analogy, while bulk-sized gold remains chemically inert, when gold nanoparticles shrink to less than 3 nanometers in diameter, they exhibit excellent catalytic activity due to the relatively smaller shrinkage of their *d*-orbitals by comparison with that of the *s*- and *p*-orbitals.[6, 7] The understanding of these unique properties associated with various types of nanomaterials enables us to rationally tune these structures to meet the specific requirements of the desired applications.

Essentially, nanomaterials can be categorized by their morphologies. That is, there are four different types, including 0D, 1D, 2D, and 3D motifs. In the case of either isotropic or 0D particles (e.g. sphere), because of the spatial confinement of electrons to the same extent in all the three dimensions, most of the physical properties will remain approximately the same, regardless of direction.[8] Therefore, tuning the properties of these particles will be difficult as compared with other materials that show direction and dimension-dependent physical and chemical properties; these are generally known as anisotropic nanomaterials. Indeed, anisotropic nanomaterials come under the category of 1, 2, and 3D nanostructures, wherein electron movement is possible in these many different dimensions. Specifically, the restricted, i.e. the spatially confined motion of electrons, holes, excitons, phonons, and plasmons with respect to the physical shape of an object is the reason for the change in properties of typical nanosystems.[9] The most important and visible change that is often manifested is in color, due to the confinement of electrons and consequent changes in electronic energy levels.[10] The unique and finely-tuned physical and chemical properties of nanomaterials indeed render them as ideal candidates for devising new applications.

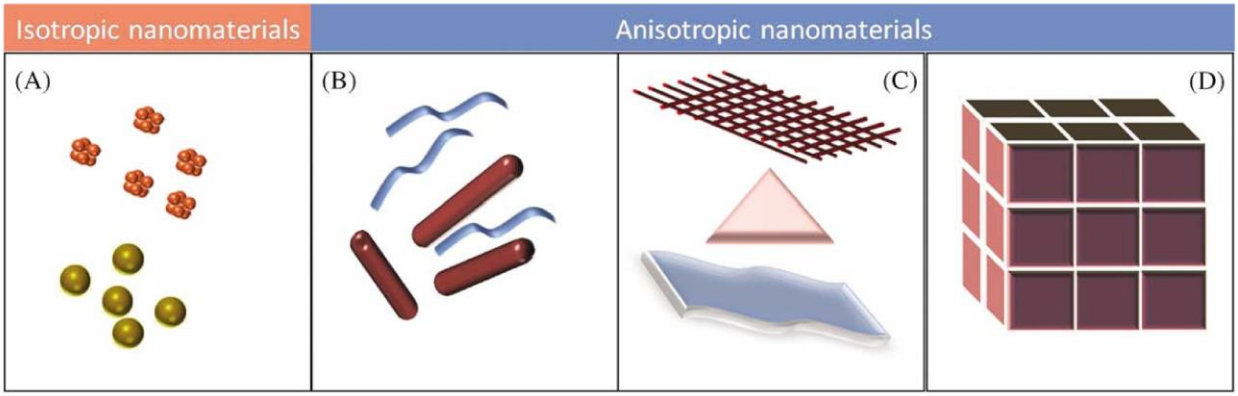

Figure 1.1. Various kinds of nanomaterials. (A) 0D spheres and clusters. (B) 1D nanofibers, wires, and rods. (C) 2D films, plates, and networks. (D) 3D nanomaterials. Reprinted with permission from ref 8. Copyright 2011, Co-Action Publishing.

After the discovery of carbon nanotubes,[11] which are considered as a standard example of nanomaterials exhibiting unique physiochemical properties, considerable attention has been paid to the shape-dependent synthesis of diverse nanomaterials. In addition, the assembly of ordered one-dimensional (1D), two-dimensional (2D), and three-dimensional (3D) arrays of anisotropic nanoparticles brings novel properties into the resulting system, which may be entirely different from the properties of individual nanoparticles. A diverse spectrum of anisotropic nanomaterials have been reported in the literature including nanorods,[12, 13] nanowires,[14-16] nanotubes,[17] and so forth, belonging to 1D; triangles,[18-20] plates and sheets,[21, 22] ribbons,[23] and so on are associated with 2D; whereas pyramids,[24, 25] stars,[26] flowers,[27-29] nanourchins,[30] tadpoles,[31] nanocages,[32, 33] nanorice,[34] nanocorns,[35] nanoboxes,[36, 37] nanocubes,[38] triangular nanoframes,[39] nanodumbbells,[40] and others are often ascribed to 3D nanostructures.

Nanomaterials offer many advantages in terms of energy conversion and storage applications. Energy conversion and storage involve physical interaction and/or chemical reaction at the surface or interface, so the specific surface area, surface energy, and surface chemistry all play a very important role.[41] The surface impacts are not limited to the kinetics and rate only; the surface energy and surface chemistry can have either appreciable or significant influences upon the thermodynamics of heterogeneous reactions occurring at the interface as well as the nucleation and subsequent growth processes, when phase transitions are involved.[42] The smaller dimensions of nanomaterials may also offer more favorable mass, heat, and charge transfer, as well as accommodate for dimensional changes associated with some chemical reactions and phase transitions.[43]

Specifically, regarding fuel cells, 1-D materials possess high aspect ratios, fewer lattice boundaries, longer segments of smooth crystal planes, and a relatively low number of surface defect sites, all of which are desirable attributes for fuel cell catalysts.[14, 44-47] As an example, in-situ grown Pt nanowire arrays have demonstrated superior performance as compared with their Pt nanoparticle counterparts, as noted through relevant membrane electrode assembly measurements.[48] By analogy, when it comes to solar cells, silicon nanowire array (SiNWA) photoelectrodes with well-defined morphologies exhibit a high efficiency of carrier collection, which correlates directly with a much larger short-circuit photocurrent density (J_{SC}) and a higher photoelectric conversion efficiency (η) as compared with those of their film counterparts possessing relatively random structures.[49] Thus, the main focus of this thesis, not unlike many other previous works, is to design nanomaterials with tunable chemical compositions as well as well-defined morphologies towards energy-related applications including both fuel cells and photovoltaic cells.

In the following sections, we will be providing a brief introduction to fuel cells (Section 1.2), with a focus on their categorization and structure. We will also discuss the key chemical reactions associated with the electrocatalysts being utilized, as well as recent advances and shortfalls, associated with these catalysts. Specifically, the mechanisms and common catalysts associated with small molecule reactions including oxygen reduction reaction (ORR), formic acid oxidation reaction (FAOR), methanol oxidation (MOR) reaction, and ethanol oxidation reaction (EOR) will be discussed in Section 1.2.2. In Section 1.3, we will be describing the current status of the development of the upconversion material-based solar cells, as well as remaining issues to be resolved. Section 1.4 highlights the objectives of this dissertation, which incorporates a brief description of each individual project.

1.2. Fuel Cells

A fuel cell is a device that converts the chemical energy from a fuel into electricity through a chemical reaction.[50] Fuel cells have a variety of different categories; however, they all work in a similar manner. In general, they are composed of three adjacent segments: the anode, the electrolyte, and the cathode. Two half-reactions occur at the interfaces of the three different segments, while the net result is that fuel (e.g., hydrogen, methanol and so on) is consumed, water or carbon dioxide is created, and an electric current is thereby generated.

1.2.1. Categories and Structures

Fuel cells are conventionally categorized according to their electrolyte material. They differ in their power outputs, operating temperatures, electrical efficiencies, and typical applications. PEMFCs have the largest range of applications, as they are extremely flexible. PEMFCs also are the most promising candidates for transport applications, due to their high power density, fast startup time, high efficiency, low operating temperature, as well as easy and safe handling.[51] In terms of their structure, the PEMFC (proton exchange membrane fuel cell) uses a water-based, acidic polymer membrane as the electrolyte and electrodes composed of platinum-based catalysts. It primarily utilizes pure hydrogen as the fuel, but can also employ reformed natural gas, thereby removing carbon monoxide.[52] Generally, the operating temperature is below 100 °C. Meanwhile, a sub-category of PEMFCs, i.e., high temperature PEMFC (HT-PEMFC), can be designed by changing the electrolyte from a water-based to a mineral acid-based system, which operates up to 200°C. Typically, commercialized PEMFCs are primarily focused on the small scale (i.e. 50-250 kW for decentralized use or <10 kW for households).[53] However, PEMFCs are generally too expensive to be either functionally competitive or economically feasible. Therefore, other types of fuel cells, including but not limited to alkaline fuel cells (AFC), phosphoric acid fuel cells (PAFCs), molten carbonate fuel cells (MCFCs) and solid oxide fuel cells (SOFCs), have been developed and optimized throughout the past few decades to cater to various applications.

An AFC (alkaline fuel cell) uses an alkaline electrolyte and is fueled with pure hydrogen and oxygen. AFCs offer some advantages over other fuel cells, such that they are easier to handle because their operating temperature is relatively low (roughly 23-70°C).[54] Another advantage is the higher reaction kinetics at the electrodes as compared with acidic conditions typically utilized in PEMFCs, thereby resulting in higher cell voltages. This high electrical efficiency permits the use of a lower quantity of a noble metal catalyst, such as platinum, which is expensive.[55] AFCs maintain the best performance when operating on pure hydrogen and oxygen, yet their intolerance to impurities, e.g., CO_x species, and short lifetimes hinder their role for terrestrial applications. Thus, they are predominantly used for extraterrestrial purposes.

The PAFC (phosphoric acid fuel cell) consists of electrodes composed of finely dispersed platinum catalyst on carbon as well as a silicon carbide structure that stores the phosphoric acid electrolyte. Phosphoric acid fuel cells (PAFCs) are possibly the most commercially well-developed fuel cells, operating at temperatures of 150 to 200°C.[56] One of the shortfalls of these devices lies in their relatively high operating temperature, which will cause heat and energy loss if the heat is not removed and used properly. Thus, efforts have been spent on reusing such energy in co-generation, and this work could potentially enhance the overall efficiency of phosphoric acid fuel cells from 40–50% to about 80%.[57] Meanwhile, the excessive heat generated by PAFCs can also be utilized to produce steam for air conditioning systems, combined-heat-and-power (CHP) applications, or other thermal energy consuming systems.[58]

The MCFC (molten carbonate fuel cell) uses a molten carbonate salt suspended in a porous ceramic matrix as the electrolyte with coal-derived fuel gas, methane, or natural gas, operating at temperatures of about 650°C.[59] MCFCs have the highest energy efficiency attainable from methane-to-electricity conversion, in the magnitude range of 250 kW to 20 MW.[60]

The SOFC (solid oxide fuel cell) uses a solid ceramic electrolyte that is composed of nonporous metal oxide. Typically, the electrolyte is composed of zirconium oxide (ZrO_2) treated with Y_2O_3, and O_2^- is transported from the cathode to the anode.[61] Any CO in the reformate gas is oxidized to CO_2 at the anode. Temperatures of operation are typically 800-1000°C. This system is best suited for base-load utility applications, operating on coal-based gasses.[62]

Despite their differences in terms of either incorporated electrolyte and/or the presence of electrocatalysts, all of the different types of fuel cells described above possess a similar structure. Hence, we herein utilize the schematic of a typical PEMFC, shown in Figure 1.2, to illustrate various components of a fuel cell, especially the key constituent components and in particular, the catalyst layers.

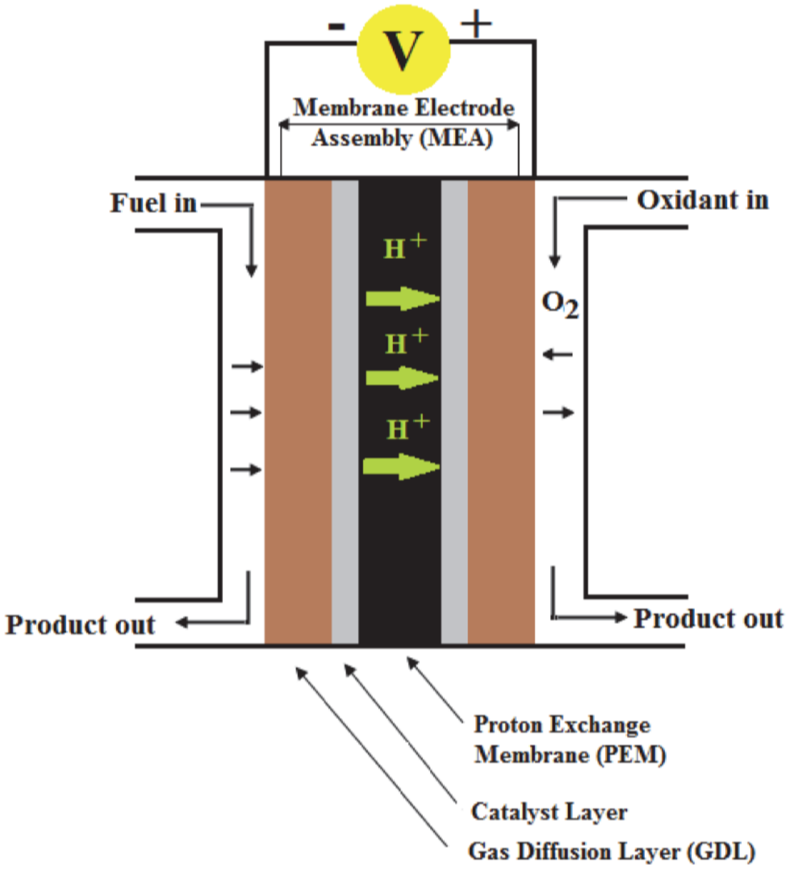

Figure 1.2. Schematic of a single typical PEMFC. Reprinted with permission from ref 63. Copyright 2011 InTech Open.

The most direct and effective method for the activity validation of the synthesized catalysts is to directly use them in a single fuel cell. For fuel cells, the activity of a catalyst can be deduced from their performance. The most commonly used way to reflect the performance of the fuel cells is the polarization (or current-voltage) curve of the MEA which is the core of the PEM fuel cell,[63] which itself is composed of an anode gas diffusion layer (GDL), an anode catalyst layer, a membrane (the PEM), a cathode catalyst layer, and a cathode gas diffusion layer. Figure 1.2 schematically shows the components of a single typical PEMFC.

Two data collection modes are frequently used in obtaining the polarization curve, conducted either by (i) adjusting the cell voltage then recording the current density, or by (ii) adjusting the current density and then recording the cell voltage, with the latter being the most popularly used in the fuel cell performance data collection.[64] A typical polarization curve of a cell obtained by collecting the cell voltage as a function of current density is shown in Figure 1.3,[65] which can then be used to yield the power density of the MEA (cell voltage × current density), plotted as a function of current density. From the power density curve, the maximum power density of the fuel cell MEA can then be calculated; other parameters that can be computed include the maximum volume power density and the mass power density of a fuel cell stack. In principle, apart from the catalysts, the performance of a fuel cell (i.e. the polarization curve) is also affected by the quality and property of the MEA as well as the operating conditions, such as temperature, pressure, relative humidity (RH), gas flow rates, and so forth. Therefore, for the sake of systematic improvements in the efficiency of the fuel cell, a better understanding of the effects of the quality and property of the MEA upon the performance of the fuel cell is essential.

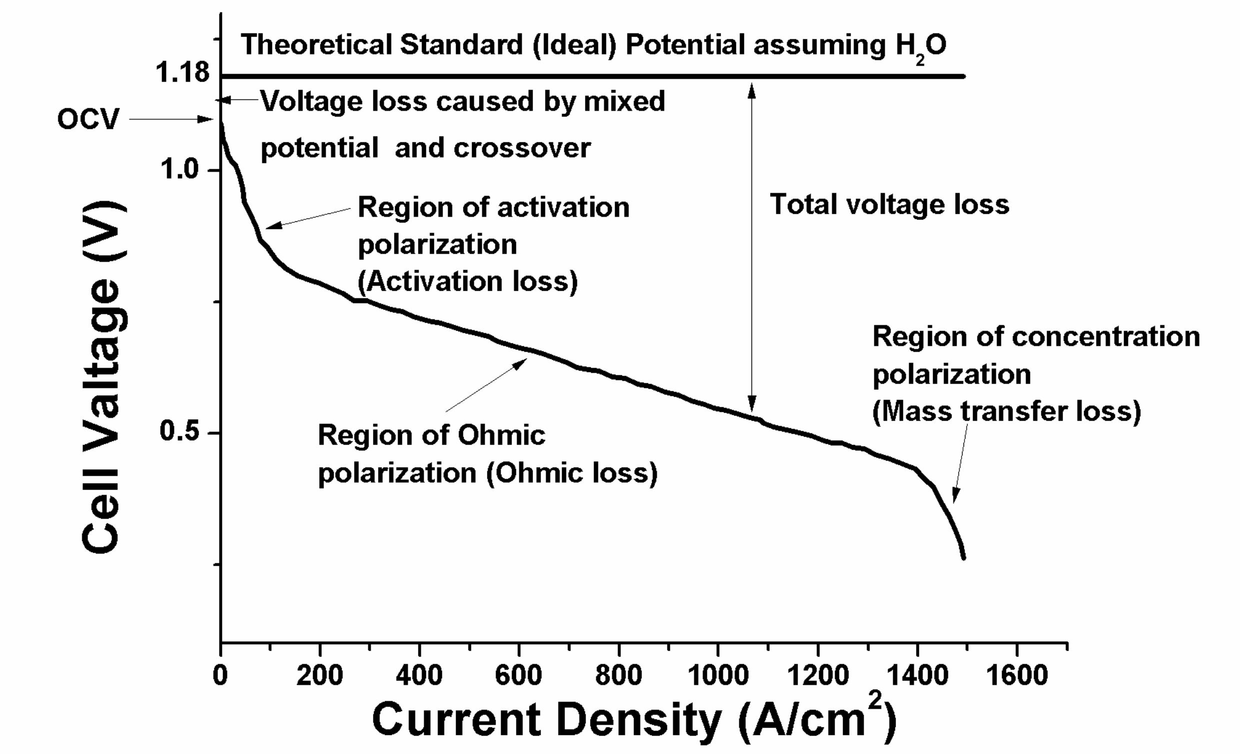

Figure 1.3. Typical polarization curve of PEMFCs. Reprinted with permission from ref 65. Copyright 2011 Springer.

1.2.2. Fuel Cell Catalysts and Their Issues

In this section, we will be discussing the chemical reactions involved in two of the most common types of fuel cells, including both proton exchange membrane fuel cells (PEMFCs) and alkaline fuel cells (AFCs), along with their corresponding electrocatalysts. Specifically, the focus will be placed upon catalysts for the oxygen reduction reaction (ORR) and the formic acid oxidation (FAOR) in PEMFCs, as well as for the methanol oxidation reaction (MOR) and the ethanol oxidation reaction (EOR) in AFCs.

1.2.2.1. Electrocatalysts for Proton Exchange Membrane Fuel Cells (PEMFCs)

(A) Cathodic Reaction

In a fuel cell, oxygen (O_2) is electrochemically reduced at the cathode through the mediation of the oxygen reduction reaction (ORR). Fundamentally, the mechanism of oxygen reduction reaction in acidic media involves either the direct 4-electron reduction pathway from O_2 to produce H_2O or the 2-electron reduction pathway from O_2 to form hydrogen peroxide (H_2O_2) in one of the following steps (Equations 1.1 and 1.2).

$$O_2 + 4\ H^+ + 4\ e^- \rightarrow 2\ H_2O \text{ (four-electron pathway)} \qquad (1.1)$$

$$O_2 + 4\ H^+ + 4\ e^- \rightarrow H_2O_2 + 2\ H^+ + 2\ e^- \rightarrow 2\ H_2O \text{ (two-electron pathway)} \qquad (1.2)$$

Water is directly produced when oxygen is reduced through the four-electron reduction mechanism. On the other hand, the two-electron reduction occurs at low potentials and produces hydrogen peroxide as an intermediate byproduct. As previously alluded to, the most commonly employed metal in catalysts for ORR in acidic media is Pt, due to its ability to reduce oxygen efficiently at low temperatures (normally 60~120°C).[66] We should note that previous reports have shown that the formation of Pt-OH beyond 0.8 V is derived not only from the interaction of O_2 with Pt, but also from the reaction of H_2O with Pt, thereby inhibiting O_2 reduction.[67, 68]

In terms of relevant benchmarks, the ORR activity is usually expressed in terms of two types of measurements, namely the specific area activity (SA) and the Pt mass activity (MA). In particular, SA possesses a unit of mA/cm^2, indicating a current response that is normalized to surface area, i.e., per cm^2 of catalyst surface, while MA maintains a unit of A/mg_{Pt}, denoting that the current is normalized to the actual amount of Pt being utilized. The United States Department of Energy (DOE)[69] has proscribed a set of 'benchmark' standards for research purposes, with an MA target of 0.44 A/mg_{Pt} @ 900 $mV_{iR\ free}$ and a corresponding SA target of 0.72 mA/cm^2 @ 0.9 V for electrocatalysts for use in the portable applications market by the year 2017. By comparison, the currently commonly employed commercial catalyst, Etek Pt/C, typically achieves an SA of 0.2 mA/cm^2 and MA of 0.1 A/mg_{Pt}. This reality further supports the notion that the electrochemical activity needs to be dramatically and tangibly improved upon for widespread commercial applicability.

Reduction of Pt usage

One of the most common strategies to reduce the amount of Pt employed in a catalyst is by alloying Pt itself with either another metal or metals. Studies have shown that alloying with 3*d* transition metals, such as Mn, Fe, Ni, Co, and Cu, could enhance the ORR performance.[70] Specifically, the origin behind the observed improvement in activity is believed to be attributed to the downshift of the *d*-band center[71] of the Pt catalyst induced by the presence of the additional 3*d* transition metal(s), thereby leading to a lower coverage of oxygenated species (i.e. OH^-) at normal operating potentials, and thus increasing the number of Pt active sites, accessible to oxygen molecules and protons. This will, in turn, render these oxygenated species present to be more mobile on the surface, such that they can interact with available protons, and thereby favor the desorption of water molecules. As a result, these alloyed structures do typically exhibit higher ORR activities as compared with commercial, pure Pt NPs.

More recently, controlling the morphology of as-prepared Pt-based metal alloy nanostructures has become a primary area of focus. To emphasize the significance of morphology, Yang et al.[72] noted that alloyed Cu_3Pt nanoframes are more effective for ORR by comparison with analogous core-shell Cu-Pt nanoparticles. Similarly, a Pt mass activity record of 3.3 A/mg_{Pt} has been observed by Xia et al. with 9 nm Pt-Ni octahedra, representing over a ten-fold activity improvement as compared with their spherical NP counterparts.[73] In effect, the reported Pt−Ni octahedra gave rise to a 17-fold higher Pt mass activity at 0.9 V along with a ~50-fold improvement in specific activity at 0.93 V, all relative to the behavior of conventional, state-of-the-art Pt/C catalysts.

The concept of developing even more sophisticated Pt-based hierarchical structures has materialized and manifested itself in the production of novel core-shell, ternary alloy, hierarchical ternary, and quaternary core-shell structures.[74] Specifically, the core-shell motif itself has three primary benefits toward enhancing the intrinsic activity of electrocatalysts.[71] *First*, a so-called advantageous 'ligand effect', induced by the dopant metal upon the overall catalytic performance, is hypothesized in which the transition metal 'M' core will couple with the external Pt shell, thereby resulting in a beneficial coupled electronic and structural effect, which should increase reaction kinetics. *Second*, it optimizes the use of Pt, thereby minimizing Pt loading, and allows for every surface Pt atom to be catalytically accessible. *Third*, the addition of the transition metal 'M' will lower the energy of the Pt *d*-band and create *d*-band vacancies, thereby enabling a lowered binding energy of oxygen-containing species.

Nevertheless, due to their structural complexity as compared with simple alloys, core-shell structures remain controversial due to potential issues associated with their degradation behavior and corresponding durability. To mitigate for such problems, many recent studies have deliberately sought to optimize the distribution of different elements. For instance, one of the reported strategies has sought to utilize gold (Au) as an "interlayer" between a Ni core and a Pt-

Ni alloy shell.[75] According to Stamenkovic et al., this complex hierarchical material combined the stabilizing effect of Au with the use of a low-cost core material, i.e. Ni. Based upon experimental results, their catalysts exhibited an 8-fold increase in activity as compared with Pt NPs alone. In addition, this core-shell catalyst underwent less than 10% activity loss after 10,000 potential cycles, thereby representing a far better result than what has been previously obtained with comparative structures such as (i) PtNi/C with a multilayered Pt-skin, (ii) Pt/C, and (iii) PtNi/C with Pt-skeleton surfaces, respectively.

Design one-dimensional Pt-monolayer catalysts

Following up on previous studies, in recent years, a new approach has been developed towards designing and synthesizing electrocatalysts that significantly reduce the Pt content and surpass the oxygen reduction reaction (ORR) activity of state-of-the-art carbon-supported Pt electrocatalysts.[76] These electrocatalysts consist of a monolayer of Pt on carbon-supported metal or metal-alloy nanoparticles and maintain the highest utilization of Pt, since almost every Pt atom is present on the surface and can participate in the electrocatalytic reactions. These electrocatalysts are referred to as platinum monolayer (Pt_{ML}) electrocatalysts.

Meanwhile, our lab has expended a good deal of effort in developing ultrathin Pt-based nanowires (diameters less than 5 nm) as viable structural motifs. As we have previously discussed, one-dimensional materials possess several beneficial merits toward fuel cell applications, including high aspect ratios, fewer lattice boundaries, longer segments of smooth crystal planes, and a relatively low number of surface defect sites.[77] As an extreme case for one-dimensional materials, ultrathin motifs not only maximize the surface area-to-volume ratio but also decrease the amount of catalytically inaccessible material within the interior of the wire. These ultrathin nanowires can therefore generate superior activity as compared with both larger Pt nanotubes as well as Pt nanoparticles.[77] As one key salient example relevant to the current paper, we have demonstrated that our ultrathin, acid-treated, unsupported nanowires displayed an electrochemical surface area activity (ECSA) of 1.45 mA/cm^2, which was nearly 4 and 7 times greater than that of analogous, unsupported 200 nm-diameter Pt NTs and of commercial-supported Pt NPs, respectively.

Combining both of these two favorable principles of one-dimensionality coupled with the core-shell motif, our group has previously synthesized hierarchical 1D nanostructures possessing a Pt-monolayer-shell combined with a Pd_9Au core.[78] Specifically, a volcano-type composition dependence was observed in the ORR activity of the $Pt{\sim}Pd_{1-x}Au_x$ NWs as the Au content is increased from 0 to 30% with the activity of the $Pt{\sim}Pd_9Au$ NWs (0.98 mA/cm^2, 2.54 A/mg_{Pt}), representing the optimum performance. We also found that the structural integrity of the 1D morphology was still well preserved even after a run of 30,000 potential cycles, and furthermore, a slight enhancement in activity was observed, possibly due to a preferential restructuring of the thin, outer Pt monolayer.

In this thesis, as a continuation of our previous successful exploration, we have fabricated ultrathin (~2 nm) Pd-Ni nanowires. We aim to (1) develop a synthesis approach that enable us to deliberately tune the chemical compositions of these nanowires; (2) determine the relationship between chemical composition and ORR activity; as well as (3) fabricate Pt~PdNi hierarchical ultrathin nanowires and examine its ORR performances. Our results have demonstrated that our most optimized sample, i.e. $Pt{\sim}Pd_{0.90}Ni_{0.10}$ ultrathin nanowires, exhibited a specific activity of

0.62 mA/cm^2 and a corresponding mass activity of 1.44 A/mgPt at 0.9 V, representing 3-fold and 14-fold increases in activities over commercial Pt nanoparticles, respectively.

(B) Anodic Reaction

The electro-oxidation of formic acid (FA) on Pt and Pd electrodes has attracted much attention since the 1960s,[79-81] mainly due to its importance in the understanding of the oxidation of methanol and formaldehyde, as well as the development of direct formic acid fuel cells (DFAFCs).[82] Specifically, DFAFCs possess the advantages of high power density, fast oxidation kinetics, high theoretical cell potential, and less severe fuel crossover issue over analogous fuel cells, utilizing other fuels such as methanol and ethanol.[83, 84]

Dual pathways are widely recognized[85] for the net decomposition of FA, namely, dehydrogenation (direct pathway), and dehydration (indirect pathway), as shown in the following equations 1.3 through 1.7:

Direct Pathway:

$$HCOOH \rightarrow \text{active intermediate} \rightarrow CO_2 + 2H^+ + 2e^- \text{ (electrooxidation)} \qquad (1.3)$$

$$\rightarrow CO_2 + H_2 \text{ (self-dehydrogenation)} \qquad (1.4)$$

Indirect pathway:

$$HCOOH + M \rightarrow M\text{-}CO_{ad} + H_2O \qquad (1.5)$$

$$H_2O + M \rightarrow M\text{-}OH_{ad} + H^+ + e^- \qquad (1.6)$$

$$M\text{-}CO_{ad} + M\text{-}OH_{ad} \rightarrow 2M + CO_2 + H^+ + e^- \qquad (1.7)$$

(In equations 1.5~1.7, M = Pt or Pd)

In terms of the catalysts, unlike ORR, Masel and coworkers have discovered that carbon-supported Pd is superior in terms of activity for formic acid oxidation as compared with Pt, because it favors the direct oxidation pathway, which avoids the formation of the catalyst poisoning intermediate (CO).[86] In other words, in the indirect pathway, formic acid adsorbs onto the Pt surface which thereby forms an intermediate consisting of an adsorbed CO species, blocking the Pt active sites and thereby causing a reduction in overall activity. According to Eq. 1.6, the adsorbed OH groups are required to further oxidize the adsorbed CO intermediate into the gaseous CO_2 end product, which is unlikely to occur within the potential range of a typical FAOR (0.1V~0.7V, vs. RHE).

Towards the goal of understanding the mechanism of formic acid electrooxidation on Pd-based surfaces, a variety of nanocatalysts with high catalytic activity, durability, and lower cost have been produced. In terms of the size, the smaller the nanoparticle, the lower its *d*-band center, which in turn results in a decrease in its adsorption energy. With respect to the oxidation of formic acid, the lowering of the *d*-band center reduces the binding energy of hypothetical intermediates, thereby enhancing the rate of reaction.[87] Such size effects in formic acid electro-oxidation have been investigated and verified by Zhou and Lee using a series of carbon-supported Pd nanoparticles.[88]

In terms of the chemical composition, the expectation is that alloys should facilitate and hopefully improve upon the resulting catalytic reactivity. Hence, as a relatively less costly, earth-abundant, and benign metal, Cu represents a particularly promising candidate for forming Pd-M alloy-based electrocatalysts. Therefore, considerable efforts have been devoted towards experimentally preparing various types of Pd-Cu binary nanomaterials in order to improve upon overall catalytic activity. In a previous study, PdCu bimetallic films with 3D porous structures were generated using a modified template method coupled with a subsequent galvanic replacement reaction; these as-prepared nanostructures yielded over a 30% improvement in mass activity as compared with commercial Pd nanoparticles (NPs).[89] Xu *et al.* also examined the electrocatalytic activities of PdCu alloys possessing different chemical compositions.[90] According to their analysis, the $Pd_{50}Cu_{50}$ chemical composition gave rise to superior catalytic activities, i.e. roughly 4-times higher than analogous elemental Pd nanostructures, and these particular high-performance materials were also more resistant to surface poisoning as compared with either other PdCu alloys or Pd itself.

In this thesis, we have also combined the ideas of (1) reduced size, (2) alloying, as well as the (3) one-dimensional motif discussed previously in the ORR section and have fabricated ultrathin (d ~ 2 nm) 1-D PdCu alloys with tunable chemical compositions, towards FAOR. To the best of our knowledge, in terms of novelty, this is the first time that one-dimensional $Pd_{1-x}Cu_x$ alloys of such small sizes have been utilized in catalyzing FAOR. Our results have demonstrated a “volcano”-shaped relationship between the chemical composition and the FAOR activities, peaking with a chemical composition of Pd_9Cu.

1.2.2.2. Electrocatalysts for Alkaline Fuel Cells (AFCs)

Alkaline fuel cells (AFCs) denote a sub-category of fuel cells that utilize anion-exchange membranes and hydroxide ion-based electrolytes. In recent years, they have been considered as viable alternatives to PEMFCs, among other types of fuel cells.[91] In fact, under similar operating conditions, AFCs produce current densities comparable to those of PEMFCs.[92] Moreover, cost analysis has shown that AFCs are at least competitive with PEMFCs for low power applications, such as hybrid vehicles.[92] More importantly, alkaline fuel cells possess numerous advantages over those of proton exchange membrane fuel cells in terms of both reaction kinetics and ohmic polarization. Specifically, in alkaline media, the reaction kinetics of both cathodic[93] and anodic[94] reactions are enhanced as compared with acidic media, and therefore, the same current density can often be obtained with lower catalyst loadings. Moreover, the less corrosive nature of an alkaline environment ensures a potentially greater longevity for these catalysts.[95] Therefore, AFCs represent a viable alternative to PEMFCs, and are competitive with their analogous, acidic media-based counterparts. In this section, we will be discussing the basics of both the cathodic reaction (i.e., alkaline ORR) and the anodic reaction (including both methanol oxidation and ethanol oxidation reactions in alkaline media), their corresponding electrocatalysts as well as current issues for these catalyst candidates, with a focus on the anodic reactions.

(A) Oxygen Reduction Reaction in Alkaline Media

Owing to the relatively less corrosive chemical environment associated with AFCs as compared with its acidic analogues, i.e. for PEMFCs, the possibility of utilizing non-precious metals has drawn much attention. In fact, ever since Jasinski reported cobalt phthalocyanine as an ORR electrocatalyst capable of operating in alkaline electrolytes in 1964,[96] an enormous amount of effort has been spent in terms of developing carbon-supported non-precious metal (Co, Fe, etc.) and even metal-free catalysts to replace the expensive Pt-based electrode within alkaline fuel cells.[97-100] Among non-precious metal catalysts, N, Fe-codoped carbon-based (Fe/N/C) electrocatalysts (Fe-based catalysts) denote some of the most promising candidates, because some of them exhibit high ORR activity in both acidic and alkaline media.[101-103] Fe-based catalysts can also be obtained through the high-temperature pyrolysis of either iron N_4 chelate complexes[104-106] or simple precursors of iron salts, i.e. nitrogen-containing components (aromatic[107] and aliphatic ligands[108-110] or other nitrogen-rich small molecules[111, 112]) on carbon supports. To date, state-of-the-art Fe-based catalysts have been found to exhibit much higher ORR activity and durability as compared with those of Pt-based catalysts in alkaline electrolytes.[103, 113-115] However, the detailed reaction mechanism associated with the Pt-free, porphyrin-based electrocatalyst remain unclear to this date.[116] Though the Fe-N-C site is considered to be mechanistically involved, a detailed understanding of its fundamental role and functionality in ORR remains sadly lacking. The fundamentals of and recent advances with respect to improving the performance of these catalysts can be found in several comprehensive reviews[101, 117, 118], but ORR in alkaline media will not be the focus of the work described herein.

(B) Methanol Oxidation Reaction

The methanol oxidation reaction (MOR) is the anodic reaction in alkaline fuel cells which utilizes methanol as their fuel; these are also known as alkaline direct methanol fuel cells (alkaline DMFCs).[119, 120] Historically, alkaline DMFCs suffered from problems resulting from the carbonation of the alkaline electrolyte, but several fuel cell platforms have been suggested which can overcome these problems, including the use of cells designed to operate with either carbonate electrolytes,[121] the use of recirculating electrolytes,[122, 123] or the use of anion-exchange membrane electrolytes.[119, 124-126]

A brief overview of some possible MOR pathways is given below. Both carbonate (complete oxidation) and formate (incomplete oxidation) species have been detected as products of the MOR in alkaline media. The half-cell reactions leading to the formation of these products are represented by equations 1.8 through 1.12

Mechanism (1):

$$CH_3OH + 4OH^- \rightarrow CO_{ads} + 4H_2O + 4e^- \quad (1.8)$$

$$CO_{ads} + 2OH_{ads} \rightarrow CO_2 + H_2O \quad (1.9)$$

$$CO_2 + 2OH^- \rightarrow CO_2^{3-} + H_2O \quad (1.10)$$

$$\text{Overall: } CH_3OH + 8OH^- \rightarrow CO_3^{2-} + 6H_2O + 6e^- \quad (1.11)$$

Mechanism (2):

$$CH_3OH + 5OH^- \rightarrow HCOO^- + 4H_2O + 4e^- \quad (1.12)$$

It has been demonstrated that in Pt-based catalysts, mechanism (1) will be dominant. In fact, on Pt surfaces, formate production commences at much higher potentials (> 0.7 V vs. RHE).[127, 128] In general, the steady-state methanol oxidation is a slow reaction.[129, 130] Methanol adsorption and dehydrogenation still proceed at a relatively low potential (< 0.4V vs. RHE), but the process is rapidly poisoned by the accumulation of CO (Eq. 1.8),[130] which is not readily oxidized at low potentials. As a result, resolving the CO-poisoning issue has been the main focus of designing highly active MOR electrocatalysts.

Meanwhile, MOR rates have been reported to be higher on both unsupported and carbon-supported Pt nanoparticle catalysts in alkaline electrolytes, especially as compared with analogous acidic media (sulfuric acid),[122, 123, 131] which is another reason why MOR in AFC has attracted relatively more attention in recent years as compared with its acidic counterpart, i.e. direct methanol fuel cells (DMFCs). The enhanced activity in alkaline media results from at least two factors: the lack of specifically-adsorbing spectator ions in alkaline solutions, and the higher coverage of adsorbed OH species at low potential, which are required for methanol oxidation.[132] Thus, two of the key approaches for improving reaction kinetics have been to (1) incorporate more oxophilic heteroatoms to provide OH_{ads} species at lower potential or to (2) deliberately alter the electronic structure of Pt, in order to achieve the most favorable affinity towards reaction intermediates, namely CO.

In terms of the catalysts being utilized, Pt-Ru binary nanoparticles have been the most thoroughly explored, since they provide for superior activity towards MOR in acidic media. Two effects are considered for the superior activity of binary Pt-Ru catalysts: the ligand effect and the bifunctional mechanism.[133-136] The ligand effect results from the modification of the electronic properties of platinum by ruthenium, thereby causing a decrease in the strength of the CO bond to the catalyst surface, as previously discussed in analogous ORR systems.[137] Meanwhile, in the bifunctional mechanism, ruthenium is believed to provide for oxygen-containing adsorbates at comparably negative potentials, which can thereby lead to oxidation of CO at nearby platinum sites.[138] Nonetheless, the overall cost-effectiveness of such Pt-alloy catalysts is still far from satisfactory, as the price of Pt remains high.

To mitigate for such issues, bimetallic Pd-M (where M = Fe, Co, Ni, Zn, Cu, or Au) alloys have been fabricated, because they can induce strain and ligand (electronic) effects.[139] Essentially, the strain effect manifests itself as a compressive strain within the Pt- or Pd- based alloy systems, which originates from the relatively smaller radius of the transition metals, as compared with that of either Pt or Pd.[76, 140-142] By contrast, the ligand effect denotes electric coupling between the overlayer and its supporting substrate, thereby resulting in electron redistribution between the noble metal skin and subsurface layers.[143, 144] Both of these two effects could effectively weaken the interaction between Pd and CO, thereby inducing high catalytic activities for the MOR and highlighting the great potential of these materials for the oxidation of methanol through a direct dehydrogenation pathway. As another example, PdCu bimetallic films with 3D porous structures were generated using a modified template method coupled with a subsequent galvanic replacement reaction; these as-prepared nanostructures possessed over a 30% improvement in mass activity as compared with commercial Pd nanoparticles (NPs).[89]

Moreover, the concept of core-shell structures has also been investigated. Indeed, in a Pt~Pd core-shell nanoparticular systems, the surface hydroxides (OH) are more readily formed in the presence of Pd within the catalyst matrix at relatively low potentials (0.6V), whereas the hydroxides are mainly supplied by the solution OH^- ion species at higher potential (> 0.8V) in Pt-only systems.[145-147] As demonstrated in the literature, this hydroxide species supplies the active oxygen atom that can oxidize both the intermediate carbon monoxide and other organic impurities.[128, 148] Thus, the poisoning effect of CO_{ad} is efficiently reduced. Moreover, when Pd atoms are effectively incorporated into the Pt matrix, the hydrogen desorption at the Pd sites, which occurs at a significantly lower potential as compared with that on the Pt alone, plays an important role in the anodic potential region in alkali medium and activates the catalyst surface for deprotonation.[145]

However, the combination of both principles, namely the use of both an alloyed chemical composition coupled with a core-shell motif,has yet to be thoroughly explored in the field. That is, the fabrication and optimization of a Pt~Pd-M system are lacking. Nonetheless, their successful generation would be able to employ the advantages of these architectures, including the ligand effect, the electronic effect, and the bifunctional effect. Hence, in this thesis, we have deliberately designed a series of hierarchical Pt monolayer shell (ML) - PdCu core structures for MOR. To the best of our knowledge, we are the first to report on the fabrication of hierarchical ultrathin Pt~PdCu nanowires with controllable chemical compositions. Furthermore, we have observed significantly enhanced MOR activities for our series of Pt~PdCu ultrathin nanowires as compared with commercial Pt nanoparticles.

(C) Ethanol Oxidation Reaction

As compared with another common fuel, i.e. methanol, ethanol complements the shortcomings of methanol, owing to its relative non-toxicity, higher boiling point, and most importantly, the reusability of its possible products, i.e., acetaldehyde and acetic acid. In addition, ethanol possesses a high specific energy of 8.01 kWh·kg^{-1}, which is comparable to that of gasoline.[149, 150] Contemporaneously, activity, selectivity, and stability denote critical issues that need to be addressed for any catalysts. Comprehensive fundamental studies of EOR form the basis of design rules for high efficiency catalysts.[151-154] A great deal of work on the mechanisms of either Pt- or Pd-based catalysts has been devoted to resolving the long-standing puzzle concerning the intermediates and the products emanating from EOR. It is now commonly accepted that the dual-pathway mechanism[155] proposed for either Pt- or Pd-based catalysts in alkaline media, as shown in Figure 1.4, is likely to be both plausible and reasonable.

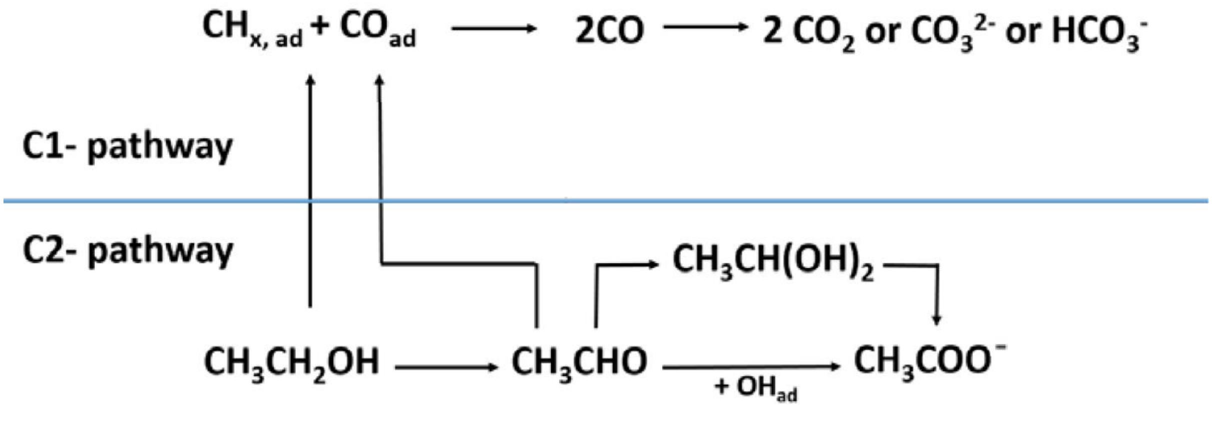

Figure 1.4. Proposed reaction mechanism for EOR on Pt electrodes. Reprinted with permission from ref 155. Copyright 2010, Elsevier B.V.

Collectively, regarding both plausible pathways, adsorbed CO, C1, and C2 hydrocarbon residues have been identified as the major adsorbed intermediates on either Pt- or Pd-based catalysts, while acetaldehyde and acetic acid have been detected as the main by-products using techniques such as infrared spectroscopy,[156-160] online DEMS (Differential Electrochemical Mass Spectrometry),[161-164] ion chromatography,[165, 166] and liquid chromatography.[156] Detailed, plausible chemical reactions describing the reactants and products involved in both C1 and C2 pathways are listed in Equations 1.13 through 1.17:

C1 pathway: $CH_3\text{-}CH_2OH + 12OH^- \rightarrow 2CO_2 + 9H_2O + 12e^-$ (1.13)

$CH_3\text{-}CH_2OH + 14OH^- \rightarrow 2HCO_3^- + 9H_2O + 12e^-$ (1.14)

$CH_3\text{-}CH_2OH + 16OH^- \rightarrow 2CO_3^{2-} + 11H_2O + 12e^-$ (1.15)

C2 pathway: $CH_3\text{-}CH_2OH + 4OH^- \rightarrow CH_3\text{–}COOH + 3H_2O + 4e^-$ (1.16)

$CH_3\text{-}CH_2OH + 2OH^- \rightarrow CH_3\text{–}CHO + 2H_2O + 2e^-$ (1.17)

However, EOR has been shown to occur via a series of complex reactions involving a number of sequential and parallel reaction steps, thereby resulting in more than 40 possible volatile and adsorbed intermediates or oxidative derivatives.[167] Previous studies concur that CO is a dominant adsorbed species formed during EOR. However, they disagree on details such as the nature of the adsorbed state of other intermediates and on the question of the nature of the rate limiting steps, i.e. whether it be the adsorption of the intermediate or the cleavage of the C–C bond or the formation of OH or oxides.[94, 152, 159, 160, 162, 168, 169]

Due to the extremely complex possible pathways associated with EOR, the focus has been shifted towards the determination of the relative concentrations between the final products, namely CO_2 (and its derivative forms, CO_3^{2-} and HCO_3^-). Indeed, Weaver and co-workers[170-172] have adapted real-time FTIR spectroscopy to study EOR on Pt surfaces in acidic media, and found that the final reaction products included acetic acid and acetaldehyde along with a smaller amount of CO_2. Their work provides values for the effective absorption coefficient, ε_{eff} of CO_2, acetic acid, and acetaldehyde, to be 3.5×10^4, 5.8×10^3, and 2.2×10^3 $M^{-1}\cdot cm^{-2}$, respectively. The yields of the oxidation products have been calculated using data for the respective integrated band intensities (A_i) and the amount of a given species Q ($mol\cdot cm^{-2}$) trapped inside the thin layer between the electrode surface and the optical window. This quantity followed the relationship, described in Equation 1.18:

$$Q = \frac{A_i}{\varepsilon_{eff}} \tag{1.18}$$

To better compare the selectivity and activity of EOR for catalysis, the Adzic group applied *in situ* infrared reflection-absorption spectroscopy (*in situ* IRRAS) to quantify the ratio of the products of the C1 pathway to those of the C2 pathway using the following equation[149]:

$$\frac{C_{CO_2}}{C_{CH_3COOH} + C_{CH_3CHO}} = \frac{6 \times Q_{CO_2}}{4 \times Q_{CH_3COOH} + 2 \times Q_{CH_3CHO}} \tag{1.19}$$

wherein C_{CO_2} and $C_{CH_3COOH} + C_{CH_3CHO}$ represent the charges associated with the total oxidation pathway (C1) and the partial oxidation pathway (C2), respectively.

When it comes to designing new catalysts, there has been a surge of interest in developing Pd-based catalysts, mainly because more facile EOR kinetics are expected in alkaline media on the less costly and more abundant Pd, based upon both theoretical calculations and spectroscopic observations.[153, 173, 174] However, the use of Pd itself may be insufficient to meet the practical commercial demand, due to its relative deficiencies in terms of activity and durability. In particular, a great deal of interest has been focused on the utilization of Pd-based alloy catalysts as an alternative for EOR wherein the catalytic activity may be further increased by the addition of either a second metal or metal oxide promoters that incorporate the effects mentioned above.

As such, various Pd-based catalysts have been synthesized with the addition of one or more elements including Ni,[175] Au,[176-178] Co,[179] Cu,[180, 181] and Sn,[182-184] as well as metal oxides such as SnO_2, CeO_x, Co_3O_4, Mn_3O_4, and NiO.[185-188] In particular, for Pd/Cu bimetallic electrocatalysts, it is worth noting that much of the previous research has focused on modifying bulk materials by the use of either functional alloys or via the electrodeposition process. Only a few investigations have concentrated on the utilization of supported Pd/Cu bimetallic nanostructures, let alone either more complex ternary or core-shell structures.[189, 190] Furthermore, most strategies for synthesizing Pd/Cu electrocatalysts have failed to demonstrate the ability to deliberately control the shape and size distribution of supported nanostructures through a relatively mild wet chemistry technique.

On the other hand, even though previous studies have shown that Pt yields a poor selectivity for the oxidation of ethanol to CO_2 of 0.5%-7.5%,[191] because of a complex reaction route composed of multiple pathways, Pt-based materials still represent the benchmark catalysts for ethanol oxidation as compared with Pd-based analogues.[192] Also, as discussed previously, the Pt monolayer (Pt_{ML}) strategy represent the ideal approach for utilizing Pt with the lowest loading. Nonetheless, to the best of our knowledge, only one paper has previously reported upon the electrochemical examination of Pt_{ML}~M structures towards EOR in alkaline media,[193] and most of the structures fabricated have been composed of Pt_{ML} deposited on top of bulk, single-crystalline metals instead of practical, nanosized materials.

As such, in this work, we aim to utilize the aforementioned series of Pt~PdCu ultrathin nanowires as a viable candidate towards alkaline EOR, in order to provide for an alternative motif for highly-active, low-Pt-containing electrocatalysts.

1.3. Upconversion Material-Based Solar Cells

Photovoltaic (PV) devices, or solar cells, also have been described as the ‘art of converting sunlight directly into electricity’,[194] and these are capable of using incident illumination to supply electrons to an external circuit. One of the most promising solar cell candidates has been dye-sensitized solar cells (DSSCs), which utilize organic dye molecules as the light sensitizer and direct the photo-induced electrons and holes to two respective electrodes, thereby generating electricity. Specifically, the cell structure of a DSSC has attracted considerable attention over the past 25 years, because of the advantages of its potential roll-to-roll fabrication procedure, use of cost-effective materials, efficient manufacturing technique, as well as high energy conversion efficiency. Until now, a maximum power conversion efficiency of 13% has been recorded for optimized DSSCs.[195] However, the relatively high cost synthesis procedures associated with organic dyes coupled with their intrinsically limited solar-to-electric conversion efficiency restrict the commercialization of DSSCs.

Meanwhile, quantum dots (QDs), a class of narrow bandgap semiconductors, possess several optically interesting and relevant properties, such as tunable bandgaps, due to quantum confinement effects, higher absorption coefficients as compared with most organic dyes,[196] and the capacity for multiple exciton generation (MEG).[197, 198] Thus, solar cell devices using quantum dots (QDs), especially II-VI group QDs (CdSe, CdTe, etc.), as sensitizers in order to substitute for organic dyes, are considered to be promising alternatives to DSSCs. Statistically, the number of research articles discussing quantum dot sensitized solar cells (QDSSCs) has increased rapidly from 5 in 2004 to over 500 in 2014,[199] a finding which demonstrates that semiconductor QDSSCs as a branch of DSSCs are becoming one of the most promising devices for the PV market. Among various systems, TiO_2/QD composite heterostructures have been thoroughly explored, due to their chemical simplicity as well as relatively high cell efficiencies (over 4%), achieved thus far.[200]

Wavelength conversions of light photons denote a promising route to reduce spectral mismatch losses that are considered to be the major part of the efficiency losses in single-junction solar cells. Specifically, upconversion is a process wherein low-energy photons (infrared and near-infrared) are converted into high-energy visible photons. This process could enable the conversion of incident light with energies lower than the semiconductor band gap and can significantly reduce transmission energy losses. Amongst many different candidates, $NaYF_4$ compounds denote a material of exceptional interest as a host lattice of UC materials, because they possess inherently lower phonon energies, and can thereby minimize non-radiative phonon relaxation processes in the dopants (rare-earth ions) by alleviating interactions between electrons and phonons as compared with most other upconversion materials.[201-204]

In 2002, Trupke, Green, and co-workers[205] proposed that the upconversion of sub-band gap light can result in significant improvements in the conversion efficiency of solar cells. They investigated a system of bifacial silicon solar cells with upconversion layers placed on the rear side. The upper limit of the energy conversion efficiency of the system was predicted to be

63.2% for concentrated sunlight and 47.6% for non-concentrated sunlight. In terms of experimental results, recent reports have suggested that increases from 5 to 20% in the overall cell efficiency can be expected in devices incorporating UC materials as compared with ‘dye-only’ controls for DSSCs.[206-208] As for QDSSCs, an increase in the overall cell efficiency from 3.43 to 4.37% was noted when CdSe QD - $NaYF_4$ hybrid nanostructures had been incorporated into TiO_2-based photoanodes.[209]

In this thesis, we aim to tune our chemical synthesis protocols to investigate the effect of the defined morphology of the energy donor, i.e. phase-pure $NaYF_4$, upon the resulting energy transfer behavior of the corresponding CdSe QD-$NaYF_4$ heterostructures. Specifically, we have varied the morphology of the $NaYF_4$ substrate, which in turn has given rise to distinctive interplay and interactions between the CdSe QDs and the $NaYF_4$ upconverting material within 0D-0D, 0D-1D, and 0D-3D nanocomposites, respectively. In other words, our results have provided for a far more comprehensive understanding of the structure-dependent energy transfer behavior between $NaYF_4$ and CdSe QDs within novel architectures, with important implications for the rational design of promising new classes of photovoltaic devices.

1.4. Objectives of Current Work

In summary, some of the key issues remaining for current fuel cell catalysts as well as for upconversion solar cell materials include but are not limited to: (1) the exact role of the transition metal atoms within the alloy-based materials in terms of the alteration of the electronic structure of the noble metals (i.e., either Pt or Pd); (2) the effect of the metal-alloy core towards enhancing the electrocatalytic activities of the Pt adatoms, e.g. a Pt monolayer on top of these alloyed structures; (3) whether there will be any local restructuring phenomena associated with the formation of complex, multi-element core-shell catalysts; and (4) whether the interface between upconversion materials and the light absorber affects the overall efficiency of the solar cells.

Therefore, the purpose of this thesis is to design high quality nanostructures and to systematically investigate and address these aforementioned topics by:

(a) Synthesizing a series of ultrathin Pd-M (M = Ni or Cu) nanowires, probing their respective crystallographic structures as well as surface profiles by means of XRD and electrochemical probing, and correlating these physical properties with the corresponding electrocatalytic performance towards various reactions including ORR, MOR, and EOR;

(b) Fabricating a series of ultrathin Pt_{ML}~Pd-M (M = Ni or Cu) core-shell nanowires, investigating their electrochemical properties, especially their affinity toward plausible reaction intermediates, and comparing these properties with those of analogous Pt nanowires as well as with those of Pd-M nanowires without any Pt monolayer in order to illustrate and highlight the contribution of the metal-alloy core;

(c) Combining both density functional theory (DFT) calculations and spectroscopic techniques, i.e. Extended X-ray Absorption Fine Structure (EXAFS), to predict and thereby demonstrate the actual structure of Pt~PdAu hierarchical tri-metallic ultrathin nanowires which otherwise are very difficult to probe using conventional techniques owing to the very small dimensions of the nanowires and the rather similar and hard-to-distinguish physical properties between Pt and Au elements;

(d) Synthesizing $NaYF_4$ nanostructures with distinctive morphologies along with CdSe QD-$NaYF_4$ heterostructures with the objective of probing the CdSe quantum dot (QD) loading, which is governed by the intrinsic external surface profiles of $NaYF_4$ possessing different shapes and surface areas, and of investigating the corresponding efficiencies of energy transfer occurring between the $NaYF_4$ motifs and the immobilized CdSe QDs.

In this light, Chapters 3 and 4 will focus upon the fabrication of Pt~PdM ultrathin ternary nanowires and the examination of their catalytic performances towards fuel cell-related reactions. Chapter 5 will highlight a combination of theoretical and experimental techniques aiming to unveil the spatial distribution of atoms within our as-synthesized Pt~PdAu ultrathin nanowires, with the intention of probing the actual active sites in such hierarchical, complex structures. Furthermore, Chapter 6 will center on the synthesis of single-crystalline $NaYF_4$ nanomaterials with various, well-defined shapes, including 0D, 1D, and 3D motifs. Subsequently, a series of $NaYF_4$ nanocrystals will be attached onto QDs, and their optical properties will be subsequently examined in order to investigate the morphology-dependent energy transfer behavior between these two constituent components.

1.4.1. Ultrathin One-Dimensional Pd-Ni Nanostructures as Oxygen Reduction Reaction Catalysts

An ambient, surfactant-based synthetic means was used to prepare ultrathin binary (diameter of ~2 nm) Pd–Ni nanowires, which were subsequently purified using a novel butylamine-based surfactant-exchange process coupled with an electrochemical CO adsorption and stripping treatment to expose active surface sites. We were able to systematically vary the chemical composition of as-prepared Pd–Ni nanowires from pure elemental Pd to $Pd_{0.50}Ni_{0.50}$ (atomic ratio), as verified using EDS analysis. The overall morphology of samples possessing >60 atom % Pd consisted of individual, discrete one-dimensional nanowires. The electrocatalytic performances of elemental Pd, $Pd_{0.90}Ni_{0.10}$, $Pd_{0.83}Ni_{0.17}$, and $Pd_{0.75}Ni_{0.25}$ nanowires in particular were examined. Our results highlight a “volcano”-type relationship between chemical composition and the corresponding ORR activities with $Pd_{0.90}Ni_{0.10}$, yielding the highest activity (i.e., 1.96 mA/cm^2 at 0.8 V) among all nanowires tested. Moreover, the $Pd_{0.90}Ni_{0.10}$ sample exhibited outstanding methanol tolerance ability. In essence, there was only a relatively minimal 15% loss in the specific activity in the presence of 4 mM methanol, which was significantly better than analogous data on Pt nanoparticles and Pt nanowires. In addition, we also studied ultrathin, core–shell Pt~$Pd_{0.90}Ni_{0.10}$ nanowires, which exhibited a specific activity of 0.62 mA/cm^2 and a corresponding mass activity of 1.44 A/mg$_{Pt}$ at 0.9 V. Moreover, our as-prepared core–shell electrocatalysts maintained excellent electrochemical durability. We postulate that one-dimensional Pd–Ni nanostructures represent a particularly promising platform for designing ORR catalysts with high performance.

1.4.2. Ultrathin One-Dimensional Pd_xCu_{1-x} and Pt~Pd_xCu_{1-x} Nanowires as Multifunctional Electrocatalysts for Various Small Molecule Oxidation Reactions

Developing novel electrocatalysts for small molecule oxidation processes, including formic acid oxidation (FAOR), methanol oxidation reaction (MOR), and ethanol oxidation reaction (EOR), denoting the key anodic reactions for their respective fuel cell configurations, is a significant and relevant theme of recent efforts in the field. Herein, we have demonstrated a concerted effort to couple and combine the benefits of small size, anisotropic morphology, and tunable chemical composition in order to devise a novel “family” of functional architectures. In particular, we have fabricated not only ultrathin 1-D $Pd_{1-x}Cu_x$ alloys but also Pt-coated $Pd_{1-x}Cu_x$ (i.e., Pt~$Pd_{1-x}Cu_x$; herein the ~ indicates an intimate association, but not necessarily actual bond formation, between the inner bimetallic core and the Pt outer shell) core‒shell hierarchical nanostructures with readily tunable chemical compositions by utilizing a facile, surfactant-based, wet chemical synthesis coupled with a Cu underpotential deposition technique. Our main finding is that our series of as-prepared nanowires are functionally flexible. More precisely, we demonstrate that various examples within this “family” of structural motifs can be tailored for exceptional activity with all 3 of these important electrocatalytic reactions. In particular, we note that our series of $Pd_{1-x}Cu_x$ nanowires all exhibit enhanced FAOR activities as compared with not only analogous Pd ultrathin nanowires but also commercial Pt and Pd standards, with Pd_9Cu representing the “optimal” composition. Moreover, our group of $Pt\sim Pd_{1-x}Cu_x$ nanowires consistently outperformed not only commercial Pt NPs but also ultrathin Pt nanowires by several fold orders of magnitude for both the MOR and EOR reactions in alkaline media. The variation of the MOR and EOR performance with the chemical composition of our ultrathin $Pt\sim Pd_{1-x}Cu_x$ nanowires was also discussed.

1.4.3. In Situ Probing of the Active Site Geometry of Ultrathin Pt@Pd_9Au Hierarchical Nanowires for the Oxygen Reduction Reaction

To create truly effective electrocatalysts for the cathodic reaction governing proton exchange membrane fuel cells (PEMFC), namely the oxygen reduction reaction (ORR), necessitates an accurate and detailed structural understanding of these electrocatalysts, especially at the nanoscale, and to precisely correlate that structure with demonstrable performance enhancement. To address this key issue, we have combined and interwoven theoretical calculations with experimental, spectroscopic observations in order to acquire useful structural insights into the active site geometry with implications for designing optimized nanoscale electrocatalysts with rationally predicted properties. Specifically, we have probed ultrathin (~2 nm) core–shell $Pt\sim Pd_9Au$ nanowires, which have been previously shown to be excellent candidates for ORR in terms of both activity and long-term stability, from the complementary perspectives of both DFT calculations and X-ray absorption spectroscopy (XAS). The combination and correlation of data from both experimental and theoretical studies has revealed for the first time that the catalytically active structure of our ternary nanowires can actually be ascribed to a PtAu~Pd configuration, comprising a PtAu binary shell and a pure inner Pd core. Moreover, we have plausibly attributed the resulting structure to a specific synthesis step, namely the Cu underpotential deposition (UPD) followed by galvanic replacement with Pt. Hence, the fundamental insights gained into the performance of our ultrathin nanowires from our demonstrated approach will likely guide future directed efforts aimed at broadly improving upon the durability and stability of nanoscale electrocatalysts in general.

1.4.4. Synthesis-Driven Enhanced Up-Conversion Luminescence and Energy Transfer Behavior in Phase-Tunable $NaYF_4$:Yb, Er-based Nanoscale Motifs and Associated QD-Coupled Heterostructures

Understanding the key parameters necessary for generating uniform and nanoscale Er,Yb co-activated $NaYF_4$ possessing various selected phases (i.e., cubic or hexagonal) represents an important chemical strategy towards tailoring optical behavior in these systems. Herein, we report on a straightforward hydrothermal synthesis in which the separate effects of reaction temperature, reaction time, and precursor stoichiometry in the absence of any surfactant were independently investigated. Interestingly, the presence and concentration of NH_4OH appear to be the most critical determinant of phase and morphology. For example, with NH_4OH as an additive, we have observed the formation of novel hierarchical nanowire bundles which possess overall lengths of ~5 μm and widths of ~1.5 μm but are composed of constituent component sub-units of long, ultrathin (~5 nm) nanowires. These motifs have yet to be reported as distinctive morphological manifestations of fluoride nanomaterials. The optical properties of as-generated nanostructures have also been carefully analyzed. Specifically, we have observed tunable, structure-dependent energy transfer behavior associated with the formation of a class of $NaYF_4$-CdSe quantum dot (QD) heterostructures, incorporating zero-dimensional (0D), one-dimensional (1D), and three-dimensional (3D) $NaYF_4$ nanostructures. Our results have demonstrated the key roles of the intrinsic morphology-specific physical surface area and porosity as factors in governing the resulting opto-electronic behavior. Specifically, the trend in energy transfer efficiency correlates very well with the corresponding QD loading within these heterostructures, thereby implying that the efficiency of FRET is directly affected by the amount of QDs immobilized onto the external surfaces of the underlying fluoride host materials.

1.5. References

1. Klaine, S. J.; Alvarez, P. J. J.; Batley, G. E.; Fernandes, T. F.; Handy, R. D.; Lyon, D. Y.; Mahendra, S.; McLaughlin, M. J.; Lead, J. R. *Environ Toxicol Chem* **2012,** 31, (12), 2893-2893.
2. *Chem Eng News* **2007,** 85, (16), 24-24.
3. *Anti-Corros Method M* **2014,** 61, (6), 450-451.
4. Freedonia Group., World nanomaterials. In *Industry study*, Freedonia Group: Cleveland, Ohio, p v.
5. Alivisatos, A. P. *Science* **1996,** 271, (5251), 933-937.
6. Sardar, R.; Funston, A. M.; Mulvaney, P.; Murray, R. W. *Langmuir* **2009,** 25, (24), 13840-13851.
7. Guczi, L.; Beck, A.; Frey, K. *Gold Bull* **2009,** 42, (1), 5-12.
8. Sajanlal, P. R.; Sreeprasad, T. S.; Samal, A. K.; Pradeep, T. *Nano Rev* **2011,** 2.
9. Daniel, M. C.; Astruc, D. *Chem Rev* **2004,** 104, (1), 293-346.
10. El-Sayed, M. A. *Accounts Chem Res* **2004,** 37, (5), 326-333.
11. Iijima, S. *Nature* **1991,** 354, (6348), 56-58.
12. Perez-Juste, J.; Pastoriza-Santos, I.; Liz-Marzan, L. M.; Mulvaney, P. *Coordin Chem Rev* **2005,** 249, (17-18), 1870-1901.
13. Busbee, B. D.; Obare, S. O.; Murphy, C. J. *Adv Mater* **2003,** 15, (5), 414-+.
14. Xia, Y. N.; Yang, P. D.; Sun, Y. G.; Wu, Y. Y.; Mayers, B.; Gates, B.; Yin, Y. D.; Kim, F.; Yan, Y. Q. *Adv Mater* **2003,** 15, (5), 353-389.
15. Wang, F.; Dong, A.; Buhro, W. E. *Chem Rev* **2016**.
16. Chen, J. Y.; Wiley, B. J.; Xia, Y. N. *Langmuir* **2007,** 23, (8), 4120-4129.
17. Hu, J. T.; Odom, T. W.; Lieber, C. M. *Accounts Chem Res* **1999,** 32, (5), 435-445.
18. Millstone, J. E.; Park, S.; Shuford, K. L.; Qin, L. D.; Schatz, G. C.; Mirkin, C. A. *Journal of the American Chemical Society* **2005,** 127, (15), 5312-5313.
19. Jin, R. C.; Cao, Y. W.; Mirkin, C. A.; Kelly, K. L.; Schatz, G. C.; Zheng, J. G. *Science* **2001,** 294, (5548), 1901-1903.
20. Scarabelli, L.; Coronado-Puchau, M.; Giner-Casares, J. J.; Langer, J.; Liz-Marzan, L. M. *Acs Nano* **2014,** 8, (6), 5833-5842.
21. Tan, C. L.; Zhang, H. *Chem Soc Rev* **2015,** 44, (9), 2713-2731.
22. Fan, Z. X.; Huang, X.; Tan, C. L.; Zhang, H. *Chem Sci* **2015,** 6, (1), 95-111.
23. Dutta, S.; Pati, S. K. *J Mater Chem* **2010,** 20, (38), 8207-8223.
24. Henzie, J.; Kwak, E. S.; Odom, T. W. *Nano Lett* **2005,** 5, (7), 1199-1202.
25. Lee, J.; Hasan, W.; Stender, C. L.; Odom, T. W. *Accounts Chem Res* **2008,** 41, (12), 1762-1771.
26. Burt, J. L.; Elechiguerra, J. L.; Reyes-Gasga, J.; Montejano-Carrizales, J. M.; Jose-Yacaman, M. *J Cryst Growth* **2005,** 285, (4), 681-691.
27. Wang, L.; Zhang, Y. M.; Scofield, M. E.; Yue, S. Y.; McBean, C.; Marschilok, A. C.; Takeuchi, K. J.; Takeuchi, E. S.; Wong, S. S. *Chemsuschem* **2015,** 8, (19), 3304-3313.
28. Jena, B. K.; Raj, C. R. *Langmuir* **2007,** 23, (7), 4064-4070.
29. Kharisov, B. I. *Recent Pat Nanotech* **2008,** 2, (3), 190-200.
30. O'Dwyer, C.; Navas, D.; Lavayen, V.; Benavente, E.; Santa Ana, M. A.; Gonzalez, G.; Newcomb, S. B.; Torres, C. M. S. *Chem Mater* **2006,** 18, (13), 3016-3022.
31. Hu, J. Q.; Zhang, Y.; Liu, B.; Liu, J. X.; Zhou, H. H.; Xu, Y. F.; Jiang, Y. X.; Yang, Z. L.; Tian, Z. Q. *Journal of the American Chemical Society* **2004,** 126, (31), 9470-9471.

32. Xia, X. H.; Xia, Y. N. *Front Phys-Beijing* **2014,** 9, (3), 378-384.
33. Sutter, E.; Jungjohann, K.; Bliznakov, S.; Courty, A.; Maisonhaute, E.; Tenney, S.; Sutter, P. *Nat Commun* **2014,** 5.
34. Wang, H.; Brandl, D. W.; Le, F.; Nordlander, P.; Halas, N. J. *Nano Lett* **2006,** 6, (4), 827-832.
35. Teranishi, T.; Inoue, Y.; Nakaya, M.; Oumi, Y.; Sano, T. *Journal of the American Chemical Society* **2004,** 126, (32), 9914-9915.
36. Yun, S.; Lee, Y. C.; Park, H. S. *Sci Rep-Uk* **2016,** 6.
37. Ma, C. M.; Zhang, R. F.; Liaw, J. W.; Cheng, J. C. *Appl Phys a-Mater* **2014,** 115, (1), 31-37.
38. Lin, X.; Chu, D. W.; Younis, A.; Li, S.; Dang, F. *Curr Org Chem* **2013,** 17, (15), 1666-1679.
39. Métraux, G. S.; Cao, Y. C.; Jin, R.; Mirkin, C. A. *Nano Lett* **2003,** 3, (4), 519-522.
40. Yu, H.; Chen, M.; Rice, P. M.; Wang, S. X.; White, R. L.; Sun, S. H. *Nano Lett* **2005,** 5, (2), 379-382.
41. Cahen, D.; Hodes, G.; Gratzel, M.; Guillemoles, J. F.; Riess, I. *J Phys Chem B* **2000,** 104, (9), 2053-2059.
42. Wan, J. Y.; Song, T.; Flox, C.; Yang, J. Y.; Yang, Q. H.; Han, X. G. *J Nanomater* **2015**.
43. Robertson, N. *Angew Chem Int Edit* **2006,** 45, (15), 2338-2345.
44. Weber, J.; Singhal, R.; Zekri, S.; Kumar, A. *Int Mater Rev* **2008,** 53, (4), 235-255.
45. Wang, N.; Cai, Y.; Zhang, R. Q. *Mat Sci Eng R* **2008,** 60, (1-6), 1-51.
46. Cademartiri, L.; Ozin, G. A. *Adv Mater* **2009,** 21, (9), 1013-1020.
47. Lim, B.; Jiang, M. J.; Camargo, P. H. C.; Cho, E. C.; Tao, J.; Lu, X. M.; Zhu, Y. M.; Xia, Y. N. *Science* **2009,** 324, (5932), 1302-1305.
48. Du, S. F.; Lin, K. J.; Malladi, S. K.; Lu, Y. X.; Sun, S. H.; Xu, Q.; Steinberger-Wilckens, R.; Dong, H. S. *Sci Rep-Uk* **2014,** 4.
49. Foley, J. M.; Price, M. J.; Feldblyum, J. I.; Maldonado, S. *Energ Environ Sci* **2012,** 5, (1), 5203-5220.
50. Larminie, J.; Dicks, A., *Fuel cell systems explained*. 2nd ed.; J. Wiley: Chichester, West Sussex, 2003; p xxii, 406 p.
51. Wang, Y.; Chen, K. S.; Mishler, J.; Cho, S. C.; Adroher, X. C. *Appl Energ* **2011,** 88, (4), 981-1007.
52. Lucia, U. *Renew Sust Energ Rev* **2014,** 30, 164-169.
53. Vielstich, W.; Lamm, A.; Gasteiger, H. A., *Handbook of fuel cells : fundamentals, technology, and applications*. Wiley: Chichester, England ; Hoboken, N.J., 2003; p 4 v.
54. Grubb, W. T.; Niedrach, L. W. *J Electrochem Soc* **1960,** 107, (2), 131-135.
55. Merle, G.; Wessling, M.; Nijmeijer, K. *J Membrane Sci* **2011,** 377, (1-2), 1-35.
56. Behling, N. H., *Fuel cells : current technology challenges and future research needs*. 1st ed.; Elsevier: Amsterdam ; Boston, 2013; p xiv, 685 p.
57. Anahara, R. *Int J Hydrogen Energ* **1992,** 17, (5), 375-379.
58. Choudhury, S. R., Phosphoric Acid Fuel Cell Technology. In *Recent Trends in Fuel Cell Science and Technology*, Basu, S., Ed. Springer New York: New York, NY, 2007; pp 188-216.
59. Plomp, L.; Veldhuis, J. B. J.; Sitters, E. F.; Vandermolen, S. B. *J Power Sources* **1992,** 39, (3), 369-373.
60. Leo, T. *Comprehensive Renewable Energy, Vol 4: Fuel Cells and Hydrogen Technology* **2012**, 247-259.

61. Stambouli, A. B.; Traversa, E. *Renew Sust Energ Rev* **2002,** 6, (5), 433-455.

62. Adams, T. A.; Nease, J.; Tucker, D.; Barton, P. I. *Ind Eng Chem Res* **2013,** 52, (9), 3089-3111.

63. Jiang, Z. Q.; Jiang, Z. J. *Carbon Nanotubes - Growth and Applications* **2011**, 567-604.

64. Kim, G.; Eom, K.; Kim, M.; Yoo, S. J.; Jang, J. H.; Kim, H. J.; Cho, E. *Acs Appl Mater Inter* **2015,** 7, (50), 27581-27585.

65. Pilatowsky, I.; Romero, R. J.; Isaza, C. A.; Gamboa, S. A.; Sebastian, P. J.; Rivera, W. *Green Energy Technol* **2011**, 25-36.

66. *Fuel Cell Catalysis: A Surface Science Approach*. John Wiley and Sons: Hoboken, NJ, 2009; p 1-632.

67. Murthi, V. S.; Urian, R. C.; Mukerjee, S. *J Phys Chem B* **2004,** 108, (30), 11011-11023.

68. Xu, Y.; Zhang, B. *Chem Soc Rev* **2014,** 43, (8), 2439-2450.

69. *Fuel Cell Technologies: Multi-Year Research, Development, and Demonstration Plan*; U.S. Department of Energy: 2012; pp 3.4-1 - 3.4-49.

70. Greeley, J.; Stephens, I. E. L.; Bondarenko, A. S.; Johansson, T. P.; Hansen, H. A.; Jaramillo, T. F.; Rossmeisl, J.; Chorkendorff, I.; Norskov, J. K. *Nat Chem* **2009,** 1, (7), 552-556.

71. Kitchin, J. R.; Norskov, J. K.; Barteau, M. A.; Chen, J. G. *Phys Rev Lett* **2004,** 93, (15), 156801/1-156801/4.

72. Han, L.; Liu, H.; Cui, P. L.; Peng, Z. J.; Zhang, S. J.; Yang, J. *Sci Rep-Uk* **2014,** 4.

73. Choi, S. I.; Xie, S. F.; Shao, M. H.; Odell, J. H.; Lu, N.; Peng, H. C.; Protsailo, L.; Guerrero, S.; Park, J. H.; Xia, X. H.; Wang, J. G.; Kim, M. J.; Xia, Y. N. *Nano Lett* **2013,** 13, (7), 3420-3425.

74. Oezaslan, M.; Hasche, F.; Strasser, P. *Journal of Physical Chemistry Letters* **2013,** 4, (19), 3273-3291.

75. Kang, Y.; Snyder, J.; Chi, M.; Li, D.; More, K. L.; Markovic, N. M.; Stamenkovic, V. R. *Nano Lett* **2014,** 14, (11), 6361-6367.

76. Adzic, R. R.; Zhang, J.; Sasaki, K.; Vukmirovic, M. B.; Shao, M.; Wang, J. X.; Nilekar, A. U.; Mavrikakis, M.; Valerio, J. A.; Uribe, F. *Top Catal* **2007,** 46, (3-4), 249-262.

77. Koenigsmann, C.; Scofield, M. E.; Liu, H. Q.; Wong, S. S. *J Phys Chem Lett* **2012,** 3, (22), 3385-3398.

78. Koenigsmann, C.; Sutter, E.; Adzic, R. R.; Wong, S. S. *J Phys Chem C* **2012,** 116, (29), 15297-15306.

79. Capon, A.; Parson, R. *Journal of Electroanalytical Chemistry and Interfacial Electrochemistry* **1973,** 44, (1), 1-7.

80. Capon, A.; Parsons, R. *Journal of Electroanalytical Chemistry and Interfacial Electrochemistry* **1973,** 44, (2), 239-254.

81. Capon, A.; Parsons, R. *Journal of Electroanalytical Chemistry and Interfacial Electrochemistry* **1973,** 45, (2), 205-231.

82. Jeong, K. J.; Miesse, C. A.; Choi, J. H.; Lee, J.; Han, J.; Yoon, S. P.; Nam, S. W.; Lim, T. H.; Lee, T. G. *J Power Sources* **2007,** 168, (1), 119-125.

83. Yu, X. W.; Pickup, P. G. *J Power Sources* **2008,** 182, (1), 124-132.

84. Uhm, S.; Lee, H. J.; Lee, J. *Phys Chem Chem Phys* **2009,** 11, (41), 9326-9336.

85. Jiang, K.; Zhang, H. X.; Zou, S. Z.; Cai, W. B. *Phys Chem Chem Phys* **2014,** 16, (38), 20360-20376.

86. Rice, C.; Ha, R. I.; Masel, R. I.; Waszczuk, P.; Wieckowski, A.; Barnard, T. *J Power Sources* **2002,** 111, (1), 83-89.

87. Zhou, W. P.; Lewera, A.; Larsen, R.; Masel, R. I.; Bagus, P. S.; Wieckowski, A. *J Phys Chem B* **2006,** 110, (27), 13393-13398.
88. Zhou, W. J.; Lee, J. Y. *J Phys Chem C* **2008,** 112, (10), 3789-3793.
89. Ojani, R.; Abkar, Z.; Hasheminejad, E.; Raoof, J. B. *Int J Hydrogen Energ* **2014,** 39, (15), 7788-7797.
90. Xu, C. X.; Liu, Y. Q.; Wang, J. P.; Geng, H. R.; Qiu, H. J. *J Power Sources* **2012,** 199, 124-131.
91. Antolini, E.; Gonzalez, E. R. *J Power Sources* **2010,** 195, (11), 3431-3450.
92. McLean, G. F.; Niet, T.; Prince-Richard, S.; Djilali, N. *Int J Hydrogen Energ* **2002,** 27, (5), 507-526.
93. Ramaswamy, N.; Mukerjee, S. *Advances in Physical Chemistry* **2012,** 2012, 17.
94. Lai, S. C. S.; Koper, M. T. M. *Phys Chem Chem Phys* **2009,** 11, (44), 10446-10456.
95. Kimble, M. C.; White, R. E. *J Electrochem Soc* **1991,** 138, (11), 3370-3382.
96. Jasinski, R. *Nature* **1964,** 201, (4925), 1212-1213.
97. Jeon, I. Y.; Choi, H. J.; Choi, M.; Seo, J. M.; Jung, S. M.; Kim, M. J.; Zhang, S.; Zhang, L. P.; Xia, Z. H.; Dai, L. M.; Park, N.; Baek, J. B. *Sci Rep-Uk* **2013,** 3.
98. Wu, G.; More, K. L.; Johnston, C. M.; Zelenay, P. *Science* **2011,** 332, (6028), 443-447.
99. Sun, X. J.; Zhang, Y. W.; Song, P.; Pan, J.; Zhuang, L.; Xu, W. L.; Xing, W. *Acs Catal* **2013,** 3, (8), 1726-1729.
100. Oh, H. S.; Kim, H. *J Power Sources* **2012,** 212, 220-225.
101. Chen, Z. W.; Higgins, D.; Yu, A. P.; Zhang, L.; Zhang, J. J. *Energ Environ Sci* **2011,** 4, (9), 3167-3192.
102. Jaouen, F.; Proietti, E.; Lefevre, M.; Chenitz, R.; Dodelet, J. P.; Wu, G.; Chung, H. T.; Johnston, C. M.; Zelenay, P. *Energ Environ Sci* **2011,** 4, (1), 114-130.
103. Xiang, Z. H.; Xue, Y. H.; Cao, D. P.; Huang, L.; Chen, J. F.; Dai, L. M. *Angew Chem Int Edit* **2014,** 53, (9), 2433-2437.
104. Koslowski, U. I.; Abs-Wurmbach, I.; Fiechter, S.; Bogdanoff, P. *J Phys Chem C* **2008,** 112, (39), 15356-15366.
105. Bouwkamp-Wijnoltz, A. L.; Visscher, W.; van Veen, J. A. R.; Boellaard, E.; van der Kraan, A. M.; Tang, S. C. *J Phys Chem B* **2002,** 106, (50), 12993-13001.
106. Rigsby, M. L.; Wasylenko, D. J.; Pegis, M. L.; Mayer, J. M. *Journal of the American Chemical Society* **2015,** 137, (13), 4296-4299.
107. Liu, H. S.; Shi, Z.; Zhang, J. L.; Zhang, L.; Zhang, J. J. *J Mater Chem* **2009,** 19, (4), 468-470.
108. Choi, J. Y.; Hsu, R. S.; Chen, Z. W. *J Phys Chem C* **2010,** 114, (17), 8048-8053.
109. Hsu, R. S.; Chen, Z. W. *Electrode Processes Relevant to Fuel Cell Technology* **2010,** 28, (23), 39-46.
110. Ye, S. Y.; Vijh, A. K. *Electrochem Commun* **2003,** 5, (3), 272-275.
111. Tian, J.; Morozan, A.; Sougrati, M. T.; Lefevre, M.; Chenitz, R.; Dodelet, J. P.; Jones, D.; Jaouen, F. *Angew Chem Int Edit* **2013,** 52, (27), 6867-6870.
112. Wang, M. Q.; Yang, W. H.; Wang, H. H.; Chen, C.; Zhou, Z. Y.; Sun, S. G. *Acs Catal* **2014,** 4, (11), 3928-3936.
113. Liu, J.; Sun, X. J.; Song, P.; Zhang, Y. W.; Xing, W.; Xu, W. L. *Adv Mater* **2013,** 25, (47), 6879-6883.
114. Xiao, M. L.; Zhu, J. B.; Feng, L. G.; Liu, C. P.; Xing, W. *Adv Mater* **2015,** 27, (15), 2521-2527.

115. Niu, W. H.; Li, L. G.; Liu, X. J.; Wang, N.; Liu, J.; Zhou, W. J.; Tang, Z. H.; Chen, S. W. *Journal of the American Chemical Society* **2015,** 137, (16), 5555-5562.
116. Ge, X. M.; Sumboja, A.; Wuu, D.; An, T.; Li, B.; Goh, F. W. T.; Hor, T. S. A.; Zong, Y.; Liu, Z. L. *Acs Catal* **2015,** 5, (8), 4643-4667.
117. Liu, J.; Li, E. L.; Ruan, M. B.; Song, P.; Xu, W. L. *Catalysts* **2015,** 5, (3), 1167-1192.
118. Morozan, A.; Jousselme, B.; Palacin, S. *Energ Environ Sci* **2011,** 4, (4), 1238-1254.
119. Varcoe, J. R.; Slade, R. C. T. *Electrochem Commun* **2006,** 8, (5), 839-843.
120. Sylwan, C. L. *Energ Convers* **1977,** 17, (2-3), 67-72.
121. Cairns, E. J.; Bartosik, D. C. *J Electrochem Soc* **1964,** 111, (3), C78-C78.
122. Jayashree, R. S.; Egas, D.; Spendelow, J. S.; Natarajan, D.; Markoski, L. J.; Kenis, P. J. A. *Electrochem Solid St* **2006,** 9, (5), A252-A256.
123. Choban, E. R.; Spendelow, J. S.; Gancs, L.; Wieckowski, A.; Kenis, P. J. A. *Electrochim Acta* **2005,** 50, (27), 5390-5398.
124. Yu, E. H.; Scott, K. *J Appl Electrochem* **2005,** 35, (1), 91-96.
125. Matsuoka, K.; Iriyama, Y.; Abe, T.; Matsuoka, M.; Ogumi, Z. *J Power Sources* **2005,** 150, 27-31.
126. Huang, A. B.; Xia, C. Y.; Xiao, C. B.; Zhuang, L. *J Appl Polym Sci* **2006,** 100, (3), 2248-2251.
127. Morallon, E.; Rodes, A.; Vazquez, J. L.; Perez, J. M. *J Electroanal Chem* **1995,** 391, (1-2), 149-157.
128. Matsuoka, K.; Iriyama, Y.; Abe, T.; Matsuoka, M.; Ogumi, Z. *Electrochim Acta* **2005,** 51, (6), 1085-1090.
129. Bagotzky, V. S.; Vassilyev, Y. B. *Electrochim Acta* **1967,** 12, (9), 1323-1343.
130. Spendelow, J. S.; Goodpaster, J. D.; Kenis, P. J. A.; Wieckowski, A. *Langmuir* **2006,** 22, (25), 10457-10464.
131. Tripkovic, A. V.; Popovic, K. D.; Grgur, B. N.; Blizanac, B.; Ross, P. N.; Markovic, N. M. *Electrochim Acta* **2002,** 47, (22-23), 3707-3714.
132. Spendelow, J. S.; Wieckowski, A. *Phys Chem Chem Phys* **2007,** 9, (21), 2654-2675.
133. Lu, C.; Rice, C.; Masel, R. I.; Babu, P. K.; Waszczuk, P.; Kim, H. S.; Oldfield, E.; Wieckowski, A. *J Phys Chem B* **2002,** 106, (37), 9581-9589.
134. Ishikawa, Y.; Liao, M. S.; Cabrera, C. R. *Surf Sci* **2000,** 463, (1), 66-80.
135. Liu, P.; Logadottir, A.; Nørskov, J. K. *Electrochim Acta* **2003,** 48, (25–26), 3731-3742.
136. Rolison, D. R.; Hagans, P. L.; Swider, K. E.; Long, J. W. *Langmuir* **1999,** 15, (3), 774-779.
137. Davies, J. C.; Bonde, J.; Logadottir, A.; Norskov, J. K.; Chorkendorff, I. *Fuel Cells* **2005,** 5, (4), 429-435.
138. Roth, C.; Papworth, A. J.; Hussain, I.; Nichols, R. J.; Schiffrin, D. J. *J Electroanal Chem* **2005,** 581, (1), 79-85.
139. Meng, H.; Zeng, D. R.; Xie, F. Y. *Catalysts* **2015,** 5, (3), 1221-1274.
140. Rodriguez, J. A.; Goodman, D. W. *Accounts Chem Res* **1995,** 28, (12), 477-478.
141. Zhou, W. P.; Lewera, A.; Bagus, P. S.; Wieckowski, A. *J Phys Chem C* **2007,** 111, (36), 13490-13496.
142. Kitchin, J. R.; Norskov, J. K.; Barteau, M. A.; Chen, J. G. *Phys Rev Lett* **2004,** 93, (15).
143. Greeley, J.; Mavrikakis, M. *Nat Mater* **2004,** 3, (11), 810-815.
144. Xu, Y.; Ruban, A. V.; Mavrikakis, M. *Journal of the American Chemical Society* **2004,** 126, (14), 4717-4725.

145. Mahapatra, S. S.; Datta, J. *International Journal of Electrochemistry* **2011,** 2011, 16.
146. Prabhuram, J.; Manoharan, R. *J Power Sources* **1998,** 74, (1), 54-61.
147. Manoharan, R.; Prabhuram, J. *J Power Sources* **2001,** 96, (1), 220-225.
148. Lamy, C.; Lima, A.; LeRhun, V.; Delime, F.; Coutanceau, C.; Leger, J. M. *J Power Sources* **2002,** 105, (2), 283-296.
149. Li, M.; Kowal, A.; Sasaki, K.; Marinkovic, N.; Su, D.; Korach, E.; Liu, P.; Adzic, R. R. *Electrochim Acta* **2010,** 55, (14), 4331-4338.
150. Demirci, U. B. *J Power Sources* **2007,** 173, (1), 11-18.
151. Kamarudin, M. Z. F.; Kamarudin, S. K.; Masdar, M. S.; Daud, W. R. W. *Int J Hydrogen Energ* **2013,** 38, (22), 9438-9453.
152. Shao, M. H.; Adzic, R. R. *Electrochim Acta* **2005,** 50, (12), 2415-2422.
153. Liang, Z. X.; Zhao, T. S.; Xu, J. B.; Zhu, L. D. *Electrochim Acta* **2009,** 54, (8), 2203-2208.
154. Hammer, B.; Norskov, J. K. *Adv Catal* **2000,** 45, 71-129.
155. Lai, S. C. S.; Kleijn, S. E. F.; Ozturk, F. T. Z.; Vellinga, V. C. V.; Koning, J.; Rodriguez, P.; Koper, M. T. M. *Catal Today* **2010,** 154, (1-2), 92-104.
156. Hitmi, H.; Belgsir, E. M.; Leger, J. M.; Lamy, C.; Lezna, R. O. *Electrochim Acta* **1994,** 39, (3), 407-415.
157. Vigier, F.; Coutanceau, C.; Hahn, F.; Belgsir, E. M.; Lamy, C. *J Electroanal Chem* **2004,** 563, (1), 81-89.
158. Rasko, J.; Domok, A.; Baan, K.; Erdohelyi, A. *Appl Catal a-Gen* **2006,** 299, 202-211.
159. Christensen, P. A.; Jones, S. W. M.; Hamnett, A. *J Phys Chem C* **2012,** 116, (46), 24681-24689.
160. Yang, Y. Y.; Ren, J.; Li, Q. X.; Zhou, Z. Y.; Sun, S. G.; Cai, W. B. *Acs Catal* **2014,** 4, (3), 798-803.
161. Iwasita, T.; Pastor, E. *Electrochim Acta* **1994,** 39, (4), 531-537.
162. Wang, H.; Jusys, Z.; Behm, R. J. *Fuel Cells* **2004,** 4, (1-2), 113-125.
163. Wang, H.; Jusys, Z.; Behm, R. J. *J Power Sources* **2006,** 154, (2), 351-359.
164. Wang, Q.; Sun, G. Q.; Jiang, L. H.; Xin, Q.; Sun, S. G.; Jiang, Y. X.; Chen, S. P.; Jusys, Z.; Behm, R. J. *Phys Chem Chem Phys* **2007,** 9, (21), 2686-2696.
165. Belgsir, E. M.; Bouhier, E.; Yei, H. E.; Kokoh, K. B.; Beden, B.; Huser, H.; Leger, J. M.; Lamy, C. *Electrochim Acta* **1991,** 36, (7), 1157-1164.
166. Tarnowski, D. J.; Korzeniewski, C. *J Phys Chem B* **1997,** 101, (2), 253-258.
167. Wang, H. F.; Liu, Z. P. *Journal of the American Chemical Society* **2008,** 130, (33), 10996-11004.
168. Kavanagh, R.; Cao, X. M.; Lin, W. F.; Hardacre, C.; Hu, P. *Angew Chem Int Edit* **2012,** 51, (7), 1572-1575.
169. Asiri, H. A.; Anderson, A. B. *J Electrochem Soc* **2015,** 162, (1), F115-F122.
170. Leung, L. W. H.; Chang, S. C.; Weaver, M. J. *J Electroanal Chem* **1989,** 266, (2), 317-336.
171. Leung, L. W. H.; Weaver, M. J. *J Phys Chem-Us* **1988,** 92, (14), 4019-4022.
172. Gao, P.; Chang, S. C.; Zhou, Z. H.; Weaver, M. J. *J Electroanal Chem* **1989,** 272, (1-2), 161-178.
173. Fang, X.; Wang, L. Q.; Shen, P. K.; Cui, G. F.; Bianchini, C. *J Power Sources* **2010,** 195, (5), 1375-1378.
174. Ma, L.; Chu, D.; Chen, R. R. *Int J Hydrogen Energ* **2012,** 37, (15), 11185-11194.

175. Sheikh, A. M.; Silva, E. L.; Moares, L.; Antonini, L. M.; Abellah, M. Y.; Malfatti, C. F. *American Journal of Mining and Metallurgy* **2014,** 2, (4), 64-69.
176. Zhu, L. D.; Zhao, T. S.; Xu, J. B.; Liang, Z. X. *J Power Sources* **2009,** 187, (1), 80-84.
177. Wang, H.; Xu, C. W.; Cheng, F. L.; Jiang, S. P. *Electrochem Commun* **2007,** 9, (5), 1212-1216.
178. Dutta, A.; Datta, J. *J Phys Chem C* **2012,** 116, (49), 25677-25688.
179. Bahemmat, S.; Ghassemzadeh, M.; Afsharpour, M.; Harms, K. *Polyhedron* **2015,** 89, 196-202.
180. Wang, K. W.; Kang, W. D.; Wei, Y. C.; Liu, C. W.; Su, P. C.; Chen, H. S.; Chung, S. R. *Chemcatchem* **2012,** 4, (8), 1154-1161.
181. Zhao, X.; Zhang, J.; Wang, L. J.; Liu, Z. L.; Chen, W. *J Mater Chem A* **2014,** 2, (48), 20933-20938.
182. Du, W. X.; Mackenzie, K. E.; Milano, D. F.; Deskins, N. A.; Su, D.; Teng, X. W. *Acs Catal* **2012,** 2, (2), 287-297.
183. Mao, H. M.; Wang, L. L.; Zhu, P. P.; Xu, Q. J.; Li, Q. X. *Int J Hydrogen Energ* **2014,** 39, (31), 17583-17588.
184. da Silva, S. G.; Assumpcao, M. H. M. T.; Silva, J. C. M.; De Souza, R. F. B.; Spinace, E. V.; Neto, A. O.; Buzzo, G. S. *Int J Electrochem Sc* **2014,** 9, (10), 5416-5424.
185. Carmo, M.; Sekol, R. C.; Ding, S. Y.; Kumar, G.; Schroers, J.; Taylor, A. D. *Acs Nano* **2011,** 5, (4), 2979-2983.
186. Takeguchi, T.; Anzai, Y.; Kikuchi, R.; Eguchi, K.; Ueda, W. *J Electrochem Soc* **2007,** 154, (11), B1132-B1137.
187. Shen, P. K.; Xu, C. W. *Electrochem Commun* **2006,** 8, (1), 184-188.
188. Wang, L. Q.; Lavacchi, A.; Bevilacqua, M.; Bellini, M.; Fornasiero, P.; Filippi, J.; Innocenti, M.; Marchionni, A.; Miller, H. A.; Vizza, F. *Chemcatchem* **2015,** 7, (14), 2214-2221.
189. Hu, C. G.; Cheng, H. H.; Zhao, Y.; Hu, Y.; Liu, Y.; Dai, L. M.; Qu, L. T. *Adv Mater* **2012,** 24, (40), 5493-5498.
190. Zhu, F. C.; Ma, G. S.; Bai, Z. C.; Hang, R. Q.; Tang, B.; Zhang, Z. H.; Wang, X. G. *J Power Sources* **2013,** 242, 610-620.
191. Wang, H.; Jusys, Z.; Behm, R. J. *J Phys Chem B* **2004,** 108, (50), 19413-19424.
192. Wang, Y.; Zou, S. Z.; Cai, W. B. *Catalysts* **2015,** 5, (3), 1507-1534.
193. Li, M.; Liu, P.; Adzic, R. R. *J Phys Chem Lett* **2012,** 3, (23), 3480-3485.
194. Wenham, S. R., *Applied photovoltaics*. 3rd ed.; Earthscan: London ; New York, 2012.
195. Mathew, S.; Yella, A.; Gao, P.; Humphry-Baker, R.; Curchod, B. F. E.; Ashari-Astani, N.; Tavernelli, I.; Rothlisberger, U.; Nazeeruddin, M. K.; Gratzel, M. *Nat Chem* **2014,** 6, (3), 242-247.
196. Kamat, P. V. *J Phys Chem C* **2008,** 112, (48), 18737-18753.
197. Sambur, J. B.; Novet, T.; Parkinson, B. A. *Science* **2010,** 330, (6000), 63-66.
198. Nozik, A. J.; Beard, M. C.; Luther, J. M.; Law, M.; Ellingson, R. J.; Johnson, J. C. *Chem Rev* **2010,** 110, (11), 6873-6890.
199. Duan, J. L.; Zhang, H. H.; Tang, Q. W.; He, B. L.; Yu, L. M. *J Mater Chem A* **2015,** 3, (34), 17497-17510.
200. Kouhnavard, M.; Ikeda, S.; Ludin, N. A.; Khairudin, N. B. A.; Ghaffari, B. V.; Mat-Teridi, M. A.; Ibrahim, M. A.; Sepeai, S.; Sopian, K. *Renew Sust Energ Rev* **2014,** 37, 397-407.
201. Singh, L. P.; Srivastava, K.; Mishra, R.; Ningthoujam, R. S. *J Phys Chem C* **2014,** 118, (31), 18087-18096.

202. Bender, C. M.; Burlitch, J. M.; Barber, D.; Pollock, C. *Chem Mater* **2000,** 12, (7), 1969-1976.
203. Jackson, S. D. *Opt Lett* **2003,** 28, (22), 2192-2194.
204. Di Bartolo, B.; Powell, R. C., *Crystal symmetry, lattice vibrations and optical spectroscopy of solids : a group theoretical approach*. World Scientific: Hackensack New Jersey, 2014; p xviii, 515 pages.
205. Trupke, T.; Green, M. A.; Wurfel, P. *J Appl Phys* **2002,** 92, (7), 4117-4122.
206. Zhou, Z. Y.; Wang, J. H.; Nan, F.; Bu, C. H.; Yu, Z. H.; Liu, W.; Guo, S. S.; Hu, H.; Zhao, X. Z. *Nanoscale* **2014,** 6, (4), 2052-2055.
207. Zhu, G.; Wang, H. Y.; Zhang, Q. X.; Zhang, L. *J Colloid Interf Sci* **2015,** 451, 15-20.
208. Luoshan, M. D.; Li, M. Y.; Liu, X. L.; Guo, K. M.; Bai, L. H.; Zhu, Y. D.; Sun, B. L.; Zhao, X. Z. *J Power Sources* **2015,** 287, 231-236.
209. Wang, K. F.; Jiang, J. Q.; Wan, S. J.; Zhai, J. *Electrochim Acta* **2015,** 155, 357-363.

Chapter 2. Experimental Methods for Synthesis and Characterization of Materials

2.1. Synthesis Approaches

2.1.1. Surfactant-Based Synthesis of One-Dimensional (1D) Ultrathin Nanowires

As an ‘extreme’ case of one-dimensional nanostructures, ultrathin 1D structures couple the merits not only of extended, smooth facets associated with an anisotropic morphology but also of the high surface area-to-volume ratios attributable to their nanometer-scale dimensions.[1] All of these advantages denote highly promising functional attributes for the use of these materials as electrocatalysts.

In terms of synthesis approaches, in early research, templates, such as zeolites, mesoporous materials, and nanocrystals, were widely used to generate one-dimensional ultrathin nanostructures, especially polymers, as the dimensions of the resulting product can be strictly confined and controlled by the pore size of these templates.[2] However, the removal of these templates, namely the extraction of the ultrathin wires, had become an issue, although in some cases, the template itself could serve as a mediating functional component. For instance, Au and Pt nanowires could be synthesized using 1D-channel metal organic framework (MOF) pores.[3] Together, they exhibited useful properties not found in either component separately, such as fluorescence quenching, which implies that MOFs can assist in the alteration of properties of the nanostructures. However, in most scenarios that required the removal of templates, the removal process itself resulted in instability and potential destruction of the as-synthesized nanowires.[4] Thus, such reports have been scarce in recent years.

Meanwhile, soft template and surfactant-assisted methods have been more attractive, owing to their chemical flexibility and relatively facile synthesis conditions. In recent papers, Pt-binding peptides (i.e. with an amino acid sequence of Ac-TLHVSSY-$CONH_2$, otherwise known as BP7A) have been used to generate a Pt nanowire possessing unique multiple-twinned structure with diameter of ~2 nm.[5] Other surfactants, such as benzyldimethylhexadecylammonium chloride (BDAC),[6] poly(amidoamine) dendrimers,[7] long-chain amidoamine derivatives,[8, 9] Triton X-100,[10] or X-114[11] and so forth, have been adopted as viable candidates for the preparation of noble metal (e.g., Au, Pt, etc.) ultrathin nanowires.

In this thesis, we utilized a synthetic approach which has been proven to yield long and extended polycrystalline nanowires, which possess lengths of several tens of nanometers, consisting of single crystalline segments.[12-14] Specifically, metal precursors (including Pd^{2+}, Ni^{2+}, Cu^{2+} or combinations of multiple metallic species) were reduced by sodium tetrahydroborate ($NaBH_4$) into forming thermodynamically unstable elongated primary nanostructures (PNs), due to the existence of octadecylamine (ODA) and *n*-dodecyltrimethylammonium bromide (DTAB), serving as surfactant and phase transfer agent, respectively. The secondary growth of these PNs apparently takes place in preferred equivalent directions and also along the (111) direction, which leads to the growth of thread-like quasi-nanowires.[14]

The advantages of such a technique are described as follows: (1) This synthetic protocol is one-pot and time-effective procedure. Indeed, the formation of nanowires can be completed within 1 hour. (2) The stoichiometry of the nanowires can be directly dictated by modifying the corresponding stoichiometric ratio of the relevant metallic precursors within the precursor solution. (3) This synthetic approach can be readily generalized to systems, including ultrathin Pt,[15] Pd,[12] Pd-Au,[16] Pd-Ni,[17] as well as Pd-Cu[18] nanowires with precise control over their chemical compositions. However, several disadvantages are present. First, the requirement of an inert gas atmosphere increases the overall complexity of the procedure. Second, the scale-up of this method necessitates careful refinement and adjustment of the amount of chemicals being used, especially ODA and DTAB.[19]

Briefly, in a typical synthesis experiment, palladium nitrate (Alfa Aesar, 99.9%), transition metal precursor (Nickel (II) chloride (Fisher Scientific, > 96%) in the case of the $Pd_{1-x}Ni_x$ series in Chapter 3; Copper (II) acetate (Fisher Scientific, 99%, anhydrous) in the case of the $Pd_{1-x}Cu_x$ series in Chapter 4), octadecylamine (ODA, 400 mg, Acros Organics, 90%), and dodecyltrimethylammonium bromide (DTAB, 60 mg, TCI, >99%) were dissolved in 7 mL of toluene under vigorous magnetic stirring. The amounts of the two precursors were correlated with the desired atomic ratios of these two elements, with the total sum fixed at 0.056 mmol. For example, to obtain a chemical composition of Pd_9Cu, the amount of palladium nitrate was set at 0.050 mmol, whereas the quantity of copper (II) acetate was adjusted to 0.006 mmol. The entire mixture was left to react under an argon atmosphere, utilizing standard air-sensitive Schlenk-line procedures, and it was subsequently sonicated for 20 minutes. Separately, solid sodium borohydride (13 mg, Alfa Aesar 98%) was dissolved into 2 mL of deoxygenated distilled water, and the solution was added drop-wise into the precursor mixture, while stirring.

After 1 h of reaction, the mixture was diluted with 2 mL aliquots of distilled water and chloroform, thereby resulting in the separation of the organic and aqueous phases. The black organic phase was then isolated, diluted with 10 mL of absolute ethanol, and eventually centrifuged for an additional 10 min, ultimately resulting in the precipitation of a black solid. The black solid was subsequently washed several times with ethanol, and allowed to air dry. Adsorption of these as-prepared nanowires onto a conductive carbon support (Vulcan XC-72, Cabot) was achieved by first dispersing the isolated black solid, containing a mixture of ultrathin nanowires and residual surfactant, into 6 mL of chloroform, until a homogeneous black mixture was formed. An equal mass of Vulcan carbon (i.e. ~6 mg) was then added to this mixture, and this was subsequently sonicated for 30 min in a bath sonicator. As-prepared composites were isolated by centrifugation, and fixed onto the carbon substrate by immersion in hexanes for 12 h.

2.1.2. Deposition of Pt Monolayer on 1D Electrocatalysts

As discussed in Chapter 1, most of our series of electrocatalysts consist of a monolayer of Pt coated onto either carbon-supported metal or metal-alloy nanoparticles which effectively leads to the most effective and strategic utilization of Pt, since almost every Pt atom is present on the surface and can therefore participate in the electrocatalytic reactions. These electrocatalysts are referred to as platinum monolayer (Pt_{ML}) electrocatalysts. The Pt monolayer deposition process involves the galvanic displacement of an ‘underpotentially deposited’ Cu monolayer onto a suitable substrate by Pt.[20]

$$Cu_{ML} + K_2PtCl_4\,(aq) \rightarrow Pt_{ML} + 2KCl_{aq} + CuCl_2\,(aq) \qquad (2.1)$$

Specifically, the Pt deposition process is composed of two steps. First, a monolayer of Cu was deposited onto the surface of ultrathin nanowires by Cu underpotential deposition (UPD) from a deoxygenated solution of 50 mM $CuSO_4$, maintained in a 0.10 M H_2SO_4 electrolyte.[21] Specifically, the potential was held constant at approximately 400 mV (vs. RHE) in order to deposit the Cu onto the surfaces of as-processed nanowires. The Cu monolayer-modified electrode was subsequently transferred to a solution of 1.0 mM K_2PtCl_4 solution in 50 mM H_2SO_4 for several minutes. The Pt monolayer modified electrode was subsequently removed from the cell and rinsed thoroughly, before any further measurements were performed. The Cu UPD apparatus is shown in Figure 2.1[22]:

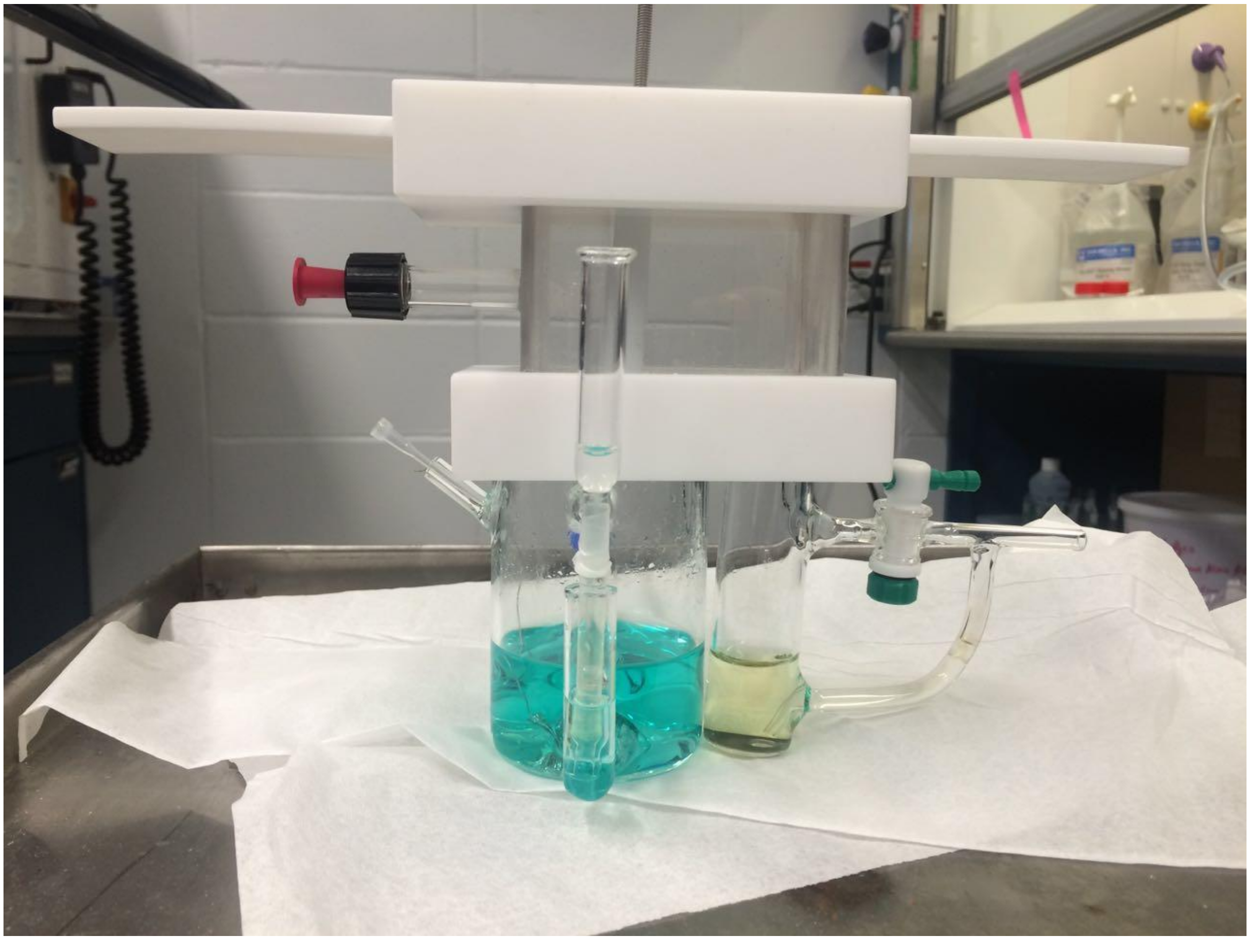

Figure 2.1 Cells and setup for Pt_{ML} deposition by displacement of Cu UPD monolayer.

In this thesis, we also introduce a modified 'bulk', gram-scale synthesis approach, initially reported by Shao *et al.*[23] to synthesize $Pt\sim Pd_9Au$ core-shell nanowires in Chapter 6. We should note that this protocol has never been previously applied to the synthesis of ultrathin nanowires. In effect, the process consists of (a) a UV/ozone treatment followed by (b) CO stripping and (c) Pt deposition. Specifically, Pd_9Au/C was first dispersed into ethanol by sonication after which it was placed onto a watch glass and subsequently dried. The watch glass was placed into a UV ozone generator (UVOCS model no. T10X10-0ES) and treated for 15 min. As-treated nanowires were then isolated from the underlying watch glass by sonication. The ‘reactor’ environment, where the CO stripping and Pt deposition processes were allowed to occur, consisted of a graphite sheet working electrode, a platinum black (porous Pt film) counter electrode, and an Ag/AgCl (BASi) leak-free reference electrode.

The UV/ozone treated sample was pre-dispersed in 50 mM H_2SO_4, and then added to the ‘reactor’, prior to the ‘CO stripping’ step. Adsorption of CO was achieved by bubbling in CO gas into the electrolyte for 30 minutes, thereby forming a CO-saturated solution. Then the adsorbed CO was subsequently stripped from the surface by a potential sweep, running up to 1.1 V at 20 mV/s. After pretreatment, a de-aerated aqueous $CuSO_4$ solution in 50 mM H_2SO_4 was added to the ‘reactor’ in order to obtain a Cu^{2+} concentration of 50 mM. After addition of $CuSO_4$, the potential was held constant at approximately 400 mV (vs. RHE) in order to deposit a monolayer of Cu onto the Pd_9Au nanowires. A de-aerated aqueous solution of K_2PtCl_4 in 50 mM H_2SO_4 was immediately added dropwise to the ‘reactor’ in order to initiate galvanic replacement of the Cu by the Pt. After 5~10 minutes, the reaction was complete. The catalysts were subsequently washed with MilliQ UV-plus water, and centrifuged. The resulting catalyst powder, denoted as Pt~Pd_9Au/C, was dried in vacuum at 80ºC prior to further analysis.

The Cu UPD technique possesses several advantages. First, the amount of the metal deposited can be accurately quantified by examining the corresponding cyclic voltammetry (CV) curves. Second, the process is extremely time-effective, and can be completed within 30 mins or so. Third, as compared with the core–shell nanostructured catalysts prepared by other methods, those fabricated using the UPD method tend to exhibit either much higher mass activity or much greater Pt utilization.[24-26] Nevertheless, the UPD method does yield some disadvantages. Indeed, the relative complexity of the process, as well as the large amount of inert gas needed to protect the system from unwanted oxidation processes for example, hinder it from being readily utilizable on a large scale. Furthermore, stability remains an issue for monolayer core–shell catalysts. In fact, there has been an on-going debate as to whether the so-called "monolayer" could be preserved without forming Pt "islands" after a thorough electrochemical cycling process, which is essential for practical fuel cell applications.[27] Overall, nevertheless, UPD still represents a viable and generalizable method for the preparation of high-performance core-shell nanostructured catalysts.

In this thesis, the process has been applied to a number of ultrathin nanowires including the $Pd_{1-x}Ni_x$ series (in Chapter 3), the $Pd_{1-x}Cu_x$ series (in Chapter 4) and the $Pd_{1-x}Au_x$ series (in Chapter 6), described in this thesis. These as-prepared core-shell NWs exhibited outstanding performance towards respective reactions including ORR, alkaline MOR, and alkaline EOR, and the results are described in detail in Chapters 3, 4, and 6, respectively.

2.1.3. Hydrothermal Synthesis of Nanocrystals

The hydrothermal synthesis process can be defined as a method for the formation and growth of crystals by chemical reactions and solubility changes of substances within a sealed and heated aqueous solution prepared above ambient temperature and pressure.[28, 29] Precise control over hydrothermal synthetic conditions is key to the success for the preparation of inorganic semiconducting nanostructures. These controllable reaction conditions usually include concentration, pH value, time, pressure, organic additives, and/or templates. Based upon the adjustment of these parameters, various hydrothermal synthetic strategies of inorganic nanostructures have been developed.

In terms of apparatus, the crystallization vessels normally used are autoclaves.[30] They typically consist of thick-walled steel cylinders with a hermetic seal which must be able to withstand high temperatures and pressures for prolonged periods of time. Furthermore, the autoclave material must be inert with respect to the solvent. To prevent corrosion of the internal cavity of the autoclave, protective inserts are generally used. These may have the same shape as the autoclave and fit in the internal cavity, which may be composed of either carbon-free iron, copper, glass (or quartz), or Teflon. A schematic of an autoclave is shown in Figure 2.2. Owing to the relatively facile synthetic conditions, the hydrothermal approach possesses its intrinsic advantages and disadvantages.[31, 32] The advantages of the hydrothermal synthesis method include the ability to synthesize crystals of substances which are unstable near the melting point, and the ability to synthesize large crystals possessing high quality. The disadvantages of this technique are the high cost of the equipment and the inability to properly monitor crystals during the process of their growth.

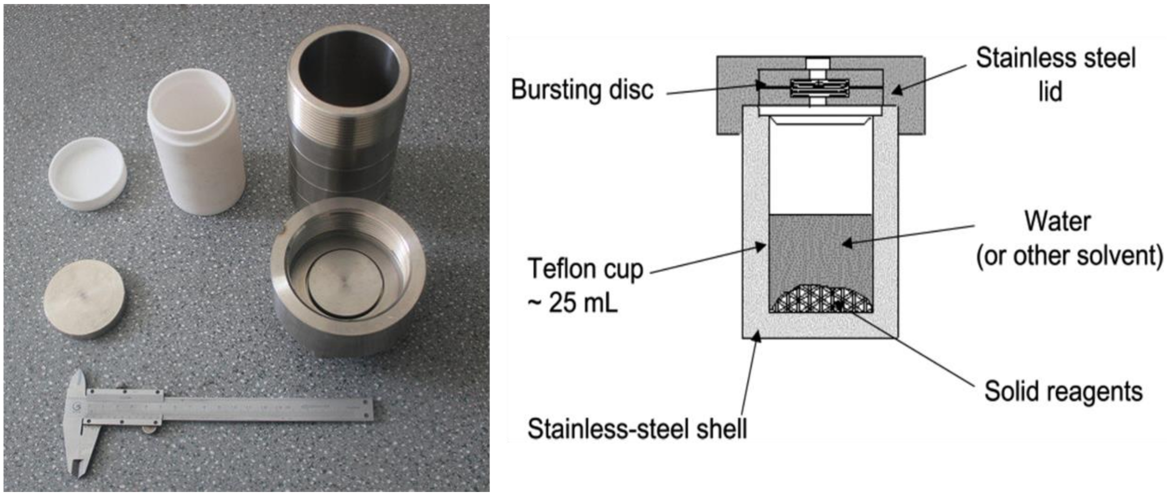

Figure 2.2. A schematic of a Teflon-lined stainless steel autoclave typically used for hydrothermal synthesis. Reprinted with permission from Ref 32. Copyright 2014, The Royal Society of Chemistry.

In this thesis, we have utilized two different hydrothermal approaches to prepare sodium yttrium fluoride ($NaYF_4$) nanocrystals with controllable morphologies and sizes. Specifically, zero-dimensional (0D) and three-dimensional (3D)) Er^{3+}, Yb^{3+} co-doped $NaYF_4$ have been prepared, based upon a previously reported hydrothermal approach with a slight modification. Briefly, a total of 0.1 mmol of YCl_3, $YbCl_3$, and $ErCl_3$ were weighed out and dissolved in 10 mL of water. The molar ratio amongst these three metal precursors is 74: 18: 8. Then, 2 mL of 1 M NaF solution was added in, followed by the addition of 2 mmol of NaCl. Thereafter, a desired amount (i.e. from 0 to 2 mL) of 5 M $NH_3 \cdot H_2O$ was added in drop-wise to alter the pH of the final solution. The solution was then vigorously stirred for 15 min, transferred into a Teflon-lined stainless-steel autoclave (with a capacity of 20 mL), and finally sealed. In a systematic series of individual experiments aimed at acquiring mechanistic insights, the autoclave was subsequently oven heated to the desired temperature (i.e. 100°C to 220°C) for a designated amount of reaction time (i.e. 1 hour to 6 hours), and naturally left to cool to room temperature. As-prepared samples were later isolated from solution by centrifugation upon washing with water and ethanol (EtOH), followed by air drying at 80°C overnight.

In addition, one-dimensional (1D) $NaYF_4$ nanorods have also been synthesized, based upon another previously reported modification of an existing solvothermal protocol.[33, 34] In a typical preparation, 0.7 g (i.e. 17.5 mmol) of NaOH, 14.2 g (i.e. 45.2 mmol) of oleic acid (90% purity, Sigma-Aldrich), and 10.0 g of ethanol were mixed together to obtain a white viscous solution. 12 mL (i.e. 7.2 mmol) of a 0.58 M NaF solution was added under vigorous stirring, until a translucent solution was obtained. Then 1.5 ml (1.2 mmol) of a 0.80 M ethanolic solution of $Y(NO_3)_3$ incorporating an optically desirable, optimal Ln^{3+} doping content (18% Yb and 8% Er, molar ratio) was poured into the solution under vigorous stirring. Before transferring to a Teflon-lined autoclave with an internal volume of 23 mL, the solution was aged for 20 min at room temperature. The solvothermal reaction was then conducted in a drying oven at a relatively high temperature of 210°C for a longer reaction period of up to 10 h. After the reaction, the white products isolated by centrifugation were thoroughly washed with deionized water, and later dried at 60°C for 48 h.

2.2. Computational

Density functional theory (DFT) is a computational quantum mechanical modelling method used in physics, chemistry, and materials science to investigate the electronic structure (principally the ground state) of many-body systems, and in particular, atoms, molecules, and condensed phases. Using this theory, the properties of a many-electron system can be determined by using functionals, i.e. functions of another function, which in this case is represented by the ‘spatially-dependent’ electron density.[35] Hence, the name, density functional theory, comes from the use of functionals associated with the electron density. Herein, we utilized DFT calculations mainly to simulate the oxygen binding energy (O-BE) of our series of Pt~$Pd_{1-x}Au_x$ ultrathin nanowires in order to gain theoretical perspectives of their corresponding ORR performances.

Specifically, pertaining to the work described in Chapter 5, the DFT calculations were performed by using the Vienna *ab initio* simulation package (VASP).[36, 37] The spin-restricted GGA-PW91 functional,[38] a plane-wave basis set with an energy cutoff of 400 eV, and the projector augmented wave (PAW) method[39] were adopted. The Brillouin zone of the supercell was sampled by 1×1×5 k-points using the Monkhorst–Pack scheme.[40] The conjugate gradient algorithm was used in optimization, allowing for the convergence of 10^{-4} eV in total energy and 0.02 eV/Å in the Hellmann-Feynman force on each atom.

To model nanowires (NW) using DFT, we constructed cylinder-like $Pd_{1-x}Au_x$@Pt core-shell NWs measuring 2.2 nm in diameter, based upon the experimental observations,[16, 41, 42] showing that the (111) and (200) surfaces were the dominant facets. Three different chemical compositions of the PdAu core were considered, namely Pd_9Au, Pd_8Au_2, and Pd_7Au_3, which we associated with the experimentally measured lattice parameters of 3.923 Å, 3.934 Å, and 3.948 Å, respectively, and which helped to define the periodic boundary conditions along the wire direction. Two unit cells along the wire direction were included in a cubic supercell whose size was sufficiently large enough that the separation between the NW sidewalls and their images in the other two directions was >15.0 Å. Furthermore, Pd@Pt and Pt NWs possessing the same size and shape were also included by means of comparison.

The relative stability of various core-shell nanowires (NW) was evaluated using the formation energy in eV/atom, which is defined in Equation 2.2 as:

$$E_{Form} = [E(NW) - j_{Pt}E(Pt) - m_{Pd}E(Pd) - n_{Au}E(Au)]/(j_{Pt} + m_{Pd} + n_{Au}) \qquad (2.2)$$

wherein E(NW), E(Pt), E(Pd), and E(Au) represent total energy of the NW, gas-phase Pt, Pd, and Au atom, respectively, while j_{Pt}, m_{Pd}, and n_{Au} designate the corresponding number of Pt, Pd, and Au atoms in the NW.

Atomic O was used as a probing adsorbate for the ORR activity. The O-binding energy (denoted as BE-O) has been used as a good “descriptor” for probing the ORR,[43] wherein the calculated BE-O was correlated with theoretically predicted and experimentally measured ORR activity.[44, 45] BE-O is defined in Equation 2.3 as:

$$BE\text{-}O = E(O/NW) - E(H_2O) + E(H_2) - E(NW) \qquad (2.3)$$

wherein E(O/NW), $E(H_2O)$, and $E(H_2)$ correspond to the total energy of O-adsorbed NW, water, and hydrogen in the gas phase, respectively. Hence, a more positive BE-O implies weaker O-binding. To calculate BE-O, we chose *fcc* and *hcp* 3-fold hollow sites on (111) terraces far away and nearly equidistant away from the edge, as the (111) terraces of a nanoparticle were found to contribute the most to the observed ORR.[46, 47] No geometric constraints were applied during the optimization process, which was found to be essential in order to explicitly capture the subtle and actual size- and shape-effect of real nanocatalysts.[48]

2.3. Characterization Techniques

2.3.1. X-ray Diffraction (XRD)

It has been proven by the Braggs that cleavage of particular faces of crystals reflect X-ray beams at certain prescribed and well-defined angles of incidence (theta, θ), a phenomenon also known as Bragg's law[49]:

$$n \lambda = 2d \sin \theta \tag{2.4}$$

The variable 'd' is the distance between the atomic layers in a crystal; the variable lambda (λ) is the wavelength of the incident X-ray beam; and 'n' is an integer. This observation is an example of X-ray wave interference, commonly known as X-ray diffraction (XRD), and provided for direct evidence for the periodic atomic structure of crystals. Typically, the XRD technique is utilized towards one or more goals including but not limited to: (a) measure the average spacings between either layers or rows of atoms; (b) determine the orientation of a single crystal or grain; (c) find the crystal structure of an unknown material; and (d) measure the size, shape, and internal stress of small crystalline regions.

In this thesis, XRD measurements were carried out using a Scintag diffractometer, in order to verify the chemical composition of the various ultrathin nanowires (Chapters 3 and 4) as well as to probe the composition and crystallinity of as-synthesized $NaYF_4$ nanocrystals (Chapter 5). For the $Pd_{1-x}Ni_x$ series (Chapter 3) and the $Pd_{1-x}Cu_x$ series (Chapter 4), the patterns were typically collected over a range of 35° to 95°; for $NaYF_4$ nanocrystals (Chapter 6), the patterns were characteristically acquired over a range of 15° to 60°. All patterns have been collected in the Bragg configuration with a step size of 0.25° using Cu Kα radiation ($\lambda = 1.5415$ nm).

2.3.2. Electron Microscopy

2.3.2.1. Transmission Electron Microscopy (TEM) and Selected Area Electron Diffraction (SAED)

Transmission electron microscopy (TEM) is a microscopy technique in which a beam of electrons is transmitted through an ultra-thin specimen, interacting with the specimen as it passes through it. An image is formed from the interaction of the electrons transmitted through the specimen; the image is magnified and focused onto an imaging device, usually a sensor such as a CCD camera. TEM instruments are capable of imaging at a significantly higher resolution than light microscopes, owing to the small de Broglie wavelength of electrons.[50] This enables examination of structures as small as a single column of atoms, which is at least three orders of magnitude smaller in terms of dimensions than the smallest possible resolvable object that can be detected using an optical microscope.[51, 52]

Typically, the TEM is composed of components including (1) an electron emission source for the generation of the electron stream; (2) a vacuum system in which the electrons travel; (3) a series of electromagnetic lenses, as well as (4) electrostatic plates. The lenses and plates allow the operator to guide and manipulate the beam as required. Imaging devices are subsequently used to create an image from the electrons that exit the system. The components of a representative TEM system are depicted in Figure 2.3:

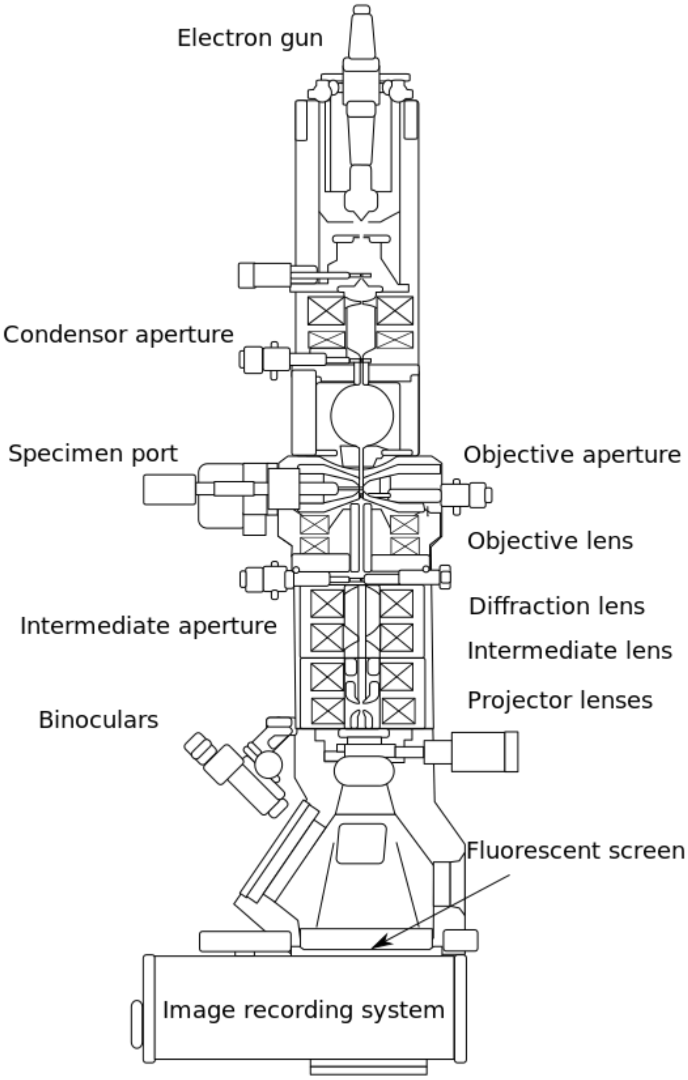

Figure 2.3. Layout of optical components in a basic TEM. Reprinted with permission from ref 52. Copyright 2005, Creative Commons.

Theoretically, the maximum resolution, ‘d’, that one can obtain with a microscope, has been limited by the wavelength of the photons that are being used to probe the sample, λ and the numerical aperture of the system, NA, which represent a dimensionless number that characterizes the range of angles over which the system can either accept or emit light[53]:

$$d = \frac{\lambda}{2n\sin\alpha} \approx \frac{\lambda}{2NA} \tag{2.5}$$

One of the advanced categories of TEM, namely, high-resolution transmission electron microscopy (HRTEM), uses both the transmitted and the scattered beams to create an interference image. At present, the highest point resolution realizable in TEM is around 0.5 Å (0.050 nm).[54] At these small scales, the individual atoms of a crystal and its defects can be resolved.

Selected area electron diffraction (SAED) is a crystallographic experimental technique that can be performed inside a TEM.[55, 56] In terms of the mechanism, electrons are diffracted by the atoms within a specific material, and the pattern is mainly determined by the crystal structure. As a result, the image on the screen of the TEM will be a series of spots with each spot corresponding to a satisfied diffraction condition of the sample's crystal structure. If the material is polycrystalline and possesses many different constituent subcrystals with various orientations, rings are formed as a result of an averaging of the spots, similar to what is attained by XRD, thereby allowing for identification.

In Chapters 3 through 6, all TEM images were obtained on a JEOL 1400 transmission electron microscope (TEM) equipped with a 2048 x 2048 Gatan CCD camera and operated at an accelerating voltage of 120 kV. HRTEM and SAED patterns were collected on a JEOL 2100F analytical TEM, equipped with a Gatan CCD camera and a Gatan HAADF detector, operating at an accelerating voltage of 200 kV.

2.3.2.2. Scanning Electron Microscopy (SEM)

A scanning electron microscope (SEM) is a type of electron microscope that produces images of a sample by scanning it with a focused beam of electrons. The electrons interact with atoms in the sample, producing various signals that contain information about the sample's surface topography and composition.[57] Magnification in an SEM can be controlled over a range of about 6 orders of magnitude from about 10 to 500,000 times. The electron beam is generally scanned in a raster scan pattern, and the beam's position is combined with the detected signal to produce an image. Specimens can be observed in high vacuum, in low vacuum, in wet conditions (in environmental SEM), and at a wide range of either cryogenic or elevated temperatures.[58] A schematic demonstrating the structure of a SEM is depicted in Figure 2.4:

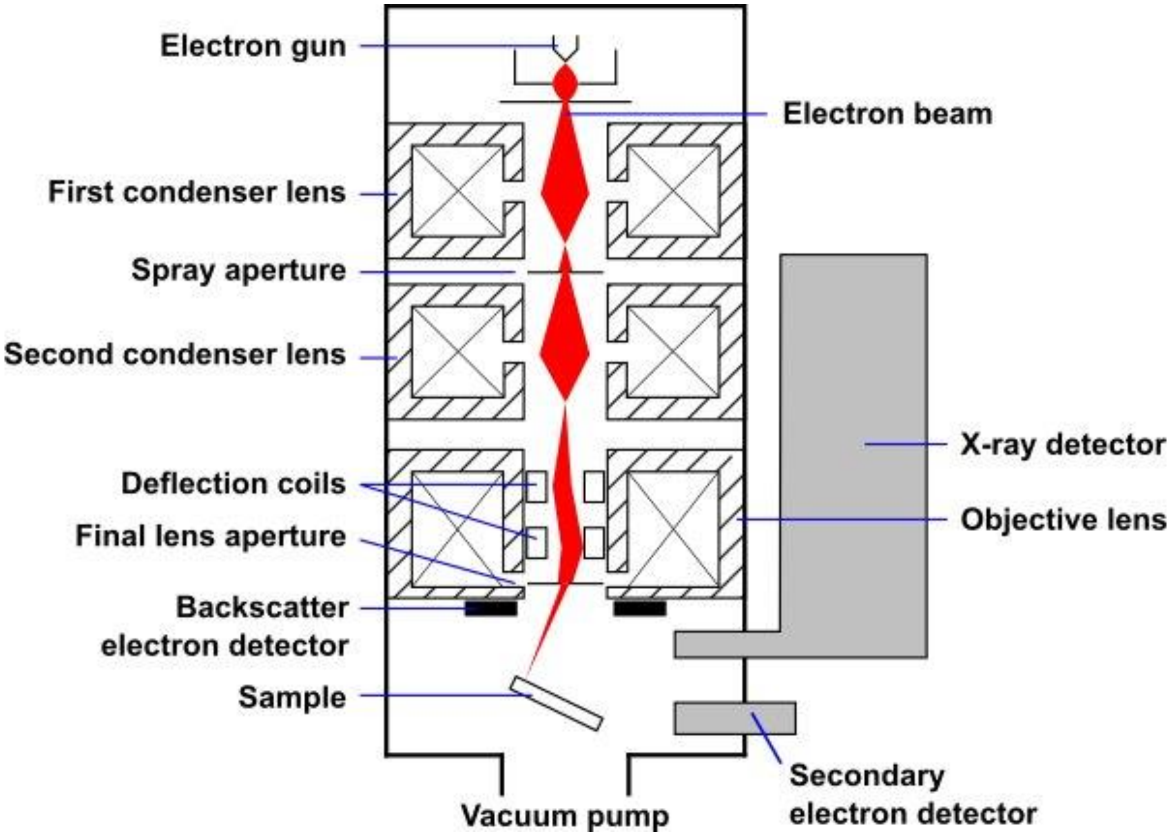

Figure 2.4 Schematic of an SEM. Taken from the Biological Electron Microscopy Website.

A modern SEM is usually equipped with energy-dispersive X-ray spectroscopy (EDS) capabilities. EDS, also known as EDAX, is an analytical technique used for either the elemental analysis or chemical characterization of a sample. It relies upon an interaction of some source of X-ray excitation and a sample. Its characterization capabilities are due in large part to the fundamental principle that each element has a unique atomic structure, thereby allowing for an exclusive and characteristically defining set of peaks within its X-ray emission spectrum.[59] To stimulate the emission of characteristic X-rays from a specimen, a high-energy beam of charged particles such as electrons or protons, or a beam of X-rays, is focused into the sample being studied. At rest, an atom within the sample contains either ground state (or unexcited) electrons in discrete energy levels or electron shells bound to the nucleus. The incident beam may excite an electron in an inner shell, ejecting it from the shell, while creating an electron hole where the electron had originally been. An electron from an outer, higher-energy shell then fills the hole, and the difference in energy between the higher-energy shell and the lower energy shell may be released in the form of an X-ray. The number and energy of the X-rays emitted from a specimen can be measured by an energy-dispersive spectrometer.

In Chapters 3 through 6, all the relevant SEM images were collected at 10 kV on a JEOL 7600F instrument. Energy dispersive X-ray spectroscopy (EDAX) was performed on a Leo 1550 field-emission scanning electron microscope (FE-SEM), run at an accelerating voltage of 20 kV.

2.3.3. X-ray Absorption Fine Structure (XAFS) Spectroscopy

X-ray absorption fine structure (XAFS) refers to the details of how X-rays are absorbed by an atom at energies near and above the core-level binding energies of that atom.[60] Specifically, XAFS denotes the modulation of an atom’s x-ray absorption probability due to the chemical and physical state of the atom. XAFS spectra are especially sensitive not only to the formal oxidation state and coordination chemistry but also to the distances, coordination number, and species of the atoms immediately surrounding the selected element. Because of this dependence, XAFS provides a practical and relatively simple, way to determine the chemical state and local atomic structure for a selected atomic species.[61]

X-rays are light with energies ranging from ~500 eV to 500 keV. At this energy regime, light is absorbed by all matter through the photo-electric effect.[62, 63] In this process, an X-ray photon is absorbed by an electron in a tightly bound quantum core level (such as the 1*s* or 2*p* level) of an atom (Figure 2.5). In order for a particular electronic core level to participate in the absorption, the binding energy of this core level must be less than the energy of the incident X-ray. If the binding energy is greater than the energy of the X-ray, the bound electron will not be perturbed from its well-defined quantum state and will not absorb the X-ray. If the binding energy of the electron is less than that of the X-ray excitation energy, the electron may be removed from its quantum level. In this case, the X-ray is destroyed (i.e., absorbed) and any energy in excess of the electronic binding energy is given to a photo-electron that is ejected from the atom with a characteristic energy.

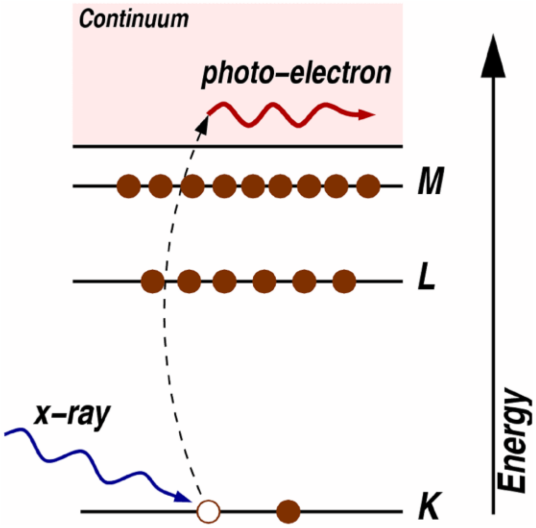

Figure 2.5 The relevant process associated with XAFS, in which an X-ray is absorbed and a core level electron is ejected out of the atom with a characteristic energy. Reprinted with permission from ref 63. Copyright 2011, John Wiley and Sons, Inc.

When the incident X-ray has an energy equal to that of the binding energy of a core-level electron, there is a sharp rise in absorption: an absorption edge corresponding to the promotion of this core level to the continuum. At most X-ray energies, the absorption coefficient μ is a smooth function of the energy (usually denoted as μ(E)) , with a value that depends on the sample density ρ, the atomic number Z, the atomic mass *A*, and the X-ray energy *E* itself, roughly as:

$$\mu(E) \approx \frac{\rho Z^4}{AE^3} \tag{2.6}$$

A typical XAFS spectrum measured for a powder of FeO is shown in Figure 2.6.[64] The sharp rise in the μ(E) due to the Fe 1*s* electron level (at 7112 eV) is clearly visible in the spectra, as are the oscillations in μ(E) that comprise the XAFS. Generally, the XAFS is composed of at least two distinctive portions: the near-edge spectra (XANES) - typically within 30 eV of the main absorption edge, and the extended fine-structure (EXAFS).

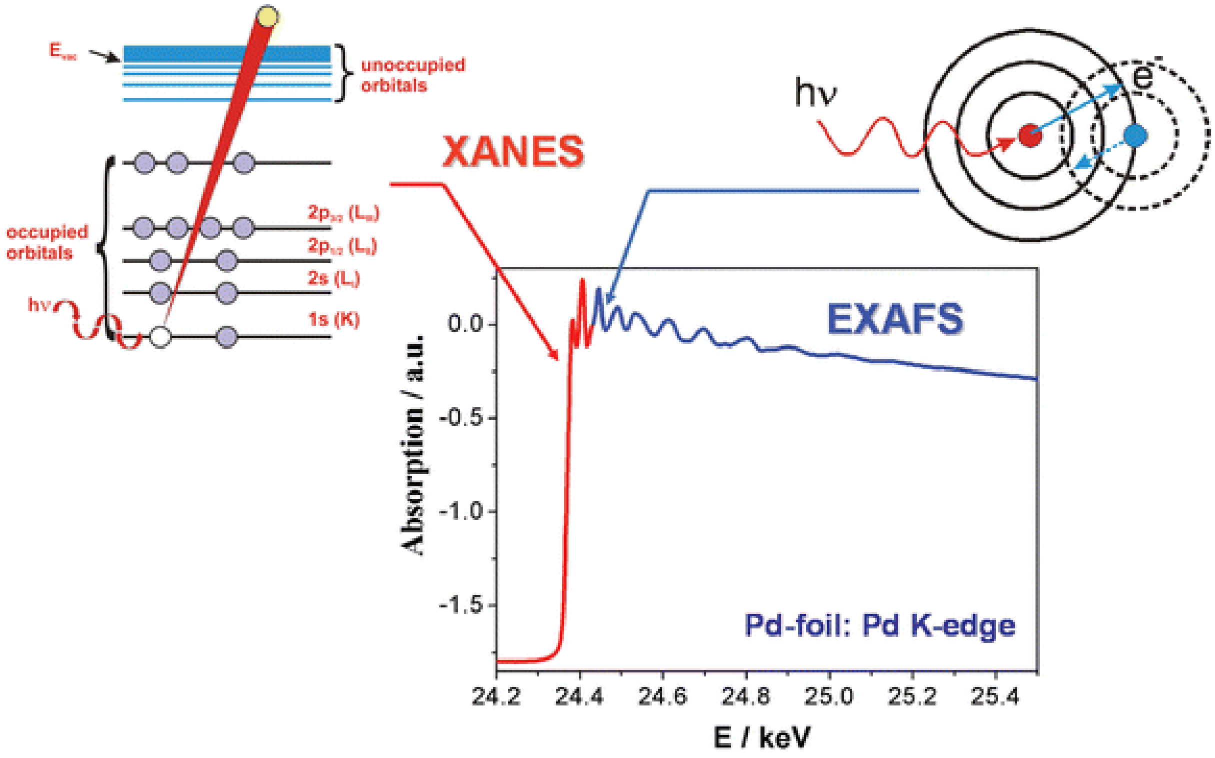

Figure 2.6. XAFS spectrum for Pd foil, shown with the XANES and EXAFS regions identified. Reprinted with permission from ref 64, Copyright 2005, The Royal Society of Chemistry.

Specifically, for the EXAFS, we are interested in the oscillations well above the absorption edge, and we define the EXAFS fine-structure function $\chi(E)$, as

$$\chi(E) = \frac{\mu(E) - \mu_0(E)}{\Delta\mu_0(E)} \tag{2.7}$$

wherein $\mu(E)$ is the measured absorption coefficient, $\mu_0(E)$ is a smooth background function representing the absorption of an isolated atom, and $\Delta\mu_0$ is the measured jump in the absorption $\mu(E)$ at the threshold energy E_0. EXAFS is best understood in terms of the wave behavior of the photo-electron created in the absorption process. Because of this, it is common to convert the X-ray energy to k, the wave number of the photo-electron, which has dimensions of 1/distance and is defined as:

$$k = \sqrt{\frac{2m(E - E_0)}{\hbar^2}} \tag{2.8}$$

wherein E_0 is the absorption edge energy and m is the electron mass. The primary quantity for EXAFS is then $\chi(k)$. The different frequencies apparent in the oscillations in $\chi(k)$ correspond to different near-neighbor coordination shells which can be described and modeled according to Equation 2.9:

$$\chi(k) = \sum_j \frac{N_j f_j(k) e^{-2k^2 \sigma_j{}^2}}{kR_j{}^2} \sin[2kR_j + \delta_j(k)] \tag{2.9}$$

wherein $f(k)$ and $\delta(k)$ are scattering properties of the atoms neighboring the excited atom, N is the number of neighboring atoms (i.e., coordination number), R is the distance to the neighboring atom, and σ^2 represents the variation in the neighbor-to-neighbor distance. Hence, the EXAFS equation allows one to determine N, R, and σ^2, by knowing the scattering amplitude $f(k)$ and phase-shift $\delta(k)$, which can be calculated through the fitting processes.

Therefore, we have utilized EXAFS to probe the coordination number (N) and interatomic distances (R) in Chapter 6, in order to determine the relative distribution of Pt, Pd and Au atoms within our Pt~Pd_9Au ultrathin nanowire structures. At the National Synchrotron Light Source, both Pt L_3-edge and Au L_3-edge data (L-edge refers to the process of transition from a metal 2*p* electron to unfilled *d* orbitals, in this case 5*d*) were collected at the X18A beamline with both sets of measurements obtained in the fluorescence mode. Different parameters contributing to the theoretical EXAFS equation (e.g., bond distances and energy origin correction or coordination numbers and the bond length disorder parameters) correlate into the resulting fit. Constraining them during the fit improves the stability and viability of the results. In our analysis, we modeled the Pt and Au L_3-edge data concurrently by applying multiple constraints.[65] Only Pt-Au and Pt-Pt as well as Au-Pt, Au-Au, and Au-Pd data contributed to the Pt and Au EXAFS results, respectively.

After data collection, data set fitting was preformed concurrently for Pt L_3 and Au L_3 edge EXAFS spectra using FEFF6 theory and IFEFFIT data analysis package. For the Pt edge, only the first nearest neighbor theoretical Pt- Pt path was used for fitting of Pt-Au/Pt contributions. The disorder factor (σ^2) and the correction in threshold energy (ΔE_0) were constrained to be the same for all conditions for Pt edge spectra. The k-range (limited at the upper end by the appearance of the Au L_3 edge) of 2.5-8.7 $Å^{-1}$ and R-range of 1.8-3.4 Å were used in the fits. For the Au edge, the model included two paths: Au-Au (to simulate the Au-Pt/Au pairs) and Au-Pd. The disorder factors of these bond lengths were constrained so as to not vary with reaction conditions. The ΔE_0 parameters for the both paths were limited to be the same for all conditions. The fitting k-range and R-range were 2.5-11 $Å^{-1}$ and 1.8-3.4 Å, respectively.

2.3.4. Surface Profile

2.3.4.1. Infrared Spectra

Infrared spectroscopy (i.e. IR spectroscopy) is associated with the infrared region of the electromagnetic spectrum, specifically light with a longer wavelength and lower frequency than visible light. A basic IR spectrum is essentially a graph of infrared light absorbance (or transmittance) on the vertical axis vs. either frequency or wavelength on the horizontal axis.[66]

Typical units of frequency used in IR spectra are wavenumbers, which are defined in terms of reciprocal centimeters, with the symbol cm^{-1}.

The IR instrumentation is comparatively simple, and can deliver accurate and precise measurements. Basically, infrared light is guided through an interferometer and then through the sample. A moving mirror inside the apparatus alters the distribution of infrared light that passes through the interferometer. The signal directly recorded, also known as “interferogram”, represents light output as a function of the mirror position.[67] Through Fourier transform, the raw data is converted into the desired spectrum, which essentially denotes light output as a function of wavenumber. Therefore, modern IR instruments incorporate Fourier transform infrared (FTIR) spectroscopy.

FTIR measures the fundamental vibrations and associated overtones of the chemical species present in a sample in the infrared region of the electromagnetic spectrum.[68] In other words, it exploits the fact that molecules absorb specific frequencies that are characteristic of their structure. These absorptions are resonant frequencies, i.e. the frequency of the absorbed radiation matches the transition energy of the bond or group that vibrates. The energies are determined by the shape of the molecular potential energy surfaces, the masses of the atoms, and the associated vibronic coupling.

In order for a vibrational mode in a molecule to be "IR active", it must be associated with changes in the dipole.[69] A permanent dipole is not necessary, as the rule requires only a change in dipole moment. A molecule can vibrate in many ways, and each way is known as a vibrational mode. For molecules with N number of atoms in them, linear molecules have 3N-5 degrees of vibrational modes, whereas nonlinear molecules possess 3N-6 degrees of vibrational modes (also called vibrational degrees of freedom). As an example, H_2O, a non-linear molecule, will maintain 3×3–6 = 3 degrees of vibrational freedom, or modes.

Simple diatomic molecules possess only one bond and only one vibrational band. If the molecule is symmetric, e.g. N_2, the band is not observed in the IR spectrum. Asymmetric diatomic molecules, e.g. CO, absorb in the IR spectrum. More complex molecules give rise to many bonds, and their vibrational spectra are correspondingly more complex, i.e. big molecules maintain many peaks in their IR spectra. For instance, the atoms in a CH_2X_2 (X = Cl, Br or I) group, commonly found in organic compounds and where X can represent any other atom, can vibrate in nine different ways. Six of these vibrations involve only the CH_2 portion: symmetric and antisymmetric stretching, scissoring, rocking, wagging, and twisting, as shown below. Structures that do not possess the two additional X groups attached have fewer modes, because some modes are defined by specific relationships to those other attached groups. For example, in water, the rocking, wagging, and twisting modes do not exist, because these types of motions of the H represent simple rotation of the whole molecule rather than vibrations within it.

In this thesis, FT-IR analysis was conducted in order to characterize the nature of the external functional groups situated on the surfaces of all of the OA-capped $NaYF_4$ samples (in Chapter 6). Specifically, 6 mg of each of the as-prepared $NaYF_4$ samples was mixed with 0.1 g OA in 6 mL of hexane, sonicated, centrifuged, and oven dried at 90°C overnight. In particular, a Nexus 670 instrument (ThermoNicolet) equipped with a Smart Orbit diamond ATR accessory, a KBr beam splitter, and a DTGS KBr detector was used to collect FT-IR spectra. Data were obtained by placing the dried powder samples onto a ZnSe crystal and applying a reproducible pressure. Measurements were performed over the wavelength range of 1000 to 4000 cm^{-1} using the OMNIC software with a spatial resolution of 4 cm^{-1} in the transmittance mode.

2.3.4.2 Brunauer–Emmett–Teller (BET)

The BET theory refers to multilayer adsorption of non-corrosive gases (such as nitrogen, argon, carbon dioxide, etc.) as adsorbates. In other words, the processes involved are physical adsorption resulting from relatively weak forces (van der Waals forces) between the adsorbate gas molecules and the adsorbent surface area of the test powder. BET technique refers to the determination of a specific surface area of a powder by physical adsorption of a gas onto the surface of the solid and the subsequent calculation of the amount of adsorbate gas corresponding to a mono-molecular layer on the surface. BET is usually carried out at the temperature of liquid nitrogen. The amount of gas adsorbed can be measured by either a volumetric or continuous flow procedure.

The concept of the BET theory is an extension of the Langmuir theory, which is a theory for monolayer molecular adsorption, to multilayer adsorption with the following hypotheses: (1) gas molecules physically adsorb on a solid in infinite layers; (2) no interaction between each adsorption layer; and (3) the Langmuir theory can be applied to each layer.

Meanwhile, the Langmuir model includes five assumptions:[70] (1) the surface containing the adsorbing sites is a perfectly flat plane with no corrugations (assume the surface is homogeneous); (2) the adsorbing gas adsorbs into an immobile state; (3) all sites are equivalent; (4) each site can hold at most one molecule (mono-layer coverage only); and (5) there are no interactions between adsorbate molecules on adjacent sites.

The resulting BET equation is expressed as:

$$\frac{1}{v[(p_0/p)-1]} = \frac{c-1}{v_m c}\left(\frac{p}{p_0}\right) + \frac{1}{v_m c} \tag{2.10}$$

wherein p and p_0 are the equilibrium and the saturation pressure of adsorbates at the temperature of adsorption, v is the adsorbed gas quantity, and v_m is the monolayer adsorbed gas quantity, while c is the BET constant,

$$c = \exp\left(\frac{E_1 - E_L}{RT}\right) \tag{2.11}$$

wherein E_1 is the heat of adsorption for the first layer, and E_L denotes the corresponding heat of adsorption for the second and higher layers and is equal to the heat of liquefaction.

In this thesis, BET was used to determine the surface area of as-prepared $NaYF_4$ nanocrystals possessing various morphologies. These samples were initially oven dried to remove any residual solvents. Subsequently, ~100 mg of the as-prepared $NaYF_4$ sample as well as of the corresponding anatase TiO_2 standard reference material (i.e. surface area of ~10.24 ± 0.54 $m^2\ g^{-1}$) were each placed within an individual analysis tube, and de-gassed for 2 hours at 220°C to eliminate the presence of any adsorbed species that might have been bound onto the particles' surfaces. After de-gassing, a BET surface area analysis was conducted using a Quantachrome Nova 2200e Series Instrument through the mediation of a 10-point sampling method.

2.3.5. Optical Property Characterizations

2.3.5.1 Ultraviolet–visible (UV) spectroscopy

Ultraviolet–visible spectroscopy (UV-Vis) refers to absorption spectroscopy or reflectance spectroscopy in the ultraviolet-visible spectral region. The absorption or reflectance in the visible range directly affects the perceived color of the chemicals involved.

The method is often used in a quantitative way to determine concentrations of an absorbing species in solution, using the Beer-Lambert law[71]:

$$A = \log_{10}(I_0 / I) = \varepsilon \text{ c L} \tag{2.12}$$

wherein A is the measured absorbance, in Absorbance Units (a.u.), I_0 is the intensity of the incident light at a given wavelength, I is the transmitted intensity, L denotes the path length through the sample, and c represents the concentration of the absorbing species. For each species and wavelength, ε is a constant, known as the molar absorptivity or extinction coefficient. This constant is a fundamental molecular property in a given solvent.

It can also be used to determine the bandgap width (E_g) of semiconductors:

$$E_g = \frac{hc}{\lambda_{\max}} \tag{2.13}$$

wherein h is the Planck constant, c is the speed of light, and λ_{max} is the wavelength at which absorbance reaches maximum.

In Chapter 6, UV-visible spectroscopy was utilized in order to probe optical properties of the as-prepared CdSe QDs. The corresponding absorption data were collected at high resolution on a Thermospectronics UV1 spectrometer, using quartz cells possessing a 10 mm path length.

2.3.5.2 Upconversion Property

As previously mentioned in Chapter 1, upconversion photoluminescence (UC) refers to the phenomenon occurring in optical materials, that are capable of absorbing low energy photons and emitting photons of higher energy and shorter wavelength. NIR ($\lambda \sim 980$nm)-to-visible upconversion (UC) in Er^{3+}, Yb^{3+} co-doped inorganic hosts has been the subject of very active research in recent years, particularly with the advent of methods for synthesizing highly dispersible upconverting nanomaterials.[72] One of the most active areas of research is with respect to hexagonal-phase $NaYF_4$ host materials, often designated as β-$NaYF_4$. This host supports the most efficient documented upconversion efficiency, although, at low pump power densities, the La_2O_2S host is reported to be superior.[73] The mechanism for upconversion from NIR excitation to green emission was established by Auzel in 1966 as a two-step Yb → Er energy transfer upconversion (ETU) process, as illustrated in Figure 2.7:[74]

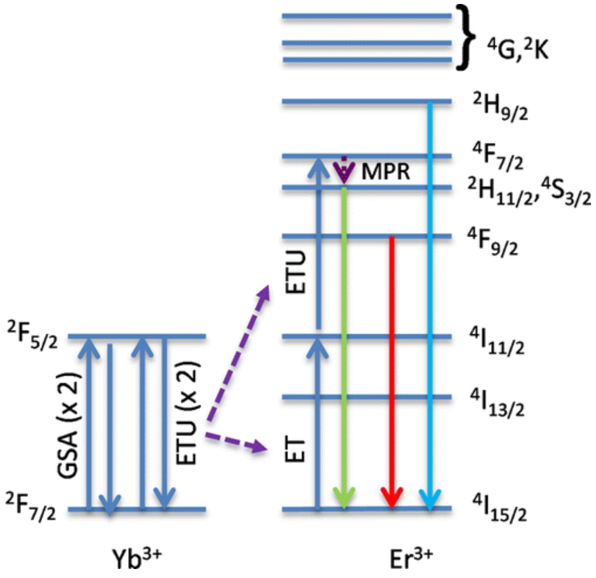

Figure 2.7. Well-established mechanism for production of green UC luminescence involves ground state absorption (GSA) by Yb^{3+} followed by two-step energy transfer upconversion (ETU) to Er^{3+}. Reprinted with permission from ref 74. Copyright 2015, American Chemical Society.

For efficient upconversion, rapid energy migration among the Yb^{3+} ions is required. The two Yb^{3+} ground state absorption (GSA) events in Figure 2.7 do not generally occur at the same Yb^{3+} center, or even at Yb^{3+} ions that are nearest neighbors to Er^{3+}, but rather, the energy migrates from the absorption site to Yb^{3+} sites that are adjacent to the Er^{3+} upconversion centers. Thus, the Yb^{3+} energy-level diagram in Figure 2.7 represents two Yb^{3+} ions within the lattice, whereas the Er^{3+} energy-level diagram can be ascribed to a single Er^{3+} ion.

In this work, upconversion spectra were measured on a home-built Olympus IX 71 inverted microscope equipped with a 100x, 1.4 NA oil immersion objective lens and an Ocean Optics QE65000 multimode fiber optics spectrometer. The excitation source employed was a 980 nm pulse light operating at a 80 MHz repetition rate and a 85 fs pulse width delivered by a Maitai Spectra Physics solid state diode pumped laser which was spectrally separated from the upconverted signal by a dichroic mirror (Semrock short pass 690 nm) and a short pass interference filter (Semrock 700 nm). Upconversion spectra were recorded using an average laser power excitation source of 10 mW focused onto the sample with an integration time of 2 seconds.

2.3.6. Electrochemistry

2.3.6.1 Cyclic Voltammetry

Cyclic Voltammetry (CV) is inarguably the most popular electrochemical technique. The analysis of CV curves enables one to deduce reaction mechanisms with relatively low-cost equipment and quick experimentation. Hence, it has become the centerpiece of any electrochemical study.[75, 76]

CV involves sweeping the potential linearly between two limits at a given sweep-rate while measuring current. The sweep rates are usually at a level of few microvolts per second. CV curves can be obtained by application of sufficiently negative potentials to the electrode when it is in contact with an aqueous solution, as shown in Figure 2.8.[75] There are several distinctive regions in the CV profile.[77] Starting from the negative end of the voltammogram, the first region up to ~0.1 V denotes the adsorption (reductive peaks) and desorption of hydrogen. In the center of the voltammetric curve, i.e. from 0.1 V to about 0.6 V, no faradaic reactions occur. This is the double-layer region, wherein only capacitive processes take place. The third region refers to the oxide-formation region starting at ~0.6 V.[78] The reduction of platinum oxide (negative currents) occurs at ~0.5 V. This voltammetry behavior has been well-studied and understood.

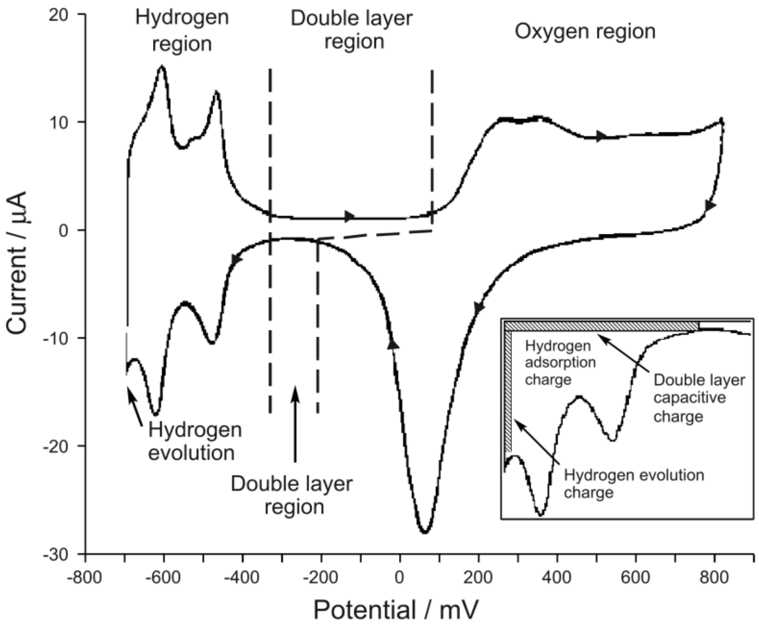

Figure 2.8. Cyclic voltammetric current potential curve for a platinum electrode in contact with a 0.5 M H_2SO_4 solution. The electrode potential is referenced to the mercury sulfate reference electrode. The inset shows the different charge contributions in the hydrogen region. Reprinted with permission from ref 75. Copyright 2000, American Chemistry Society.

Amongst these features, the H-adsorption region plays a significant role, as it is often used as a tool to deduce the electrochemically active area of the Pt electrode. In this thesis, in order to determine the electrochemically active surface area (ESA), CVs were collected in deoxygenated electrolyte at a scan rate of 20 mV/s. The ESA is calculated in this case by converting the average of the hydrogen adsorption (H_{ads}) and desorption (H_{des}) charge (after correcting for the double layer) into a real actual surface area by utilizing 210 $\mu C/cm^2$ as a known conversion factor.

2.3.6.2 Surface Activation Processes

Due to the high surface energy of Pt and Pd nanostructures,[79] the ultrathin nanowires synthesized based upon surfactant-assisted approaches are usually capped by residual organic surfactants, which blocks the active sites, namely Pt atoms when these nanostructures are in contact with electrolyte. In prior studies from our group, a treatment protocol was developed for the removal of residual organic impurities from the surfaces of analogous ultrathin Pd nanowires, which combined (i) a UV-ozone atmosphere pretreatment with (ii) a selective CO adsorption process.[12, 13, 42] In this thesis, we have developed a more facile two-step protocol to include a facile and 'greener' pre-treatment process, involving a simple surface capping ligand substitution with butylamine. In previous reports, ligand substitution reactions were effectively employed to remove a mixture of a borane-*tert*-butylamine complex and hexadecanediol from the surfaces of Pt_3Ni nanoparticles, for instance.[80] Herein, the ligand substitution process was accomplished by dispersing as-synthesized ODA-capped PdNi alloy nanowires into pure butylamine for a period of three days under completely ambient conditions. The subsequent butylamine-capped nanowires could be activated with a selective CO-adsorption process, which is capable of displacing organic capping ligands with alkyl-chains of up to six carbons in length.[13, 42, 81]

Experimentally, in the first step, a surface ligand exchange process was performed by dispersing the as-prepared composites into *n*-butylamine (Acros Organics, +99.5%) by sonication, and the resulting dispersion was stirred for a period of three days in order to ensure complete exchange of the ODA with the butylamine. The treated product was subsequently isolated by centrifugation and washed with ethanol in order to remove excess butylamine.

In the second step, the butylamine ligands and other organic impurities were removed by selective CO adsorption process, previously described by one of our groups.[12] Briefly, the supported nanowires were deposited onto a glassy carbon electrode and the potential was cycled in deoxygenated 0.1 M $HClO_4$ up to a potential of 1.3 V at a rate of 100 mV/s until a stable profile was obtained. Thereafter, the electrode was immersed in a CO-saturated electrolyte for 30-45 min, so as to selectively displace residual organic impurities from the surfaces of the NWs. The electrode was then washed in ultrapure water and transferred to a freshly deoxygenated electrolyte, wherein a CO stripping cyclic voltammogram (CV) was obtained by cycling the potential up to 1.15 V. The CO adsorption/stripping process was ultimately repeated for an additional two times or until the CO stripping profile was deemed to be reproducible.

Aside from the function of cleansing the surface of our as-prepared ultrathin nanowires, CO stripping is also an important tool for determining electrochemical surface area (ESA),[82] since the oxidation of the CO monolayer is related to the geometric surface area in an analogous manner to H_{ads}. The ESA can be obtained from the following equation:

$$ESA = \frac{Q_{CO}}{0.420 mCcm^{-2}} \tag{2.14}$$

wherein Q_{CO} denotes the CO stripping charge in mC derived by integrating the CO stripping peak over relevant potential window; while 0.420 mC cm^{-2} represents the charge associated with the oxidation of nearly a CO monolayer.

2.3.6.3 ORR measurements and Stability test

Typically, the electrocatalytic activity of nanomaterials toward ORR is measured by obtaining a linear sweep voltammogram or so-called “polarization curves” in an oxygen-saturated 0.1 M $HClO_4$ electrolyte at 20°C with the electrode, rotating at a rate of 1600 rpm and at a scan rate of 10 mV/s.[83]. In this thesis, both the activities and stabilities of $Pd_{1-x}Ni_x$ series as well as of selected Pt~$Pd_{1-x}Ni_x$ core-shell structures have been measured.

After obtaining the polarization curves, the Koutecky-Levich relationship (Equation 2.15) was employed to calculate the kinetic ORR current (I_k), which serves as an intrinsic measurement of ORR activity at a desired potential. The Koutecky-Levich relationship can be rearranged (Equation 2.16), so that I_k can be calculated at 0.9 V from the measured disk current ($I_{0.9V}$) and the diffusion controlled current (I_D), which are themselves obtained from the polarization curve at 0.9 V and 0.4 V, respectively. The I_k is typically calculated at 0.9 V in accordance with the U.S. Department of Energy (DOE)[84] protocol and the existing precedence in the literature.[83] Once calculated, the measured I_k is then normalized to either the ESA or the platinum mass of the catalyst involved in the experiment, in order to obtain surface area or mass normalized kinetic current (J_k) densities.

$$\frac{1}{I_{0.9V}} = \left(\frac{1}{I_k} + \frac{1}{I_D} \right) \tag{2.15}$$

$$I_k = \frac{I_D - I}{I_D I_{0.9V}} \tag{2.16}$$

The catalyst's durability has been tested by a protocol defined by the U.S. DOE for simulating a catalyst lifetime under MEA conditions. The procedure though has been modified for use with a thin catalyst layer supported onto a GC-RDE under half-cell conditions.[84] Specifically, the electrode is cycled from 0.6 to 1.0 V at 50 mV/s in a 0.1 M $HClO_4$ solution, left open to the air for up to 10,000 cycles. The ESA and specific activity are measured incrementally after every 5,000 cycles. As an internal standard, we have run the identical durability protocol on state-of-the-art Pt NP/C, so as to understand the durability in a practical context.

In addition, we have also examined the stability of the ORR performance in the presence of small organic molecule impurities. The testing protocol utilized herein is designed to simulate the effects of methanol crossover from the anode to the cathode in functional Direct Methanol Fuel Cell (DMFC) designs, which can be a critical technological challenge in terms of the fabrication of electrocatalysts for DMFC cathodes. The stability of ORR performance in the presence of methanol was examined by obtaining a series of polarization curves in electrolytes with increasing methanol concentration. For selected compositions within the $Pd_{1-x}Ni_x$ ultrathin nanowire series, polarization curves were obtained in 0.1 M $HClO_4$ solutions, containing methanol concentrations of 0, 1, 2, 3, 4, 25, 50, 75, and 100 mM, respectively. The relative methanol tolerance was estimated by normalizing the measured specific activity in the presence of methanol (J_k [MeOH]) to the measured specific activity in a pure solution, containing no methanol (J_k). The measurement of the fraction of specific activity in the presence of methanol with respect to the activity in a pure electrolyte (*i.e.* J_k [MeOH] /J_k) provides for evaluation of the level of methanol tolerance.

2.3.6.4 Small Molecule Oxidation measurements and Chronoamperometry

In Chapter 4, the electrocatalytic performances and activities of all the $Pd_{1-x}Cu_x$ series as well as of the Pt~$Pd_{1-x}Cu_x$ series of ultrathin nanowires towards reactivity in the formic acid oxidation reaction (FAOR), the methanol oxidation reaction (MOR) ,and the ethanol oxidation reaction (EOR), respectively, have been determined by linear sweep voltammograms using appropriate electrolytes.

FAOR-related electrochemical measurements were collected in a 0.1 M perchloric acid (Fisher Scientific, Optima Grade) solution, prepared using high-purity type 1 water possessing a high resistivity of 18.2 MΩ·cm. An Ag/AgCl (3M Cl^-) combination isolated in a double junction chamber (Cypress) and a platinum foil served as the reference electrode and the counter electrode, respectively. By contrast, MOR- and EOR- related measurements were obtained in a 1 M sodium hydroxide (NaOH, Fisher Scientific, Pellets/Certified ACS) solution, prepared using high-purity type 1 water. A non-leaking Ag/AgCl (3M Cl^-) reference electrode (World Precision, Dri-Ref Reference Electrode) and a platinum foil served as the reference electrode and the counter electrode, respectively. All of the potentials in this paper have been reported with respect to the reversible hydrogen electrode (RHE), unless otherwise mentioned.

In terms of the activities, the FAOR kinetics were gauged by first collecting CVs at a scan rate of 20 mV/s in deoxygenated 0.5 M formic acid (EMD, 98% ACS reagent grade), supported in a 0.1 M $HClO_4$ electrolyte. MOR kinetics were analyzed by obtaining CVs at a scan rate of 20 mV/s within a deoxygenated 1 M methanol (Macron, anhydrous) solution, supported in a 1 M NaOH electrolyte (created using NaOH pellets, Fisher Scientific, Certified ACS). Analogous EOR kinetics were evaluated in a similar fashion to MOR, except with the use of a solution of 1 M ethanol (Pharmco-AAPER, 200 proof). Typically, a linear-sweep voltammogram (LSV) was obtained in the anodic sweep direction, in order to collect either the FAOR, MOR, or EOR kinetics curves. The observed current was subsequently normalized to the surface area, which could be determined from the H_{ads} charge. After the initial LSV, collection of the CVs was repeated in order to ensure that the surface of the catalyst was sufficiently stable in order to generate more reproducible CVs.

Chronoamperometry was also initiated to test the stability of our as-prepared catalysts. Specifically, a number of chronoamperograms were acquired in the same solution that the individual activity measurement was performed. The electrode was submerged and tested for 1 hour, while the potential was maintained at a value of 0.4 V, 0.65 V, and 0.65 V for FAOR, MOR, and EOR, respectively. These specific potentials were used, as they reside within the onset region of all of the catalysts tested herein, thereby allowing for a meaningful comparison of relative activities. Moreover, all electrodes in this manuscript have been examined and run under identical conditions, in order to ensure data self-consistency and hence, ease of interpretability.

2.4. References

1. Liu, H. Q.; Li, L. Y.; Scofield, M. E.; Wong, S. S. *Apl Mater* **2015,** 3, (8).
2. Johnson, S. A.; Khushalani, D.; Coombs, N.; Mallouk, T. E.; Ozin, G. A. *J Mater Chem* **1998,** 8, (1), 13-14.
3. Volosskiy, B.; Niwa, K.; Chen, Y.; Zhao, Z. P.; Weiss, N. O.; Zhong, X.; Ding, M. N.; Lee, C.; Huang, Y.; Duan, X. F. *Acs Nano* **2015,** 9, (3), 3044-3049.
4. Cademartiri, L.; Ozin, G. A. *Adv Mater* **2009,** 21, (9), 1013-1020.
5. Ruan, L. Y.; Zhu, E. B.; Chen, Y.; Lin, Z. Y.; Huang, X. Q.; Duan, X. F.; Huang, Y. *Angew Chem Int Edit* **2013,** 52, (48), 12577-12581.
6. Qian, Z. X.; Park, S. J. *Chem Mater* **2014,** 26, (21), 6172-6177.
7. Liu, H.; Cao, X. M.; Yang, J. M.; Gong, X. Q.; Shi, X. Y. *Sci Rep-Uk* **2013,** 3.
8. Morita, C.; Tanuma, H.; Kawai, C.; Ito, Y.; Imura, Y.; Kawai, T. *Langmuir* **2013,** 29, (5), 1669-1675.
9. Morita, C.; Kawai, C.; Tsujimoto, K.; Kasai, K.; Ogue, Y.; Imura, Y.; Kawai, T. *J Oleo Sci* **2013,** 62, (2), 81-87.
10. Shi, L. H.; Wang, A. Q.; Huang, Y. Q.; Chen, X. W.; Delgado, J. J.; Zhang, T. *Eur J Inorg Chem* **2012**, (16), 2700-2706.
11. Zhao, X.; Zhang, J.; Wang, L. J.; Liu, Z. L.; Chen, W. *J Mater Chem A* **2014,** 2, (48), 20933-20938.
12. Koenigsmann, C.; Santulli, A. C.; Gong, K. P.; Vukmirovic, M. B.; Zhou, W. P.; Sutter, E.; Wong, S. S.; Adzic, R. R. *J Am Chem Soc* **2011,** 133, (25), 9783-9795.
13. Koenigsmann, C.; Sutter, E.; Adzic, R. R.; Wong, S. S. *The Journal of Physical Chemistry C* **2012,** 116, (29), 15297-15306.
14. Teng, X. W.; Han, W. Q.; Ku, W.; Hucker, M. *Angew Chem Int Edit* **2008,** 47, (11), 2055-2058.
15. Koenigsmann, C.; Zhou, W. P.; Adzic, R. R.; Sutter, E.; Wong, S. S. *Nano Lett* **2010,** 10, (8), 2806-2811.
16. Koenigsmann, C.; Sutter, E.; Adzic, R. R.; Wong, S. S. *J Phys Chem C* **2012,** 116, (29), 15297-15306.
17. Liu, H. Q.; Koenigsmann, C.; Adzic, R. R.; Wong, S. S. *Acs Catal* **2014,** 4, (8), 2544-2555.
18. Liu, H. Q.; Adzic, R. R.; Wong, S. S. *Acs Appl Mater Inter* **2015,** 7, (47), 26145-26157.
19. Liu, H. Q.; An, W.; Li, Y. Y.; Frenkel, A. I.; Sasaki, K.; Koenigsmann, C.; Su, D.; Anderson, R. M.; Crooks, R. M.; Adzic, R. R.; Liu, P.; Wong, S. S. *Journal of the American Chemical Society* **2015,** 137, (39), 12597-12609.
20. Brankovic, S. R.; Wang, J. X.; Adzic, R. R. *Surf Sci* **2001,** 474, (1-3), L173-L179.
21. Wang, J. X.; Inada, H.; Wu, L.; Zhu, Y.; Choi, Y.; Liu, P.; Zhou, W.-P.; Adzic, R. R. *J Am Chem Soc* **2009,** 131, (47), 17298-17302.
22. Vukmirovic, M. B.; Bliznakov, S. T.; Sasaki, K.; Wang, J. X.; Adzic, R. R. *Electrochem. Soc. Interface* **2011,** 20, (2), 33-40.
23. Zhou, W. P.; Sasaki, K.; Su, D.; Zhu, Y. M.; Wang, J. X.; Adzic, R. R. *J Phys Chem C* **2010,** 114, (19), 8950-8957.
24. Wang, D. L.; Xin, H. L. L.; Hovden, R.; Wang, H. S.; Yu, Y. C.; Muller, D. A.; DiSalvo, F. J.; Abruna, H. D. *Nat Mater* **2013,** 12, (1), 81-87.

25. Mazumder, V.; Chi, M. F.; More, K. L.; Sun, S. H. *Journal of the American Chemical Society* **2010,** 132, (23), 7848-+.
26. Gong, K. P.; Su, D.; Adzic, R. R. *Journal of the American Chemical Society* **2010,** 132, (41), 14364-14366.
27. Chen, D.; Li, Y. X.; Liao, S. J.; Su, D.; Song, H. Y.; Li, Y. W.; Yang, L. J.; Li, C. *Sci Rep-Uk* **2015,** 5.
28. Feng, S. H.; Xu, R. R. *Accounts Chem Res* **2001,** 34, (3), 239-247.
29. Cundy, C. S.; Cox, P. A. *Chem Rev* **2003,** 103, (3), 663-701.
30. Byrappa, K.; Yoshimura, M., *Handbook of hydrothermal technology : a technology for crystal growth and materials processing*. Noyes Publications: Norwich, N.Y., 2001.
31. Lobachev, A. N., *Hydrothermal synthesis of crystals*. Consultants Bureau: New York,, 1971; p xiii, 153 p.
32. Einarsrud, M. A.; Grande, T. *Chem Soc Rev* **2014,** 43, (7), 2187-2199.
33. Yang, L. W.; Zhang, Y. Y.; Li, J. J.; Li, Y.; Zhong, J. X.; Chu, P. K. *Nanoscale* **2010,** 2, (12), 2805-2810.
34. Yang, L. W.; Han, H. L.; Zhang, Y. Y.; Zhong, J. X. *J Phys Chem C* **2009,** 113, (44), 18995-18999.
35. *Chemsuschem* **2010,** 3, (9), 1006-1006.
36. Kresse, G.; Furthmuller, J. *Phys. Rev. B* **1996,** 54, (16), 11169-11186.
37. Kresse, G.; Hafner, J. *Phys. Rev. B* **1993,** 47, (1), 558-561.
38. Perdew, J. P.; Chevary, J. A.; Vosko, S. H.; Jackson, K. A.; Pederson, M. R.; Singh, D. J.; Fiolhais, C. *Physical Review B* **1992,** 46, (11), 6671-6687.
39. Blochl, P. E. *Phys. Rev. B* **1994,** 50, (24), 17953-17979.
40. Monkhorst, H. J.; Pack, J. D. *Physical Review B* **1976,** 13, (12), 5188-5192.
41. Koenigsmann, C.; Scofield, M. E.; Liu, H. Q.; Wong, S. S. *J Phys Chem Lett* **2012,** 3, (22), 3385-3398.
42. Koenigsmann, C.; Sutter, E.; Chiesa, T. A.; Adzic, R. R.; Wong, S. S. *Nano Lett* **2012,** 12, (4), 2013-2020.
43. Norskov, J. K.; Rossmeisl, J.; Logadottir, A.; Lindqvist, L.; Kitchin, J. R.; Bligaard, T.; Jonsson, H. *J Phys Chem B* **2004,** 108, (46), 17886-17892.
44. Stamenkovic, V.; Mun, B. S.; Mayrhofer, K. J. J.; Ross, P. N.; Markovic, N. M.; Rossmeisl, J.; Greeley, J.; Norskov, J. K. *Angew Chem Int Edit* **2006,** 45, (18), 2897-2901.
45. Shao, M.; Liu, P.; Adzic, R. R. *J. Phys. Chem. B* **2007,** 111, 6772-6775.
46. Wang, J. X.; Inada, H.; Wu, L. J.; Zhu, Y. M.; Choi, Y. M.; Liu, P.; Zhou, W. P.; Adzic, R. R. *J Am Chem Soc* **2009,** 131, (47), 17298-17302.
47. Zhang, J.; Yang, H. Z.; Fang, J. Y.; Zou, S. Z. *Nano Lett* **2010,** 10, (2), 638-644.
48. An, W.; Liu, P. *J Phys Chem C* **2013,** 117, (31), 16144-16149.
49. Wolfers, F. *Cr Hebd Acad Sci* **1923,** 177, 759-762.
50. Barer, R.; Cosslett, V. E., Advances in optical and electron microscopy. Academic Press: London, New York,, 1966; p 14 volumes.
51. Hawkes, P. W., *The Beginnings of electron microscopy*. Academic Press: Orlando, 1985; p xix, 633 p.
52. Egerton, R. F., *Physical principles of electron microscopy : an introduction to TEM, SEM, and AEM*. Springer: New York, NY, 2005; p xii, 202 p.
53. Fultz, B.; Howe, J. M., *Transmission electron microscopy and diffractometry of materials*. 4th ed.; Springer: Heidelberg ; New York, 2013; p xx, 761 p.

54. Ke, X. X.; Bittencourt, C.; Van Tendeloo, G. *Beilstein J Nanotech* **2015,** 6, 1541-1557.

55. Thomas, G.; Goringe, M. J., *Transmission electron microscopy of materials*. Wiley: New York, 1979; p xiv, 388 p.

56. Williams, D. B.; Carter, C. B., *Transmission electron microscopy : a textbook for materials science*. Plenum Press: New York, 1996; p xxvii, 729 p.

57. McMullan, D. *Adv Imag Elect Phys* **2004,** 133, 59-91.

58. Danilatos, G. D. *J Microsc-Oxford* **1986,** 142, 317-325.

59. Goldstein, J., *Scanning electron microscopy and x-ray microanalysis*. 3rd ed.; Kluwer Academic/Plenum Publishers: New York, 2003; p xix, 689 p.

60. Teo, B. K., *EXAFS : basic principles and data analysis*. Springer-Verlag: Berlin ; New York, 1986; p xviii, 349 p.

61. Teo, B. K.; Joy, D. C.; Materials Research Society., *EXAFS spectroscopy, techniques and applications*. Plenum Press: New York, 1981; p viii, 275 p.

62. Das, N. C.; Bhabha Atomic Research Centre., *Optical and mechanical design of the extended x-ray absorption fine structure (EXAFS) beam-line at Indus-II synchrotron source*. Bhabha Atomic Research Centre: Mumbai, 2002; p 28 p.

63. Als-Nielsen, J.; McMorrow, D., *Elements of modern X-ray physics*. 2nd ed.; Wiley: Hoboken, 2011; p xii, 419 p.

64. Grunwaldt, J. D.; Baiker, A. *Phys Chem Chem Phys* **2005**, *7*, 3526-3539.

65. Frenkel, A. I. *Chem Soc Rev* **2012,** 41, (24), 8163-8178.

66. Gadaleta, S. J.; Mendelsohn, R.; Paschalis, E. L.; Camacho, N. P.; Betts, F.; Boskey, A. L. *Mineral Scale Formation and Inhibition* **1995**, 283-294.

67. Tan, T. L.; Lau, S. Y.; Ong, P. P.; Goh, K. L.; Teo, H. H. *J Mol Spectrosc* **2000,** 203, (2), 310-313.

68. Toyran, N. *Turk Klin Tip Bilim* **2008,** 28, (5), 704-714.

69. Burkholder, J. B.; Sinha, A.; Hammer, P. D.; Howard, C. J. *J Mol Spectrosc* **1987,** 126, (1), 72-77.

70. Masel, R. I., *Principles of adsorption and reaction on solid surfaces*. Wiley: New York, 1996; p xiv, 804 p.

71. Carr, D. O. *Abstr Pap Am Chem S* **1982,** 184, (Sep), 76-&.

72. Heer, S.; Kompe, K.; Gudel, H. U.; Haase, M. *Adv Mater* **2004,** 16, (23-24), 2102-+.

73. Pokhrel, M.; Gangadharan, A. K.; Sardar, D. K. *Mater Lett* **2013,** 99, 86-89.

74. Berry, M. T.; May, P. S. *J Phys Chem A* **2015,** 119, (38), 9805-9811.

75. Rodriguez, J. M. D.; Melian, J. A. H.; Pena, J. P. *J Chem Educ* **2000,** 77, (9), 1195-1197.

76. Shain, I. *J Electrochem Soc* **1970,** 117, (3), C119-&.

77. Millar, J.; Barnett, T. G. *J Neurosci Meth* **1988,** 25, (2), 91-95.

78. *Zeitschrift für Elektrochemie und angewandte physikalische Chemie* **1951,** 55, (4), 336-336.

79. Ginley, D. S.; Kahen, D. i., *Fundamentals of materials for energy and environmental sustainability*. Cambridge University Press: Cambridge ; New York, 2012; p xvi, 753 p.

80. Wu, J.; Zhang, J.; Peng, Z.; Yang, S.; Wagner, F. T.; Yang, H. *J Am Chem Soc* **2010,** 132, (14), 4984-4985.

81. Adzic, R. R.; Zhang, J.; Sasaki, K.; Vukmirovic, M. B.; Shao, M.; Wang, J. X.; Nilekar, A. U.; Mavrikakis, M.; Valerio, J. A.; Uribe, F. *Top Catal* **2007,** 46, (3-4), 249-262.

82. Vidakovic, T.; Christov, M.; Sundmacher, K. *Electrochim Acta* **2007,** 52, (18), 5606-5613.

83. Garsany, Y.; Baturina, O. A.; Swider-Lyons, K. E.; Kocha, S. S. *Anal Chem* **2010,** 82, (15), 6321-6328.

84. *Fuel Cell Technologies Office Multi-Year Research, Development, and Demonstration Plan*; Department of Energy, 2012.

Chapter 3: Probing Ultrathin One-Dimensional Pd-Ni Nanostructures As Oxygen Reduction Reaction Catalysts

3.1. Introduction.

As previously discussed in Chapter 1, metallic platinum is commonly used as a cathodic catalyst, *i.e.* the catalyst for the oxygen reduction half-cell reaction (ORR) in low-temperature fuel cells. However, the generally high cost and the limited global abundance of platinum represent significant barriers to the widespread use of these types of fuel cells. On the other hand, palladium possesses very similar physical properties to platinum, including an *fcc* crystal structure and a similar atomic size and electronic configuration, and yet, it is much less costly than Pt. Hence, Pd is considered to be a good substitute for Pt as a catalyst in fuel cells.[1, 2] As ORR catalysts have evolved, electro-active Pd, in general, and Pd-based alloy catalysts, more specifically, have been proposed as cathode materials for ORR in acidic media,[3, 4] since Pd possesses an ORR activity relatively close to that of Pt, amongst various metals.

Among a number of alloys studied, Pd-Ni catalysts in particular have received significant attention over the years because of the reasonable abundance, low cost, and relative non-toxicity of Ni. In fact, catalytic hydrogenation reactions have been known to improve as a result of adding Ni to Pd, partly because of electronic modification of Pd by surrounding Ni atoms.[5] From a theoretical perspective, DFT calculations performed on binary transition metal surface alloys had shown that by doping in Ni, there would be a 1.00 eV downshift in the position of the Pd weighted *d*-band center.[6] Such an effect originates from (A) the compression strain induced by the incorporation of Ni atoms into the Pd lattice and (B) a ligand effect arising from the electronic interaction between the Pd atoms and the Ni atoms. As a result, the oxygen binding energy for a Pd-Ni surface should be reduced by 0.86 eV as compared with Pd alone, which is extremely beneficial for its ORR performance. Furthermore, as observed from the alloy phase diagram, Pd and Ni form a homogeneous solid solution with a face centered cubic structure at all compositions and within a large range of temperatures,[7] which renders their synthesis relatively facile.

Accordingly, over the years, it has been verified from the perspective of both kinetic[8] studies as well as data on actual catalytic performance[9-11] that Pd-Ni is a viable and effective ORR catalyst candidate. For instance, Ramos-Sanchez *et al.*[12] have reported that the incorporation of less electronegative Ni shifted the onset potential for the ORR by approximately 110 mV to more positive values, and at 0.5 mA/cm^2, the cathode overpotential was reduced by 260 mV as compared with Pd alone in a 0.5 M H_2SO_4 solution at 25°C. Moreover, a hierarchical architecture of Pt-coated PdNi catalyst was observed to have possessed the highest ORR activity as compared with pure Pt/C, Pd/C, and PdNi/C catalysts.[13] Similarly, Pt~$PdNi_6$ core–shell nanoparticles, measuring approximately 20 nm in diameter, not only possess an activity that is 7-fold higher than the state-of-the-art Pt/C but also exhibit excellent long-term electrochemical stability.[14] As an additional plausible explanation for the enhanced performance experimentally noted in these Pd-based binary systems, Tarasevich *et al*.[15] proposed that the presence of the second metal (i.e. Ni) alloyed with Pd can potentially influence catalytic activity in two ways, namely (i) through the stabilization of Pd nanoparticles and (ii) by hindering palladium oxide formation.

Recently, our group has developed a class of electrochemically active single-crystalline one-dimensional (1-D) nanostructures. In general, 1-D materials possess high aspect ratios, fewer lattice boundaries, longer segments of smooth crystal planes, and a relatively low number of surface defect sites, all of which are desirable attributes for fuel cell catalysts.[16-20] In this context, the performance of binary Pd-based alloys (*i.e.* $Pd_{1-x}Au_x$ and $Pd_{1-x}Pt_x$) toward ORR and the methanol oxidation reaction (MOR) has been dramatically improved by tailoring the morphology, size, and chemical composition. As a salient example,[21] we have recently demonstrated that optimization of size and composition in “Pt-free” Pd_9Au NWs can lead to a measured ORR activity of 0.49 mA/cm^2, which represents more than two-fold improvement over commercial Pt NP/C catalysts. For PdAu systems, our studies showed that the enhanced performance likely arises from the structural and electronic properties associated with their alloy-type structure and not simply due to the coincidental physical presence of interfacial Pd-Au pair sites.[22]

Ultrathin 1-D structures combine the merits of extended, smooth facets associated with an anisotropic morphology along with high surface area-to-volume ratios due to their nanometer-scale dimensions, all of which combine to give rise to highly promising functional attributes for these materials as electrocatalysts. Not surprisingly, excellent enhancements have also been noted with ultrathin, core-shell $Pt{\sim}Pd_{1-x}Au_x$ NWs,[22] wherein the mutual benefits of the 1D morphology and ultrathin size are combined with a hierarchical structural motif. After the deposition of a Pt monolayer, a volcano-type composition dependence was observed in the ORR activity values of the $Pt{\sim}Pd_{1-x}Au_x$ NWs as the Au content is increased from 0 to 30% with the activity of the $Pt{\sim}Pd_9Au$ NWs (0.98 mA/cm^2, 2.54 A/mg_{Pt}), representing the optimum performance.

However, in the prior literature, there have been very few reports of ultrathin Pd-based alloys, incorporating inexpensive and abundant first-row transition metal dopants. Moreover, the relationship between composition and the corresponding ORR activity has yet to be systematically analyzed. Therefore, in this current study, we have developed an ambient surfactant-based synthetic approach for preparing ultrathin Pd-based NWs, wherein the electrochemical activity is controllably increased by substituting Pd atoms for more abundant and less expensive first-row transition metals. Moreover, the distinctive novelty of our work is associated with (a) a comprehensive study of the composition-activity relationship of Pd-Ni binary catalysts; (b) an analysis of the methanol tolerance abilities of nanowires possessing optimized chemical composition; and (c) the feasibility of employing our as-processed ultrathin nanowires as the template for Pt monolayer deposition towards the development of a highly stable and durable anisotropic core-shell catalytic platform.

In terms of tangible results, our high-quality, carbon-supported Pd-Ni nanowires possessing ultrathin 2 nm diameters were found to maintain a “volcano-type” dependence as well with respect to chemical composition, wherein the $Pd_{0.90}Ni_{0.10}$ NW/C composite represented the peak activity among the series. Moreover, 85% of its original activity was preserved in an electrolyte containing a relatively high 4 mM methanol concentration, implying a correspondingly high methanol tolerance ability. In addition, we were able to test the electrochemical properties of $Pd_{0.90}Ni_{0.10}$ nanowires, possessing a Pt monolayer shell. Our results demonstrate outstanding ORR performance with a measured specific activity and platinum mass activity of 0.62 mA/cm^2 and 1.44 A/mg$_{Pt}$, respectively. Finally, after 10000 cycles of durability testing under realistic simulated conditions, the corresponding specific activity of our as-prepared Pt~$Pd_{0.90}Ni_{0.10}$ electrocatalyst actually increased by more than 20% from 0.62 mA/cm^2 to 0.76 mA/cm^2.

3.2. Results and Discussion

3.2.1. Synthesis and Structural Characterization of Pd-Ni nanowires with various chemical compositions

We employed an ambient, surfactant-based technique to synthesize Pd-Ni ultrathin nanowires with a diameter of ~2 nm. This synthetic approach has been previously used to yield long, extended polycrystalline nanowires, which possess lengths of several tens of nanometers and consist of single crystalline constituent segments.[22-24] Specifically, appropriate metal precursors, namely Pd^{2+} and Ni^{2+}, were reduced by sodium borohydride ($NaBH_4$) in the presence of octadecylamine (ODA) and *n*-dodecyltrimethylammonium bromide (DTAB), serving as surfactant and phase transfer agent, respectively, to create thermodynamically unstable elongated primary nanostructures (PNs). The secondary growth of these PN 'nuclei' along preferred growth directions including the (111) direction leads to the formation of thread-like nanowire networks.[24] The stoichiometry of the NW can be directly altered by modifying the corresponding stoichiometric ratio of the metallic precursors within the precursor solution. In this case, Pd-Ni nanowire samples can be routinely and controllably prepared with chemical compositions ranging from $Pd_{0.90}Ni_{0.10}$ to $Pd_{0.50}Ni_{0.50}$.

X-ray powder diffraction (XRD) obtained on the as-prepared Pd-Ni nanowires series (Figure 3.1) has revealed that the NWs are composed of homogeneous alloys with a face-centered cubic (*fcc*) crystal structure. We did not observe any obvious peaks associated with either metallic nickel or nickel oxides observed, thereby suggesting the incorporation of Ni atoms within the *fcc* structure of Pd.

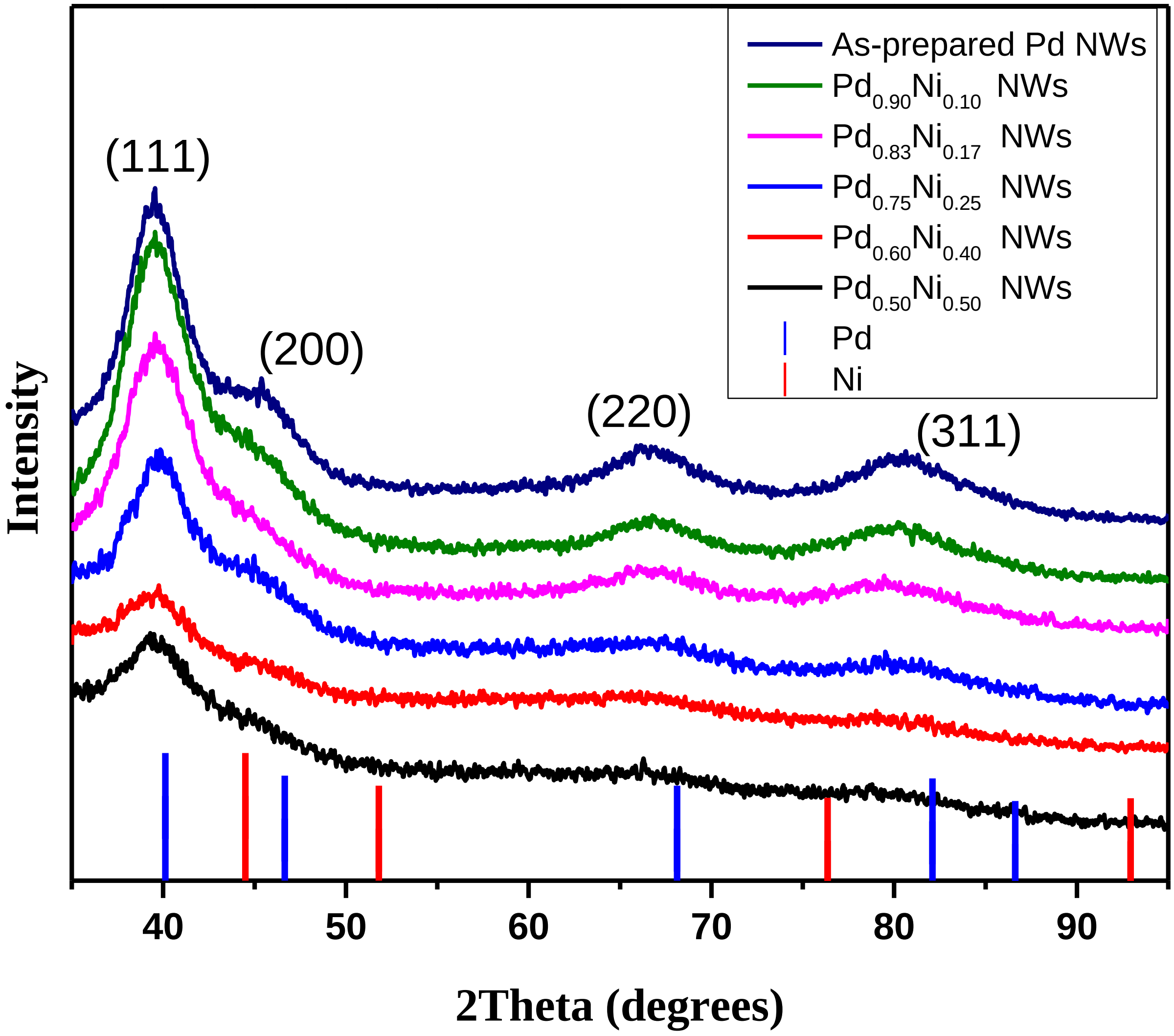

Figure 3.1. X-ray diffraction patterns of as-prepared Pd-Ni nanowires. The Pd content decreases from top to bottom, in the order of elemental Pd, $Pd_{0.90}Ni_{0.10}$, $Pd_{0.83}Ni_{0.17}$, $Pd_{0.75}Ni_{0.25}$, $Pd_{0.60}Ni_{0.40}$, and $Pd_{0.50}Ni_{0.50}$, respectively. The XRD patterns have been indexed to Pd (blue, JCPDS # 46-1043) and Ni (red, JCPDS # 04-0850). Database standards are shown immediately below the experimentally determined patterns.

Nonetheless, based on studies that involve a cross-sectional composition analysis of Pd- or Pt-Ni nanostructures, it is possible that though the valence of Ni in the core-region is 0, the Ni on surface may actually exist as a form of oxide, such as NiO or $Ni(OH)_2$ due to the presence of surface oxidation.[14, 25] Therefore, it is likely that our as-prepared nanostructures possess a variant of nickel oxide on their surface as well. Nevertheless, the patterns of the peaks can be attributed to the elemental Pd phase with a slight shift towards higher 2θ angle, indicating possible lattice contraction. Such a phenomenon reflects a partial substitution of Pd atoms with Ni atoms, possessing a smaller atomic radius. Due to a broadening of the peaks, which likely originates from the small crystallite size, calculations of lattice parameters based on XRD patterns tend to be difficult and hence could be somewhat imprecise.

Transmission electron microscopy (TEM) was employed to examine the morphology, crystallinity, and uniformity of a series of as-prepared Pd-Ni nanowires. As shown in Figure 3.2, the overall structure of the samples with greater than 60 atom % Pd consists of discrete individual one-dimensional nanowires, clustered together as part of a larger three-dimensional aggregated network.

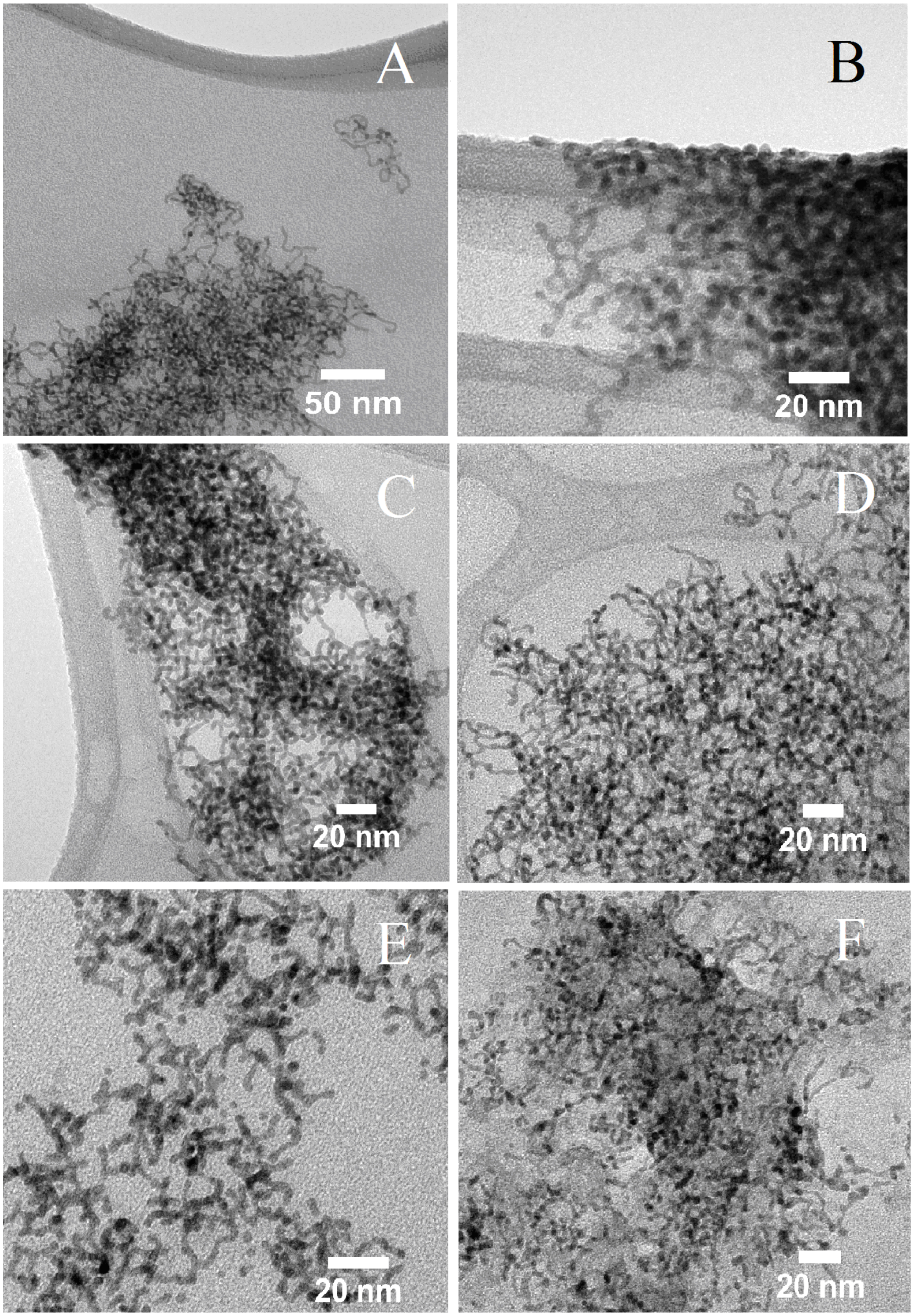

Figure 3.2. Representative TEM images of as-prepared (A) Pd, (B) $Pd_{0.90}Ni_{0.10}$, (C) $Pd_{0.83}Ni_{0.17}$, (D) $Pd_{0.75}Ni_{0.25}$, (E) $Pd_{0.60}Ni_{0.40}$, and (F) $Pd_{0.50}Ni_{0.50}$ free-standing ultrathin nanowires.

To the best of our knowledge, this specific synthetic protocol has only been applied to noble metals and noble metal alloys in the past, namely Pt, Pd, and Au. In addition, it is proposed that the growth mechanism involves the surfactant-directed assembly of discrete anisotropic seed nanocrystals into elongated nanowires composed of individual segments. An analogous way of describing this growth mechanism, especially for ultrathin nanowires, is that it can be viewed as not only ligand-controlled but also associated with an oriented attachment of nanoparticulate building blocks.[18] This unique growth mechanism renders the reaction process itself sensitive to the presence of oxygen, which can selectively adsorb onto and etch the edges of the growing nanowire, thereby leading to shorter nanorods in the presence of dissolved O_2 and longer nanowires in the absence of O_2.[24] Thus, it is not surprising that the introduction of non-noble metals, e.g. Ni, which are much more prone to oxidation than their noble metal counterparts, may likely hinder the assembly of constituent sub-structural seeds. Moreover, the higher content of Ni, the more difficult the assembly process, and hence, the more challenging the resulting nanowire formation is.

A high-resolution TEM (HRTEM) image (inset of Figure 3.3A) revealed that the NWs are actually polycrystalline and are composed of multiple single crystalline segments, as we had expected based on previous work.[22, 23] The selected area electron diffraction (SAED) pattern shown in Figure 3.3B highlights the likelihood of such structure by showing not only continuous rings which can be indexed to the (111), (200), (220), (222), and (331) reflections for the calculated *fcc* $Pd_{0.90}Ni_{0.10}$ alloy but also discrete diffraction spots, indicative of the high degree of crystalline substructure. Therefore, on the basis of the collected electron diffraction data, the $Pd_{0.90}Ni_{0.10}$, $Pd_{0.83}Ni_{0.17}$, and $Pd_{0.75}Ni_{0.25}$ NWs were experimentally determined to possess lattice parameters of 3.856 Å, 3.836 Å, and 3.796 Å, respectively, which are in agreement with the calculated values of 3.861 Å, 3.831 Å, and 3.806 Å for the respective alloys.

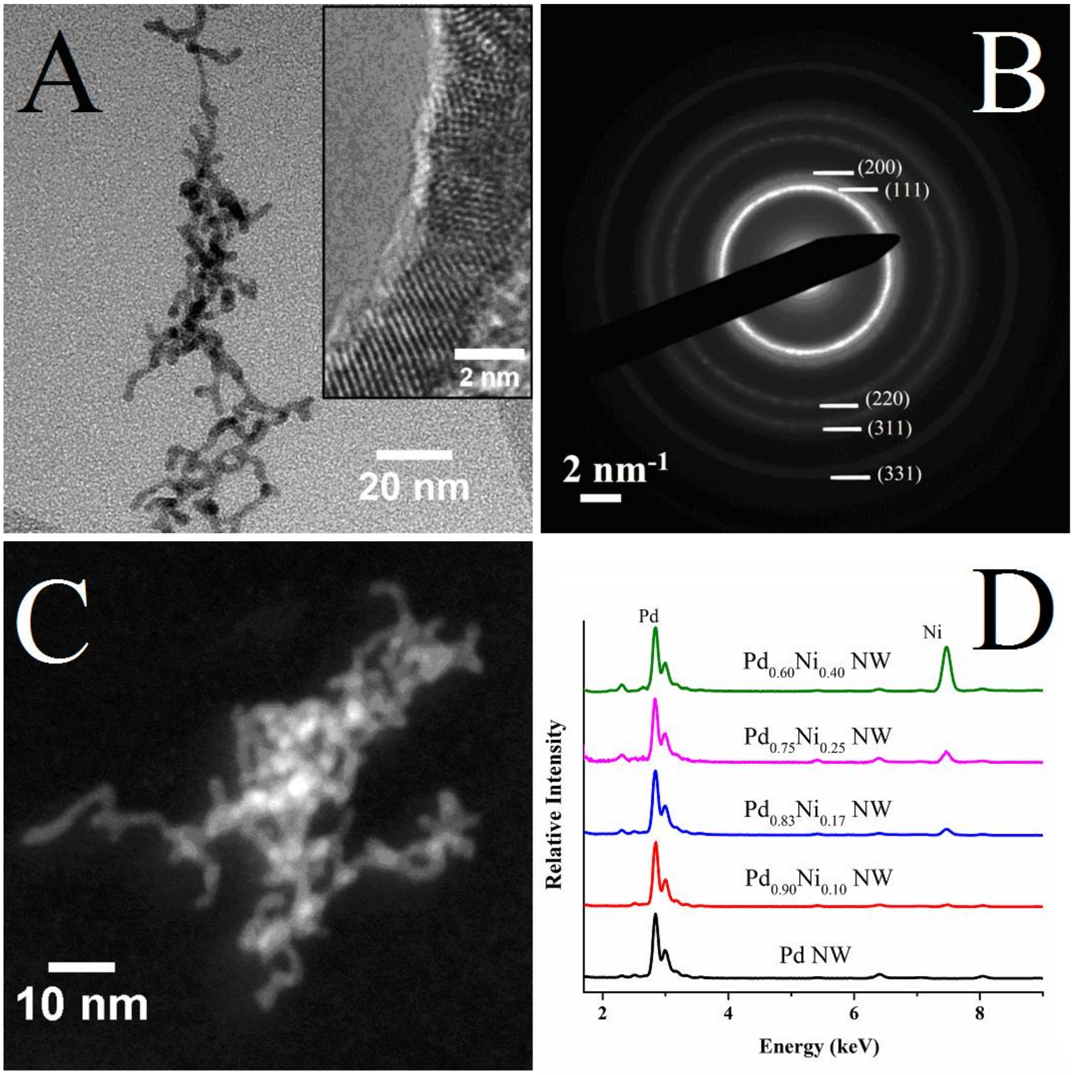

Figure 3.3. Representative TEM image (A) of $Pd_{0.90}Ni_{0.10}$ NWs supported on Vulcan XC-72R carbon support. The inset shows a high resolution TEM image, highlighting the segmented nature of the individual nanowire. The SAED pattern (B) obtained from a set of NWs is highlighted. An HAADF image taken from a representative aggregate of $Pd_{0.90}Ni_{0.10}$ NWs is presented in (C). Characteristic EDAX spectra (D) have been collected from various Pd-Ni NW composites of various chemical compositions.

Theoretical calculations generated by utilizing the Phase Diagram Software have shown that $Pd_{1-x}Ni_x$ tends to form a homogeneous alloy with an *fcc* structure under ambient conditions wherein '*x*' is no greater than 0.7 (Figure 3.4).[26]

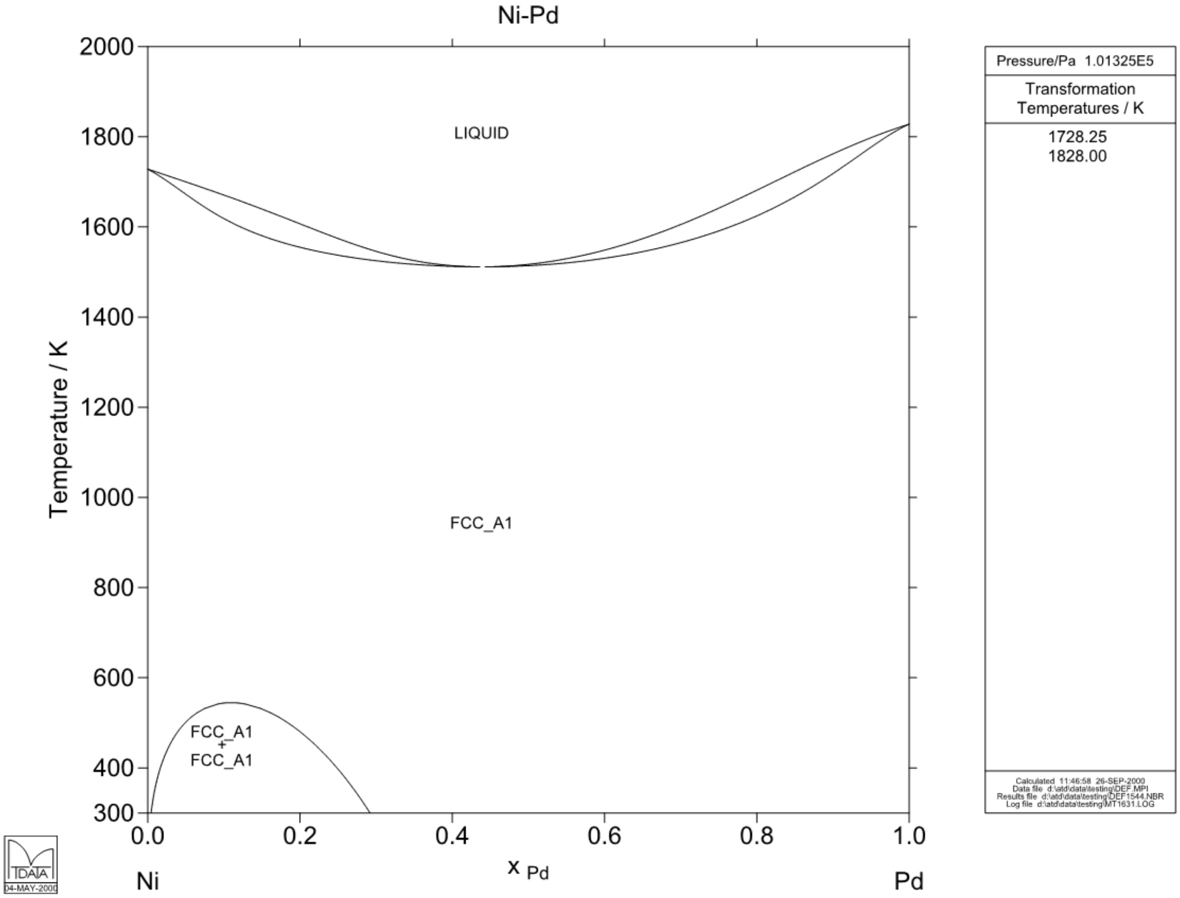

Figure 3.4. Pd-Ni phase diagram calculated by MTDATA – a phase diagram software program, developed by National Physical Laboratory of United Kingdom. The image was obtained from the open-source online database associated with the program.

In other words, for all of the sample compositions synthesized herein, the corresponding alloys should possess a homogeneous chemical structure. Indeed, the XRD and HRTEM data collectively suggest that our as-prepared $Pd_{1-x}Ni_x$ NWs are in fact uniform and homogeneous, since no diffraction data or other compelling evidence were observed for the formation of either Pd, Ni, or their related oxides.

We have also used a high angle annular dark field (HAADF) imaging technique, which is sensitive to atomic number (Z), to further examine the homogeneity of chemical composition along the lengths of our as-prepared wires. Figure 3.3C shows a representative HAADF image collected from a typical $Pd_{0.90}Ni_{0.10}$ sample. The largely uniform contrast observed over the collection of individual discrete NWs present is suggestive of a high degree of homogeneity of chemical composition. The brighter contrast at the center of the collection and within some spherical areas can be attributed to signals emanating from physically overlapping nanowires as well as from discrete interconnects amongst the NW segments. Such an observation has also been noted in analogous Pd_9Au NWs in previous reported work from our group.[22] Although it is beyond the scope of this project, we intend to further examine the structure and chemical composition of our $Pd_{1-x}Ni_x$ NWs, utilizing techniques such as X-ray absorption spectroscopy.

Representative point EDS spectra, corresponding to the elemental composition of areas measuring as small as several nm^2, were collected over multiple locations for all of our as-prepared 1D nanostructures and these are shown in Figure 3.3D. The diameters of various as-prepared $Pd_{0.90}Ni_{0.10}$, $Pd_{0.83}Ni_{0.17}$, $Pd_{0.75}Ni_{0.25}$, $Pd_{0.60}Ni_{0.40}$, and $Pd_{0.50}Ni_{0.50}$ nanostructures along with their actual chemical compositions obtained thorough EDAX analysis are summarized in Table 3.1.

Precursor Metal Composition	Morphology	Diameters (in nm)	Actual Composition (Pd: Ni, molar ratio)*	Standard Deviation of Chemical composition*
$Pd_{0.90}Ni_{0.10}$	Wires	2.7 ± 0.3	$Pd_{0.92}Ni_{0.08}$	0.02
$Pd_{0.83}Ni_{0.17}$	Wires	2.3 ± 0.2	$Pd_{0.84}Ni_{0.16}$	0.04
$Pd_{0.75}Ni_{0.25}$	Wires	2.1 ± 0.3	$Pd_{0.77}Ni_{0.23}$	0.03
$Pd_{0.60}Ni_{0.40}$	Short wires	2.4 ± 0.2	–	–
$Pd_{0.50}Ni_{0.50}$	Short wires/segments	2.3 ± 0.4	–	–

Table 3.1. Summary of the morphologies, diameters, and actual chemical compositions, as determined by EDAX analysis, of as-prepared Pd-Ni nanowires with various Pd: Ni molar ratios.

*Chemical compositions of $Pd_{0.60}Ni_{0.40}$ and $Pd_{0.50}Ni_{0.50}$ short wires were not precisely examined, as these materials were not used in subsequent electrochemical tests.

The small deviation in both diameter and atomic composition observed validates the idea of a high uniformity of these as-prepared nanowires in terms of both (a) morphology as well as (b) Pd and Ni content.

Regarding electrochemical characterization, our main focus has been directed to $Pd_{0.90}Ni_{0.10}$, $Pd_{0.83}Ni_{0.17}$, and $Pd_{0.75}Ni_{0.25}$ since they represent promising candidates for ORR, based on prior reports involving Pd-Ni nanoparticles.[9, 27] Our nanowire samples maintained chemical compositions that were rather close to the expected values with a minimal deviation of 3% from batch-to-batch. Specifically, the actual compositions of these three nanostructures were deemed to be $Pd_{0.92}Ni_{0.08}$ (± 0.02), $Pd_{0.84}Ni_{0.16}$ (± 0.04), and $Pd_{0.77}Ni_{0.23}$ (± 0.03), respectively.

3.2.2. Electrochemical Properties and ORR performance of Pd-Ni nanowire series.

In prior studies from our group, a treatment protocol was developed for the removal of residual organic impurities from the surfaces of analogous ultrathin Pd nanowires, which combined (i) a UV-ozone atmosphere pretreatment with (ii) a selective CO adsorption process.[21-23] In this specific case, however, we have developed our two-step protocol to include a more facile and potentially 'greener' pre-treatment process involving a simple surface capping ligand substitution with butylamine. In previous reports, ligand substitution reactions were effectively employed to remove a mixture of a borane-*tert*-butylamine complex and hexadecanediol from the surfaces of Pt_3Ni nanoparticles, for instance.[28] Herein, the ligand substitution was accomplished by dispersing as-synthesized ODA-capped PdNi alloy nanowires into pure butylamine for a period of three days under completely ambient conditions. The subsequent butylamine-capped nanowires could be activated toward a selective CO-adsorption process, which is capable of displacing organic capping ligands with alkyl-chains of up to six carbons in length.[21, 22, 29] That is, we have demonstrated that the selective CO stripping process alone is not capable of fully removing the ODA. However, in combination with ligand substitution using the 4-carbon butylamine molecule, the selective CO adsorption process can successfully produce electrochemical features in the CV profile, associated with pristine Pd nanostructures, while at the same time, conserving its overall wire morphology (Figure 3.5).

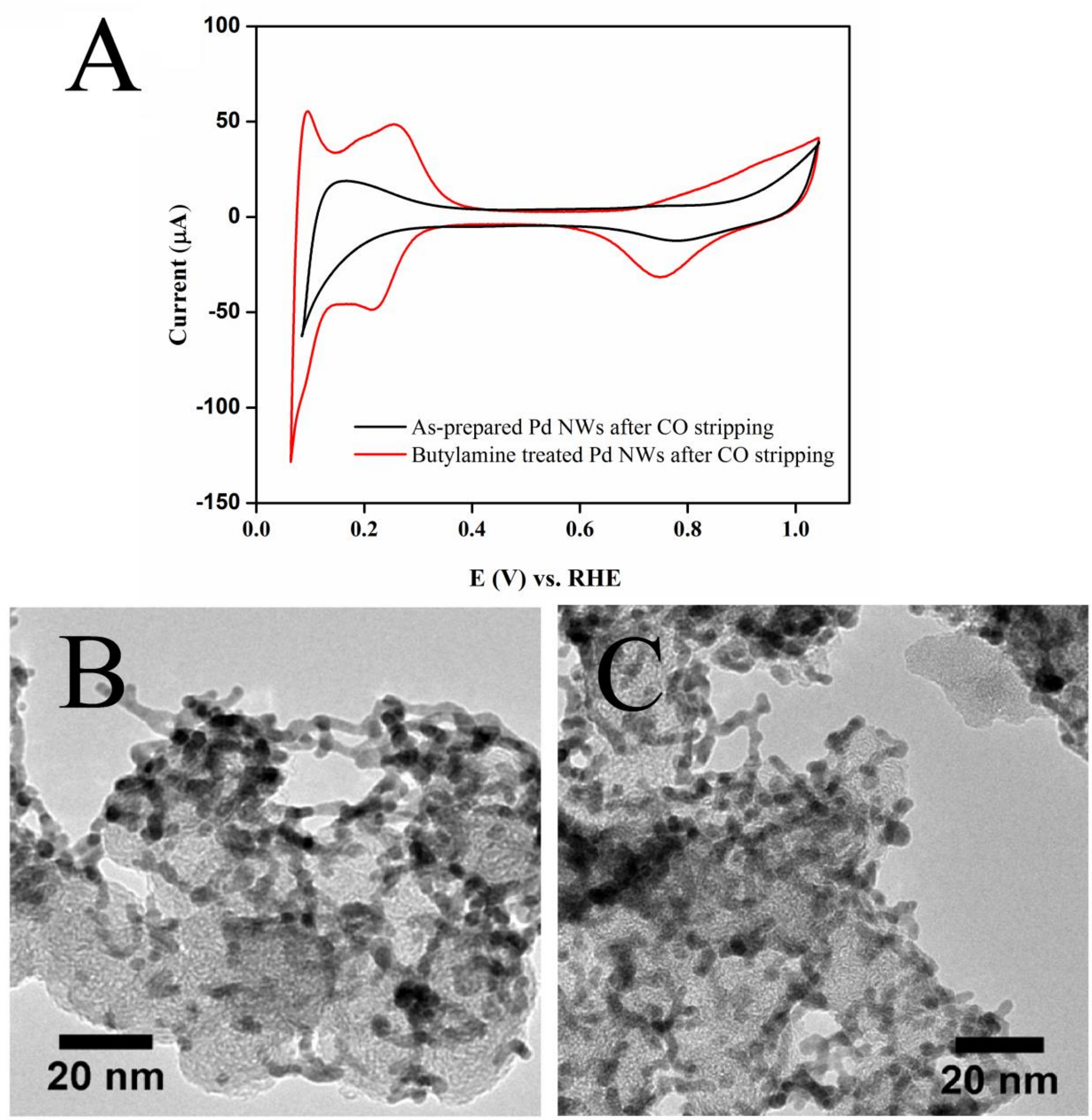

Figure 3.5. Cyclic voltammograms (A) obtained for the carbon-supported, as-prepared and butylamine-treated Pd nanowires after CO adsorption and CO stripping, in an argon-saturated 0.1 M $HClO_4$ solution at 20 mV/s. Representative images of the carbon-supported Pd nanowires both before (B) and after (C) butylamine treatment indicate that the processing method had no apparent effect on the resulting morphology of the NWs.

The cyclic voltammograms along with the associated specific ORR activities measured at 0.8 V are displayed in Figure 3.6A and 3.6B.

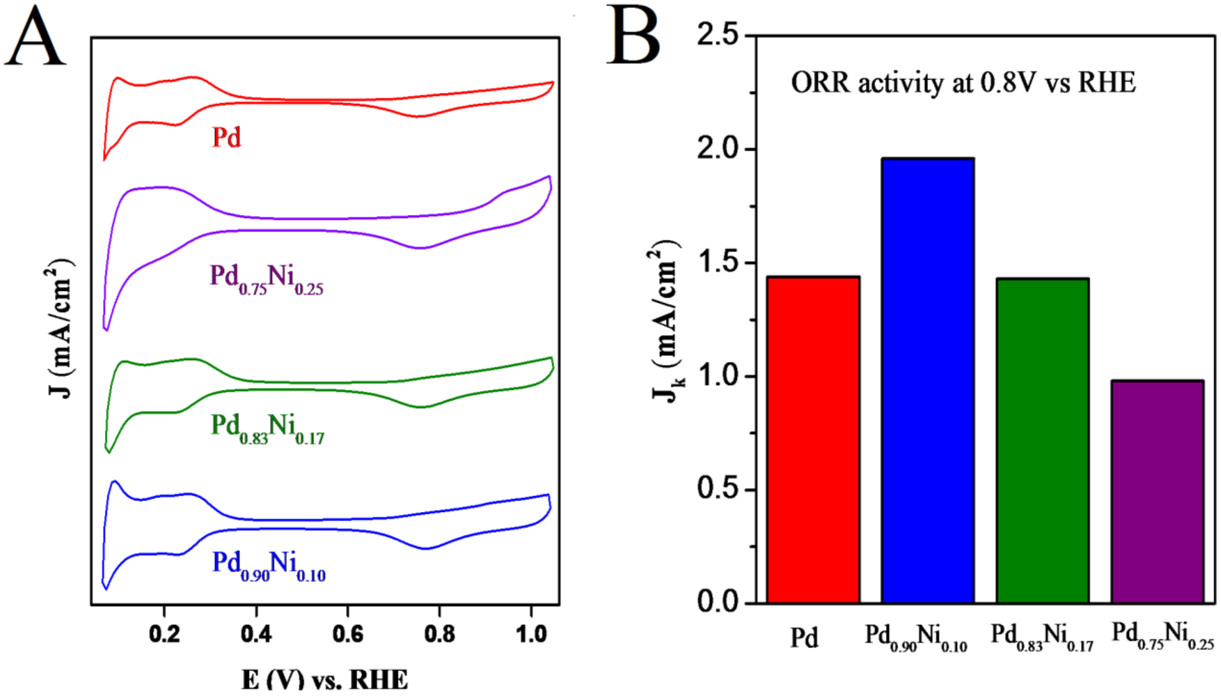

Figure 3.6. Cyclic voltammograms obtained from a series of butylamine-treated ultrathin Pd-Ni NW by comparison with elemental Pd NWs (A). The corresponding experimentally calculated area-normalized kinetic current densities (J_k, mA/cm^2) are shown in (B).

As compared with elemental palladium, the onset potentials for the oxide species in the cyclic voltammograms of the Pd-Ni series have been shifted to lower potentials, an observation which is consistent with the incorporation of Ni into the Pd-based alloy, thereby leading to a lower overall potential for the onset of surface oxide formation. Moreover, the positions of the oxide reduction peaks in Pd-Ni CVs shifted towards higher potential (relative to Pd) as a result of the “ligand effect” arising from the Ni content. This could be rationalized by the Nørskov-Hammer theory, which implies that Ni as a dopant withdraws electron density away from Pd, thereby weakening the interaction between Pd itself and the resulting oxide species. Interestingly, however, $Pd_{0.90}Ni_{0.10}$ shows the largest shift (769.3 mV as compared with 752.2 mV for elemental Pd), followed by $Pd_{0.83}Ni_{0.17}$ (759.8 mV) and finally $Pd_{0.75}Ni_{0.25}$ (755.2 mV).

We attribute such observations to the combination of the Ni doping effect and the oxophilic nature of Ni atoms themselves. In essence, the doping effect or “ligand effect” should imply a direct proportional relationship between the amount of dopant and the magnitude of the shift in the oxide reduction peak. However, this is only true with a small quantity of dopant. In fact, when the molar percentage of the non-noble metal exceeds a certain value (in this case, 10% of Ni), the oxophilicity of nickel was a more significant factor than the ligand effect, thereby rendering the wire structure more prone to oxidation. Nonetheless, deducing the exact relationship between the amount of Ni dopant present and the oxide reduction peak position is beyond the scope of this research, and a more thorough investigation involving probing of the Pd electronic structure will need to be conducted in order for this issue to be properly resolved.

As Figure 3.6B has shown, the activities of the series (including elemental Pd) exhibited a “volcano”-shaped trend where the highest activity was provided by $Pd_{0.90}Ni_{0.10}$ sample, namely at 1.96 mA/cm^2. A direct comparison of the specific activities of our supported $Pd_{0.90}Ni_{0.10}$ and elemental Pd nanowires is shown in Figure 3.7.

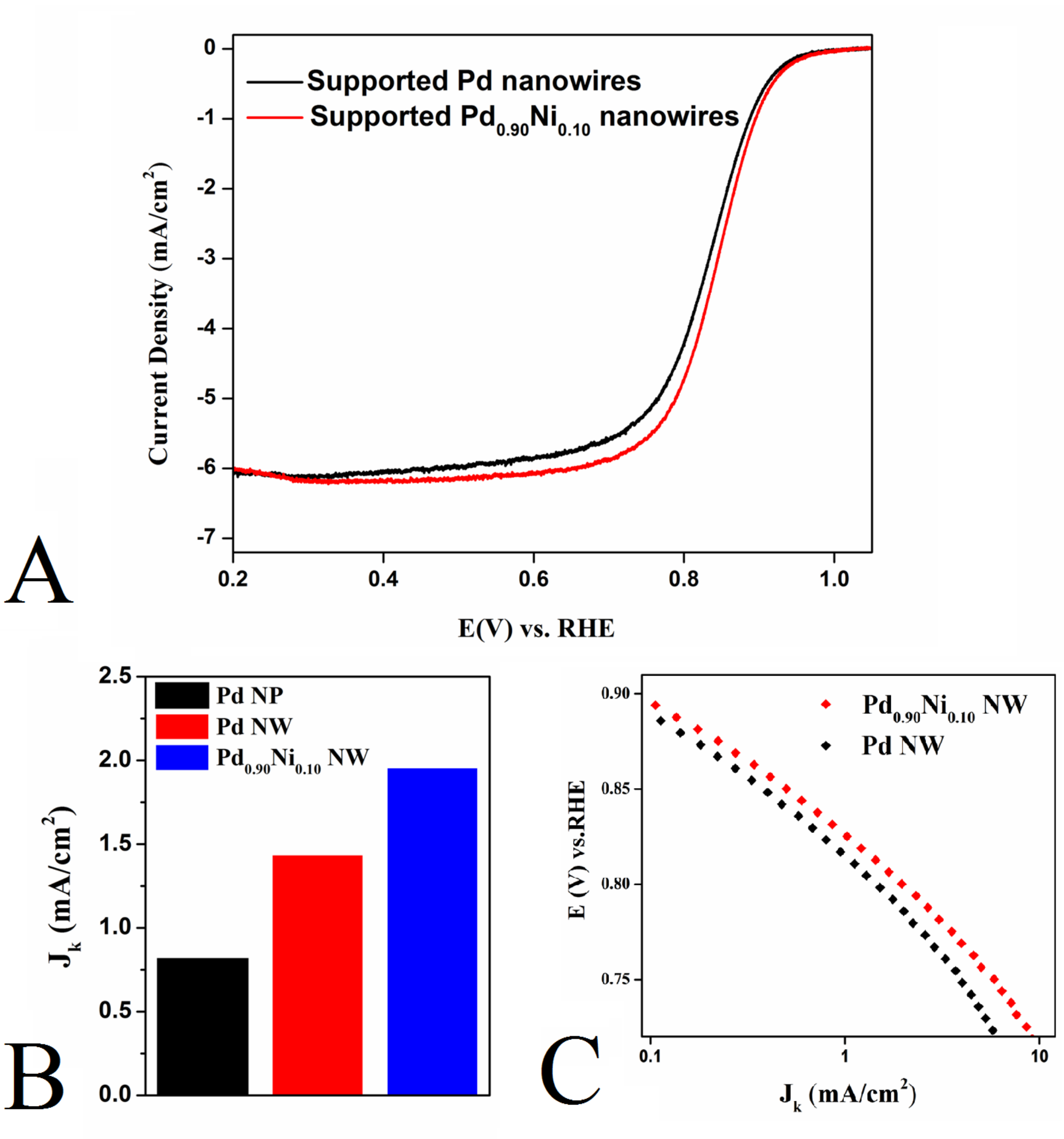

Figure 3.7. Representative polarization curves (A) obtained from $Pd_{0.90}Ni_{0.10}$ NWs with analogous Pd NWs serving as a comparison. Specific activities (mA/cm^2) of $Pd_{0.90}Ni_{0.10}$ nanowires, elemental Pd nanowires, and commercial Pd nanoparticles are summarized in (B). A potential versus specific activity plot (E vs. J_k) for these two nanostructures is presented in (C).

On the basis of the polarization curves obtained in an oxygen-saturated electrolyte (Figure 3.7A), the $Pd_{0.90}Ni_{0.10}$ NWs possess significantly enhanced performance, especially as compared with elemental Pd NWs and commercial Pd NP/C (Figure 3.7B). Moreover, the potential vs. specific activity (E vs. J_k) plot (Figure 3.7C) further confirms the consistently improved performance of $Pd_{0.90}Ni_{0.10}$ nanowires with respect to analogous elemental Pd nanowires over a broad range of plausible fuel cell potentials. The polarization curves of the rest two compositions, namely $Pd_{0.83}Ni_{0.17}$ and $Pd_{0.75}Ni_{0.25}$, can be found in Figure 3.8.

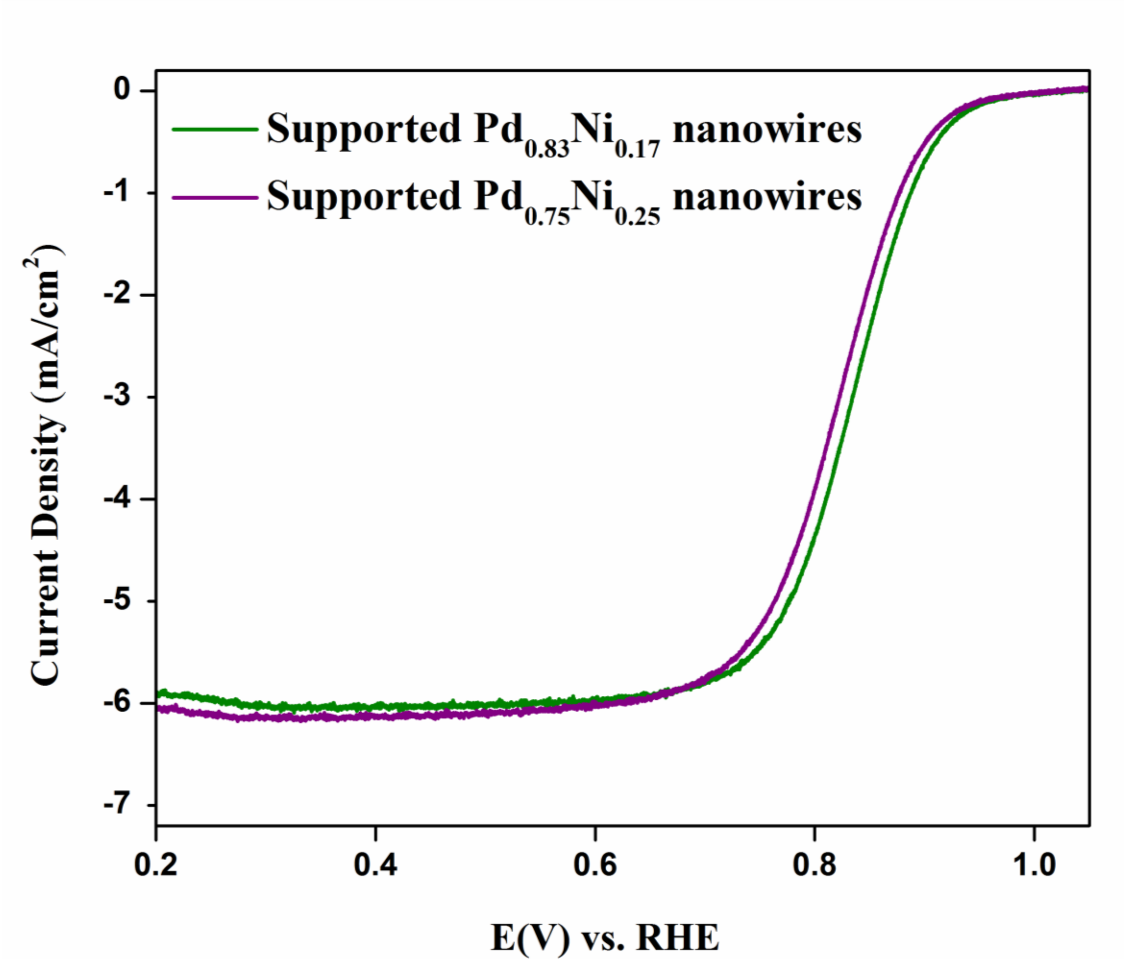

Figure 3.8. Representative polarization curves obtained from $Pd_{0.83}Ni_{0.17}$ and $Pd_{0.75}Ni_{0.25}$ NWs using a rotation rate of 1600 rpm in a 0.1 M $HClO_4$ solution at 20ºC.

In prior research studying the utilization of Pd-Ni nanoparticles as ORR electrocatalysts,[27, 30] the “optimum composition” was found to be $Pd_{0.60}Ni_{0.40}$. By contrast, we find herein that the $Pd_{1-x}Ni_x$ NW electrocatalysts maintain an optimum performance with a composition of Pd_9Ni. This interesting morphology-dependent finding may have several plausible explanations. *First*, this difference in behavior can be potentially attributed to a corresponding difference between the surface structure and composition of the Pd-Ni NPs and NWs. Specifically, recent theoretical work has demonstrated that the surface segregation of Pd atoms occurs at the catalytic interface (i.e. the 1 – 3 uppermost atomic layers) and that the surface composition and structure of the de-alloyed surface varies significantly for exposed (111), (100), and (110) facets, respectively.[31] It is typically observed that noble metal NWs possessing diameters measuring 2 nm expose primarily (111) and (100) facets with a relatively low defect site density, whereas the corresponding analogous NPs maintain predominantly (111)-terminated facets with a relatively large density of (110)-type defect sites.[2, 32] In addition, the degree of Pd enrichment and the corresponding surface structure are also highly dependent upon the surface strain, which is known to be comparatively different for nanoparticles versus nanowires, due to their isotropic and anisotropic geometries, respectively.

Hence, on the basis of this theory, we believe that significant differences in the surface structure and strain of the NWs and NPs may lead to differing degrees of surface segregation at the catalytic interface. What we propose herein therefore is that as a result of the morphology-dependent Pd enrichment, the surface layers of reported $Pd_{0.60}Ni_{0.40}$ nanoparticles and of our $Pd_{0.90}Ni_{0.10}$ nanowires likely possess approximately the same chemical composition at the interface and therefore a similar ‘active site’ profile, thereby resulting in the comparably favorable ORR activities, experimentally recorded.

Second, as an alternative, complementary explanation for the observed activity enhancement of Pd alloys as compared with Pd alone, it is worth noting, from previous studies,[33, 34] that one of the roles of the second metal 'dopant', i.e. Ni, is to lower the amount of potentially deleterious OH coverage on Pd by inducing lateral repulsion between OH species adsorbed on Pd and neighboring OH or O species adsorbed on Ni. The net effect of this interaction is to yield a positive shift associated with the formation of OH on Pd or conversely, the oxidation of PdNi itself. In principle, decreasing OH coverage on Pd should increase the number of free Pd 'active' sites.[35] Although it is beyond the scope of this research, additional insights into the physico-chemical origins of the enhanced performance can be garnered by techniques such as X-ray absorption and X-ray photoelectron spectroscopies, which can likely provide detailed information concerning surface structure and surface chemical composition. We intend to perform these types of characterization experiments in the future.

In the operation of DMFCs, the migration of methanol from the anodic half-cell to the cathodic half-cell often results in a de-activation of the catalyst. To further prove that our $Pd_{0.90}Ni_{0.10}$ nanowires are promising as actual, practical ORR candidates, we have conducted methanol tolerance experiments. Figure 3.9A displays polarization curves obtained from $Pd_{0.90}Ni_{0.10}$ NWs in the presence of varying methanol concentrations (i.e. 0 − 4 mM).

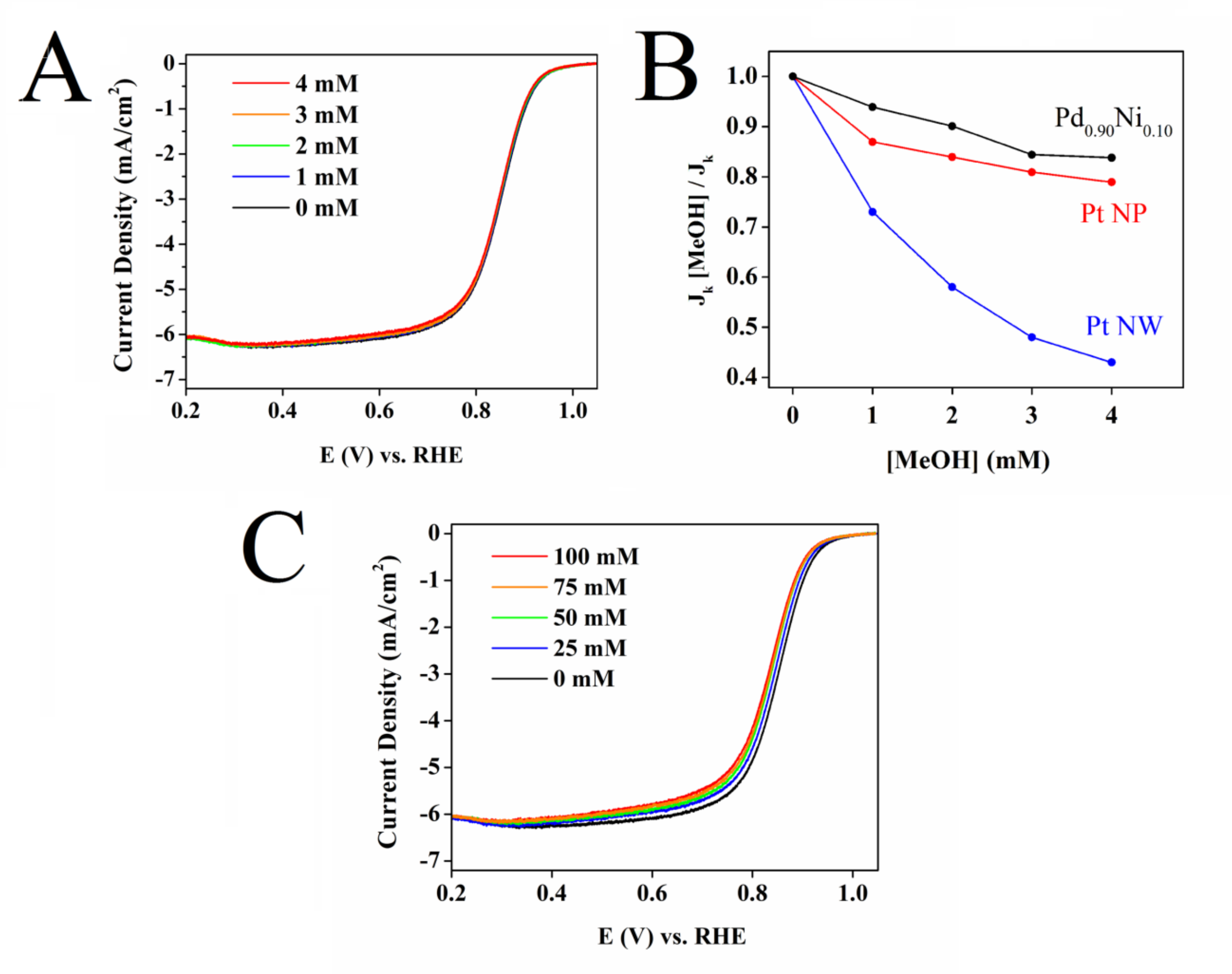

Figure 3.9. Probing the methanol tolerance capability of as-processed $Pd_{0.90}Ni_{0.10}$ NWs. Polarization curves were obtained in the presence of various methanol concentrations, ranging from 0 to 4 mM. (A) A plot of the ratio of the specific activity values measured in the presence of methanol (J_K [MeOH]) to that measured in pure electrolyte (J_K) as a function of increasing methanol concentration (B) for $Pd_{0.90}Ni_{0.10}$ NWs, with both Pt NWs and commercial Pt NP/C serving as controls. In (C), polarization curves were obtained from $Pd_{0.90}Ni_{0.10}$ in 0.1 M $HClO_4$ with increasing methanol concentrations of 25, 50, 75, and 100 mM, respectively.

It can be inferred from these data that at these levels, methanol exerts minimal effect on the shape and intensity of the measured polarization curves. A more quantitative analysis (shown in Figure 3.9B) validates a high methanol tolerance ability for our systems. In fact, our purified $Pd_{0.90}Ni_{0.10}$ NWs maintain a significantly improved tolerance to methanol by maintaining 85% of their initial activity in the presence of 4 mM methanol, which designates a tangible improvement especially as compared with controls consisting of commercial elemental 0D Pt NP/C (79%) and 1D Pt NWs (43%).

Moreover, Figure 3.9C shows a minimal difference of 20 mV in half-wave potential for polarization curves obtained in a mixture of 0.1 M $HClO_4$ and 100 mM MeOH solution as compared with an analogous polarization curve obtained in 0.1 M $HClO_4$ solution, thereby corroborating the high methanol tolerance ability of our nanowires. The fact that 55% of the initial activity for our $Pd_{0.90}Ni_{0.10}$ nanowires was retained after these experiments should be considered noteworthy, especially given the fact that commercial Pt nanoparticles likely maintain either little or no ORR activity under identical experimental conditions and protocols. In addition, a comparison of CVs both in the presence of as well as in the absence of MeOH, serving as a component of the electrolyte, further highlights that the main defining features of $Pd_{0.90}Ni_{0.10}$ cyclic voltammograms are indeed preserved even after the addition of methanol (Figure 3.10). Both the polarization curves as well as CV comparative analysis imply the absence of a CO-poisoning effect on the actual $Pd_{0.90}Ni_{0.10}$ surface which would have been particularly detrimental to ORR performance.

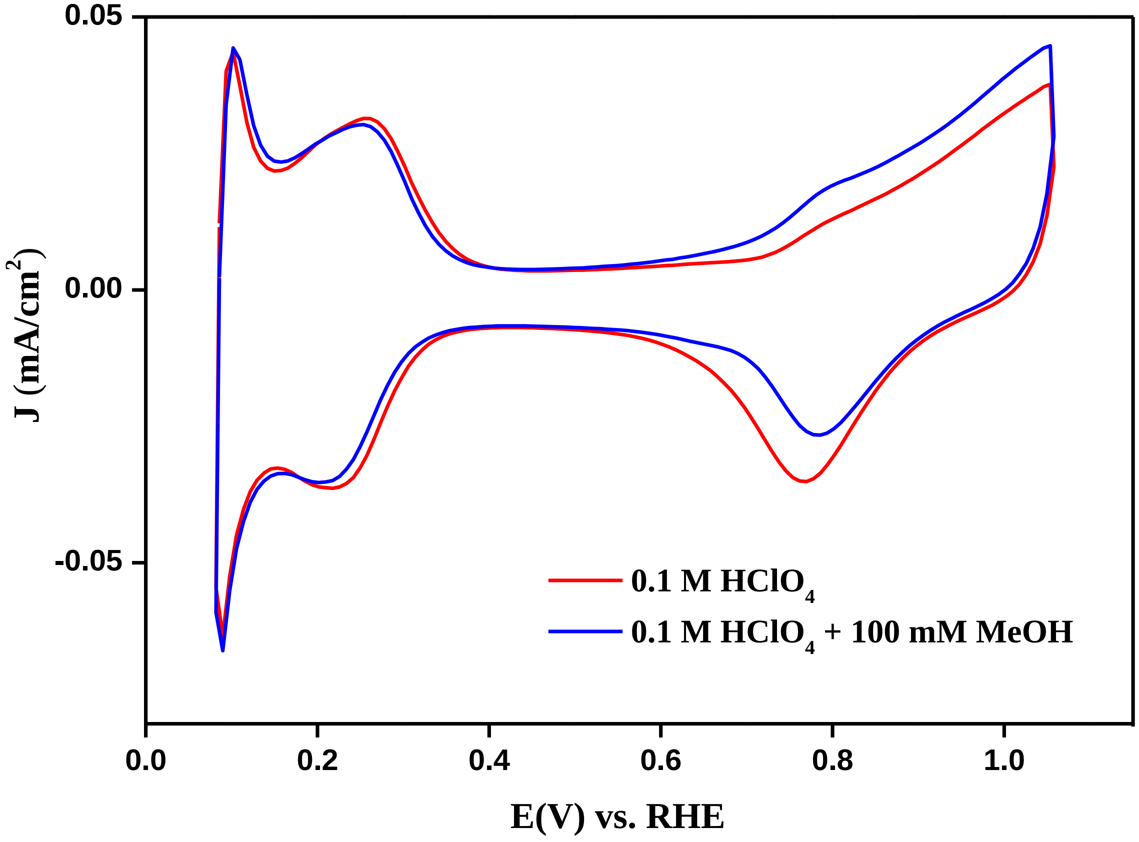

Figure 3.10. Cyclic voltammograms of $Pd_{0.90}Ni_{0.10}$ in an argon-saturated 0.1 M $HClO_4$ solution, both in the presence of (blue line) and absence of (red line) 100 mM Methanol at a sweeping rate of 20 mV/s.

It has been demonstrated in our previous work and many other reports that binary nanostructures, both 0D[36] and 1D[22], represent a promising platform for the deposition of a Pt monolayer shell and hence, one can envision forming core-shell ORR catalysts possessing outstanding performance, yet with a minimum amount of Pt metal. For example, a high-performing catalyst consisting of Pt decorating PdNi nanoparticles supported on C have been shown to evince superior performance to analogous pure Pt, Pd, and PdNi, all supported on C.[13] In this current report, we have specifically designed ultrathin Pt~$Pd_{0.90}Ni_{0.10}$ core-shell nanostructures that displayed significant electrochemical improvement as compared with analogous ultrathin Pt~Pd nanowires. The deposition of the platinum monolayer was accomplished by Cu UPD followed by galvanic displacement of the Cu atoms with $[PtCl_4]^{2-}$.

Cyclic voltammetric comparison of the $Pd_{0.90}Ni_{0.10}$ and Pt~$Pd_{0.90}Ni_{0.10}$ composites (Figure 3.11A) showed that after Pt deposition, the hydrogen adsorption region resembled that of a nanostructured Pt surface.

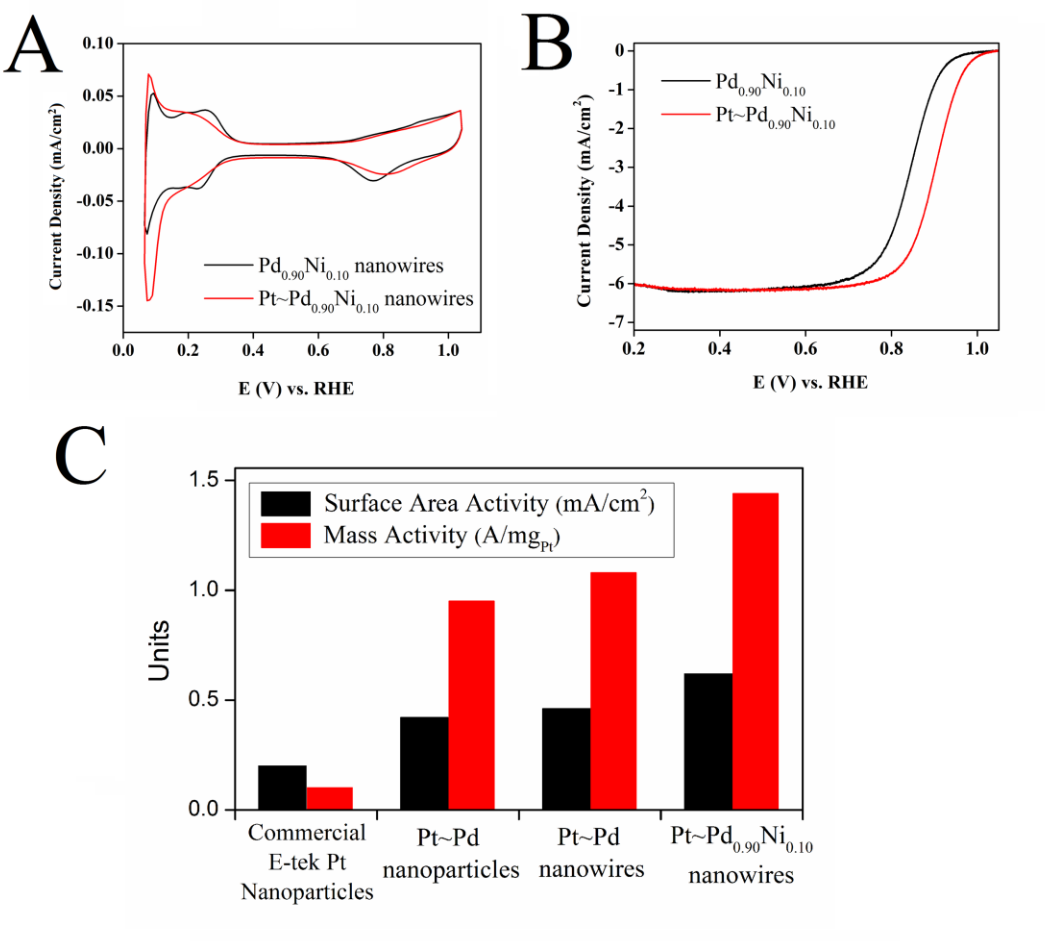

Figure 3.11. Cyclic voltammograms (A) obtained for $Pd_{0.90}Ni_{0.10}$ nanowires and Pt~$Pd_{0.90}Ni_{0.10}$ core-shell nanowires, in a 0.1 M $HClO_4$ solution at 20 mV/s. (B) The polarization curves for both of these two nanowire composites were obtained using a rotation rate of 1600 rpm in a 0.1 M $HClO_4$ solution at 20ºC. The electrochemical surface area activity and mass activity at 0.9 V for Pt~$Pd_{0.90}Ni_{0.10}$ are shown by comparison with commercial carbon-supported Pt nanoparticles, analogous Pt~Pd nanoparticles, and ultrathin Pt~Pd nanowires, respectively (C).

Moreover, the oxidation and reduction peaks were shifted to higher potential. All of these observations support the findings from our prior observations.[23] The polarization curves of the corresponding samples are displayed in Figure 3.11B. We note that the Pt~$Pd_{0.90}Ni_{0.10}$ NWs possessed an ORR onset in the region of 0.9 ~ 1.0 V, which is consistent with that of nanostructured Pt catalysts. Based on the polarization curves, the specific activities and mass activities at 0.9 V were measured and are shown in Figure 3.11C, by comparison with commercial platinum nanoparticles. Specifically, the Pt~$Pd_{0.90}Ni_{0.10}$ nanowires yielded area- and mass activities of 0.62 mA/cm^2 and 1.44 A/mg_{Pt}, respectively.

Moreover, we have tested the electrochemical durability of our processed Pt~$Pd_{0.90}Ni_{0.10}$ composites under half-cell conditions. Specifically, the electrode was immersed in naturally aerated 0.1M $HClO_4$ solution while the potential was cycled between 0.6 to 1.0V in order to properly simulate the relevant electrochemical environmental conditions associated with ORR feasibly occurring within a functional working fuel cell configuration. On the basis of this protocol, the ESA as well as the specific activities could be independently probed by obtaining cyclic voltammograms (Figure 3.12A) and polarization curves (Figure 3.12B) through potential cycling at a high scan rate, i.e. through an accelerated degradation test (ADT).

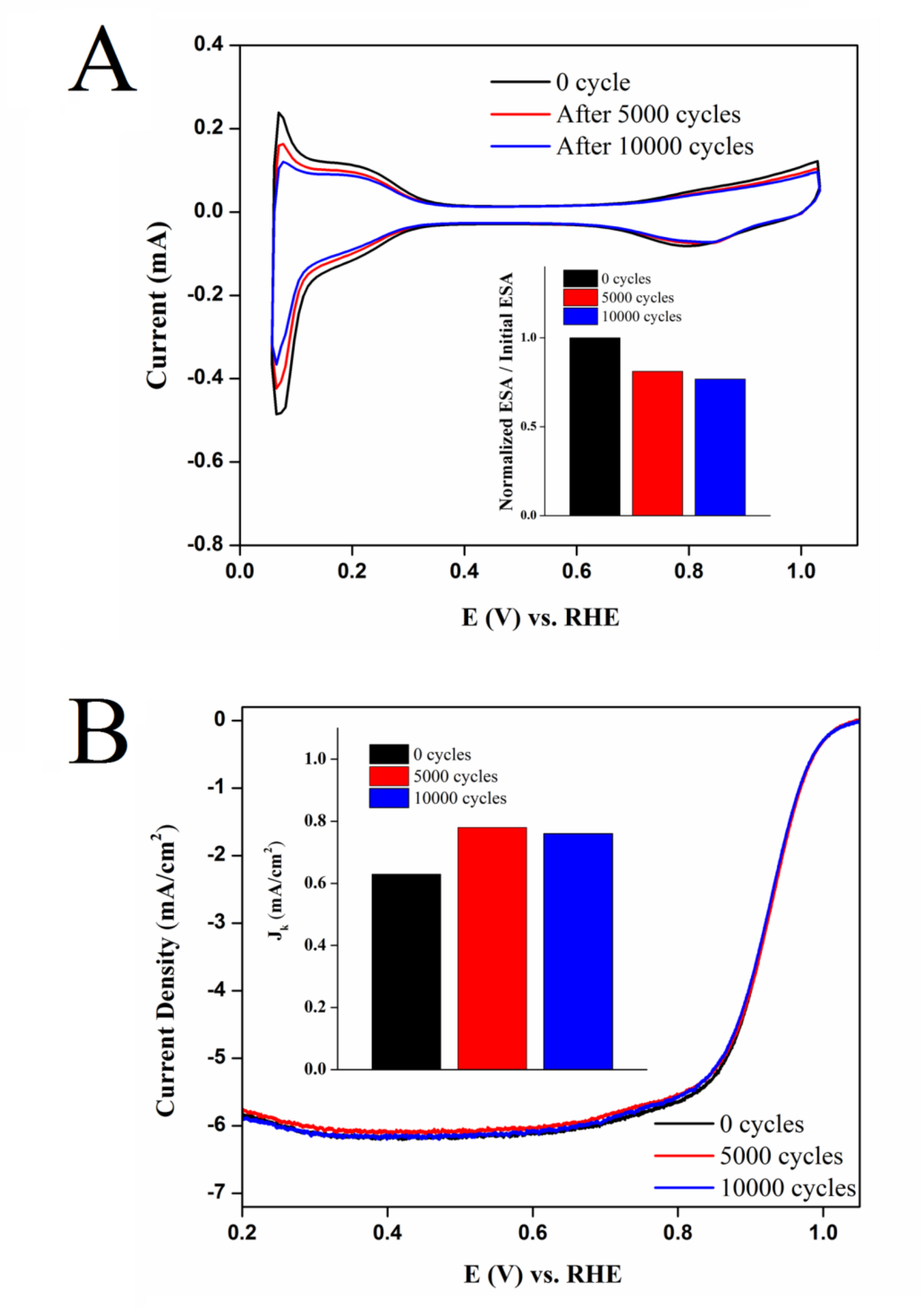

Figure 3.12. (A) Cyclic voltammograms obtained in deoxygenated 0.1M $HClO_4$ solution after every 5000 cycles for Pt~$Pd_{0.90}Ni_{0.10}$ core-shell composites. In the inset, the measured ESA loss is also shown as a function of durability cycling for the Pt~$Pd_{0.90}Ni_{0.10}$ architecture. The corresponding polarization curves, obtained in an oxygen saturated 0.1M $HClO_4$ at 1600 rpm after every 5000 cycles, are presented in (B). Area-specific activities are plotted as a function of durability in the inset to (B).

We found that the Pt~$Pd_{0.90}Ni_{0.10}$ catalytic architecture maintained 81% and 77% of their initial measured ESA values after 5000 cycles and 10000 cycles, respectively. This decline in ESA is comparatively more rapid as compared with our analogous Pt~Pd ultrathin nanowires previously reported, which maintained ~100% of ESA after 5000 cycles and 83% after 10000 cycles. This accelerated ESA loss rate can potentially be attributed to the relative instability of Ni content in our material towards an acidic testing environment, since Ni is generally less inert than Pd and hence more prone to dissolution.

In addition, the specific activity, or surface area activity, of Pt~$Pd_{0.90}Ni_{0.10}$ has also been studied as a function of durability. As shown in Figure 7B, despite a nearly 20% of ESA loss, the corresponding specific activity of our as-prepared electrocatalysts actually increased by more than 20% after 10000 cycles (from 0.62 mA/cm^2 to 0.76 mA/cm^2). As a matter of record, there was only a 2 mV loss of half-wave potential in the process. This promising result is in excellent agreement with our previous study of both Pt~Pd nanoparticles and Pt~Pd nanowires possessing analogous dimensions.[37,23] We attribute the enhanced activity to the preferential dissolution of both Pd and Ni content in the core as well as to a restructuring of the Pt monolayer. Overall, our results demonstrate that our Pt~$Pd_{0.90}Ni_{0.10}$ electrocatalysts possess excellent electrochemical stability.

3.3. Conclusions

In this Chapter, we have utilized an am11bient, surfactant-based synthetic method to prepare ultrathin, composition-tunable Pd-Ni one-dimensional nanostructures possessing high structural uniformity and a homogeneous distribution of elements. The electrochemical activities of the carbon-supported Pd-Ni were examined. Two of the compositions, namely $Pd_{0.90}Ni_{0.10}$ and $Pd_{0.83}Ni_{0.17}$, exhibited either similar or higher specific activities by comparison with elemental Pd NWs, while all four chemical compositions of the nanowires tested, which were involved in electrochemical tests (namely elemental Pd, $Pd_{0.90}Ni_{0.10}$, $Pd_{0.83}Ni_{0.17}$, and $Pd_{0.75}Ni_{0.25}$) possessed measurable enhancement as compared with commercial Pd nanoparticles. More importantly, as a positive indicator of the potential practicality of our research herein, the $Pd_{0.90}Ni_{0.10}$ sample exhibited outstanding methanol tolerance ability. In essence, there was only a 15% loss in the specific activity in the presence of 4 mM of methanol.

Moving beyond the 'bimetallic' structural motif, we also studied ultrathin, core-shell Pt~$Pd_{0.90}Ni_{0.10}$ nanowires, which exhibited a specific activity of 0.62 mA/cm^2 and a corresponding mass activity of 1.44 A/mg$_{Pt}$. Moreover, our as-prepared core-shell catalyst maintained excellent electrochemical durability under realistic testing conditions with the specific activity of our as-prepared electrocatalysts actually increasing by more than 20% after 10000 cycles from 0.62 mA/cm^2 to 0.76 mA/cm^2. We attributed the improvement in both catalytic performance and stability not only to the surface contraction of the Pt layer due to the small dimensions of the wires but also to the electronic effect that the nanoscale Pd-Ni alloy core imparts to the outer Pt monolayer shell. Further investigation in terms of determining the detailed electronic structure of ultrathin Pt~Pd-Ni nanowires may lead to a better understanding of the role of chemical composition in determining overall electrocatalytic behavior. Nonetheless, we postulate that 1-D Pd-Ni nanostructures represent a promising platform for designing ORR catalysts with respectable activity. In so doing, we are able to offer a more earth-abundant, lower cost, high-performance, and therefore attractive alternative to the conventional use of Pt nanoparticles as ORR catalysts.

3.4 References

1. Koenigsmann, C.; Wong, S. S. *Energy & Environmental Science* **2011,** 4, (4), 1161-1176.
2. Koenigsmann, C.; Scofield, M. E.; Liu, H.; Wong, S. S. *The Journal of Physical Chemistry Letters* **2012,** 3, (22), 3385-3398.
3. Savadogo, O.; Lee, K.; Oishi, K.; Mitsushima, S.; Kamiya, N.; Ota, K. I. *Electrochem Commun* **2004,** 6, (2), 105-109.
4. Savadogo, O.; Lee, K.; Mitsushima, S.; Kamiya, N.; Ota, K. I. *J New Mat Electr Sys* **2004,** 7, (2), 77-83.
5. Løvvik, O. M. *Surface Science* **2005,** 583, (1), 100-106.
6. Greeley, J.; Norskov, J. K. *Surface Science* **2005,** 592, (1-3), 104-111.
7. Li, B.; Prakash, J. *Electrochem Commun* **2009,** 11, (6), 1162-1165.
8. Li, B.; Amiruddin, S.; Prakash, J. *ECS Transactions* **2008,** 6, (25), 139-144.
9. Zhao, J.; Sarkar, A.; Manthiram, A. *Electrochimica Acta* **2010,** 55, (5), 1756-1765.
10. Liu, L.; Samjeske, G.; Nagamatsu, S.-i.; Sekizawa, O.; Nagasawa, K.; Takao, S.; Imaizumi, Y.; Yamamoto, T.; Uruga, T.; Iwasawa, Y. *Top Catal* **2013**, 1-12.
11. Ramos-Sanchez, G.; Bruno, M. M.; Thomas, Y. R. J.; Corti, H. R.; Solorza-Feria, O. *Int J Hydrogen Energ* **2012,** 37, (1), 31-40.
12. Ramos-Sanchez, G.; Yee-Madeira, H.; Solorza-Feria, O. *Int J Hydrogen Energ* **2008,** 33, (13), 3596-3600.
13. Wang, R. F.; Li, H.; Ji, S.; Wang, H.; Lei, Z. Q. *Electrochimica Acta* **2010,** 55, (5), 1519-1522.
14. Shao, M. H.; Smith, B. H.; Guerrero, S.; Protsailo, L.; Su, D.; Kaneko, K.; Odell, J. H.; Humbert, M. P.; Sasaki, K.; Marzullo, J.; Darling, R. M. *Phys Chem Chem Phys* **2013,** 15, (36), 15078-15090.
15. Tarasevich, M. R.; Zhutaeva, G. V.; Bogdanovskaya, V. A.; Radina, M. V.; Ehrenburg, M. R.; Chalykh, A. E. *Electrochimica Acta* **2007,** 52, (15), 5108-5118.
16. Weber, J.; Singhal, R.; Zekri, S.; Kumar, A. *Int Mater Rev* **2008,** 53, (4), 235-255.
17. Wang, N.; Cai, Y.; Zhang, R. Q. *Mat Sci Eng R* **2008,** 60, (1-6), 1-51.
18. Cademartiri, L.; Ozin, G. A. *Adv Mater* **2009,** 21, (9), 1013-1020.
19. Xia, Y. N.; Yang, P. D.; Sun, Y. G.; Wu, Y. Y.; Mayers, B.; Gates, B.; Yin, Y. D.; Kim, F.; Yan, Y. Q. *Adv Mater* **2003,** 15, (5), 353-389.
20. Lim, B.; Jiang, M. J.; Camargo, P. H. C.; Cho, E. C.; Tao, J.; Lu, X. M.; Zhu, Y. M.; Xia, Y. N. *Science* **2009,** 324, (5932), 1302-1305.
21. Koenigsmann, C.; Sutter, E.; Chiesa, T. A.; Adzic, R. R.; Wong, S. S. *Nano Lett* **2012,** 12, (4), 2013-2020.
22. Koenigsmann, C.; Sutter, E.; Adzic, R. R.; Wong, S. S. *The Journal of Physical Chemistry C* **2012,** 116, (29), 15297-15306.
23. Koenigsmann, C.; Santulli, A. C.; Gong, K. P.; Vukmirovic, M. B.; Zhou, W. P.; Sutter, E.; Wong, S. S.; Adzic, R. R. *J Am Chem Soc* **2011,** 133, (25), 9783-9795.
24. Teng, X. W.; Han, W. Q.; Ku, W.; Hucker, M. *Angew Chem Int Edit* **2008,** 47, (11), 2055-2058.
25. Alia, S. M.; Larsen, B. A.; Pylypenko, S.; Cullen, D. A.; Diercks, D. R.; Neyerlin, K. C.; Kocha, S. S.; Pivovar, B. S. *Acs Catal* **2014,** 4, (4), 1114-1119.

26. Calculated Ni-Pd phase diagram. National Physical Laboratory of the United Kingdom: http://resource.npl.co.uk/mtdata/phdiagrams/nipd.htm, 2000.
27. Lee, K.; Savadogo, O.; Ishihara, A.; Mitsushima, S.; Kamiya, N.; Ota, K.-i. *Journal of The Electrochemical Society* **2006,** 153, (1), A20.
28. Wu, J.; Zhang, J.; Peng, Z.; Yang, S.; Wagner, F. T.; Yang, H. *J Am Chem Soc* **2010,** 132, (14), 4984-4985.
29. Adzic, R. R.; Zhang, J.; Sasaki, K.; Vukmirovic, M. B.; Shao, M.; Wang, J. X.; Nilekar, A. U.; Mavrikakis, M.; Valerio, J. A.; Uribe, F. *Top Catal* **2007,** 46, (3-4), 249-262.
30. Ham, D. J.; Pak, C.; Bae, G. H.; Han, S.; Kwon, K.; Jin, S. A.; Chang, H.; Choi, S. H.; Lee, J. S. *Chem Commun (Cambridge)* **2011,** 47, (20), 5792-4.
31. Bozzolo, G.; Noebe, R. D.; Khalil, J.; Morse, J. *Applied Surface Science* **2003,** 219, (1-2), 149-157.
32. Koenigsmann, C.; Zhou, W. P.; Adzic, R. R.; Sutter, E.; Wong, S. S. *Nano Lett* **2010,** 10, (8), 2806-2811.
33. Zhang, J.; Vukmirovic, M. B.; Sasaki, K.; Nilekar, A. U.; Mavrikakis, M.; Adzic, R. R. *J. Am. Chem. Soc.* **2005,** 127, 12480-12481.
34. Lima, F. H. B.; Lizcano-Valbuena, W. H.; Texeira-Neto, E.; Nart, F. C.; Gonzalez, E. R.; Ticianelli, E. A. *Electrochimica Acta* **2006,** 52, 385-393.
35. Hsu, S.-P.; Liu, C.-W.; Chen, H.-S.; Chen, T.-Y.; Lai, C.-M.; Lee, C.-H.; Lee, J.-F.; Chan, T.-S.; Tsai, L.-D.; Wang, K.-W. *Electrochimica Acta* **2013,** 105, 180-187.
36. Xing, Y.; Cai, Y.; Vukmirovic, M. B.; Zhou, W.-P.; Karan, H.; Wang, J. X.; Adzic, R. R. *The Journal of Physical Chemistry Letters* **2010,** 1, (21), 3238-3242.
37. Sasaki, K.; Naohara, H.; Cai, Y.; Choi, Y. M.; Liu, P.; Vukmirovic, M. B.; Wang, J. X.; Adzic, R. R. *Angewandte Chemie International Edition* **2010,** 49, (46), 8602-8607.

Chapter 4: Multi-functional ultrathin Pd_xCu_{1-x} and Pt~Pd_xCu_{1-x} one-dimensional nanowire motifs for various small molecule oxidation reactions

4.1. Introduction

Noble metals, including Pt and Pd, are known to give rise to excellent electrocatalytic performance towards the anodic reaction associated with proton exchange membrane fuel cells (PEMFCs), i.e. methanol/ethanol/formic acid oxidation reactions, depending on which one of these fuels is actually being employed.[1-3] As previously mentioned in Chapter 1, the relevant half-reactions for the formic acid oxidation reaction (FAOR), the methanol oxidation reaction (MOR), and the ethanol oxidation reaction (EOR) are highlighted in Equations (4.1), (4.2) and (4.3), respectively.

$$HCOOH \rightarrow CO_2 + 2H^+ + 2e^- \qquad (4..1)$$

$$CH_3OH + H_2O \rightarrow CO_2 + 6H^+ + 6e^- \qquad (4.2)$$

$$CH_3CH_2OH + 3H_2O \rightarrow 2CO_2 + 12H^+ + 12e^- \qquad (4.3)$$

Hence, interest in optimizing these small molecule oxidation catalysts has been a main focus of efforts in electrocatalysis, since this process defines a key and underlying anodic reaction of a succession of related fuel cell configurations, i.e., direct methanol fuel cell (DMFCs), direct ethanol fuel cells (DEFCs), direct formic acid fuel cells (DFAFCs), and so on. In this context, various types of nanomaterials have already been fabricated as potentially superior catalysts for these aforementioned reactions as viable replacements for costly, potentially less abundant elemental Pt.[4]

The creation of ‘alloyed’ motifs has been one of the most common strategies used for mitigating the cost associated with the heavy use of noble metals in these systems as well as for improving electrochemical activities in general.[5, 6] From the theoretical point of view, the origin of the enhanced catalytic performance can be rationalized on the basis of a sensible alteration of the electronic structure of these materials, due to transition metal doping as an example, i.e. use of the so-called *d*-band theory.[7] In particular, the *d*-band center (ε_d) shift has been used to describe the variation of not only the electronic structure but also the binding energies of surface poisoning species and reactive intermediates on catalyst surfaces.[8, 9] In other words, a suitable down-shift of the Pd *d*-band, an effect originating from alloying with other transition metals, should play an important role in governing the kinetics and thermodynamics of adsorption and/or desorption of intermediates during small molecule (ethanol, methanol, or formic acid) oxidation. The expectation is that judicious ‘alloying’ should facilitate and hopefully improve upon the resulting catalytic reactivity. Hence, as a relatively less costly, earth-abundant, and benign metal, Cu represents a particularly promising candidate for forming Pd-M alloy-based electrocatalysts. Therefore, considerable efforts have been devoted towards experimentally preparing various types of Pd-Cu binary nanomaterials in order to improve upon overall catalytic activity.

Regarding FAOR, the main focus has been to generate porous, high surface area materials, based on either de-alloying or other methods. For instance, nanoporous PdCu alloys have been prepared by selectively de-alloying PdCuAl ternary alloys in an alkaline solution.[10] The resulting PdCu nanostructures exhibited not only greatly enhanced electrocatalytic activity for formic acid oxidation but also a far more stable active surface area and morphology, that were largely retained even after 10,000 potential cycles. In a different study, PdCu bimetallic films with 3D porous structures were generated using a modified template method coupled with a subsequent galvanic replacement reaction; these as-prepared nanostructures possessed over a 30% improvement in mass activity as compared with commercial Pd nanoparticles (NPs).[11] Xu *et al.* also examined the electrocatalytic activities of nanoporous PdCu alloys, possessing different chemical compositions.[12] According to their analysis, the $Pd_{50}Cu_{50}$ chemical composition gave rise to superior catalytic activities, i.e. roughly 4-times higher than analogous elemental Pd nanostructures, and these particular high-performance materials were also more resistant to surface poisoning as compared with either other PdCu alloys or Pd itself. Moreover, ternary Pd-Pt-Cu electrocatalyst with molar ratio of 20:1:10 has been generated via one-pot liquid-phase chemical reduction routes.[13] The interplay between three elements had been studied, which lead to conclusion that Cu dealloying phenomenon will cause surface agglomeration of Pt atoms, thus degrade the performance of such ternary electrocatalyst. Currently, the focus of relevant system is still on Pd-Cu binary nanocomposites.

In terms of MOR and EOR, PdCu has also been considered as a promising candidate. In most studies, the utilization of PdCu nanostructures mainly involves morphological variants such as monodisperse NPs,[14-16] de-alloyed nanoporous particles,[10, 17] and electrodeposited mesoporous films.[18] It is worth noting that that most of these nanostructures gave rise to significant enhancements of activity in either EOR or MOR relative to Pd nanoparticles but lagged behind in performance as compared with analogous, state-of-the-art Pt-based catalysts. Therefore, some recent studies have focused on synthesizing Pt-shell, Pd-Cu core heterostructures in order to (1) immobilize and concentrate Pt at the surface and thereby (2) reduce the amount of Pt being used so as to maximize cost-effectiveness. These unique heterostructures achieved a comparable, if not higher, activity as compared with that observed for commercial Pt NPs. For example, Wang *et al.* reported on Pt-shell PdCu-core catalysts with a MOR mass activity of 4.28 times as large as that of Pt/C catalyst itself.[19] A different group fabricated amorphous Pt@PdCu core-shell catalyst supported onto underlying carbon nanotubes for MOR.[20] In that case, the resulting structure exhibited a 2.7-fold increase in Pt mass activity as compared with state-of-the-art PtRu catalysts. As for EOR, Hu *et al.* were able to synthesize graphene-supported Pt-shell PdCu-core nanoboxes which demonstrated a 4-fold improvement over commercial Pt/C catalysts in terms of mass activities.[21] All of these reports have therefore confirmed that a Pt-shell, PdCu-core nanostructure represents a particularly promising motif for both EOR and MOR electrocatalysis.

As an equally important and related topic, alkaline fuel cells (AFCs), which utilize anion-exchange membranes and hydroxide ion-based electrolytes, have been considered as viable alternatives to PEMFCs in recent years.[22] In fact, under similar operating conditions, AFCs produce current densities comparable to that of PEMFCs.[23] Moreover, cost analysis showed that AFCs are at least competitive with PEMFCs for low power applications, such as hybrid vehicles.[23] Nonetheless, alkaline fuel cells possess numerous advantages over those of proton exchange membrane fuel cells in terms of both reaction kinetics and ohmic polarization. Specifically, in alkaline media, the reaction kinetics of both cathodic[24] and anodic[25] reactions are enhanced as compared with acidic media, and therefore, the same current density can often be obtained with lower catalyst loadings. Moreover, the less corrosive nature of an alkaline environment ensures a potentially greater longevity for these catalysts.[26] Therefore, AFCs represent a viable alternative to PEMFCs, and are competitive with their analogous, acidic media-based counterparts.

Nonetheless, there are only a few reports[21] that involve the use of Pt~PdCu core-shell structures as anodic catalysts for AFCs, specifically for either methanol oxidation or ethanol oxidation in alkaline media, despite the superb performance of these materials in analogous PEMFC configurations. More importantly, to the best of our knowledge, the effect of varying the relative Pd: Cu molar ratio upon the catalytic activity of the surface Pt layer has yet to be systematically probed in either acidic or alkaline media. Hence, we believe that such studies will be crucial in terms of providing guidance for developing more advanced, multi-purpose, and rationally chemically designed Pt-monolayer shell, Pd-M core electrocatalysts that can be used as functional components for a variety of applications.

As discussed in Chapters 1 through 3, ultrathin 1-D structures possess highly promising functional attributes for the use of these materials as electrocatalysts. With respect to additional small-molecule oxidation reactions described in this Chapter, prior literature has established precedence for the exceptional electrochemical performance metrics of elemental, binary, and ternary ultrathin nanowires, respectively. For instance, ultrathin Pd NWs possessing diameters of ~10 nm have been synthesized and successfully applied to the electro-oxidation of ascorbic acid.[27] In terms of EOR in alkaline media, tri-metallic $Au_{17}Pt_{24}Pd_{59}$ ultrathin NWs[28] gave rise to notably enhanced activity as compared with not only commercial Pd NPs but also analogous ultrathin AuPd and PtPd NWs. With respect to MOR, $PtCu_2$ nanowire networks (NWNs), composed of individual constituent wires possessing diameters of ~2 nm, have exhibited not only mass activities that are 3.77-fold higher but also specific activities that are 2.71-fold greater than the corresponding values associated with commercial Pt/C catalysts.[29] Similarly, X. Wang *et al.* has reported facile synthesis of three-dimensional (3D) Pt-Co nanowire assemblies (NWAs) consist of Pt-Co nanowires with diameter ranging from 5 to 10 nm.[30] The as-prepared nanowire assemblies outperformed analogous 3D Pt NWAs by nearly two-fold, and carbon-supported Pt NPs by three-fold, towards MOR. Moreover, in terms of our own group's efforts, we have synthesized ultrathin, ternary PtRuFe NWs for both (i) the methanol oxidation reaction (MOR) and (ii) the formic acid oxidation reaction (FAOR).[31] Specifically, we have shown that the Ru content within our wires impacts upon the methanol oxidation kinetics, whereas the amount of

Fe significantly affects the measured formic acid oxidation performance. Indeed, by carefully tailoring the relative quantities of both Ru and Fe, we could chemically induce a substantial enhancement in MOR and FAOR activities as compared with commercial standards.

As an added level of structural complexity, our group has demonstrated that by depositing a Pt monolayer onto ultrathin NWs, excellent performance enhancements can be achieved.[32] For example, after the deposition of a Pt monolayer, a volcano-type composition dependence was observed in the ORR activity values of $Pt \sim Pd_{1-x}Au_x$ NWs, as the Au content was systematically increased from 0 to 30% with the activity of the $Pt \sim Pd_9Au$ NWs (0.98 mA/cm^2, 2.54 A/mg_{Pt}), representing an optimum performance. Similar enhancements have also been noted with our analogous Pt~Pd-Ni ultrathin systems, as previously discussed in Chapter 3.

Hence, hierarchical Pt monolayer- PdM core ultrathin 1D nanostructures represent a particularly intriguing and promising structural motif, combining the favorable attributes of both chemical composition and structural morphology for demonstrating favorable activity in a host of complementary reactions.

Therefore, herein in this Dissertation, we have deliberately designed a series of (a) ultrathin ($d \sim 2$ nm) 1-D PdCu alloys with tunable chemical compositions for FAOR as well as (b) hierarchical Pt monolayer shell (ML) - PdCu core structures for MOR and EOR. To the best of our knowledge, in terms of novelty, this is the first time that one-dimensional PdCu alloys of such small sizes have been utilized in catalyzing FAOR. Furthermore, we are also the first to report the fabrication of hierarchical ultrathin Pt~PdCu nanowires with controllable chemical compositions. In particular, our resulting multi-purpose electrocatalysts exhibited not only superior activity but also improved long-term durability as compared with both control Pt NPs and Pt ultrathin NWs, in terms of MOR and EOR performance, yielding a clear example of the use of size and chemical composition to impact upon electrocatalytic activity.

4.2. Results and Discussion

4.2.1. Synthesis and Structural Characterization of a Series of $Pd_{1-x}Cu_x$ NWs with Various Chemical Compositions

We employed an ambient, surfactant-based technique to synthesize ultrathin $Pd_{1-x}Cu_x$ nanowires possessing diameters of ~2 nm. This synthetic approach has been previously used to generate ultrathin Pt,[33] Pd,[34] Pd-Au,[32] as well as Pd-Ni[35] nanowires with precise control over their chemical compositions. A detailed discussion of this protocol has been previously included in Chapter 3. Herein, Pd-Cu nanowire samples could be routinely and controllably prepared with a host of chemical compositions systematically ranging from Pd_9Cu to Pd_5Cu_5.

X-ray powder diffraction (XRD) data obtained on a series of as-prepared $Pd_{1-x}Cu_x$ nanowires (Figure 4.1) has revealed that these NWs are composed of homogeneous alloys with a face-centered cubic (*fcc*) crystal structure.

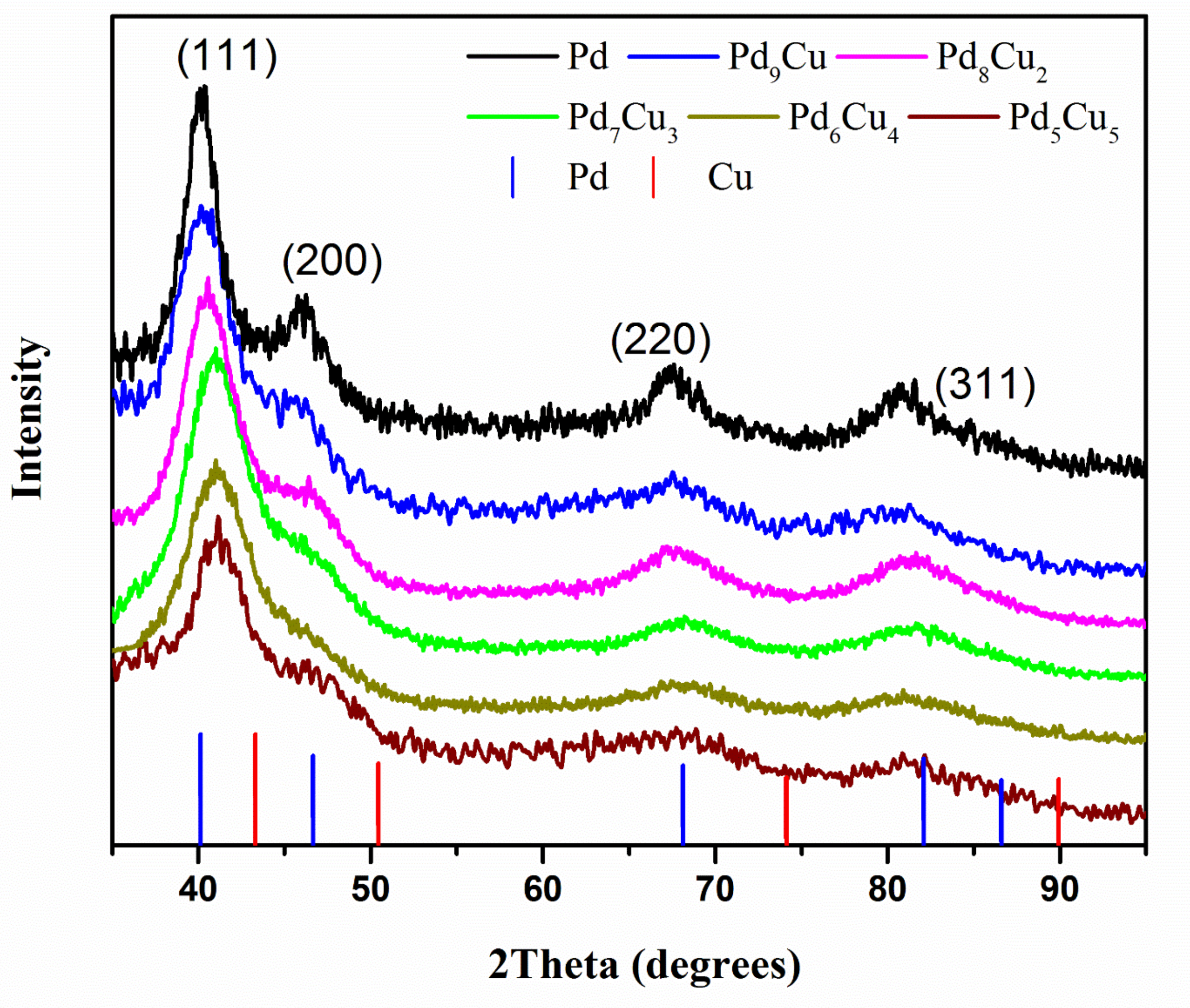

Figure 4.1. X-ray diffraction patterns of as-prepared $Pd_{1-x}Cu_x$ nanowires. The Pd content decreases from top to bottom, in the order of elemental Pd, Pd_9Cu, Pd_8Cu_2, Pd_7Cu_3, Pd_6Cu_4, and Pd_5Cu_5, respectively. The XRD patterns have been indexed to Pd (blue, JCPDS # 46-1043) and Cu (red, JCPDS # 04-0836). Database standards are shown immediately below the experimentally determined patterns.

Indeed, all of the nanowire samples possessed peaks located at 40°, 46°, 68°, and 82°, which can be ascribed to the corresponding (111), (200), (220) and (311) planes, respectively, of an underlying Pd *fcc* framework structure (JCPDS #04-0836). We did not observe any obvious peaks associated with the formation of either metallic copper or copper oxide domains, thereby suggesting the effective incorporation of Cu atoms within the *fcc* structure of Pd itself. Instead, we noted a clear shift of the peak positions of both (111) and (200) to higher angles, as the content of Cu is increased, thereby indicating a potential lattice contraction. This observation is in agreement with the fact that Cu has a smaller lattice parameter (‘a’ = 3.615 Å, JCPDS #04-0836) than that of Pd (‘a’ = 3.890 Å, JCPDS #46-1043). It is noteworthy that the positions of (220) and (311) might have undergone shifts, as well. However, the broadening effect due to the extremely small dimensions of the nanowires analyzed rendered it difficult to further verify this assumption. Similarly, due to this issue of a broadening of the peaks, calculations of exact lattice parameters based on XRD patterns tend to be difficult and imprecise. Hence, to complement these data, as discussed later, accurate lattice parameters were determined by analyzing the corresponding selective area electron diffraction (SAED) patterns.

In terms of morphologies, as shown in Figures 4.2, panel A, D, G and J, the overall structure of samples possessing ≥ 70 atom % Pd consists of discrete individual one-dimensional nanowires clustered and clumped together as part of an obviously larger three-dimensional aggregated network.

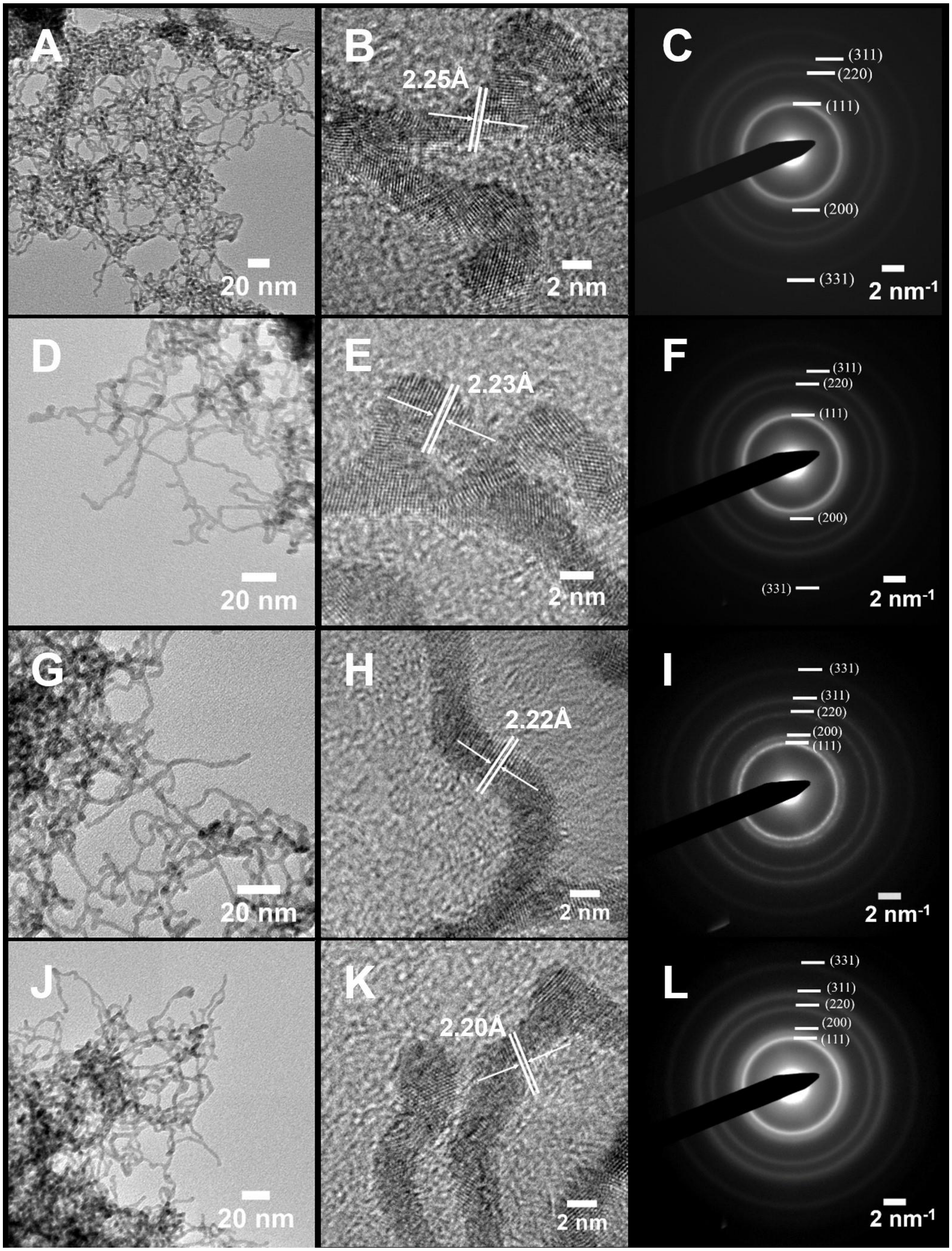

Figure 4.2. Representative TEM images (A, D, G, and J), higher-magnification HRTEM images with measured *d*-spacings (B, E, H, and K), and associated single area electron diffraction patterns (C, F, I and L) for Pd NWs (A–C), Pd_9Cu NWs (D–F), Pd_8Cu_2 NWs (G–I), and Pd_7Cu_3 NWs, respectively.

By contrast, the TEM images of Pd_6Cu_4 and Pd_5Cu_5 nanocomposites are shown in Figure 4.3, and apparently, these consist of small, interconnected nanoparticles.

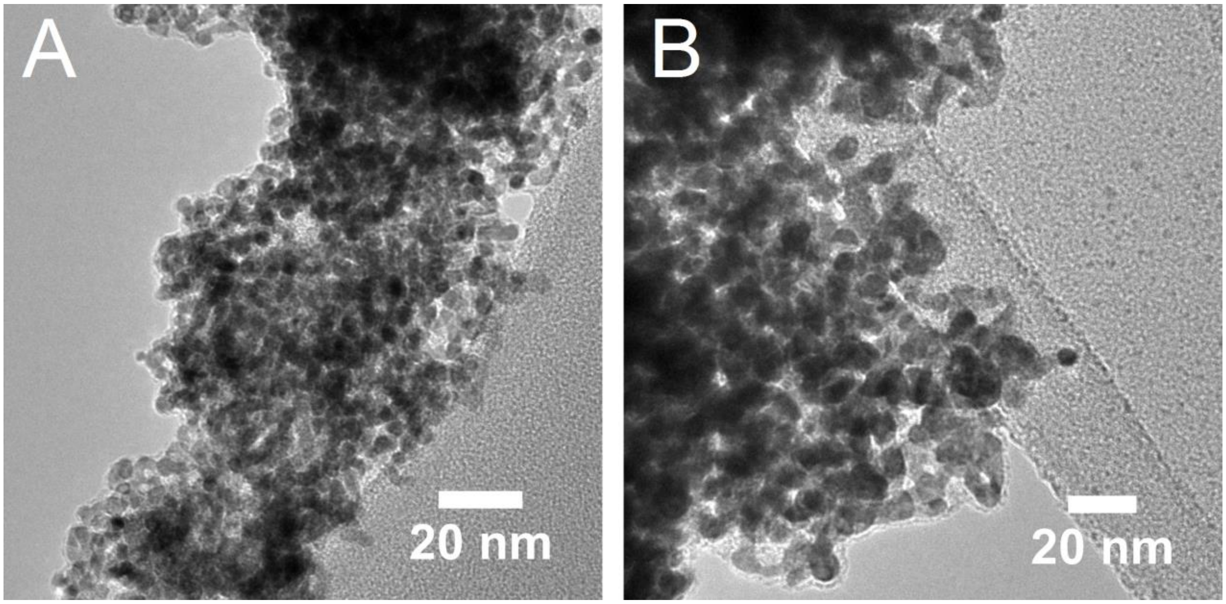

Figure 4.3. Representative TEM images of as-prepared (A) Pd_6Cu_4 and (B) Pd_5Cu_5 samples.

A similar scenario was observed with our previously reported Pd-Ni ultrathin nanowires, described in Chapter 3. In that case, we found that the synthesis reaction itself is sensitive to the presence of oxygen. Hence, by analogy with our Pd-Ni system, we can conclude that the more oxophilic atoms (i.e. Cu, in this case) present within the reaction environment, the more challenging the resulting nanowire formation happens to be.[35]

The diameters of our series of as-prepared elemental Pd, Pd_9Cu, Pd_8Cu_2, Pd_7Cu_3, Pd_6Cu_4 and Pd_5Cu_5 nanostructures, respectively, along with their actual chemical compositions as obtained through SEM-based EDAX analysis, are summarized in Table 4.1.

Precursor Metal Compositions	Morphology	Diameter (nm)	Actual Chemical Composition (Pd: Cu, molar ratio)	Standard Deviation of the chemical compositions	Electrochemical Surface Area (ECSA, m^2/g)
Pd	Wires	2.9 ± 0.4	Pd (pure)	N/A	72.2
Pd_9Cu	Wires	2.5 ± 0.3	$Pd_{0.93}Cu_{0.07}$	0.004	70.1
Pd_8Cu_2	Wires	2.3 ± 0.3	$Pd_{0.85}Cu_{0.15}$	0.016	62.3
Pd_7Cu_3	Wires	2.6 ± 0.6	$Pd_{0.76}Cu_{0.24}$	0.034	55.9
Pd_6Cu_4	Particles	2.1 ± 0.5	N/A[a]	N/A	N/A
Pd_5Cu_5	Particles	2.1 ± 0.3	N/A	N/A	N/A

Table 4.1. Summary of morphology, diameters, and actual chemical compositions, as determined by SEM-based EDAX analysis, of as-prepared Pd-Cu nanowires possessing various Pd:Cu molar ratios.

[a] Chemical compositions of Pd_6Ni_4 and Pd_5Ni_5 were not examined, due to their particulate morphology and hence, lack of applicability for our electrochemical tests.

The relatively small deviation in both the diameter and the atomic composition observed corroborates the idea of a high degree of desired uniformity and regularity within these as-prepared nanowires in terms of both morphology and chemical composition.

Nonetheless, the SAED patterns for all of the chemical compositions tested are ring-like, and are therefore consistent with the overall polycrystallinity of our as-prepared nanostructures. Yet, the lattice planes clearly highlighted within the representative Figure 4.2 (i.e. panels B, E, H, and K) suggest that our nanowires actually consist of single crystalline constituent sub-units. In addition, the SAED patterns correlate well with the face-centered cubic structure, from which we were able to compute the lattice parameters of Pd, Pd_9Cu, Pd_8Cu_2, and Pd_7Cu_3 to be 3.892 Å, 3.867 Å, 3.853 Å, and 3.820 Å, respectively. Based on our complementary EDAX results, the actual compositions of the entire nanowire series were determined to be Pd, $Pd_{93}Cu_7$, $Pd_{85}Cu_{15}$, and $Pd_{76}Cu_{24}$, which correlate well with lattice parameters of 3.890 Å, 3.871 Å, 3.849 Å, and 3.824Å, respectively. Hence, these two sets of data are consistent, and further corroborate the expected chemical compositions of our series of as-prepared $Pd_{1-x}Cu_x$ nanowires.

In the following sections, we focus on electrochemical measurements associated with Pd, Pd_9Cu, Pd_8Cu_2, and Pd_7Cu_3 ultrathin nanowires as well as with hierarchical Pt~Pd, Pt~Pd_9Cu, Pt~Pd_8Cu_2, and Pt~Pd_7Cu_3 1D structures. Our objective therefore herein has been to examine and correlate the composition-dependent electrochemical activities of these nanomaterials with respect to FAOR, MOR, and EOR, respectively.

4.2.2. Electrochemical performance of a series of alloyed $Pd_{1-x}Cu_x$ nanowires

Representative cyclic voltammograms (CVs) and the corresponding CO stripping linear-sweep voltammograms (LSVs) of our as-prepared, carbon-supported $Pd_{1-x}Cu_x$ are depicted in Figure 4.4A and 4.4B, respectively.

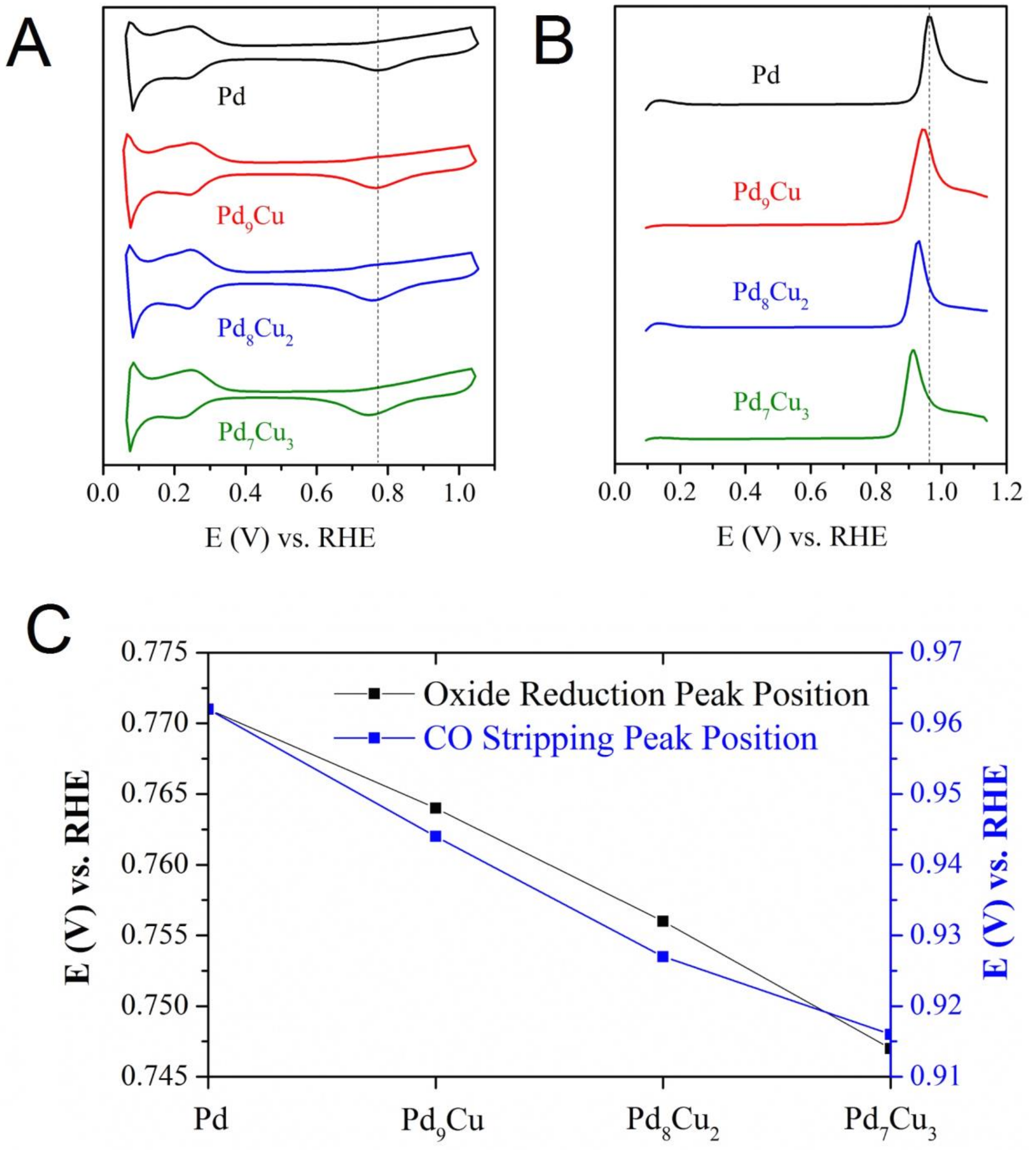

Figure 4.4. (A) Representative CV curves of Pd NWs, Pd_9Cu NWs, Pd_8Cu_2 NWs, and Pd_7Cu_3 NWs, respectively. (B) Representative CO stripping LSV curves for Pd NWs, Pd_9Cu NWs, Pd_8Cu_2 NWs, and Pd_7Cu_3 NWs, respectively. Both the CVs and LSVs were obtained in an argon-saturated 0.1 M $HClO_4$ solution, at a scan rate of 20 mV s^{-1}. (C) A plot describing the trend in the surface oxide reduction peak potential (black) and the corresponding CO stripping peak potential (blue) as a function of systematically varying chemical composition from elemental Pd NWs to Pd_7Cu_3 NWs.

We have observed that the positions of both the oxide reduction peak and the CO stripping peak followed the same trend, as the Cu content was varied. Specifically, the larger the Cu concentration, the lower the apparent peak positions were detected. This downshift in the surface oxide reduction peak suggests a strengthening of the interaction with the oxygen adsorbate, and this assertion has been previously postulated by other groups with Pd-Cu binary systems.[10] Chemically speaking, the greater the Cu incorporation, the more oxophilic the surface becomes. As a result, the CO stripping peak tends to be found at a lower potential, due to the facilitation of oxidation by the presence of surface oxide species, a scenario which is more likely to occur with structures possessing a higher overall Cu content. In the meantime, we also think it could be caused by the weakened CO adsorption strength due to the presence of another metal Cu, as described in a recent theoretical study.[36]

In addition, CO stripping profiles had been utilized to determine the electrochemical surface area of all the relevant composites, i.e., carbon supported ultrathin Pd, Pd_9Cu, Pd_8Cu_2 and Pd_7Cu_3. Indeed, by obtaining the actual amount of binary metal catalyst in each electrochemical experiment, the ESCA can be calculated using the following Equation 4.4.

$$ESCA = \frac{Q}{m \times 420} \tag{4.4}$$

where Q is the charge of the CO desorption-electrooxidation in micro-coulomb (μC), 'm' stands for the total amount of metal catalyst (both Pd and Cu) on the electrode, and 420 is the charge required to oxidize a monolayer of CO on the catalyst in $\mu C \cdot cm^{-2}$. The ECSA values calculated for all these four compositions are summarized in Table 4.1.

The as-collected FAOR curves, the peak potential activities, as well as the corresponding chronoamperometry (CA) measurements are shown in Figure 4.5.

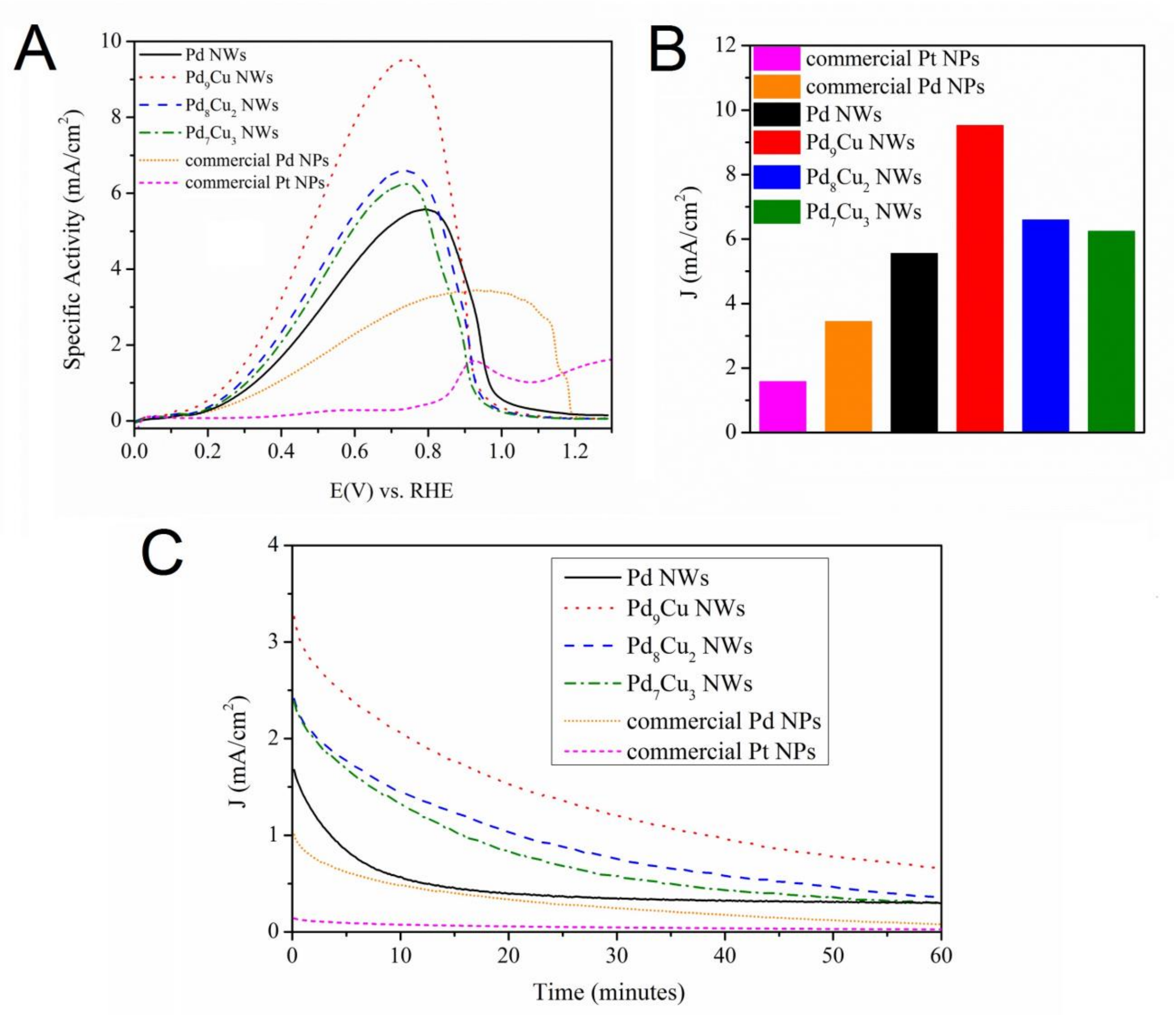

Figure 4.5. (A) Cyclic voltammograms for the formic acid oxidation reaction in an argon-saturated 0.1 M $HClO_4$ + 0.5 M HCOOH solution, obtained at a scan rate of 20 mV s^{-1} with the current normalized to ECSA. (B) Bar graph highlighting FAOR activity at respective FAOR peak potential values for commercial Pt NPs, commercial Pd NPs, Pd NWs, Pd_9Cu NWs, Pd_8Cu_2 NWs, and Pd_7Cu_3 NWs, respectively. (C) Chronoamperometry measurements of commercial Pt NPs, commercial Pd NPs, Pd NWs, Pd_9Cu NWs, Pd_8Cu_2 NWs, and Pd_7Cu_3 NWs in an argon-saturated 0.1 $HClO_4$ + 0.5 M HCOOH solution, obtained at a potential of 0.4 V vs. RHE for a period of 60 min.

According to these results, we observed a "volcano"-type relationship between the FAOR performance and the corresponding chemical compositions. Indeed, the highest activity was achieved with Pd_9Cu nanowires, wherein a value (at peak potential) of 9.52 mA/cm^2 was measured, which is almost twice as high as that of analogous ultrathin Pd NWs (i.e. 5.55 mA/cm^2) and nearly 3-fold greater than that of commercial Pd nanoparticles (i.e. 3.44 mA/cm^2). In addition, we found that the Pd_9Cu nanowires maintained the most favorable long-term stability as well, according to the chronoamperometry measurements presented in Figure 4.5C. Moreover, we note that the activity of commercial Pt nanoparticles is only 1.56 mA/cm^2, which is substantially less as compared to what has been measured for the Pd-containing samples.

We expect this unsurprising difference, because Pt and Pd-based catalysts follow intrinsically different reaction mechanisms. In the past, it has been reported that the FAOR mechanism catalyzed by Pd electrocatalysts is governed by both a "direct" pathway in which the active intermediate species, HCOOH*, is generated as well as a more traditional "indirect" pathway in which CO is produced as an intermediate.[8, 37] By contrast, the Pt catalyst tends to adhere to the "indirect" pathway only. The reaction mechanisms for both pathways are highlighted in Equations 4.5 to 4.8.

Direct Pathway: $HCOOH + M \rightarrow \text{active intermediate} \rightarrow M + CO_2 + 2H^+ + 2e^-$ (4.5)

Indirect Pathway: $HCOOH + M \rightarrow M\text{-}CO + H_2O$ (4.6)

$M + H_2O \rightarrow M\text{-}OH + H^+ + e^-$ (4.7)

$M\text{-}CO + M\text{-}OH \rightarrow 2M + CO_2 + H^+ + e^-$ (4.8)

(M = surface atom, either Pt or Pd)

Conventionally, the "direct" pathway occurs at a lower potential (i.e. 0.1 – 0.6 V vs. RHE), whereas the "indirect pathway" occurs at a higher potential (i.e. greater than 0.8 V vs. RHE). Typically, with either Pd or Pd-alloy surfaces, these two mechanistic pathways coexist. In our case, for our elemental ultrathin Pd NWs and $Pd_{1-x}Cu_x$ NWs, our onset potentials were well below 0.2 V. In addition, for all of these NWs analyzed, we recorded peak potentials at around 0.7 V, with a small "shoulder" feature at ~0.9 V. These data are indicative of a typical "dual-pathway" mechanism, as is reported in the literature.[10, 38] For commercial Pd NPs, however, despite their low onset potential, the peak potential was situated at ~0.9 V, without any apparent shoulder feature. This observation is usually understood as a consequence of the presence of a 'dual-pathway' governing the behavior of Pd, with the "indirect" pathway in the role of the more dominant component.[8] As implied earlier, the commercial Pt nanoparticles primarily pursue the "indirect" pathway.

However, in recent years, the presence of CO-free, "direct" pathway became debatable. Previous studies employing highly sensitive EC-ATR-SEIRAS measurement on Pd black and Pd/C catalysts have reported the accumulation of CO species at open circuit potential during the injection of formic acid even with its gas phase content below 1 ppm.[39, 40] In other words, although CO can be only further oxidized at higher potentials, the formation of CO was conformed either from dehydration of formic acid or from the reduction of CO_2 at relatively low oxidation potentials. Herein, our focus is not necessarily on whether CO has been formed within the reaction, but rather on the distinct electrochemical profile between $Pd_{1-x}Cu_x$ series and Pt/C catalyst. We tend to assert that the reaction mechanism of $Pd_{1-x}Cu_x$ series is different than that of Pt/C. Although more detailed, spectroscopic studies are needed in the future to further unveil the pathway and presumably the actual intermediate that is generated.

As previously noted as well, prior research on the utilization of porous Pd-Cu nanoparticles as FAOR electrocatalysts deduced the "optimum composition" to be $Pd_{50}Cu_{50}$. By contrast, we find herein that the $Pd_{1-x}Cu_x$ NW electrocatalysts yielded the best performance when 'x' = 0.1, i.e. a composition of Pd_9Cu. While ostensibly these observations appear to be conflicting, several plausible explanations are worth mentioning. *First*, it is known that Pd atoms undergo a degree of surface segregation within alloyed PdCu binary systems, thereby possibly resulting in a substantial discrepancy between surface composition and bulk composition.[41, 42]

Second, the degree of Pd surface enrichment and hence, the corresponding surface structure are highly dependent upon the surface strain, which is known to be very different for spherical (i.e. isotropic) nanoparticles versus asymmetric (i.e. anisotropic) nanowires. These ‘structural considerations’ also helped to explain the nature of comparable ORR activities between Pd-Ni ultrathin nanowires versus analogous nanoparticles, possessing very different chemical compositions.[35] Hence, it is likely that herein the surface layers of previously reported $Pd_{50}Cu_{50}$ nanoparticles and of our as-prepared Pd_9Cu nanowires maintain equivalent localized chemical compositions at their surfaces, and therefore, a very similar “active site” configuration, thereby resulting in the favorable FAOR activities, experimentally recorded for both systems.

Third, even though DFT calculations on a model Pd (111) plane[37] have supported the idea that a “dual” pathway is the origin of the enhanced FAOR activity of Pd electrocatalysts, to date, no group has convincingly isolated the proposed ‘intermediate’ species. Hence, given the fact that our system actually consists of ultrathin anisotropic wires, it is plausible to assume that the reaction kinetics for actual experimental electrocatalysts are inherently more complex and that therefore, our observations herein are reasonable.

Moreover, we have also examined the corresponding EOR and MOR activities of our as-processed $Pd_{1-x}Cu_x$ series, and these data are highlighted in Figure 4.6.

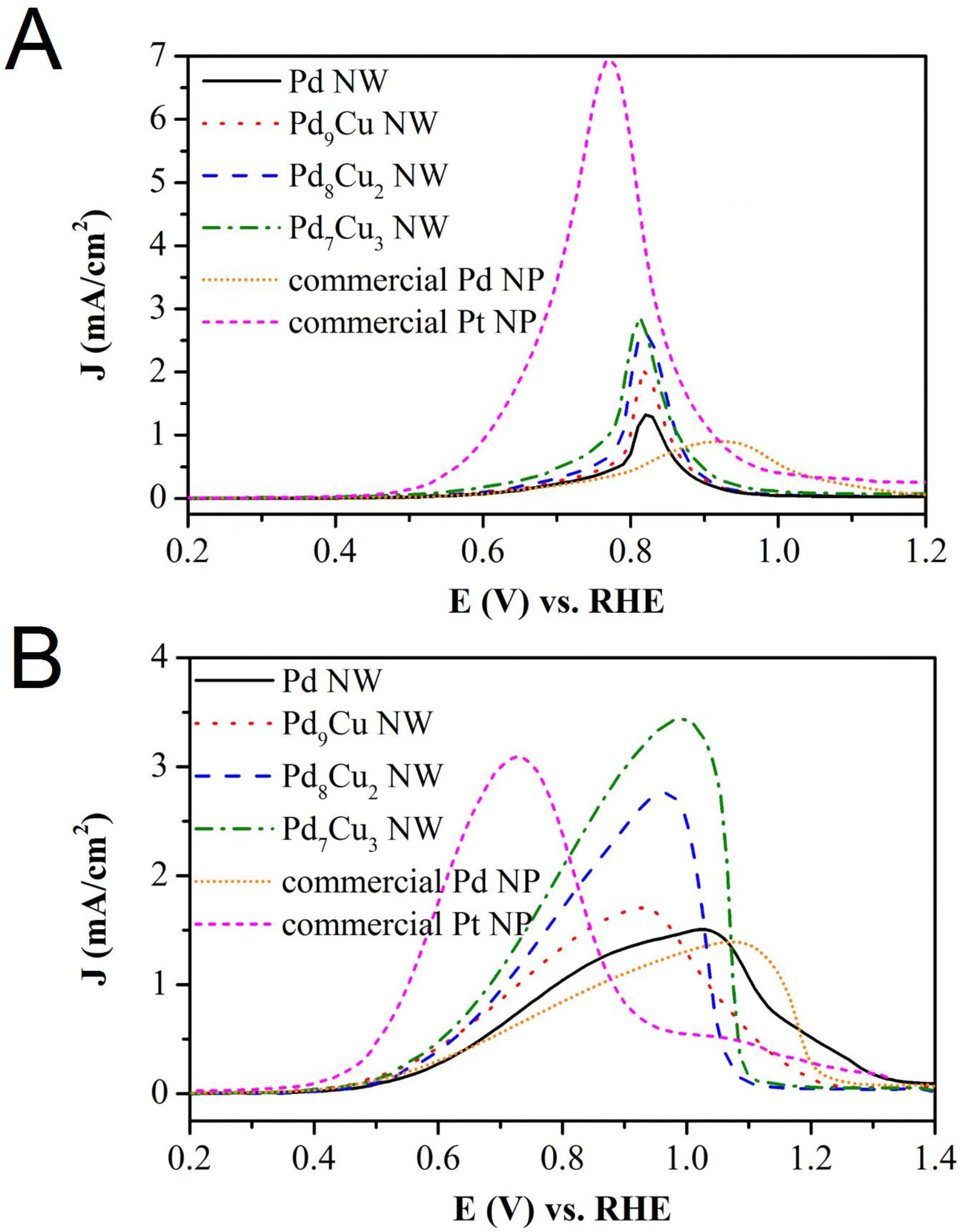

Figure 4.6. (A) Cyclic voltammograms for the methanol oxidation reaction in an argon-saturated 1 M NaOH + 1 M CH_3OH solution, obtained at a scan rate of 20 mV s^{-1} with the current normalized to the electrochemically determined surface area. (B) Cyclic voltammograms for the ethanol oxidation reaction in an argon-saturated 1 M NaOH + 1 M CH_3CH_2OH solution, obtained at a scan rate of 20 mV s^{-1} with the current normalized to the electrochemically deduced surface area.

According to these MOR results, the values of our measured catalytic activities increased with increasing amounts of Cu content. This finding is expected, since we have demonstrated previously that with rising Cu molar ratios, the CO stripping peak potential correspondingly decreased. In other words, the ability to oxidize CO, which is the intermediate species in MOR, improved as more Cu was incorporated within the nanowire structure. Furthermore, our EOR results followed a similar trend in excellent agreement with prior observations on an analogous, complementary ultrathin PdCu nanowire system.[43] Nonetheless, in our own work, we noticed that the onset regions for our $Pd_{1-x}Cu_x$ series for EOR (i.e. 0.5 V) and MOR (i.e. 0.6 V) are significantly higher than that of Pt itself with corresponding values 0.4 V and 0.5 V, respectively. Our MOR and EOR data nevertheless reinforce the effectiveness of the use of $Pd_{1-x}Cu_x$ systems (without any Pt content whatsoever) in alkaline media.

What we have sought to convincingly demonstrate as an added advance and improvement over all prior literature is a reproducible and verifiable enhancement in EOR and MOR activity for Pd-based materials. In essence, our goal has been to achieve performance comparable to Pt itself for our ultrathin alloyed wires. Our strategy has therefore been to use the minimum of Pt possible by generating hierarchical one-dimensional nanostructures, characterized by an atom-thick Pt monolayer and a central Pd-Cu core, and correspondingly examining the catalytic performance of these materials for various small-molecule oxidations, including EOR and MOR.

4.2.3. Electrochemical performance of a series of Pt~$Pd_{1-x}Cu_x$

According to Figures 4.5A and 4.5B in the previous section, commercial Pt yielded a much higher onset potential as well as a greater peak potential value for FAOR as compared with Pd. We explain this difference as originating from the aforementioned mechanistic differences characterizing Pd-based (i.e. dual pathways) versus Pt-based (i.e. indirect pathway) catalysts, which has been previously observed and investigated by others. Hence, it is not anticipated that adding in a Pt monolayer should result in a marked improvement over the inherently higher activity of Pd-based alloys for FAOR. Therefore, we focus primarily on describing and explaining the dramatically better MOR and EOR performance for the Pt~$Pd_{1-x}Cu_x$ series relative to that of Pt itself.

The Pt monolayer deposition process was conducted using a relatively straightforward approach, i.e. Cu underpotential deposition (UPD), which we have previously demonstrated to (1) generate an atomic layer of Pt on the surfaces of nanomaterials and to (2) potentially maximize Pt utilization.[44, 45] In addition, it had been shown by both DFT calculations as well as experimental results that the existence of a Pt monolayer can give rise to a largely improved activity for alcohol oxidation reactions for both single crystal samples as well as spherical nanoparticles.[46-48] Therefore, we have been interested in systematically examining the electrochemical performance of 1D ultrathin nanostructures, which possess an atom-thick Pt monolayer shell as well as a $Pd_{1-x}Cu_x$ core, towards both MOR and EOR.

First, in terms of electrochemical measurements that reveal external surface profile, representative CVs and CO stripping LSVs are shown in Figures 4.7A and 4.7B.

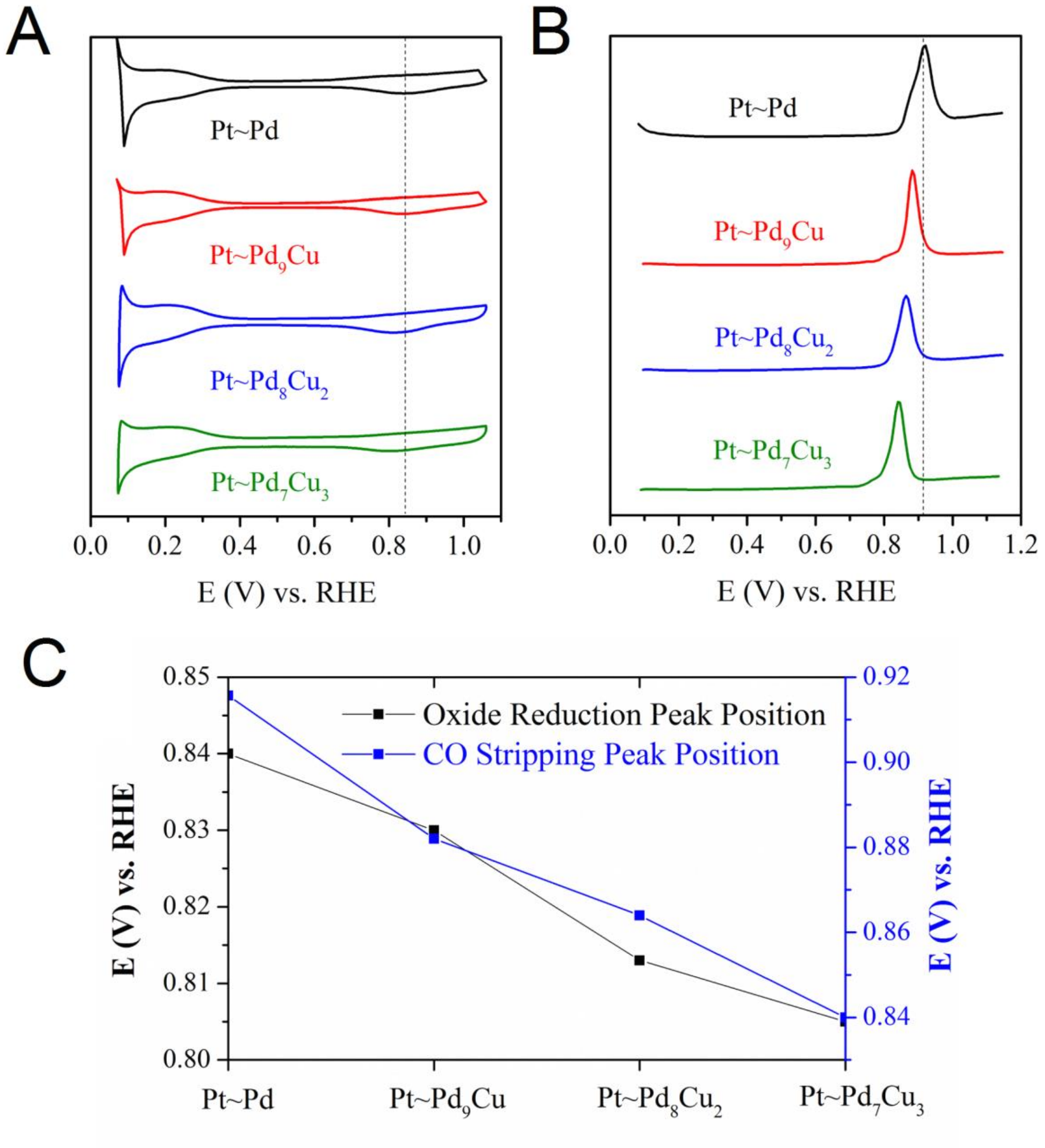

Figure 4.7. (A) Representative CV curves of Pt~Pd NWs, Pt~Pd$_9$Cu NWs, Pt~Pd$_8$Cu$_2$ NWs, and Pt~Pd$_7$Cu$_3$ NWs, respectively. (B) Representative CO stripping LSV curves for Pt~Pd NWs, Pt~Pd$_9$Cu NWs, Pt~Pd$_8$Cu$_2$ NWs, and Pt~Pd$_7$Cu$_3$ NWs, respectively. Both the CVs and LSVs were acquired in an argon-saturated 0.1 M HClO$_4$ solution, at a scan rate of 20 mV s^{-1}. (C) A plot investigating the trend in the surface oxide reduction peak potential (black) and the corresponding CO stripping peak potential (black) as a function of systematically varying chemical composition from elemental Pt~Pd NWs to Pt~Pd$_7$Cu$_3$ NWs.

Herein, we have observed a similar correlation and trend between (1) the positions of not only the oxide reduction peaks but also the CO stripping peaks and (2) the corresponding chemical compositions of the series of Pt~$Pd_{1-x}Cu_x$ nanowires, analogous to what had been previously noted with the series of unmodified $Pd_{1-x}Cu_x$ nanowires. In other words, we found that the higher the Cu content, the lower the corresponding potential at which the oxide reduction peak was situated. Such observations likely arise from a "ligand" effect in which the Cu within the core interacted with the overlying surface Pt atoms, thereby rendering the overall surface structure more oxophilic. Moreover, the positions of the CO stripping peaks followed an identical trend as the ability to oxidize CO correspondingly improved, in a very similar manner to what we had previously noted with our series of $Pd_{1-x}Cu_x$ nanowires.

Second, we probed the effect of the Pt monolayer itself by directly comparing the MOR and EOR curves of Pt~Pd nanowires with those of bare Pd nanowires. In essence, after Pt monolayer deposition, the MOR and EOR kinetics were significantly enhanced, as highlighted in Figures 4.8A and 4.8B.

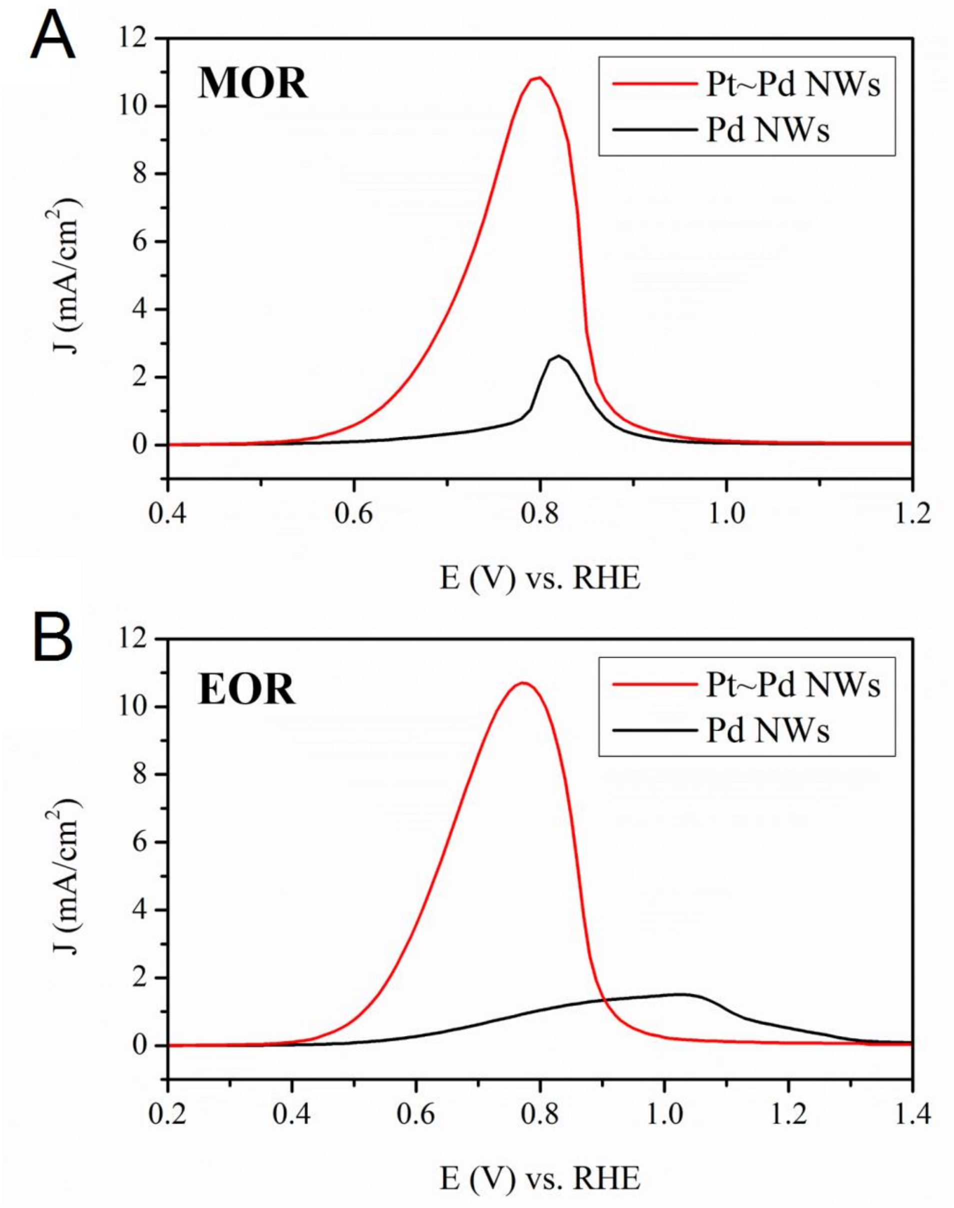

Figure 4.8. (A) Cyclic voltammograms of Pd NWs both before and after Pt monolayer deposition for the methanol oxidation reaction (MOR) in an argon-saturated 1 M NaOH + 1 M CH_3OH solution, obtained at a scan rate of 20 mV s^{-1}. (B) Cyclic voltammograms of Pd NWs both before and after Pt monolayer deposition for the ethanol oxidation reaction (EOR) in an argon-saturated 1 M NaOH + 1 M CH_3CH_2OH solution, obtained at a scan rate of 20 mV s^{-1}.

Specifically, we noted that ultrathin Pt~Pd nanowires possessed (1) a peak activity of over 5-fold greater and (2) an onset potential that was nearly 0.2 V lower than that of Pd nanowires alone for both reactions, thereby implying clearly superior reaction kinetics.

Third, in Figures 4.9 and 4.10, we examined our entire as-prepared series of Pt~$Pd_{1-x}Cu_x$ nanowires, in terms of both MOR and EOR performance, respectively.

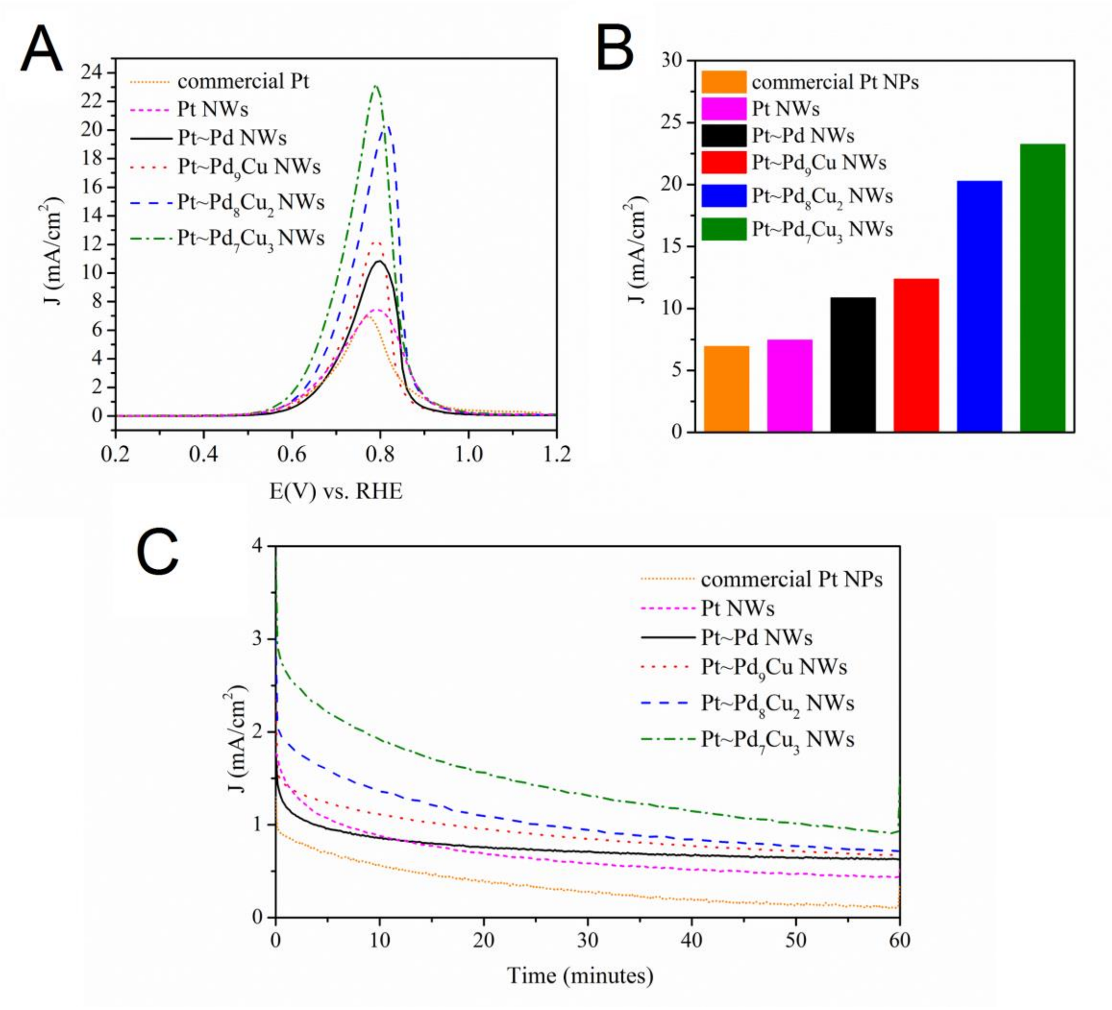

Figure 4.9. (A) Cyclic voltammograms for MOR in an argon-saturated 1 M CH_3OH + 1 M NaOH solution, obtained at a scan rate of 20 mV s^{-1} with the current normalized to ECSA. (B) Bar graph highlighting MOR activity at respective MOR peak potentials for commercial Pt NPs, ultrathin Pt NWs, Pt~Pd NWs, Pt~Pd_9Cu NWs, Pt~Pd_8Cu_2 NWs, and Pt~Pd_7Cu_3 NWs, respectively. (C) Chronoamperometry measurements of commercial Pt NPs, ultrathin Pt NWs, Pt~Pd NWs, Pt~Pd_9Cu NWs, Pt~Pd_8Cu_2 NWs, and Pt~Pd_7Cu_3 NWs in an argon-saturated 1 M CH_3OH + 1 M NaOH solution, obtained at a potential of 0.65 V vs. RHE for a period of 60 min.

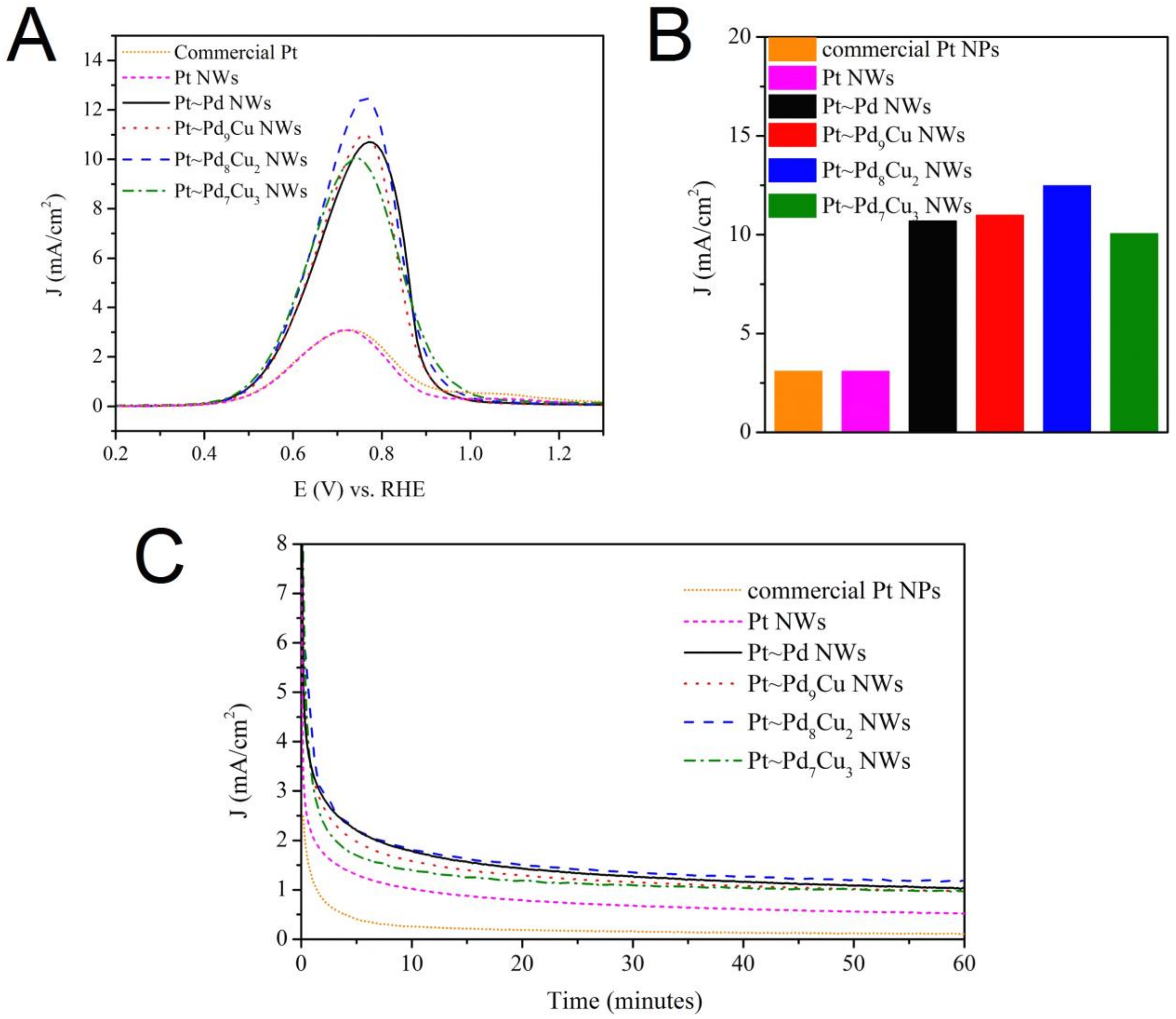

Figure 4.10. (A) Cyclic voltammograms for EOR in an argon-saturated 1 M CH_3CH_2OH + 1 M NaOH solution, obtained at a scan rate of 20 mV s^{-1} with the current normalized to ECSA. (B) Bar graph highlighting EOR activity at respective EOR peak potentials for commercial Pt NPs, ultrathin Pt NWs, Pt~Pd NWs, Pt~Pd$_9$Cu NWs, Pt~Pd$_8$Cu$_2$ NWs, and Pt~Pd$_7$Cu$_3$ NWs, respectively. (C) Chronoamperometry measurements associated with commercial Pt NPs, ultrathin Pt NWs, Pt~Pd NWs, Pt~Pd$_9$Cu NWs, Pt~Pd$_8$Cu$_2$ NWs, and Pt~Pd$_7$Cu$_3$ NWs in an argon-saturated 1 M CH_3CH_2OH + 1 M NaOH solution, obtained at a potential of 0.65 V vs. RHE for a period of 60 min.

Specifically, after Pt deposition, the "optimal" chemical composition for MOR was deduced to be Pt~Pd$_7$Cu$_3$ (Figure 4.9B), which is in excellent agreement with CO stripping results, as carbon monoxide is the intermediate species for MOR on Pt sites. Furthermore, Pt~Pd_7Cu_3 exhibited a surface area activity of 23.2 mA/cm^2, which is over 3-fold higher than that of commercial Pt NPs (i.e. 6.94 mA/cm^2) and analogous Pt ultrathin nanowires (i.e. 7.45 mA/cm^2). The corresponding CA measurements further supported our finding that Pt~Pd_7Cu_3 out-performed all of the other chemical compositions tested by possessing not only the highest peak potential activity but also the best long-term stability measured.

In terms of EOR activity, all of the Pt~$Pd_{1-x}Cu_x$ nanowires yielded a notable and routine enhancement over the corresponding data for commercial control samples, consisting of Pt NPs and Pt NWs. Overall, the series of Pt~$Pd_{1-x}Cu_x$ nanowires gave rise to a specific activity of roughly 10~12 mA/cm^2, which is over 3-fold higher than that of reported values for commercial Pt NPs and Pt NWs. Nevertheless, the variation in activity amongst these four different compositions is relatively subtle and within statistical error, so that we have not been able to conclusively determine that either one or more of these chemical compositions is necessarily better than all of the others in terms of EOR activity.

Interestingly, we found that the ultrathin Pt nanowires (~2 nm in diameter) and ultra-small commercial Pt NPs (~5 nm in size) tested possessed similar EOR curves (Figure 4.10B). Such observations have led us to postulate that for EOR conducted in an alkaline medium, chemical composition as opposed to considerations based on either electronic structure or size-induced strain effects are vital to governing the resulting electrochemical behavior in this very small size regime. In other words, the anisotropic wire-like morphology of the Pt-based electrocatalysts should yield only a limited impact upon the resulting EOR kinetics. These conclusions stand in contrast with a prior report in which it had been observed that larger Pt single-crystalline nanowires (*d* ~ 20 nm) possessed a ~2-fold EOR activity enhancement over Pt black (pore sizes of several microns) in alkaline media.[49] However, our assertions are nonetheless consistent with results indicating that ultra-small Pt nanoparticles (diameter < 5 nm) supported on carbon black and graphene appeared to give rise to similar EOR activities in KOH, despite the lower *d*-band center of Pt within these carbon black-based composites,[50, 51] an issue which had resulted in differential ORR behaviors.[52]

4.3. Conclusions

In the context of exploring one-dimensional Pd alloys as well as corresponding Pt@Pd-alloy core-shell heterostructures in terms of their potential applications as electrocatalysts in PEMFCs, we have utilized an ambient, surfactant-based synthetic means to prepare ultrathin Pd-Cu-based nanostructures with a high dimensional uniformity, a homogeneous distribution of elements, and a tunable series of chemical compositions. The corresponding electrochemical performances of these carbon-supported $Pd_{1-x}Cu_x$ as well as of the corresponding series of coated Pt_{ML}-$Pd_{1-x}Cu_x$ nanowires have been examined.

Specifically, for FAOR, we have shown that (i) the overall activities of the entire series of our as-prepared $Pd_{1-x}Cu_x$ nanowires tested were superior to that of Pd and that (ii) in part because of the low onset potentials measured. Moreover, our FAOR results as well as our CO stripping measurements confirms that the optimal composition for FAOR does not necessarily have to be the one that necessarily yields the best CO oxidation kinetics, denoting a piece of evidence supporting a “direct”, CO-free pathway in governing our system. However, more careful spectroscopic study is required to further validate such assertion.

As for MOR and EOR, both catalytic reactions benefit significantly from the deposition of Pt monolayer onto the surfaces of our series of ultrathin $Pd_{1-x}Cu_x$ nanowires. Specifically, the ‘best’ chemical composition for MOR was shown to be Pt~Pd_7Cu_3, a finding which is in excellent agreement with corresponding CO stripping experiments. The EOR kinetics of our Pd-based systems were significantly better than all of the previous data on commercial Pt NPs and Pt NWs, and in fact, activity values were rather similar across the entire Pt~$Pd_{1-x}Cu_x$ series. We ascribe this observation to the insensitivity of the overall reaction mechanism to either subtle electronic or strain effects. In effect, it is likely that the exposure of active surface active sites as well as the nature of the catalytic chemical composition itself designate more significant contributors to the overall EOR performance.

4.4. References

1. Holton, O. T.; Stevenson, J. W. *Platin Met Rev* **2013,** 57, (4), 259-271.
2. Antolini, E. *Energ Environ Sci* **2009,** 2, (9), 915-931.
3. Liu, H. S.; Song, C. J.; Zhang, L.; Zhang, J. J.; Wang, H. J.; Wilkinson, D. P. *J Power Sources* **2006,** 155, (2), 95-110.
4. Brouzgou, A.; Song, S. Q.; Tsiakaras, P. *Appl Catal B-Environ* **2012,** 127, 371-388.
5. Antolini, E.; Salgado, J. R. C.; Gonzalez, E. R. *Appl Catal B-Environ* **2006,** 63, (1-2), 137-149.
6. Demirci, U. B. *J Power Sources* **2007,** 173, (1), 11-18.
7. Bligaard, T.; Norskov, J. K. *Electrochim Acta* **2007,** 52, (18), 5512-5516.
8. Jiang, K.; Zhang, H. X.; Zou, S. Z.; Cai, W. B. *Phys Chem Chem Phys* **2014,** 16, (38), 20360-20376.
9. Hammer, B.; Norskov, J. K. *Adv Catal* **2000,** 45, 71-129.
10. Xu, C. X.; Liu, A. H.; Qiu, H. J.; Liu, Y. Q. *Electrochem Commun* **2011,** 13, (8), 766-769.
11. Ojani, R.; Abkar, Z.; Hasheminejad, E.; Raoof, J. B. *Int J Hydrogen Energ* **2014,** 39, (15), 7788-7797.
12. Xu, C. X.; Liu, Y. Q.; Wang, J. P.; Geng, H. R.; Qiu, H. J. *J Power Sources* **2012,** 199, 124-131.
13. Jiang, K.; Cai, W.-B. *Applied Catalysis B: Environmental* **2014,** 147, 185-192.
14. Yin, J.; Shan, S. Y.; Ng, M. S.; Yang, L. F.; Mott, D.; Fang, W. Q.; Kang, N.; Luo, J.; Zhong, C. J. *Langmuir* **2013,** 29, (29), 9249-9258.
15. Hu, C. G.; Zhai, X. Q.; Zhao, Y.; Bian, K.; Zhang, J.; Qu, L. T.; Zhang, H. M.; Luo, H. X. *Nanoscale* **2014,** 6, (5), 2768-2775.
16. Dong, Q.; Zhao, Y.; Han, X.; Wang, Y.; Liu, M. C.; Li, Y. *Int J Hydrogen Energ* **2014,** 39, (27), 14669-14679.
17. Shih, Z. Y.; Wang, C. W.; Xu, G. B.; Chang, H. T. *J Mater Chem A* **2013,** 1, (15), 4773-4778.
18. Hsieh, M. W.; Whang, T. J. *Appl Surf Sci* **2013,** 270, 252-259.
19. Wang, R. F.; Zhang, Z.; Wang, H.; Lei, Z. Q. *Electrochem Commun* **2009,** 11, (5), 1089-1091.
20. Wang, H.; Ji, S.; Wang, W.; Wang, R. F. *S Afr J Chem-S-Afr T* **2013,** 66, 17-20.
21. Hu, C. G.; Cheng, H. H.; Zhao, Y.; Hu, Y.; Liu, Y.; Dai, L. M.; Qu, L. T. *Adv Mater* **2012,** 24, (40), 5493-5498.
22. Antolini, E.; Gonzalez, E. R. *J Power Sources* **2010,** 195, (11), 3431-3450.
23. McLean, G. F.; Niet, T.; Prince-Richard, S.; Djilali, N. *Int J Hydrogen Energ* **2002,** 27, (5), 507-526.
24. Ramaswamy, N.; Mukerjee, S. *Advances in Physical Chemistry* **2012,** 2012, 17.
25. Lai, S. C. S.; Koper, M. T. M. *Phys Chem Chem Phys* **2009,** 11, (44), 10446-10456.
26. Kimble, M. C.; White, R. E. *J Electrochem Soc* **1991,** 138, (11), 3370-3382.
27. Wen, D.; Guo, S. J.; Dong, S. J.; Wang, E. K. *Biosens Bioelectron* **2010,** 26, (3), 1056-1061.
28. Zhu, C. Z.; Guo, S. J.; Dong, S. J. *J Mater Chem* **2012,** 22, (30), 14851-14855.
29. Xiao, M. L.; Li, S. T.; Zhao, X.; Zhu, J. B.; Yin, M.; Liu, C. P.; Xing, W. *Chemcatchem* **2014,** 6, (10), 2825-2831.

30. Xia, B. Y.; Wu, H. B.; Li, N.; Yan, Y.; Lou, X. W.; Wang, X. *Angewandte Chemie International Edition* **2015,** 54, (12), 3797-3801.
31. Scofield, M. E.; Koenigsmann, C.; Wang, L.; Liu, H. Q.; Wong, S. S. *Energ Environ Sci* **2015,** 8, (1), 350-363.
32. Koenigsmann, C.; Sutter, E.; Adzic, R. R.; Wong, S. S. *J Phys Chem C* **2012,** 116, (29), 15297-15306.
33. Koenigsmann, C.; Zhou, W. P.; Adzic, R. R.; Sutter, E.; Wong, S. S. *Nano Lett* **2010,** 10, (8), 2806-2811.
34. Koenigsmann, C.; Santulli, A. C.; Gong, K. P.; Vukmirovic, M. B.; Zhou, W. P.; Sutter, E.; Wong, S. S.; Adzic, R. R. *J Am Chem Soc* **2011,** 133, (25), 9783-9795.
35. Liu, H. Q.; Koenigsmann, C.; Adzic, R. R.; Wong, S. S. *Acs Catal* **2014,** 4, (8), 2544-2555.
36. Yu, Y.; Lim, K. H.; Wang, J. Y.; Wang, X. *The Journal of Physical Chemistry C* **2012,** 116, (5), 3851-3856.
37. Wang, Y. Y.; Qi, Y. Y.; Zhang, D. J. *Comput Theor Chem* **2014,** 1049, 51-54.
38. Mazumder, V.; Sun, S. H. *J Am Chem Soc* **2009,** 131, (13), 4588-+.
39. Zhang, H.-X.; Wang, S.-H.; Jiang, K.; André, T.; Cai, W.-B. *J Power Sources* **2012,** 199, 165-169.
40. Jiang, K.; Xu, K.; Zou, S.; Cai, W.-B. *J Am Chem Soc* **2014,** 136, (13), 4861-4864.
41. Wang, L.; Zhai, J. J.; Jiang, K.; Wang, J. Q.; Cai, W. B. *Int J Hydrogen Energ* **2015,** 40, (4), 1726-1734.
42. Noakes, T. C. Q.; Bailey, P.; Laroze, S.; Bloxham, L. H.; Raval, R.; Baddeley, C. J. *Surf Interface Anal* **2000,** 30, (1), 81-84.
43. Zhao, X.; Zhang, J.; Wang, L. J.; Liu, Z. L.; Chen, W. *J Mater Chem A* **2014,** 2, (48), 20933-20938.
44. Adzic, R. R.; Zhang, J.; Sasaki, K.; Vukmirovic, M. B.; Shao, M.; Wang, J. X.; Nilekar, A. U.; Mavrikakis, M.; Valerio, J. A.; Uribe, F. *Top Catal* **2007,** 46, (3-4), 249-262.
45. Adzic, R. *Electrocatalysis-Us* **2012,** 3, (3-4), 163-169.
46. Zhang, Y.; Hsieh, Y. C.; Volkov, V.; Su, D.; An, W.; Si, R.; Zhu, Y. M.; Liu, P.; Wang, J. X.; Adzic, R. R. *Acs Catal* **2014,** 4, (3), 738-742.
47. Li, M.; Liu, P.; Adzic, R. R. *J Phys Chem Lett* **2012,** 3, (23), 3480-3485.
48. Kang, Y. J.; Qi, L.; Li, M.; Diaz, R. E.; Su, D.; Adzic, R. R.; Stach, E.; Li, J.; Murray, C. B. *Acs Nano* **2012,** 6, (3), 2818-2825.
49. Hong, W.; Wang, J.; Wang, E. *Nano Res.* **2015**, 1-9.
50. Cuong, N. T.; Fujiwara, A.; Mitani, T.; Chi, D. H. *Comp Mater Sci* **2008,** 44, (1), 163-166.
51. Kim, G.; Jhi, S. H. *Acs Nano* **2011,** 5, (2), 805-810.
52. Zhou, X. J.; Qiao, J. L.; Yang, L.; Zhang, J. J. *Adv Energy Mater* **2014,** 4, (8).

Chapter 5: In situ Probing of the Active Site Geometry of Ultrathin Nanowires for the Oxygen Reduction Reaction

5.1. Introduction

As discussed in Chapters 1 through 4, our group has been probing the effect of systematic variations in size as well as chemical composition in various types of Pt-based 1-D catalysts.[1-5] In terms of trends, we noted that as the nanowire diameter decreases, the corresponding ORR performance increases dramatically, presumably due to lattice contraction of surface atoms originating from surface strain effects.[6, 7] Moreover, our group examined the composition and size-dependent performance in $Pd_{1-x}Au_x$ nanowires (NWs) encapsulated with a conformal Pt monolayer shell (Pt~$Pd_{1-x}Au_x$). We noted a volcano-type composition-dependence in the ORR activity of ultrathin Pt~$Pd_{1-x}Au_x$ NWs as the Au content was increased from 0 to 30% with the activity of the Pt~Pd_9Au NWs (i.e. 0.98 mA/cm^2, 2.54 A/mg$_{Pt}$, measured at 0.9 V vs. RHE), representing the optimum performance.[3] Although significant enhancements in ORR activity were observed as a function of NW composition, the precise origin of the enhanced performance as a function of NW composition and size remains unclear, since these variables can yield complex and often unforeseen effects on the electronic and structural properties of the analyzed nanostructures and the corresponding catalytic performance.

As a logical extension of that prior finding, in this Chapter, we probe the intimate physical and electronic structure of these 'optimized' Pt~$Pd_{1-x}Au_x$ core-shell type nanostructures used as the starting point with the objective of deducing the nature of the accompanying catalytic interface therein. Synchrotron X-ray absorption spectroscopy (XAS)-based techniques represent an exciting platform with which to examine the nature of the electronic properties and bonding of 1D catalysts under standard operating electrochemical conditions.[8-11] Extended X-ray absorption fine structure (EXAFS) spectroscopy is known to be as valuable if not superior to other conventional structural analysis techniques, such as TEM or XRD, for obtaining relevant structural information for small, catalytically relevant particles of less than 5 nm.[12-17] Indeed, by analyzing the EXAFS spectrum of each metal within the context of either binary or ternary metallic nanomaterials, information about local structural parameters (i.e. metal-metal coordination number, bond length, and the extent of disorder) can be obtained.[12, 18-25] By tuning the X-ray energy to the absorbing edge of each metal, the local environment surrounding atoms of each resonant element can be separately analyzed and compared. For instance, EXAFS has been utilized in not only verifying chemical composition but also probing the detailed formation mechanism of ultrathin Pd-Au alloy nanowires, fabricated through galvanic displacement.[26]

Therefore, the novelty and significance of this current study is that we have not only utilized EXAFS to (i) compare and (ii) differentiate amongst different plausible structural models (i.e. the presence of islands, partial monolayers, or localized alloys) of our as-synthesized Pt~Pd_9Au ultrathin core-shell nanowires under *in situ* electrochemical conditions but also corroborated these data with the net results of well-designed DFT-based computational models. Therefore, the judicious combination and subsequent correlation of data from both experimental and theoretical studies has revealed for the first time that the catalytically active structure of our ternary nanowires can actually be ascribed to PtAu~Pd possessing a PtAu outer binary shell and a pure inner Pd core. Moreover, we have plausibly attributed the resulting structure to a specific synthesis step, namely the Cu underpotential deposition (UPD) followed by galvanic replacement with Pt. Hence, it is likely that the fundamental insights gained into the performance of our 1-D electrocatalysts using these complementary tools will likely guide future research in terms of defining new directions for substantially improving upon durability and stability.

5.2. Results and Discussion

5.2.1. Theoretical calculations

DFT calculations were performed to determine the distribution of Au in our NWs. It is known[27] that Au-metal alloy systems appear to undergo some level of Au surface segregation. This phenomenon is even more apparent and noticeable when either (a) the metal content or particle size is increased or when (b) the temperature is elevated.[28] In our DFT calculations, we first mapped out the adsorption preference of a single Au atom on a Pd NW (Figure 5.1).

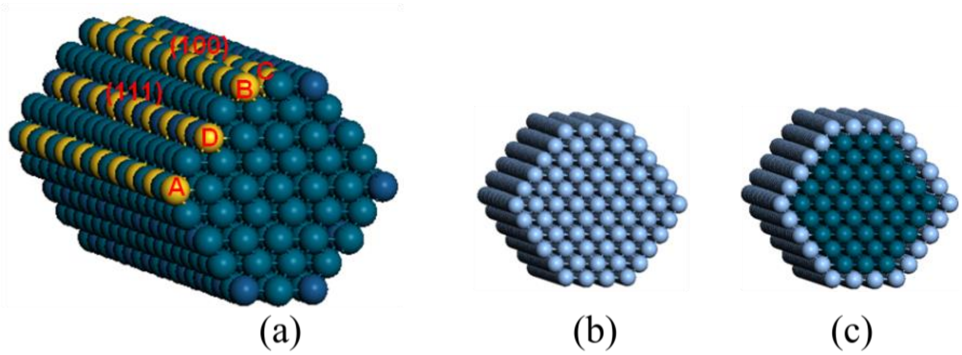

Figure 5.1. (a) Single Au atom sitting at various sites of a Pd NW. A: Edge (111)/(111); B: Edge (111)/(100); C: Terrace (100); D: Terrace (111); (b) Pt NW; and (c) Pd@Pt NW.

Similar to the case of nanoparticles,[29, 30] a decreasing sequence was observed: edge (111) / (111) (A, 0.00 eV/atom, Figure 5.1) > edge (111) / (100) (B, 0.02 eV/atom) > Terrace (100) (C, 0.05 eV/atom) > Terrace (111) (D, 0.09 eV/atom). That is, the more active the Pd on the NW surface, the more energetically favorable it is to be replaced by Au. Moreover, we also noticed that adsorption of oxygen species during the ORR could induce either a surface restructuring or reconstruction process in Pt core-shell nanoparticles, which favored surface segregation of oxophilic core elements;[31] yet for an PtAu system, at least up to 0.25 ML of O was required in vacuum to allow for the segregation of Pt back to the shell.[32]

Accordingly, for a PdAu@Pt NW, we simulated three possible variations in structural configurations in order to obtain details concerning Au distribution within these ultrathin NWs, as shown in Figure 5.2.

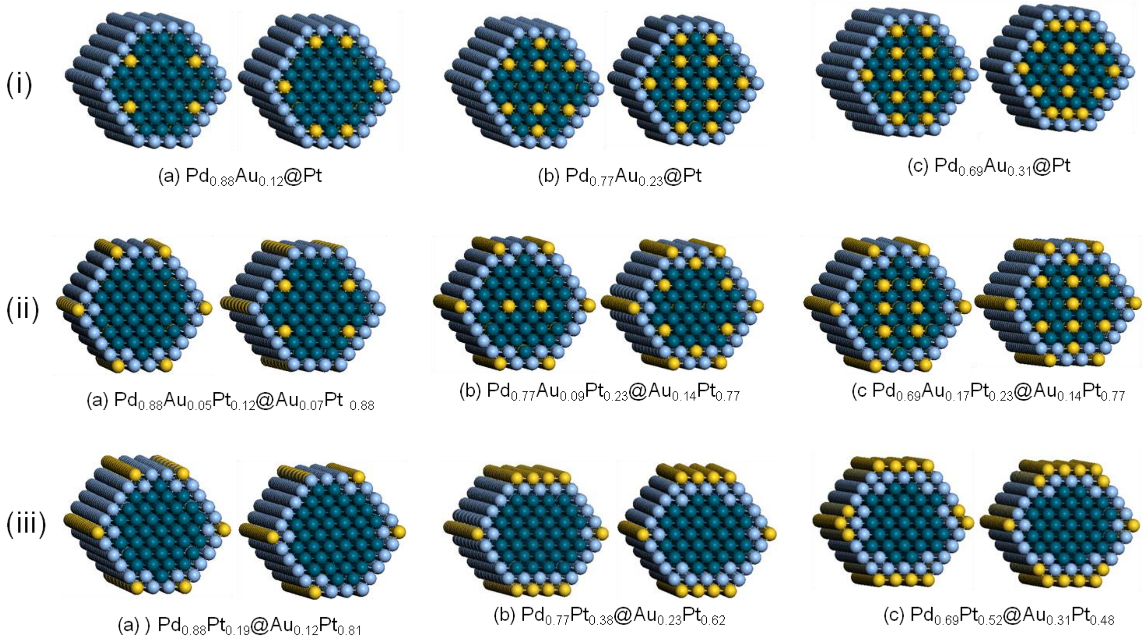

Figure 5.2. Hexagonal 2.2-nm-diameter $[(111)_4,(200)_2]$ nanowire models with various Au distributions. (a) Pd_9Au@Pt NWs, (b) Pd_8Au_2@Pt NWs, and (c) Pd_7Au_3@Pt NWs. Upper panel: (i) $Pd_{(1-x)}Au_x$@Pt NWs; Middle panel: (ii) $Pd_{(1-x)}Au_{(x-y)}Pt_z$@$Au_yPt_{(1-z)}$ NWs; Lower panel: (iii) $Pd_{(1-x)}Pt_z$@$Au_xPt_{(1-z)}$ NWs (see text). For clarity, eight supercells along the axis and bases at both ends were displayed.

These three models includes: (i) $Pd_{(1-x)}Au_x$@Pt NWs with all Au atoms staying within the core; (ii) $Pd_{(1-x)}Au_{(x-y)}Pt_z$@$Au_yPt_{(1-z)}$ NWs with a portion of Au atoms segregated to the edge of the Pt shell; and (iii) $Pd_{(1-x)}Pt_z$@$Au_xPt_{(1-z)}$ NWs with all Au atoms segregated to the Pt shell. Herein, (x, y) and z denote the mole ratios of Au/(Au+Pd) and Pt, respectively. $Pd_{(1-x)}Au_x$@Pt was used to model the as-prepared sample, while $Pd_{(1-x)}Au_{(x-y)}Pt_z$@$Au_yPt_{(1-z)}$ and $Pd_{(1-x)}Pt_z$@$Au_xPt_{(1-z)}$ were included in consideration of either partial or full segregation of Au to the shell during the ORR. We arranged Au atoms symmetrically in a way such that Au preferentially replaced the active Pd sites on the surface as demonstrated above, but avoided the formation of Au-Au bonds within the core, according to experiment (Figure 5.2).[3, 5] Such an arrangement was aimed at lowering the total energy of each type of NWs, while making the calculated BE-O comparable among three types of NWs.

It is noteworthy that we will consider the surface Pt as the only active sites for our system. Essentially, due to the filled d-band, Au is inactive towards the ORR.[33] As a matter of fact, it had been demonstrated that Au surfaces would not adsorb oxygen in the relevant potential window for ORR (~0.7-1.0V vs. RHE) in acidic media.[34] Therefore, the segregated Au atoms are largely non-active for ORR, but are rather spectators when it comes to the actual catalysis.

Figure 5.3 highlights the calculated E_{Form} for all NWs studied.

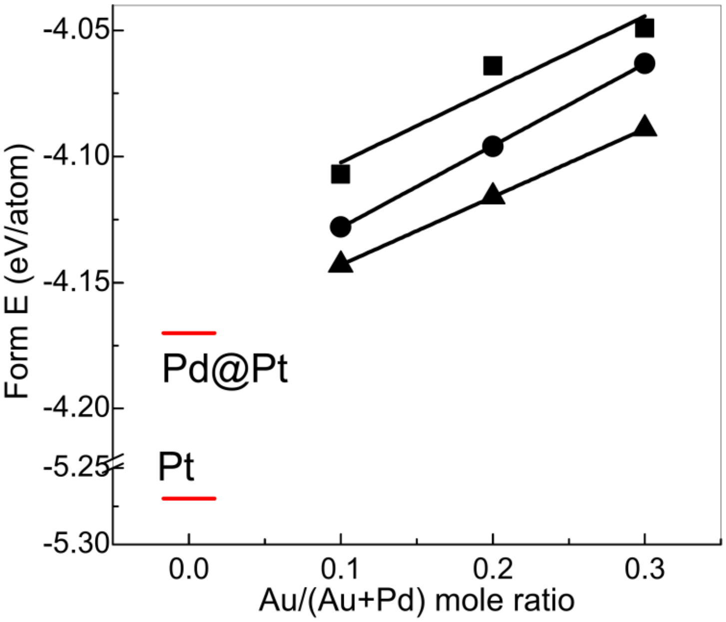

Figure 5.3. Formation energy of 2.2-nm-diameter NWs as a function of varying Au chemical compositions, as shown in Figure 2. Square: (i) $Pd_{(1-x)}Au_x$@Pt; Dot: (ii) $Pd_{(1-x)}Au_{(x-y)}Pt_z$@$Au_yPt_{(1-z)}$; Triangle: (iii) $Pd_{(1-x)}Pt_z$@$Au_xPt_{(1-z)}$. By means of comparison, pure Pt NWs and Pd@Pt NWs were also included.

When the chemical composition was kept constant, one can see that the as-prepared sample, i.e. $Pd_{(1-x)}Au_x@Pt$ NWs, is the least stable, but that the stability can be gradually increased by either partial, i.e. $Pd_{(1-x)}Au_{(x-y)}Pt_z@Au_yPt_{(1-z)}$, or full, i.e. $Pd_{(1-x)}Pt_z@Au_xPt_{(1-z)}$, segregation of Au to the shell. That is, Au within the core prefers to segregate to the shell and occupy both the active edge sites as well as the (100) terrace sites. This is in line with the strong tendency of Au atoms to segregate in the host of most metals.[35, 36] When varying the composition, the stability of alloy NWs in term of E_{Form} decreases with increasing Au. The maximum of E_{Form} is observed for pure Pt NWs (E_{Form} = -5.27 eV/atom) followed by Pd@Pt (E_{Form} = -4.17 eV/atom), while that associated with Pd@AuPt is -4.14, -4.12, and -4.09 eV/atom, corresponding to Au/(Au+Pd) ratios of 0.1, 0.2, and 0.3, respectively.

At the temperature for the ORR (i.e. below 100°C), the thermal stability of NWs is less critical than their electrochemical stability, because metal catalysts can be oxidized and dissolved into electrolyte. Since Au (1.52 V) possesses a higher reduction potential than both Pt (1.19 V) and Pd (0.92 V), alloying Au into NW structures is expected to contribute to their resistance to oxidation, though their thermal stability can be slightly compromised. This finding agrees well with the experimental observations that Au-alloyed NWs demonstrated a greatly improved electrochemical stability as compared with Pd@Pt NWs.[3, 5, 37]

To scale the ORR activity, BE-O values were calculated and plotted in Figure 5.4.

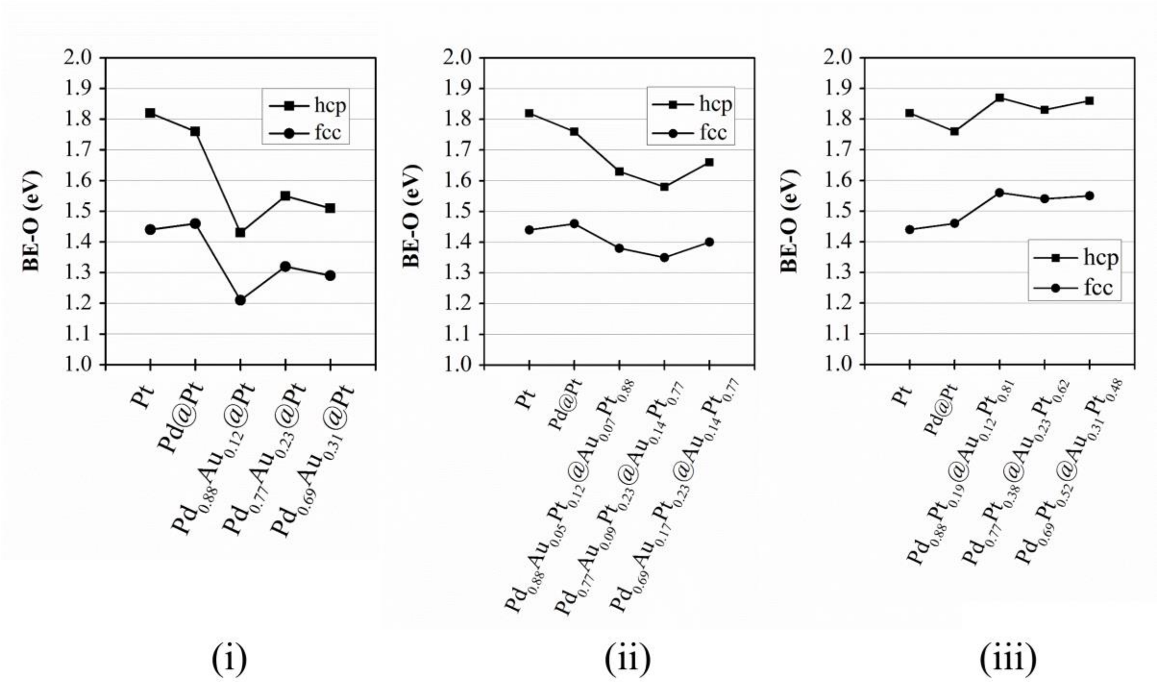

Figure 5.4. Calculated O-binding energy values at 3-fold hollow sites on Pt(111) terraces. (i) $Pd_{(1-x)}Au_x@Pt$ NWs, (ii) $Pd_{(1-x)}Au_{(x-y)}Pt_z@Au_yPt_{(1-z)}$ NWs, and (iii) $Pd_{(1-x)}Pt_z@Au_xPt_{(1-z)}$ NWs.

According to the previous study,[38] the removal of oxygen-containing species via either protonation or the formation of *O, *OH, or *O_2 was found to slow down the ORR on Pt, depending on the precise experimental conditions. Therefore, it is reasonable to assume that a higher BE-O (more positive) should lead to a weaker interaction between Pt atoms and oxygen-containing species, thereby ensuring a greater overall ORR performance.[39, 40] Of course, an excessive weakening of O-binding will hinder the ORR, wherein the adsorption of oxygen-containing species becomes problematic. One can see that Pd@Pt NWs (BE-O = 1.46 eV at the *fc*c site and 1.76 eV at the *hcp* site) can bind oxygen more weakly than Pt NWs (BE-O = 1.44 eV at the *fcc* site and 1.82 eV at the *hcp* site). The effect of adding Au on BE-O depends on the spatial distribution of Au, while BE-O is not necessarily sensitive to variation in the amount of Au.

In the case of Au with an Au/(Au+Pd) ratio of 0.12 for instance, the BE-O for Pd@Pt is decreased by 0.2 ~ 0.3 eV when adding Au into the Pd core (Figure 5.4, panel i), while it is decreased by 0.1 ~ 0.2 eV (Figure 5.4, panel ii) and increased by 0.1 ~ 0.2 eV (Figure 5.4, panel iii) by partial and full segregation of these Au atoms from the core to the shell, respectively. By comparison, we note that the corresponding variation in BE-O values for AuPd@Pt NWs as a function of the Au/(Au+Pd) ratio is smaller (within 0.1 eV), when the same spatial distribution of Au is analyzed.

The variation trend in BE-O correlates well with the surface strain before oxygen adsorption, $S_{Pt\text{-}Pt} = [d_{Pt\text{-}Pt}(NW)/d_{Pt\text{-}Pt}(Pt\ bulk) - 1] \times 100$ (Figure 5.5).

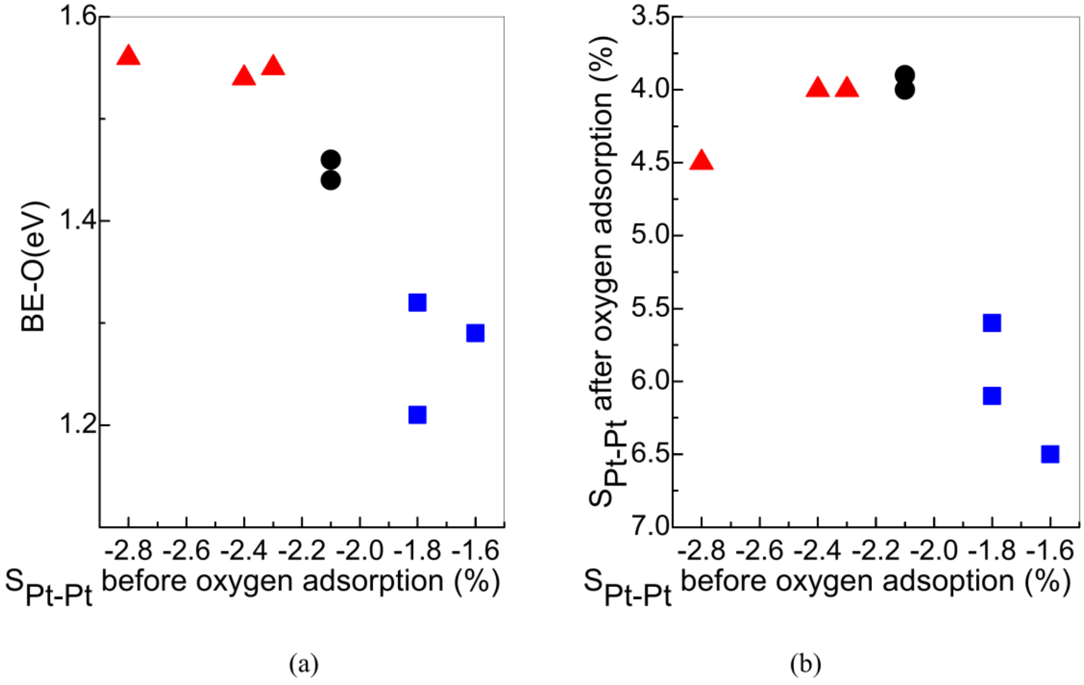

Figure 5.5. (a) Calculated O-binding energy as a function of surface strain ($S_{Pt\text{-}Pt}$, only Pt-Pt bond length of the Pt triangle where O is bound was taken into account); (b) Surface strain ($S_{Pt\text{-}Pt}$) after O-binding as a function of surface contraction before O-binding; dot: Pt and Pd@Pt NWs; square: $Pd_{(1-x)}Au_x$@Pt NWs; triangle: $Pd_{(1-x)}Pt_z$@$Au_xPt_{(1-z)}$ NWs.

Herein, only the active (111) terrace of either the Pt shell or the Pt(111) shell was considered. The lattice constants used herein for Pt, Pd, and Au, respectively, are 3.924 Å, 3.890 Å and 4.080 Å. As compared with Pt bulk, the formation of NWs introduces significant surface contraction on the Pt(111) shell (i.e. $S_{Pt\text{-}Pt}$ = -2.2 %, displayed as dots in Figure 5.5a). Due to the similar lattice between Pt and Pd, using Pd as the core only leads to small changes in the surface strain and therefore, the BE-O value. Adding Au into the core, thereby forming a PdAu alloy, diminishes the perturbative effect of contraction, and therefore, BE-O is lowered (square, Figure 5.5a), in agreement with a previous study.[41] In principle, the more Au is added into the core, the lower the surface strain will be, and therefore, the more strongly the oxygen will be bound. The caveat is that at high Au concentrations, the nanowire surface not only adopts a tensile strain but also can be fully covered by Au sites due to the segregation, all of which can potentially inhibit ORR activity.

With all Au segregated into the shell, the Pt(111) shell becomes more contracted as compared with Pt NWs, i.e. from 0.1% to 0.6% with increasing amounts of Au (triangles, Figure 5.5a). However, the corresponding BE-O therefore stays more or less around 1.55 eV. This value is associated with the local structural flexibility of NWs. The variation in the BE-O values as a function of $S_{Pt\text{-}Pt}$ prior to oxygen adsorption (Figure 5.5a) can be compared and correlated with that of $S_{Pt\text{-}Pt}$ after oxygen adsorption as a function of $S_{Pt\text{-}Pt}$ before oxygen adsorption (Figure 5.5b). For $Pd_{(1-x)}Au_x$@Pt NWs, the relatively small contraction in the Pt(111) shell promotes surface flexibility. With increasing amounts of Au in the core, the adsorption of oxygen can introduce additional surface distortion. It has been demonstrated that lowering the degree of contraction on the neighboring Pt can perceptibly introduce tensile strain with $S_{Pt\text{-}Pt}$ values, ranging from 5.5% to 6.5%. As a result, the Pt-O interaction is strengthened (Figure 5.5a). By contrast, for $Pd_{(1-x)}Pt_z$@$Au_xPt_{(1-z)}$ NWs, the strong degree of contraction renders the NW more rigid. Hence, the response to oxygen adsorption is much less ($S_{Pt-Pt} < 4.6\%$, Figure 5.5b) and the variation in S_{Pt-Pt} with the amount of Au in the shell is less significant. As a result, BE-O is more positive and is not sensitive to the amount of Au in the shell (Figure 5.5a).

Our results indicate that the distribution of Au plays an important role in tuning the surface strain of AuPd@Pt NWs and therefore of BE-O. In particular, the segregation of Au to the shell implies two specific consequences: (1) it is able to stabilize the NWs (Figure 5.3), and (2) it increases the rigidity of the NW, which prevents the structural distortion upon oxygen adsorption and thereby weakens the binding energy (Figure 5.4).

The importance of structural rigidity in influencing the observed oxygen binding energy has been highlighted in our previous theoretical analysis of ORR on Pt@Pd nanoparticles, possessing a tetrahedral shape.[42] Specifically, we determined in that prior work that for nanostructures with a relatively significant surface contraction, i.e. such as the ~2.3% noted for the PdAu@Pt NWs studied herein, the presence of oxygen adsorption can thereby lead to a more significant distortion of the localized structure of the (111) facet as compared with the corresponding (111) bulk surface. That is, nanostructures are intrinsically more flexible in their local structure as compared with bulk surfaces. This surface distortion which accommodates for the adsorption of oxygen can thereby lead to an increased binding energy of oxygen. It is noteworthy that the correlation between the metal *d*-band structure before adsorption and the oxygen binding energy, which is often used to explain the trend in binding energy on metal surfaces, does not necessarily apply for such nanostructures, since the resulting *d*-band structure of distorted metal sites at the nanoscale limit can be very different after oxygen adsorption. Hence, the rigidity of the local structure plays a more important role. That is, for the same kind of adsorption site, the more flexible the structure is, the more easily the interacted metal atoms can distort upon adsorption, all of which can thereby lead to a stronger oxygen binding. Indeed, only when the NW adopts the conformation of $Pd_{(1-x)}Pt_Z@Au_xPt_{(1-z)}$ does the BE-O of AuPd@Pt NW become weaker than that of Pd@Pt (Figure 5.5(iii)). Therefore, a higher ORR activity is expected. However, the degree of weakening is small, and hence, it is difficult to draw any clear and unequivocal conclusions that would correlate exactly with the experimentally measured ORR activity values, obtained by simply examining the trends in BE-O.[3, 5, 37]

Considering the gap between the BE-O and the ORR activity, we have taken on the additional step of estimating the mass and specific ORR activity values, based on the calculated BE-Os. Considering that the promotion of ORR activity on Pt was predicted by weakening the Pt-O bond,[38] we have estimated the mass activity as $\Delta A_M \propto \exp(-0.5*BE\text{-}O/k_bT)*N_{Pt}(111)/N_{Pt}(total)$, wherein $N_{Pt}(total)$ and $N_{Pt}(111)$ represents the number of Pt atoms in the NWs and on the (111) terrace, respectively. The charge transfer coefficient was chosen as "0.5" on the basis of previous experimental and theoretical studies.[43, 44] The specific activity was estimated as $\Delta A_S \propto \exp(-0.5*BE\text{-}O/k_bT)*N_{Pt}(111)/N_{Pt}(shell)$, wherein $N_{Pt}(shell)$ represents the number of Pt atoms in the shell of the NR. The edge and (100) terrace sites, which account for 38% of total Pt surface sites, were assumed to be inactive and not involved in the ORR process.

Figure 5.6 plots the variation of relative activity at T = 20°C, i.e. mass activity and specific activity, with respect to Pt NWs.

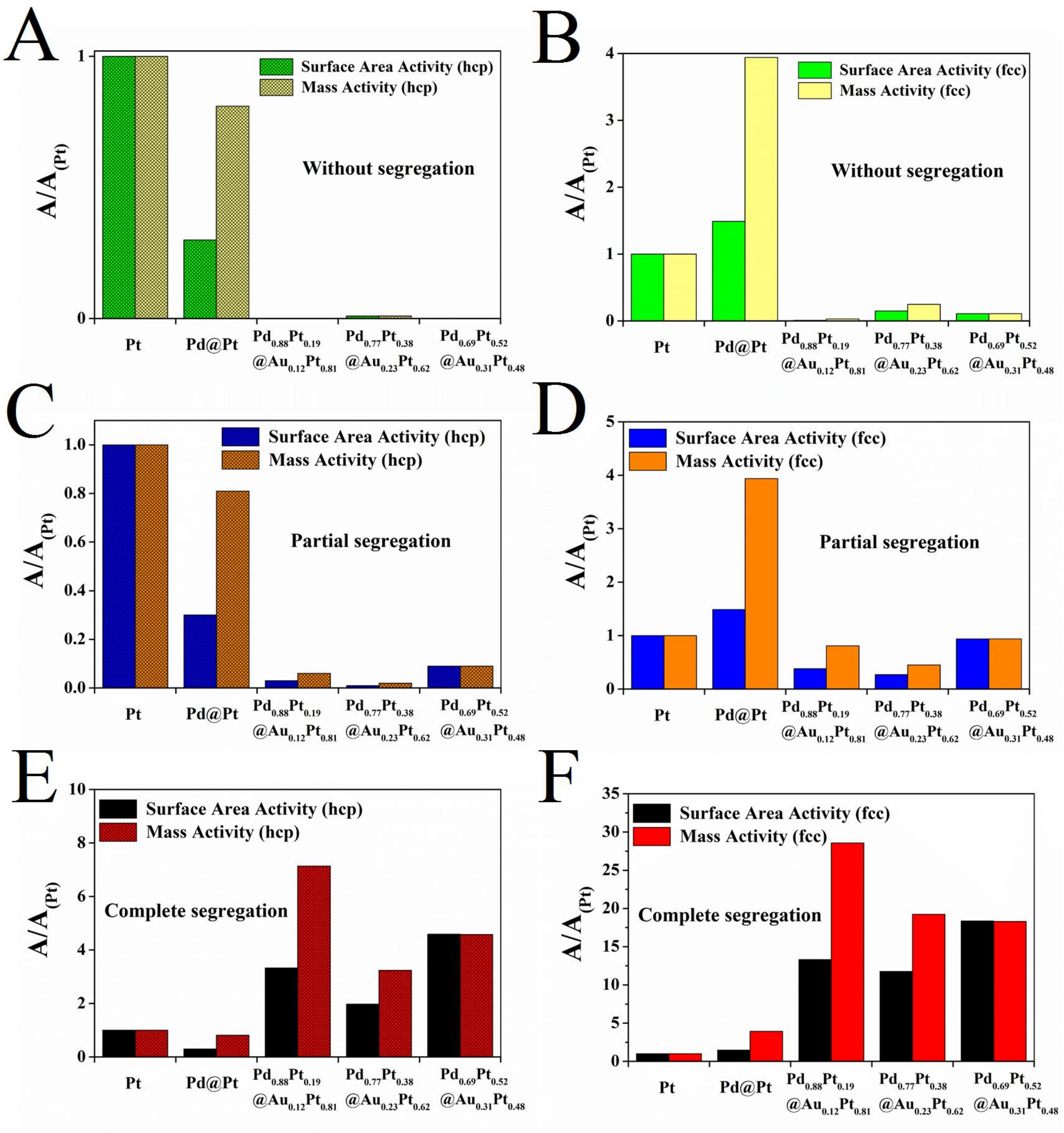

Figure 5.6. Estimated specific activity and mass activity for NWs at T = 20°C, based on the calculated BE-Os values. The top, uppermost two panels describe the predicted theoretical behavior of Pd$_{(1-x)}$Au$_x$@Pt NW systems, related with the *hcp* (A) and *fcc* (B) sites. Central, middle panels highlight the performance of Pd$_{(1-x)}$Au$_{(x-y)}$Pt$_z$@Au$_y$Pt$_{(1-z)}$ NW systems, associated with the *hcp* (C) and *fcc* (D) sites. The bottom, lowermost panels designate Pd$_{(1-x)}$Pt$_z$@Au$_x$Pt$_{(1-z)}$ NW systems, connected with the *hcp* (E) and *fcc* (F) sites.

We first want to clarify that all the activities reported here correspond to a potential of 0.9 V (vs. RHE), unless otherwise specified. We note that both mass and specific activities for pure Pt NWs are set to 1 in all the Figures involved herein. A significant variation of ORR activity with respect to both the amount and distribution of Au within the AuPd@Pt NWs was observed. For a NW with a certain quantity of Au, $Pd_{(1-x)}Pt_z@Au_xPt_{(1-z)}$ NWs possessing full segregation of Au within the shell (panels E and F) displayed the largest improvements in both mass and specific activities with respect to pure Pt NWs amongst all three types of NWs we studied. By comparison, the ORR activities of $Pd_{(1-x)}Au_{(x-y)}Pt_z@Au_yPt_{(1-z)}$ NWs with partial Au segregation (Figure 5.6, panels C and D) and of as-prepared $Pd_{(1-x)}Au_x@Pt$ NWs with Au localized in the core (Figure 5.6, panels A and B) are far lower. That is, the small variation in BE-O obtained by alloying Au (Figure 5.5a) can have a dramatic effect upon the ORR activity.

For a certain Au distribution, the observed enhancements of both mass and specific activities do depend on the amount of Au. Specifically, the experimentally observed trend in both types of activities in evolving from Pt and Pd@Pt to Au-containing analogues such as $Pd_9Au@Pt$, $Pd_8Au_2@Pt$, and $Pd_7Au_3@Pt$[3] can be well captured and described by the corresponding trend in the theoretically estimated activity only when the $Pd_{(1-x)}Pt_z@Au_xPt_{(1-z)}$ conformation is adopted and analyzed. A direct comparison between the “volcano” trend observed in our theoretical estimations and that found in our corresponding experimental data is shown in Figure 5.7.

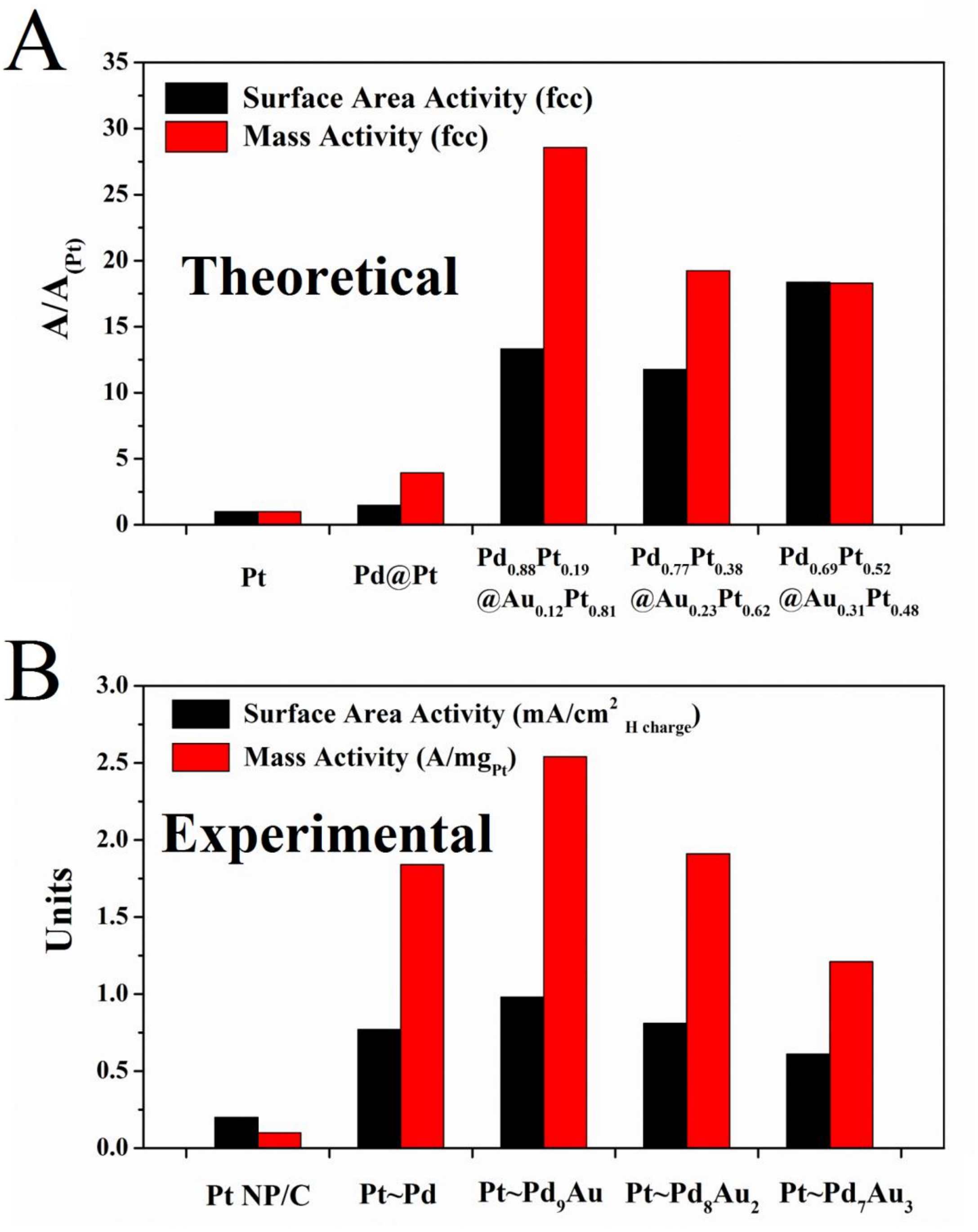

Figure 5.7. Comparison between (A) the theoretical estimated surface area activity (black) and mass activity (red) for different chemical compositions in a range of $Pd_{(1-x)}Pt_z@Au_xPt_{(1-z)}$ NWs, specifically on the *fcc* 3-fold sites, and (B) corresponding experimental results of ORR activities for a series of as-prepared $Pt{\sim}Pd_{1-x}Au_x$ nanowires. Data within Panel B are taken from *J. Phys. Chem. C,* **2012,** v.*116* (29), 15297-15306.

It is worth emphasizing that both sets of data point to $Pd_9Au@Pt$ as the optimal chemical composition of the cathode for the ORR.[3] According to our DFT calculations, either the partial or full segregation of Au is best able to stabilize the as-prepared $Pd_{(1-x)}Au_x@Pt$ NWs, which is likely to occur during the ORR process, whereas the structures of other types of as-prepared NWs may not be able to capture the behavior of the catalyst under operational ORR conditions.

Overall, our DFT calculations show that the ORR activity of AuPd@Pt NWs can be well tuned by purposefully varying the amount and distribution of Au. In effect, the segregation of Au from the core to the edge and (100) terrace sites of the shell is likely to occur during the ORR process and can promote the ORR activity significantly. We note that the more Au remains in the core, the lower the ORR activity of the corresponding AuPd@Pt NW. In addition, the amount of Au should be moderate, i.e. large enough in order to render the NW rigid and therefore weaken the O-Pt interaction, while small enough to prevent both the decrease of active Pt sites in the shell as well as the overall confinement of Au to the core.

In essence, our theoretical computations have attributed the possibility of this hierarchical architecture as emanating from the *in situ* machinations of the oxygen reduction reaction process, thereby resulting in the dynamic surface segregation of certain metal elements within Pt-outer shell, metal/metal alloy core nanoparticles. However, because prior experimental reports have been effectively bulk measurements, these have neither specifically established nor determined the validity of this hypothesis. Hence, in order to better understand and verify the plausible localized restructuring within our Pt~PdAu ultrathin nanowire systems, we have collected EXAFS data.

5.2.2. Experimentally probing core-shell nanowires with STEM, EELS, and EXAFS

We have previously reported on the synthesis of as-prepared homogeneous Pd_9Au ultrathin nanowires, which represent the precursor to the focal core-shell structure of this study.[31] According to the structural characterization results obtained from both X-ray diffraction (XRD) and TEM-based selected area electron diffraction (SAED), the measured lattice *d*-spacings in the as-prepared series of $Pd_{1-x}Au_x$ nanowires match perfectly with the predicted values calculated based on the overall chemical composition, thereby verifying the existence of a homogeneous alloy-type material as opposed to either a core-shell or even a partial alloy motif.

In addition, we would like to provide detailed rational for choosing the system itself basing off previous theoretical and experimental results. According to the "volcano" plot developed by J. K. Nørskov et al., the challenge in optimizing Pt-based electrocatalyst for ORR has always been that the adsorption energy of oxygen onto Pt is too strong.[38] In most of the Pt-Pd core-shell systems studied in the past, Pd not only acts as a support but also contributes to tuning the electronic properties of the Pt atoms.[45] However, Pt monolayer on Pd substrate might not be the optimal motif. As being discussed in the manuscript, the lattice constants of Pt, Pd, and Au are 3.924, 3.890, and 4.080 Å, respectively. Therefore, when deposited on Pd or Au, Pt monolayer experienced compressive or tensile strain, respectively, thereby altering the effective Pt-Pt interatomic distances. Prior reports have proposed and demonstrated that the ideal Pt-Pt distance can be achieved by utilizing Pd-Au alloy nanoparticle as the substrate, with a Pd: Au molar ratio that is close to 9:1, namely 10% mol of Au.[46] This supposition has actually been validated previously in our work regarding analogous ultrathin nanowire system.[3]

In this Chapter, we chose our most active ORR sample, namely Pd_9Au, as the 'foundational' model material with which to pursue our subsequent studies. Upon deposition of

Pt, the morphology and chemical composition of as-prepared carbon-supported Pt~Pd$_9$Au nanowires were characterized by electron microscopy, as shown in Figure 5.8.

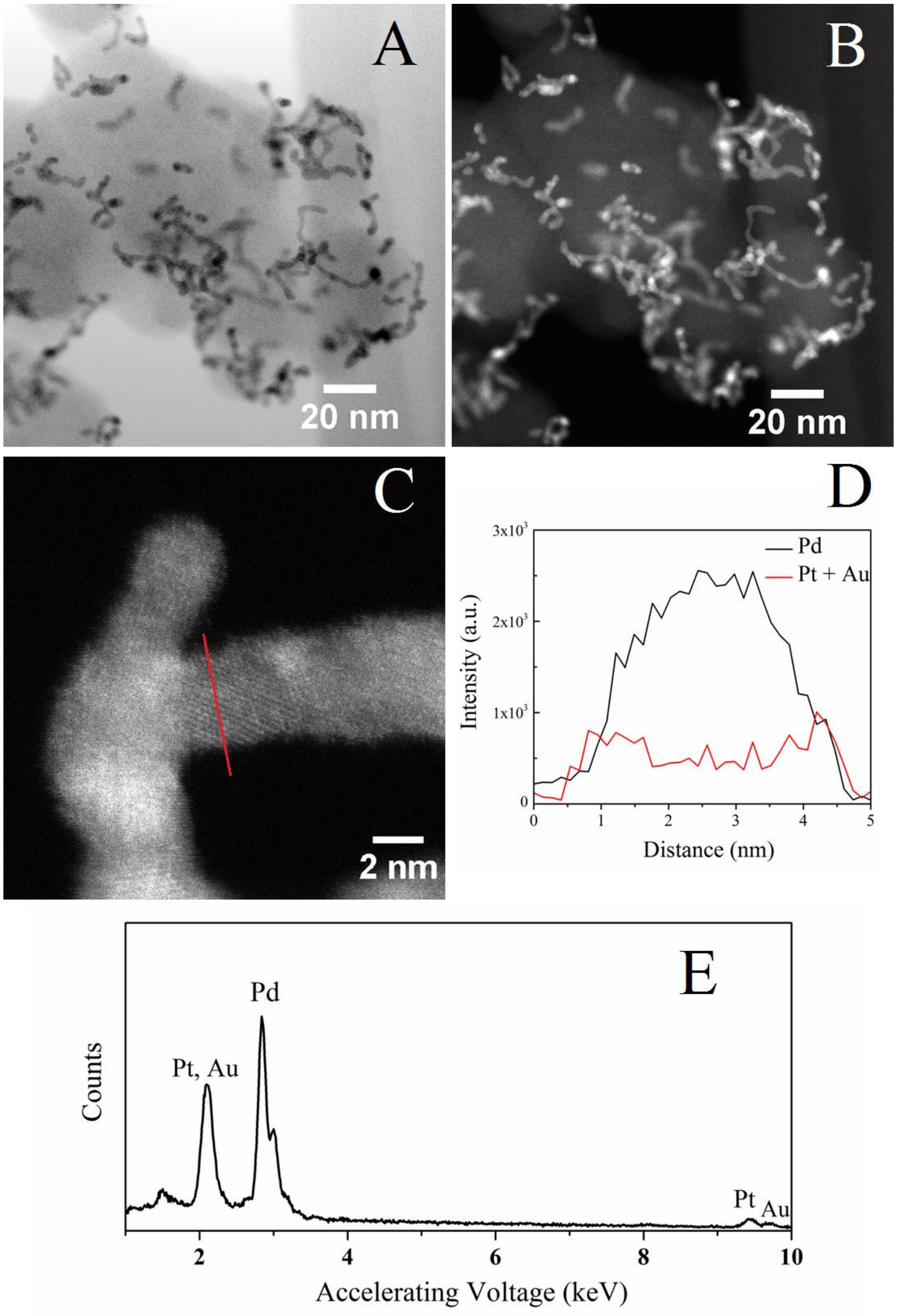

Figure 5.8. TEM results of as-synthesized Pt~Pd$_9$Au ultrathin nanowires. (A) Bright-field imaging, (B) high angle annular dark field imaging (HAADF), (C) high-resolution STEM imaging, (D) cross-sectional EELS analysis, and (E) representative EDS spectra are separately shown. The red line in panel C denotes the region where cross-sectional EELS has been taken.

Specifically, we noted that as-generated Pt~Pd_9Au ultrathin nanowires gave rise to an interconnected network morphology, with average diameters of individual wires measuring 2.5 ± 0.3 nm. As a consequence of the formation mechanism of the Pd_9Au nanowires, there was a juxtaposition of a small quantity of incompletely grown, short nanorods[47] coupled with a majority of longer nanowires possessing average lengths of several tens of nanometers.

The higher resolution STEM image coupled with the cross-sectional EELS analysis indicated that the nanowires most likely possessed a core-shell structure. What is important to note is that with STEM, the Pt and Au elements could not be readily differentiated as a result of their extremely close and potentially overlapping signature bands. However, it is clear from Figure 5.8D that both of these two elements were richer in quantity and distribution at the outer, external circumference of the wires as compared with within the inner central core-region. The overall elemental composition derived from EDS analysis was determined to be Pt: Pd: Au = 7: 81: 12, with small uncertainties of roughly 2-3% in terms of the atomic ratio reported. The Pd: Au ratio was very close to the expected ratio of 90: 10 inherent to a Pd_9Au nanowire. Therefore, our Pt~PdAu sample could be actually ascribed to a $Pt_7Pd_{81}Au_{12}$ composition.

Nevertheless, upon the deposition of that Pt outer shell, what has been missing to date has been a precise study and inherent understanding of the actual spatial distribution of all three elements, namely Pt, Pd, and Au, within the nominal Pt~PdAu core-shell motif in order to fully corroborate our computational findings. Indeed, we ourselves have previously shown[3] that even though there is a systematic trend in the oxide reduction peaks in cyclic voltammograms (CV) for the series of $Pd_{1-x}Au_x$ nanowires as a function of varying “x” values, as we proceeded to deposit an outer Pt monolayer, the aforementioned trend in CVs becomes much less defined and could therefore not serve as a means of precisely examining surface stoichiometry. We hypothesize that this is due to the fact the surface is now almost exclusively covered by Pt atoms whose electronic structure is only slightly modified by the underlying PdAu core giving rise to a subtle if almost imperceptible alteration in the accompanying CV profiles.[3]

As a means of overcoming these inherent sensitivity limitations as discussed in the Introduction, EXAFS is known as an excellent tool for probing the local atomic environment within both bulk and nanomaterial systems. Therefore, we conducted a series of time-dependent *in situ* EXAFS experiments which enabled us to examine the effect of the ORR reaction on possible restructuring of our core-shell Pt~PdAu nanowires, since we assert that surface catalysis of O_2 species lies at the origin of our observed structural modification. Specifically, we deposited Pt~Pd_9Au nanowires onto conductive carbon paper, which was then placed into an electrochemical cell, which had been specially designed for XAFS experiments. By doing so, we were able to perform the oxygen reduction reaction on our catalysts while obtaining spectra at designated time points of interest, as the reaction systematically progressed in a range spanning 0 to 1000 cycles. It should be noted at the outset that the EXAFS data support all of our previous complementary spectroscopy and microscopy data indicating the formation of a core-shell motif. In terms of actual EXAFS data, since Pt and Au atoms are similar in terms of their X-ray scattering properties, it was nearly impossible to distinguish between these two types of atoms as neighbors to either Pt or Au. Hence they are considered as equivalent in the fit. The relevant analysis details of each individual spectrum are shown in Figures 5.9 and 5.10 for Pt and Au, respectively.

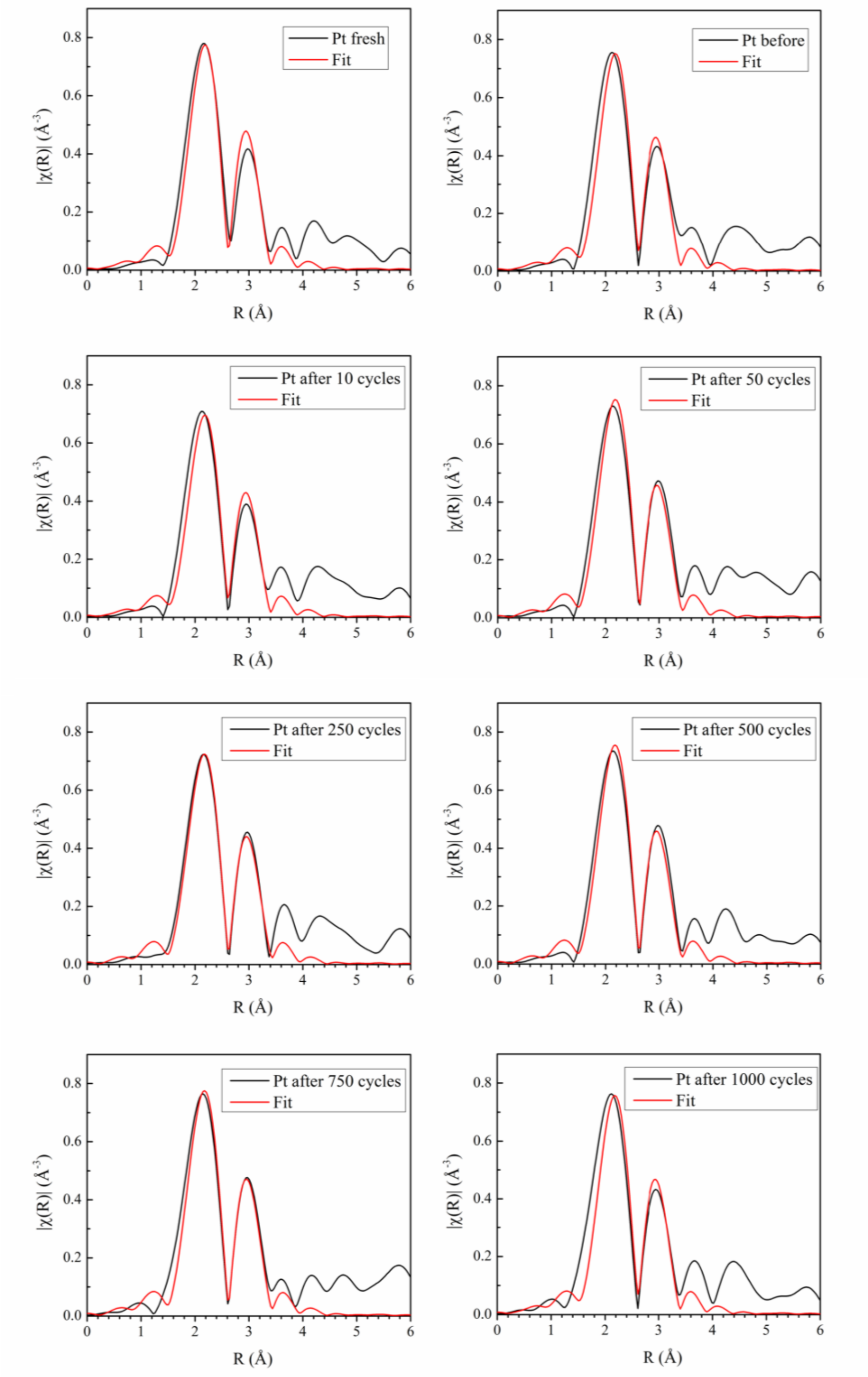

Figure 5.9. *R*-space data. Fitting of Pt L_3 edge of EXAFS spectra on the Pt~Pd_9Au sample after successive selected ORR cycles (i.e. cycling from 0.6 V to 1.0 V vs. RHE at a rate of 100 mV/s, in O_2 saturated 0.1 M $HClO_4$ electrolyte solution), ranging from 0 (denoted as "before the reaction") to 1000 in *R*-space. A fresh sample was examined independently in powder form.

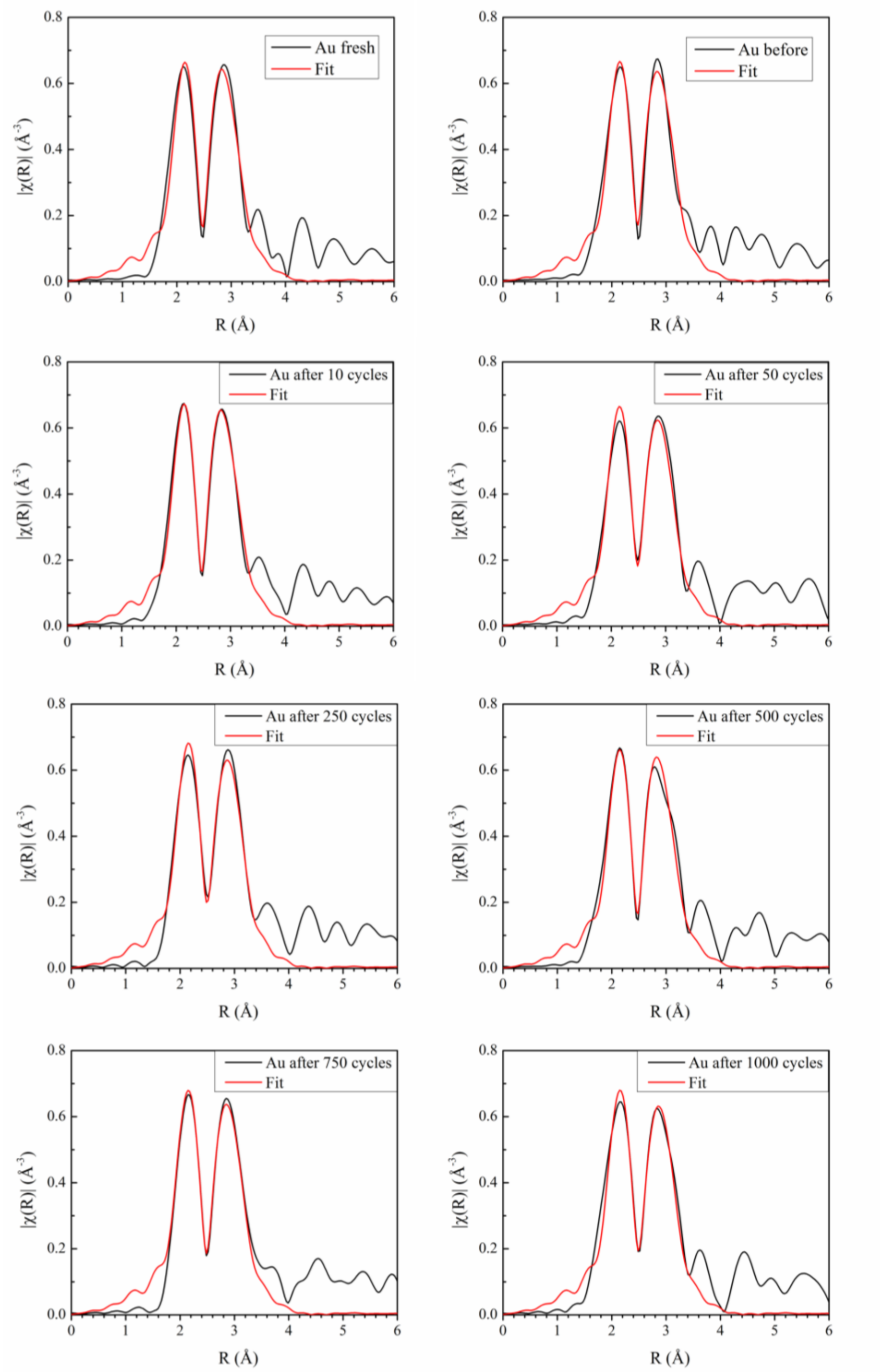

Figure 5.10. *R*-space data. Fitting of Au L_3 edge of EXAFS spectra of the Pt~Pd_9Au sample after successive, selected ORR cycles (i.e. cycling from 0.6 V to 1.0 V vs. RHE at rate of 100 mV/s, in O_2 saturated 0.1 M $HClO_4$ electrolyte solution), ranging from 0 (denoted as "before the reaction") to 1000 in *R*-space. A fresh sample was examined independently in powder form.

A summary of as-obtained structural parameters, including coordination numbers, bond lengths, and their mean square disorders, is displayed in Tables 5.1 and 5.2.

Pt L_3 edge				
Sample	**Bond**	**N**	**R (Å)**	**σ^2 (Å^2)**
Freshly Made	Pt-Au/Pt	9.7 ± 1.1	2.705 ± 0.008	0.0089 ± 0.0009
Before reaction (0 cycle)		9.3 ± 0.9	2.699 ± 0.007	0.0089 ± 0.0009
After 10 cycles		8.6 ± 1.1	2.702 ± 0.009	0.0089 ± 0.0009
After 50 cycles		9.7 ± 1.0	2.710 ± 0.007	0.0089 ± 0.0009
After 250 cycles		9.3 ± 1.1	2.703 ± 0.009	0.0089 ± 0.0009
After 500 cycles		9.7 ± 1.1	2.703 ± 0.008	0.0089 ± 0.0009
After 750 cycles		9.9 ± 1.3	2.702 ± 0.010	0.0089 ± 0.0009
After 1000 cycles		9.4 ± 1.0	2.697 ± 0.007	0.0089 ± 0.0009

Table 5.1. Summary of structural parameters, including coordination number (N), bond length (R), as well as mean square disorder in bond length (σ^2) derived from fitting of the Pt L_3 edge spectra. The Pt-Au/Pt bonding pathway is primarily considered herein.

Au L_3 edge				
Sample	**Bond**	**N**	**R (Å)**	**σ^2 (Å^2)**
Freshly Made	Au- Au/Pt	6.0 ± 0.5	2.817 ± 0.003	0.0090 ± 0.0008
	Au-Pd	5.9 ± 0.3	2.782 ± 0.003	0.0100 ± 0.0005
Before reaction (0 cycle)	Au- Au/Pt	6.2 ± 0.6	2.817 ± 0.003	0.0090 ± 0.0008
	Au-Pd	5.8 ± 0.4	2.782 ± 0.003	0.0100 ± 0.0005
After 10 cycles	Au- Au/Pt	6.1 ± 0.5	2.817 ± 0.003	0.0090 ± 0.0008
	Au-Pd	6.0 ± 0.3	2.782 ± 0.003	0.0100 ± 0.0005
After 50 cycles	Au- Au/Pt	6.4 ± 0.6	2.817 ± 0.003	0.0090 ± 0.0008
	Au-Pd	5.7 ± 0.4	2.782 ± 0.003	0.0100 ± 0.0005
After 250 cycles	Au- Au/Pt	6.7 ± 0.6	2.817 ± 0.003	0.0090 ± 0.0008
	Au-Pd	5.7 ± 0.4	2.782 ± 0.003	0.0100 ± 0.0005
After 500 cycles	Au- Au/Pt	6.0 ± 0.5	2.817 ± 0.003	0.0090 ± 0.0008
	Au-Pd	5.9 ± 0.4	2.782 ± 0.003	0.0100 ± 0.0005
After 750 cycles	Au- Au/Pt	6.5 ± 0.6	2.817 ± 0.003	0.0090 ± 0.0008
	Au-Pd	5.8 ± 0.4	2.782 ± 0.003	0.0100 ± 0.0005
After 1000 cycles	Au- Au/Pt	6.7 ± 0.5	2.817 ± 0.003	0.0090 ± 0.0008
	Au-Pd	5.7 ± 0.3	2.782 ± 0.003	0.0100 ± 0.0005

Table 5.2. Summary of structural parameters including coordination number (N), bond length (R), as well as mean square disorder in bond length (σ^2) derived from fitting of the Au L_3 edge spectra. Both the Au-Au/Pt and Au-Pd bonding paths have been primarily taken into consideration herein.

From these collected data, we should note that the atomic ratio of Au: Pt can be directly calculated from the edge step of their respective regions within the EXAFS spectra. The corresponding data are displayed in Figure 5.11.

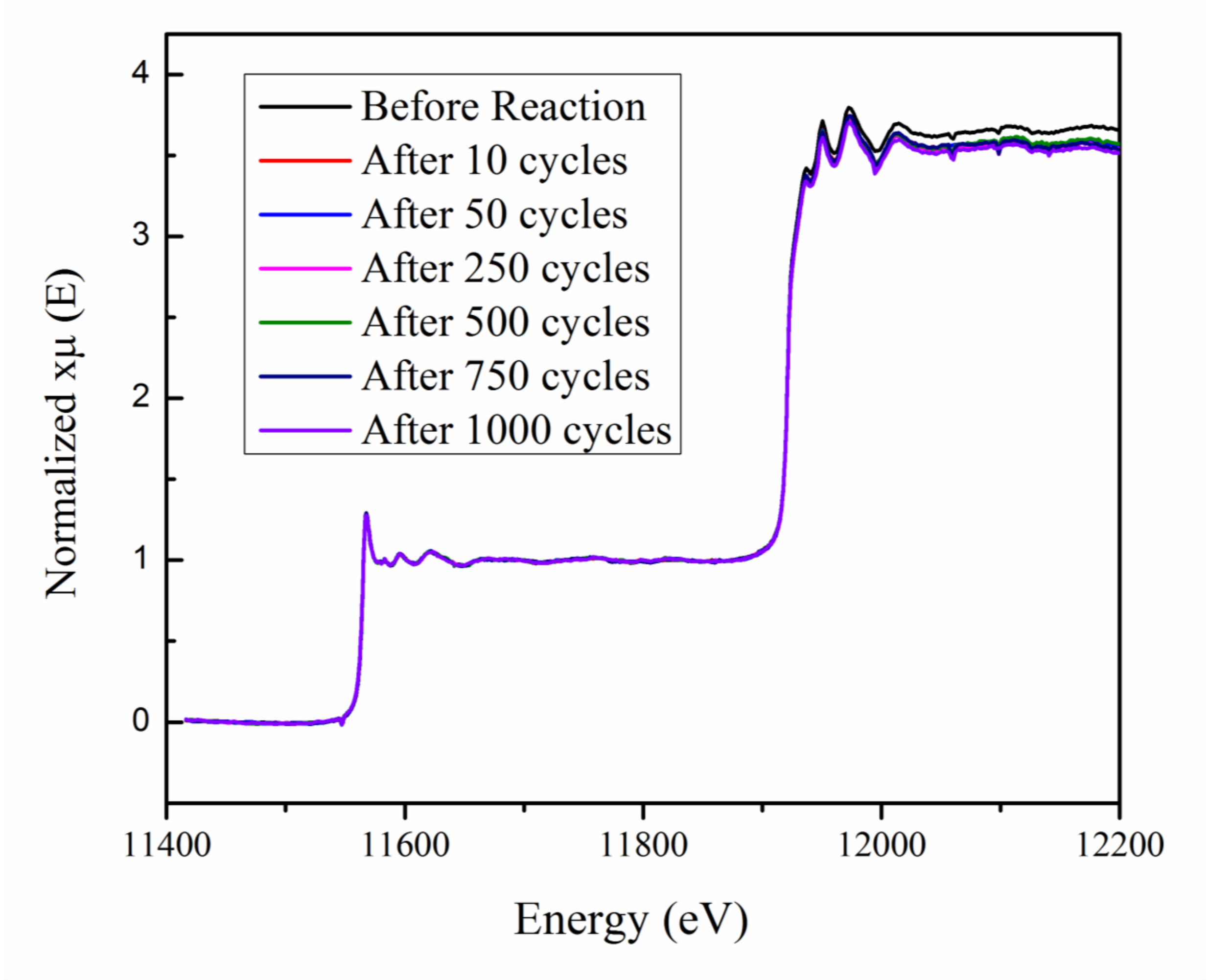

Figure 5.11. EXAFS data collected for an electrochemically treated Pt~Pd_9Au/C sample after 0 (before reaction), 10, 50, 250, 500, 750, and 1000 ORR cycles, respectively. The collected spectra were normalized and the background was subtracted.

As a result, the Au: Pt ratio was computed to be 2.5 ± 0.2, whereas the analogous ratio value derived from EDAX data was 1.7 ± 0.7. We should clarify that both Au and Pt elements constitute a minority composition of the overall core-shell Pt~Pd_9Au structure (i.e. close to 10%), thereby leading to a relatively large error (i.e. 2~3%) associated with the actual experimental percentage values themselves, i.e. 7% for Pt and 12% for Au, respectively, for our reported values. Therefore, it is reasonable to assume that the experimental ratios derived from EDAX and EXAFS, respectively, would be significantly different. Nonetheless, we noted that in fact, the two sets of data are comparatively close to each other in magnitude, thereby confirming the validity and reliability of the Pt: Pd: Au = 7: 81: 12 EDAX composition ratio we had noted earlier in the paper.

When the Pt L_3 edge was analyzed (correspond to Figure 5.9 and Table 5.1), the coordination number of the first nearest neighboring Pt-Au/Pt was determined to be 9-10, suggesting that the Pt atoms herein are predominantly surrounded by either Pt or Au atoms. According to the chemical composition determined by EDS analysis, the sum of Pt and Au was less than 20% in terms of atomic ratio. In other words, if Pt atoms were to form a random alloy with the two other elements, it is very likely that this occurred with Pd atoms, since Pd constitutes the majority of the wire composition, as opposed to either Pt or Au. Such a conclusion suggests that Pt atoms are essentially exclusively localized on the surfaces of the nanowires themselves. In effect, the EXAFS and EELS data have collectively suggested that as a result of the Cu underpotential deposition (UPD) process followed by galvanic replacement with Pt, the resulting core-shell structure likely possesses a thin outer Pt shell as opposed to a more randomized inner Pt-metal alloy.

Regarding the Au L_3 edge (correspond to Figure 5.10 and Table 5.2), the results are far more novel and intriguing. Specifically, the coordination numbers for both Au-Au/Pt and Au-Pd are quite close to 6, with a reasonably small error bar. In essence, this implies that every Au atom is surrounded by 6 Pd atoms and either 6 Pt or Au atoms. From the known actual chemical composition of Pt_7~$Pd_{81}Au_{12}$, as determined from EDS, such a conclusion is inconsistent with a picture in which Au atoms are mixing homogeneously with Pd atoms within the core. The latter model would envision Au to be almost exclusively surrounded by Pd atoms, because Pt was found (vide supra) to be localized on the surface of the nanowires.

Since from the Pt L_3 edge data, we know that Pt is exclusively localized on the surface, we can only deduce that the Au atoms either are immediately beneath this uppermost layer forming a "sublayer" or are well mixed with the Pt layer itself, thereby creating a PtAu-shell / Pd-core structure. A clear differentiation between these two plausible structural scenarios is beyond the scope of this particular work and would require a clear and obvious differentiation between signals attributed to Pt and Au atoms, respectively, in the EXAFS data, which is difficult to accomplish. Notwithstanding, our results clearly show that Au atoms are not randomly distributed within the Pd_9Au nanowires and most likely have undergone some degree of surface segregation.

Herein, we should note that consideration of oxygenated Pt, such as Pt-OH_2, Pt-OH, and Pt-O, has been excluded from the fitting process. Nonetheless, the resulting simulated data matched perfectly well with experimental curves which thereby implies that the presence of a range of Pt-O species gives rise to extremely minor, if any perceptible, influence on the EXAFS spectra. In other words, the amount of surface oxide species present, such as Pt-OH_2, Pt-OH, or Pt-O, was likely to be scarce, and coverage is expected to be low. Such an assertion is reasonable, since we have purposely minimized the potential for surface oxidation (i) through Ar purging as well as (ii) by holding the potential within a "reducing" region, i.e. 0.5 V vs. RHE in this case, during spectra collection, as mentioned in the Experimental Section.

Also, it is important to note that we have periodically collected cyclic voltammograms of the sample in between our EXAFS measurements, as shown in Figure 5.12.

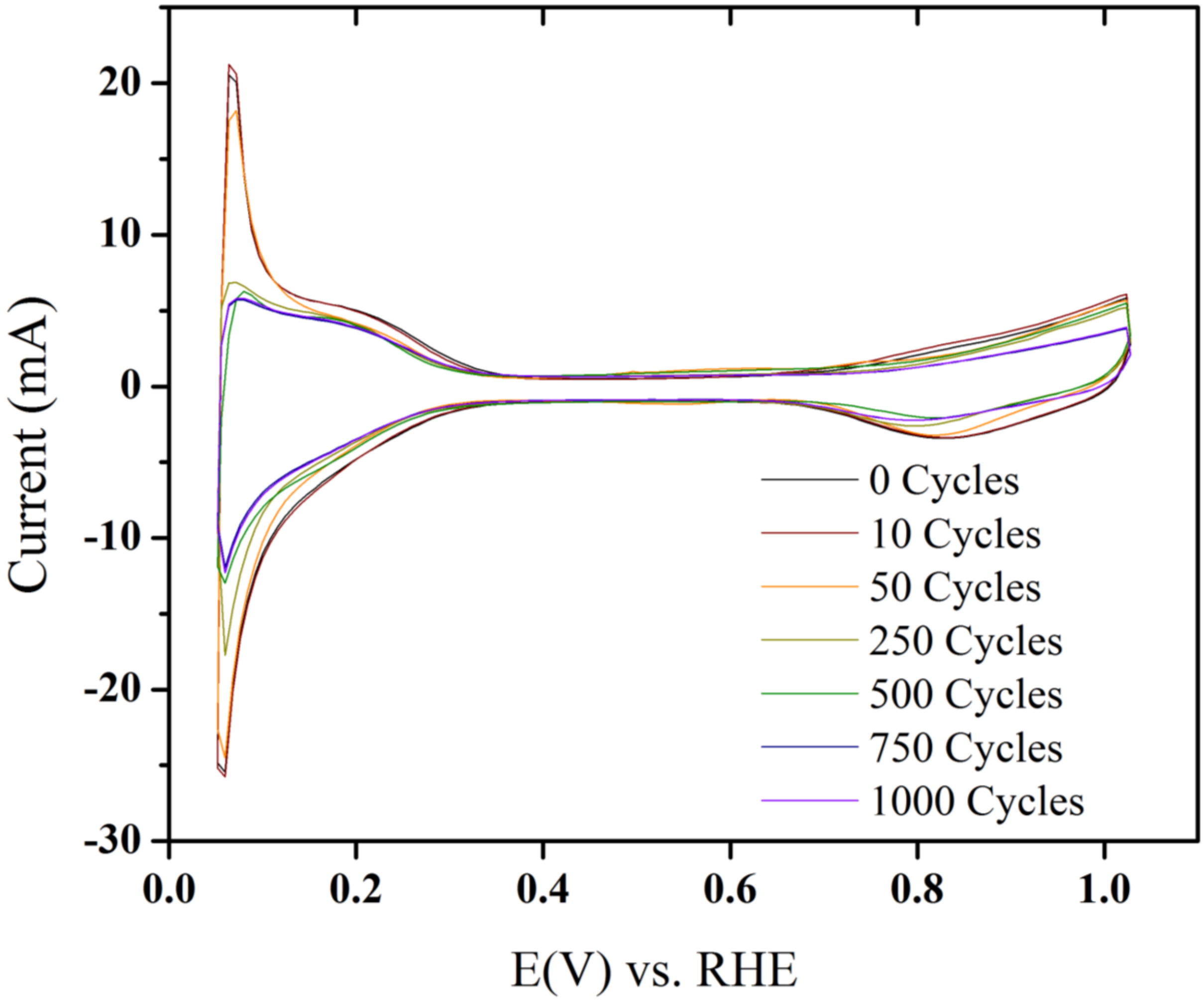

Figure 5.12. Cyclic voltammograms obtained in the XAFS cell within a deoxygenated 0.1 M $HClO_4$ solution after 0, 10, 50, 250, 500, 750, and 1000 cycles, respectively, of ORR for the Pt~Pd_9Au/C system.

Overall, there are relatively insignificant differences in the CVs obtained throughout the course of the entire experiment, namely throughout 1000 ORR cycles. Minor changes we have discerned include (a) a slight reduction in the hydrogen adsorption/desorption ($H_{ads/des}$) peaks as well as (b) a subtle fluctuation of the oxide reduction peak position. Nevertheless, both of these observations have been previously detected in our Pt~Pd ultrathin nanowires, while conducting a similar time-resolved ORR experiment.[2] More importantly, in that system, these slight variations in CVs barely affected either the corresponding ORR performance or the final morphology observed.

Moreover, to back up existing data, we also examined the morphology and chemical composition of the sample after ORR treatment, as shown in Figure 5.13.

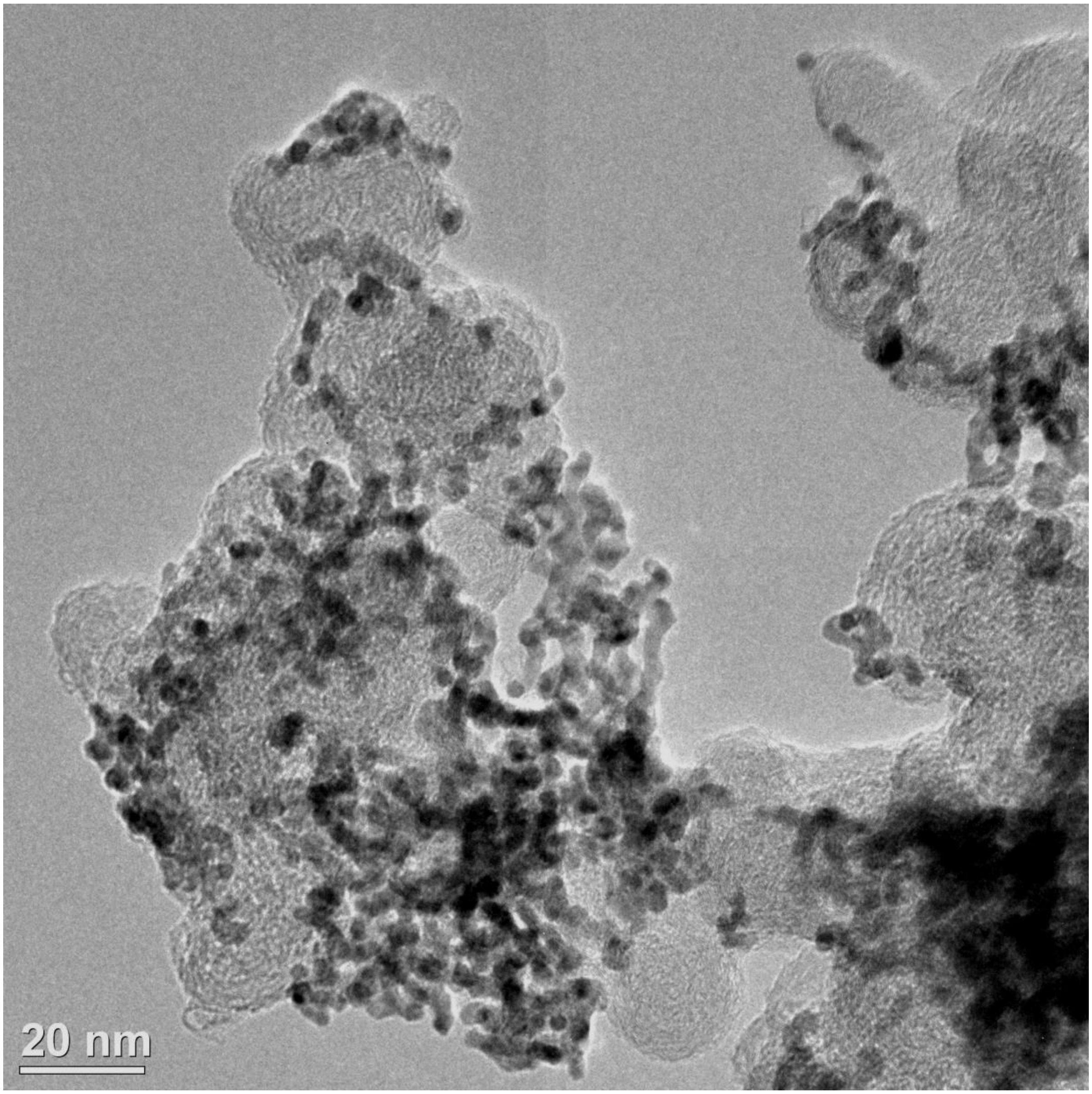

Figure 5.13. TEM image acquired of the Pt~Pd_9Au/C sample after 1000 cycles of ORR.

Even though we noted a certain degree of aggregation of the nanowires themselves, it was evident that the structural integrity of the individual wires themselves was mostly preserved. Furthermore, we obtained a chemical composition of $Pt_9Pd_{79}Au_{12}$ for the wires after electrochemical processing; these data were obtained by performing localized EDAX analysis, and were very similar to what had been observed prior to the electrochemical experiments, i.e. $Pt_7Pd_{81}Au_{12}$. Therefore, we can conclude that during the entire time-dependent EXAFS experiment, the sample remained relatively unchanged in terms of both morphology and electrochemical performance.

In terms of the origin of the outstanding stability of our nanostructures, we believe both the Pt monolayer and Au sublayer attribute to the enhancement of durability of the resulting ternary core-shell structure. On one hand, we presumed that the Pt monolayer, as opposed to relatively "bulky" Pt, such as elemental Pt nanoparticles, represents enhanced catalyst stability due to decreased oxidation of the Pt resulting from the interaction with the substrate. This has been readily demonstrated in PtRu system and can be generated to many other Pt-M binary electrocatalysts.[48] On the other hand, addition of Au atoms renders the surface as more 'noble'. Specifically, we have shown in the past that the oxide reduction peak of the Pd_9Au NWs is shifted by ~20 mV to higher potentials as compared with the Pd NWs.[3] This result showed that Pd_9Au NWs possessed weaker interaction with the adsorbed oxygen species, implying a potential enhancement against surface corrosion in acidic media. Moreover, according to the EXAFS results and our conclusions, the Au atoms had segregated onto the surface, resulting in an Au-rich sublayer in the final structure. A similar hierarchical structure, namely a Ni@Au@PtNi core-interlayer-shell, has also been designed by Y. Kang et al., wherein the Au interlayer was demonstrated to have effectively prevented surface oxide formation, thereby improving overall long-term durability.[49] These observations and illustrations supports our motive of incorporating Au into the system.

To further confirm and corroborate the observed surface segregation within our hierarchical nanowires, we also conducted EXAFS experiments on so-called “freshly-made” Pt~Pd_9Au samples, prepared as a powder as opposed to being deposited on carbon paper and immersed into electrolyte. According to Tables 5.1 and 5.2, these samples exhibited identical local structure and behavior to the sample that had undergone electrochemical testing. Such consistency in our data implies that the Au surface segregation originated from the intrinsic synthesis and treatment process prior to the exposure of the sample to electrochemical processing, as opposed to the very ORR reaction itself. In other words, by a process of elimination, we propose that the most probable initiator, i.e. the instigating event, of the observed surface segregation can be ascribed to Cu underpotential deposition followed by galvanic replacement with Pt.

To justify the validity of our conclusions, it is worth noting that similar types of behavior have been reported in cases where the presence of different absorbates can result in surface segregation in metal alloy systems. Specifically, Pt atoms in Pt_3Co nanoparticles can undergo a surface-segregation during a CO annealing process at 200°C, resulting in the formation of a Pt-shell, PtCo-core structure.[50] Moreover, high-temperature is not a necessary prerequisite for such surface restructuring to occur. For instance, Völker *et al.* have observed room-temperature O_2-induced Cu surface segregation in polycrystalline bulk Cu-Au alloys using time-resolved XPS experiments and rationalized these observations based on DFT calculations.[51] Similarly, Jirkovsky *et al.* discovered a reversible, external potential-dependent exchange process involving Pd, between the core and the shell within Pd-Au alloy (Pd-rich) nanoparticles.[52] In other words, the chemical compositions of the surfaces of these Pd-Au nanoparticles appeared to depend on the magnitude of the applied potential. For example, at low potentials (i.e. below 0.8 V vs. RHE), the surface tended to be Au-rich, whereas at correspondingly higher potentials (i.e. higher than 1.0 V vs. RHE), the surface was found to be Pd-rich.

This latter paper serves as corroboration of our hypothesis, since our entire Cu UPD process described herein was conducted under a potential range of 0.5-0.8 V (vs. RHE). Hence it is reasonable of us to propose Au segregation in the outer shell. Furthermore, it is worth noting that the relevant operating ORR potential is merely within the 0.6-1.0 V range, which might not be sufficiently high enough to initiate the generation of an alternative scenario, i.e. a Pd-rich surface.

5.3. Conclusions

In this Chapter, we have probed the local structure of our Pt~Pd_9Au ultrathin nanowires by a holistic approach consisting of a unique combination of both theoretical calculations as well as X-ray Absorption Fine Structure Spectroscopy (XAFS). Specifically, DFT calculations of the binding energy (BE-O) values of oxygen species coupled with the corresponding calculated ORR activities have allowed us to re-visit our assumed ‘Pt-shell, PdAu random-alloy-core’ model we had proposed in our previous work as a definitive description of Pt~Pd_xAu_{1-x}. In particular, the time-dependent EXAFS data on our Pt~Pd_9Au nanowires have confirmed that (a) Au atoms will likely undergo surface segregation and that (b) such segregation process likely happens during the synthesis of the core-shell structure itself, i.e., in the midst of the Cu UPD process followed by galvanic replacement with Pt, implying that the ‘restructuring’ occurs primarily upon polarization.

By contrast with many other studies which have utilized DFT calculations and/or XAFS techniques to probe structural parameters, we have used our DFT results herein as a guide towards thoughtfully designing EXAFS experiments. In other words, theoretical predictions have directed our experiments as well as simplified the resulting analysis by providing for plausible possible structural models with which to differentiate, discriminate, and ultimately verify using EXAFS. Such a synergetic, feedback-based effort will likely be important and relevant for future applications of XAFS.

Meanwhile, the discovery of structural alterations ascribed to the idiosyncrasies of specific synthesis approaches may lead to new perspectives in terms of understanding the structural basis for electrocatalysis, especially with a host of different and complementary nanoscale Pt-based hierarchical nanomaterials. To our knowledge, this is the first time that Au segregation has been reported as a result of a seemingly unrelated Cu UPD/Pt galvanic displacement process. In the future, it will be worth further differentiating between the effect of chemical composition versus that of the ultrathin size in terms of explaining the nature of the phenomena observed.

Moreover, the suite of different techniques, including (a) electrochemical tests, (b) in situ spectroscopy and (c) theoretical calculations support and validate each other in our work. We believe reports that combine all these techniques are rare within the relevant literature and that they represent a promising platform for examining functional nanostructures.[19, 53, 54] From a broader point of view, we want to emphasize that the logic behind this methodology can be generalized to other fields as well. In other words, the examination of local structures is crucial to a better understanding and design of nanomaterials in general. Hence, the combination of multiple analytical techniques, coupled with theory, especially concerning the motif involved in this current report, should not be limited either to ORR or to electrochemistry.

5.4. References

1. Koenigsmann, C.; Zhou, W. P.; Adzic, R. R.; Sutter, E.; Wong, S. S. *Nano Lett* **2010,** 10, (8), 2806-2811.
2. Koenigsmann, C.; Santulli, A. C.; Gong, K. P.; Vukmirovic, M. B.; Zhou, W. P.; Sutter, E.; Wong, S. S.; Adzic, R. R. *J Am Chem Soc* **2011,** 133, (25), 9783-9795.
3. Koenigsmann, C.; Sutter, E.; Adzic, R. R.; Wong, S. S. *J Phys Chem C* **2012,** 116, (29), 15297-15306.
4. Koenigsmann, C.; Tan, Z.; Peng, H.; Sutter, E.; Jacobskind, J.; Wong, S. S. *Israel Journal of Chemistry* **2012,** 52, (11-12), 1090-1103.
5. Koenigsmann, C.; Scofield, M. E.; Liu, H. Q.; Wong, S. S. *J Phys Chem Lett* **2012,** 3, (22), 3385-3398.
6. Strasser, P.; Koh, S.; Anniyev, T.; Greeley, J.; More, K.; Yu, C. F.; Liu, Z. C.; Kaya, S.; Nordlund, D.; Ogasawara, H.; Toney, M. F.; Nilsson, A. *Nat Chem* **2010,** 2, (6), 454-460.
7. Matanovic, I.; Kent, P. R. C.; Garzon, F. H.; Henson, N. J. *J Electrochem Soc* **2013,** 160, (6), F548-F553.
8. Russell, A. E.; Tessier, B. C.; Wise, A. M.; Rose, A.; Price, S. W. T.; Richardson, P. W.; Ball, S. C.; Theobald, B.; Thompsett, D.; Crabb, E. M. *Ecs Transactions* **2011,** 41, (1), 55-67.
9. Rettew, R. E.; Allam, N. K.; Alamgir, F. M. *Acs Appl Mater Inter* **2011,** 3, (2), 147-151.
10. Cheon, J. Y.; Kim, T.; Choi, Y.; Jeong, H. Y.; Kim, M. G.; Sa, Y. J.; Kim, J.; Lee, Z.; Yang, T. H.; Kwon, K.; Terasaki, O.; Park, G. G.; Adzic, R. R.; Joo, S. H. *Sci Rep-Uk* **2013,** 3.
11. Gao, J.; Zhong, J.; Bai, L. L.; Liu, J. Y.; Zhao, G. Q.; Sun, X. H. *Sci Rep-Uk* **2014,** 4.
12. Nashner, M. S.; Frenkel, A. I.; Adler, D. L.; Shapley, J. R.; Nuzzo, R. G. *J Am Chem Soc* **1997,** 119, (33), 7760-7771.
13. Frenkel, A. I. *J Synchrotron Radiat* **1999,** 6, 293-295.
14. Frenkel, A. I.; Hills, C. W.; Nuzzo, R. G. *J Phys Chem B* **2001,** 105, (51), 12689-12703.
15. Alayoglu, S.; Zavalij, P.; Eichhorn, B.; Wang, Q.; Frenkel, A. I.; Chupas, P. *Acs Nano* **2009,** 3, (10), 3127-3137.
16. Frenkel, A. I. *Chem Soc Rev* **2012,** 41, (24), 8163-8178.
17. Jung, U.; Elsen, A.; Li, Y.; Smith, J. G.; Small, M. W.; Stach, E. A.; Frenkel, A. I.; Nuzzo, R. G. *Acs Catal* **2015**, 1539-1551.
18. Dutta, I.; Carpenter, M. K.; Balogh, M. P.; Ziegelbauer, J. M.; Moylan, T. E.; Atwan, M. H.; Irish, N. P. *J Phys Chem C* **2010,** 114, (39), 16309-16320.
19. Sasaki, K.; Naohara, H.; Choi, Y. M.; Cai, Y.; Chen, W. F.; Liu, P.; Adzic, R. R. *Nat Commun* **2012,** 3.
20. Kuttiyiel, K. A.; Sasaki, K.; Su, D.; Vukmirovic, M. B.; Marinkovic, N. S.; Adzic, R. R. *Electrochim Acta* **2013,** 110, 267-272.
21. Anderson, R. M.; Zhang, L.; Loussaert, J. A.; Frenkel, A. I.; Henkelman, G.; Crooks, R. M. *Acs Nano* **2013,** 7, (10), 9345-9353.
22. Nashner, M. S.; Frenkel, A. I.; Somerville, D.; Hills, C. W.; Shapley, J. R.; Nuzzo, R. G. *J Am Chem Soc* **1998,** 120, (32), 8093-8101.
23. Knecht, M. R.; Weir, M. G.; Frenkel, A. I.; Crooks, R. M. *Chemistry of Materials* **2007,** 20, (3), 1019-1028.
24. Shu, Y. Y.; Murillo, L. E.; Bosco, J. P.; Huang, W.; Frenkel, A. I.; Chen, J. G. *Appl Catal a-Gen* **2008,** 339, (2), 169-179.

25. Teng, X. W.; Han, W. Q.; Wang, Q.; Li, L.; Frenkel, A. I.; Yang, J. C. *J Phys Chem C* **2008,** 112, (38), 14696-14701.

26. Teng, X. W.; Wang, Q.; Liu, P.; Han, W.; Frenkel, A.; Wen, W.; Marinkovic, N.; Hanson, J. C.; Rodriguez, J. A. *J Am Chem Soc* **2008,** 130, (3), 1093-1101.

27. Dowben, P.; Miller, A.; Vook, R. *Gold Bull* **1987,** 20, (3), 54-65.

28. Deng, L.; Hu, W. Y.; Deng, H. Q.; Xiao, S. F.; Tang, J. F. *J Phys Chem C* **2011,** 115, (23), 11355-11363.

29. Zhang, Y.; Hsieh, Y. C.; Volkov, V.; Su, D.; An, W.; Si, R.; Zhu, Y. M.; Liu, P.; Wang, J. X.; Adzic, R. R. *Acs Catal* **2014,** 4, (3), 738-742.

30. Carino, E. V.; Kim, H. Y.; Henkelman, G.; Crooks, R. M. *J Am Chem Soc* **2012,** 134, (9), 4153-4162.

31. Ramirez-Caballero, G. E.; Ma, Y. G.; Callejas-Tovar, R.; Balbuena, P. B. *Phys Chem Chem Phys* **2010,** 12, (9), 2209-2218.

32. Herron, J. A.; Mavrikakis, M. *Catal Commun* **2014,** 52, 65-71.

33. Hammer, B.; Norskov, J. K. *Nature* **1995,** 376, (6537), 238-240.

34. Rodriguez, P.; Garcia-Araez, N.; Koper, M. T. M. *Phys Chem Chem Phys* **2010,** 12, (32), 9373-9380.

35. Ruban, A. V.; Skriver, H. L. *Computational Materials Science* **1999,** 15, (2), 119-143.

36. Ruban, A. V.; Skriver, H. L.; Norskov, J. K. *Physical Review B* **1999,** 59, (24), 15990-16000.

37. Koenigsmann, C.; Sutter, E.; Chiesa, T. A.; Adzic, R. R.; Wong, S. S. *Nano Lett* **2012,** 12, (4), 2013-2020.

38. Norskov, J. K.; Rossmeisl, J.; Logadottir, A.; Lindqvist, L.; Kitchin, J. R.; Bligaard, T.; Jonsson, H. *J Phys Chem B* **2004,** 108, (46), 17886-17892.

39. Stamenkovic, V.; Mun, B. S.; Mayrhofer, K. J. J.; Ross, P. N.; Markovic, N. M.; Rossmeisl, J.; Greeley, J.; Norskov, J. K. *Angew Chem Int Edit* **2006,** 45, (18), 2897-2901.

40. Shao, M.; Liu, P.; Adzic, R. R. *J. Phys. Chem. B* **2007,** 111, 6772-6775.

41. Mavrikakis, M.; Hammer, B.; Nørskov, J. K. *Phys Rev Lett* **1998,** 81, (13), 2819-2822.

42. An, W.; Liu, P. *J Phys Chem C* **2013,** 117, (31), 16144-16149.

43. Tripkovic, V.; Skúlason, E.; Siahrostami, S.; Nørskov, J. K.; Rossmeisl, J. *Electrochim Acta* **2010,** 55, (27), 7975-7981.

44. Grgur, B. N.; Marković, N. M.; Ross, P. N. *Canadian Journal of Chemistry* **1997,** 75, (11), 1465-1471.

45. Antolini, E. *Energ Environ Sci* **2009,** 2, (9), 915-931.

46. Xing, Y. C.; Cai, Y.; Vukmirovic, M. B.; Zhou, W. P.; Karan, H.; Wang, J. X.; Adzic, R. R. *J Phys Chem Lett* **2010,** 1, (21), 3238-3242.

47. Greeley, J.; Norskov, J. K. *Surf Sci* **2005,** 592, (1-3), 104-111.

48. Adzic, R. R.; Zhang, J.; Sasaki, K.; Vukmirovic, M. B.; Shao, M.; Wang, J. X.; Nilekar, A. U.; Mavrikakis, M.; Valerio, J. A.; Uribe, F. *Top Catal* **2007,** 46, (3-4), 249-262.

49. Kang, Y. J.; Snyder, J.; Chi, M. F.; Li, D. G.; More, K. L.; Markovic, N. M.; Stamenkovic, V. R. *Nano Lett* **2014,** 14, (11), 6361-6367.

50. Mayrhofer, K. J. J.; Juhart, V.; Hartl, K.; Hanzlik, M.; Arenz, M. *Angew Chem Int Edit* **2009,** 48, (19), 3529-3531.

51. Volker, E.; Williams, F. J.; Calvo, E. J.; Jacob, T.; Schiffrin, D. J. *Phys Chem Chem Phys* **2012,** 14, (20), 7448-7455.

52. Jirkovsky, J. S.; Panas, I.; Romani, S.; Ahlberg, E.; Schiffrin, D. J. *J Phys Chem Lett* **2012,** 3, (3), 315-321.

53. Kwon, G.; Ferguson, G. A.; Heard, C. J.; Tyo, E. C.; Yin, C. R.; DeBartolo, J.; Seifert, S.; Winans, R. E.; Kropf, A. J.; Greeley, J.; Johnston, R. L.; Curtiss, L. A.; Pellin, M. J.; Vajda, S. *Acs Nano* **2013,** 7, (7), 5808-5817.

54. Shao, M. H.; Huang, T.; Liu, P.; Zhang, J.; Sasaki, K.; Vukmirovic, M. B.; Adzic, R. R. *Langmuir* **2006,** 22, (25), 10409-10415.

Chapter 6: Synthesis-driven enhanced up-conversion luminescence and energy transfer behavior in phase-tunable $NaYF_4$:Yb, Er-based nanoscale motifs and associated QD-coupled heterostructures

6.1. Introduction

In recent years, significant attention has been paid to the fabrication of up-conversion (UC) materials due to their potential applications in solar cells, solid-state lasers, optical telecommunications, flat-panel displays, biolabels, and so forth.[1-3] UC properties can be attributed to the initial absorption of infrared light in the presence of Yb^{3+} ions employed as the dominant primary sensitizing agent, followed by energy transfer to multiple energy states associated with the secondary Er^{3+} dopant. Hence, radiative relaxation in these systems leads to emission of either visible or ultraviolet light.[4, 5] Amongst many different candidates used as a host lattice, fluoride compounds have been thoroughly explored, owing to their special ability to undergo NIR-to-visible UC emission.[6] In particular, $NaYF_4$ compounds denote a material of exceptional interest as a host lattice of UC materials, because they possess inherently lower phonon energies, and can thereby minimize non-radiative phonon relaxation processes in the dopants (rare-earth ions) by alleviating interactions between electrons and phonons.[7-10]

The two most common crystal structures for $NaYF_4$ are cubic (i.e., α-phase) and hexagonal (i.e., β-phase). In terms of up-conversion efficiencies, the β-phase is superior to the α-phase of $NaYF_4$ by roughly one order of magnitude as far as the quantum yield (QY) is concerned.[11-13] Therefore, many previous reports have focused on either (i) synthesizing hexagonal (β-phase) $NaYF_4$ meso- and nano-crystals directly or (ii) developing a facile means to convert the cubic α-phase of $NaYF_4$ into its hexagonal counterpart. For instance, Sun *et al.* have reported that particle morphology and phase transformation were impacted by the reaction time and the choice of ligands.[14] Moreover, Zhuang *et al.* have reported on the synthesis of monodisperse spindle-like β-$NaYF_4$ mesocrystals via an *in situ* ion-exchange transformation from nanorod bundles of $Y(OH)_xF_{3-x}$ precursors.[15] Conversely, Yin *et al.* have demonstrated that with the proper amount of sodium hydrogen phosphate (Na_2HPO_4), the crystal structure of $NaYF_4$ can be rapidly transformed from the cubic phase to the hexagonal phase under hydrothermal conditions within as little as 3.5 hours. These as-obtained products are generally monodisperse with diameters of several tens of nanometers.[16] Similarly, small-sized (~10 nm in diameter), hexagonal-phase $NaYF_4$ can be prepared through the decomposition of CF_3COOM (M = Na, Y, Yb, Er, and Tm) precursors at high temperature (300°C).[17]

Nonetheless, the field lacks a more comprehensive and logical understanding of the synthesis of these materials, with respect to the following issues.

(1) The experimental parameters needed to generate the hexagonal phase of $NaYF_4$ under ambient, surfactantless conditions are somewhat empirical. In other words, despite many relevant reports regarding the synthesis of either β- or α- phase of $NaYF_4$, there is still a lack of fundamental understanding with respect to deducing the precise roles of the critical reaction parameters needed to generate 100% of either the β- or α- phases associated with $NaYF_4$, especially under low-temperature (< 150°C) conditions.

(2) Moreover, most of the final products are micron-scale in size. In general, it is understood that larger sized materials will give rise to improved UC properties, due to larger overall crystallite sizes possessing fewer luminescence quenching sites (i.e. surface defects). However, a reasonable assessment of the relative optical behaviors of α versus β phases of $NaYF_4$ possessing similar sizes is still lacking.

(3) Whereas pure $NaYF_4$ can be nominally synthesized, precise control over its shape and morphology is less obvious. That is, rationally altering the geometric configuration of $NaYF_4$ would provide corresponding insights into their active available physical surface area.

Therefore, in our work, we resolve all of these issues by systematically investigating the effect of varying reaction variables, such as reaction temperature, reaction time, as well as precursor stoichiometry in the hydrothermal synthesis of $NaYF_4$ nanocrystals in order to examine the critical reaction parameters that determine (or affect) the corresponding phase, size, and morphology of $NaYF_4$. Furthermore, on the basis of such understanding, we aim to deliberately control not only the physical structure but also the chemistry of the resulting family of $NaYF_4$ nanocrystalline motifs via a rational alteration of reaction conditions. That is, our work herein provides for a comprehensive strategy and a fundamental mechanistic appreciation of ways to provide reproducible and reliable control over the phase, size, and morphology of $NaYF_4$ *simultaneously*. As an illustrative example of the flexibility of our approach, we have demonstrated that by careful tuning of reaction parameters and in the absence of any surfactants, we can fabricate morphologically distinctive nanowire bundles not only possessing a pure hexagonal phase but also comprising constituent, ultrathin (diameter of ~ 5 nm) 1D subunits.

Overall, based upon our cumulative experimental results we report herein, the use of long reaction times, higher temperatures, and increased ammonia concentrations should likely promote formation of the β-phase. In terms of shape and morphology, with increasing reaction time, the shape evolves from small particles (with ~10 nm average diameter) to spherical aggregate structures (with average diameters of 308 ± 11 nm), and finally onto chromosomal-shaped, micron-sized (measuring ~ 2 μm in diameter and 5-8 μm in length) motifs. Moreover, as the reaction temperature was increased from 100 to 220°C, the morphology progressed from small particles (measuring ~150 nm average diameter) to one-dimensional nanorods (with dimensions of ~1 μm in diameter and ~5 μm in length) and ultimately onwards to chromosomal-shaped, micron-sized structures. Finally, when the concentration of ammonia was increased to 0.8 M under relatively mild, ambient synthesis conditions, the morphology consisted of nanowire bundles, with overall dimensions of ~1.5 μm in diameter and ~5 μm in length, composed of constituent, ultrathin (average diameter of ~ 5 nm), micron-long one-dimensional subunits. We should highlight that we are the first to produce and hence observe complex chromosomal-shaped, micron-sized structures pertaining to $NaYF_4$.

With respect to the intriguing idea of tailoring synthesis to impact upon the intrinsic physical properties of $NaYF_4$, there has been an interest in the synthesis of $NaYF_4$-based heterostructures with unique optical behavior.[18-20] Indeed, the presence of Förster resonance energy transfer (FRET) observed in such heterostructures could potentially render them as promising candidates for multiplex near-infrared imaging, not only due to the enhancement in the overall signal but also because several defining characteristics of the emission spectra itself, namely the numbers of peaks observed and their relative intensities, can be readily tuned by altering the excitation wavelength.[19] For example, with FRET, a reversible and stable NIR photoconductivity switch was fabricated using CdSe/$NaYF_4$ heterostructures that could up-convert NIR photons in $NaYF_4$ and use the as-generated excitons to create charge carriers within CdSe-based films.[20]

While these prior reports have provided preliminary experimental evidence for the potential of combining $NaYF_4$ and CdSe quantum dots (QDs) to create novel optically relevant composite structures, a more thorough and systematic study of this issue that transcends the use of either bulk or nanoparticulate-based heterostructures remains lacking. Moreover, we have been further inspired by previous work, incorporating similar classes of materials with unique optical properties as functional components of photovoltaic devices, such as either dye-sensitized solar cells (DSSCs) or quantum dot sensitized solar cells (QDSSCs).[21]

In particular, inclusion and integration of constituent light-converting materials including both up-converting and down-converting species have provided for a means for improving upon light harvesting efficiency and hence, the resulting solar cell performance.[22, 23] In practice, the presence of UC materials can transform lower-energy photons (> 900 nm) into higher-energy, visible photons (< 750 nm) that are easily absorbed by adjacent, associated light sensitizers, i.e. conjugated organic dye molecules or inorganic quantum dots.[24, 25] In a preliminary study, Li *et al.* confirmed the presence of effective energy transfer from $NaYF_4$: Yb, Tm to CdS, as manifested by the observation of fluorescence decay within the doped fluoride, and have incorporated such heterostructures within a photocatalytic configuration.[26] In terms of DSSCs, recent reports have suggested that increases from 5 to 20% in the overall cell efficiency can be expected in devices incorporating UC materials as compared with ‘dye-only’ controls.[21, 27, 28] As for QDSSCs, an increase in the overall cell efficiency from 3.43 to 4.37% was noted when CdSe QD - $NaYF_4$ hybrid nanostructures had been incorporated into TiO_2-based photoanodes.[25] Nevertheless, to dramatically improve upon the performance of UC material-based QDSSCs to render them as competitive as analogous DSSCs necessitates a more targeted approach.

Nevertheless, to the best of our knowledge, the fabrication of $NaYF_4$-CdSe heterostructures have focused exclusively on CdSe QD nanoparticles deposited onto $NaYF_4$ nanoparticles, i.e., 0D-0D heterostructures. Therefore, the key point of our study herein is that the morphology of the constituent materials can crucially influence the optical properties of the resulting heterostructures. To highlight the importance of this idea, we cite analogous previous work involving as-prepared $LaPO_4$-CdSe QD heterostructures, wherein we varied the morphology of the $LaPO_4$ constituent from its 1D to its 3D analogue with significant impact upon the degree of energy transfer measured between these two constituent components.[29]

Moreover, other reports associated with the formation of hybrid two-component heterostructures have demonstrated that the morphological characteristics of the energy acceptor species play a significant role in the observed energy transfer process. For instance, Erdem *et al.* fabricated hybrid composite structures composed of InGaN/GaN multiple quantum wells (MQWs) coupled with conjugated polymer nanoparticles (CPNs) in which energy transfer was found to have occurred from the MQWs to the CPNs.[30] Interestingly, non-radiative energy transfer (NRET) efficiencies were found to be nearly three-fold higher in MQW-CPN hybrids as compared with analogous hybrid systems in which the polymer constituent consisted of less organized and unfolded chains. Indeed, the morphology-dependent NRET process in that example could be attributed to corresponding alterations in the structural and chemical nature of the interface between the quantum wells and the polymer species; in effect, the observed energy transfer noticeably varied, depending upon the shape of the attached CPNs, i.e. the energy acceptor. By analogy, Stevens *et al.* have shown that in two-component nanoparticles (spherical, d ~ 80nm) composed of two distinctive types of fluorene-based amphiphilic polymeric molecules, the degree of monodispersity of the energy acceptor within the energy donor matrix (i.e., degree of phase segregation of the constituent donor and acceptor molecules) also had a significant impact upon the overall measured energy transfer efficiencies.[31]

Therefore, the objectives of our efforts within this Chapter are (i) to tune our chemical synthesis protocols to create relatively monodisperse distributions of energy donor species consisting of phase-pure, crystalline, and morphologically well-defined $NaYF_4$ with controllable size and shape and (ii) to incorporate these motifs into CdSe QD-$NaYF_4$ heterostructures in order to modulate their energy transfer behavior. Specifically, we have observed unique and distinctive optoelectronic interactions between CdSe QDs and the underlying $NaYF_4$ upconverting materials within the context of 0D-0D, 0D-1D, and 0D-3D nanocomposites, respectively. In so doing, our results have provided for a more comprehensive understanding of the structure-dependent energy transfer behavior between $NaYF_4$ and CdSe QDs within novel architectures, with implications for the rational design of new classes of photovoltaic devices.

6.2. Results and Discussion

6.2.1. Morphological Characterization

To prepare well-defined $NaYF_4$-based heterostructures in order to properly understand their optical properties, it is critically imperative to correlate the effects of tunable experimental parameters including reaction temperature, reaction time, and concentration of ammonia with the resulting phase and morphology of the constituent $NaYF_4$ structural motifs. To this end, we have employed a number of techniques including X-ray diffraction (XRD) and scanning electron microscopy (SEM) techniques to characterize the as-prepared samples.

6.2.1.1. Effect of reaction time and temperature

As discussed in the Introduction section, most of the previous reports have utilized high reaction temperatures (i.e. >200°C) coupled with long reaction times (i.e. longer than 10 h) in order to ensure formation of $NaYF_4$ nanocrystals with a pure β-phase. Herein, we show that similarly chemically pure products can be produced with relatively milder synthetic conditions.

First, we discuss the impact of reaction time. In these sets of experiments, the reaction temperature was fixed at 100°C and ammonia (i.e. standard solution with a concentration of 5 M) was used to adjust the pH of the reaction medium. Herein, the concentration of ammonia was kept constant at 0.2 M. According to the XRD results (Figure 6.1), the diffraction patterns of all four samples, corresponding to reaction times of 1 h, 2 h, 4 h, and 6 h, respectively, can be indexed to either the pure α-phase (cubic, JCPDS#77-2042) or the pure β-phase (hexagonal, JCPDS#16-0334) of $NaYF_4$, or a mixture of both, with no other apparent impurity peaks present. A detailed assignment of the various peaks detected is shown in each panel of Figure 6.1.

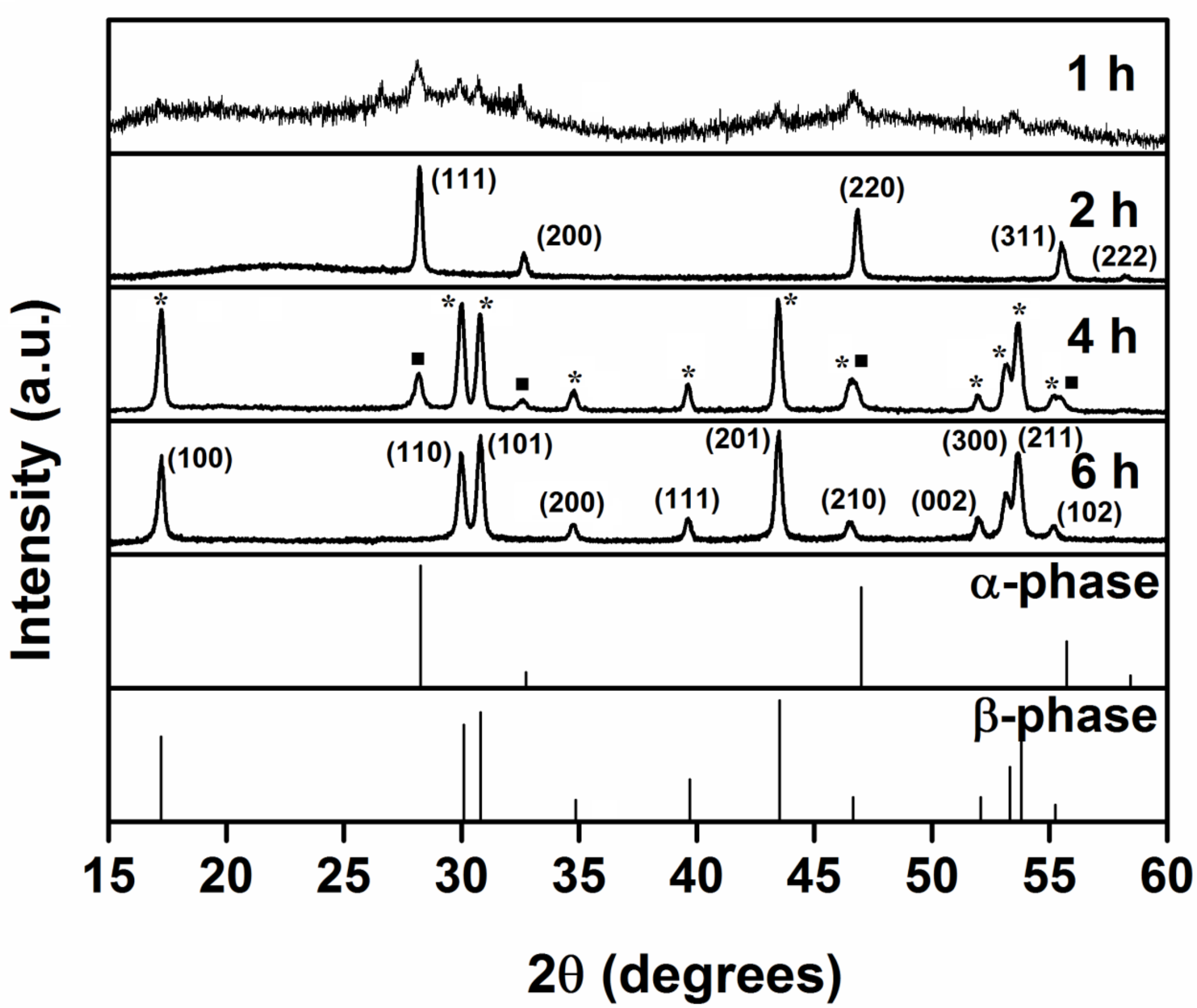

Figure 6.1. XRD patterns of as-prepared $NaYF_4$ samples, generated after *reaction times* of 1 h, 2 h, 4 h, and 6 h, respectively. The 'stars' designate hexagonal-related facets, while the 'squares' correlate with cubic-related facets. The reaction temperature has been fixed at 100°C, while the ammonia concentration has been set at 0.2 M, for all four of the samples processed herein.

In effect, a longer reaction time appears to promote formation of the β-phase. In fact, as the reaction time increases from 2 h to 6 h, a clear trend was apparent, implying the diminution of the α-phase coupled with the concomitant emergence of the β-phase. In term of morphology, with increasing reaction time, the shape evolves from small particles (with ~10 nm average diameter, Figure 6.2A) to spherical aggregate structures (with average diameters of 308 ± 11 nm, Figure 6.2B), and finally onto chromosomal-shaped, micron-sized (measuring ~ 2 μm in diameter and 5-8 μm in length, Figure 6.2C and 6.2D) motifs.

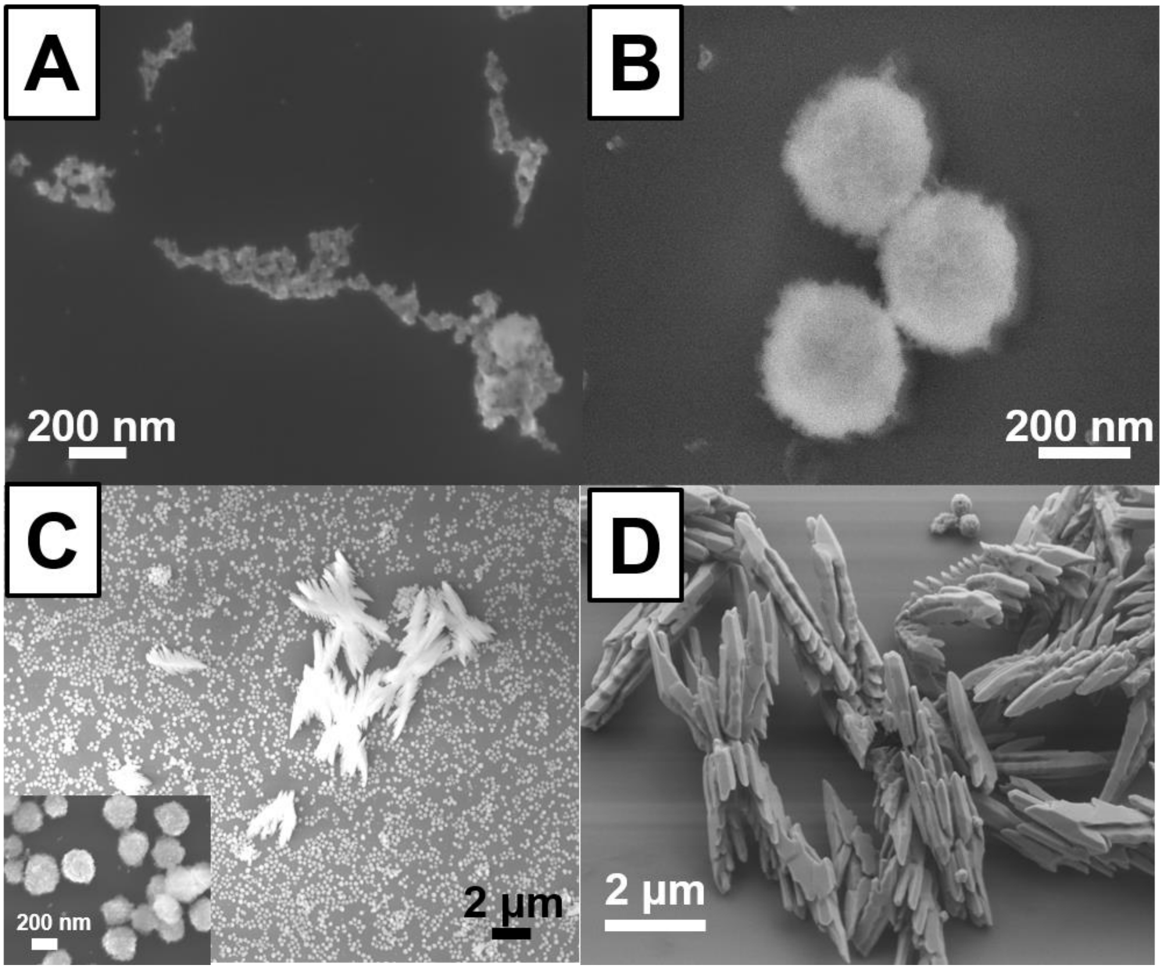

Figure 6.2. SEM images of as-prepared $NaYF_4$ samples, after *reaction times* of 1 h, 2 h, 4 h, and 6 h, respectively. The reaction temperature has been fixed at 100°C, whereas the ammonia concentration has remained constant at 0.2 M for all four samples shown herein.

Second, we probe the effect of reaction temperature. In this set of studies, the reaction time was fixed at 2 h, and the concentration of ammonia was set at 0.2 M. According to XRD, not unlike the case with varying reaction times, a higher reaction temperature appears to promote formation of the β-phase (Figure 6.3).

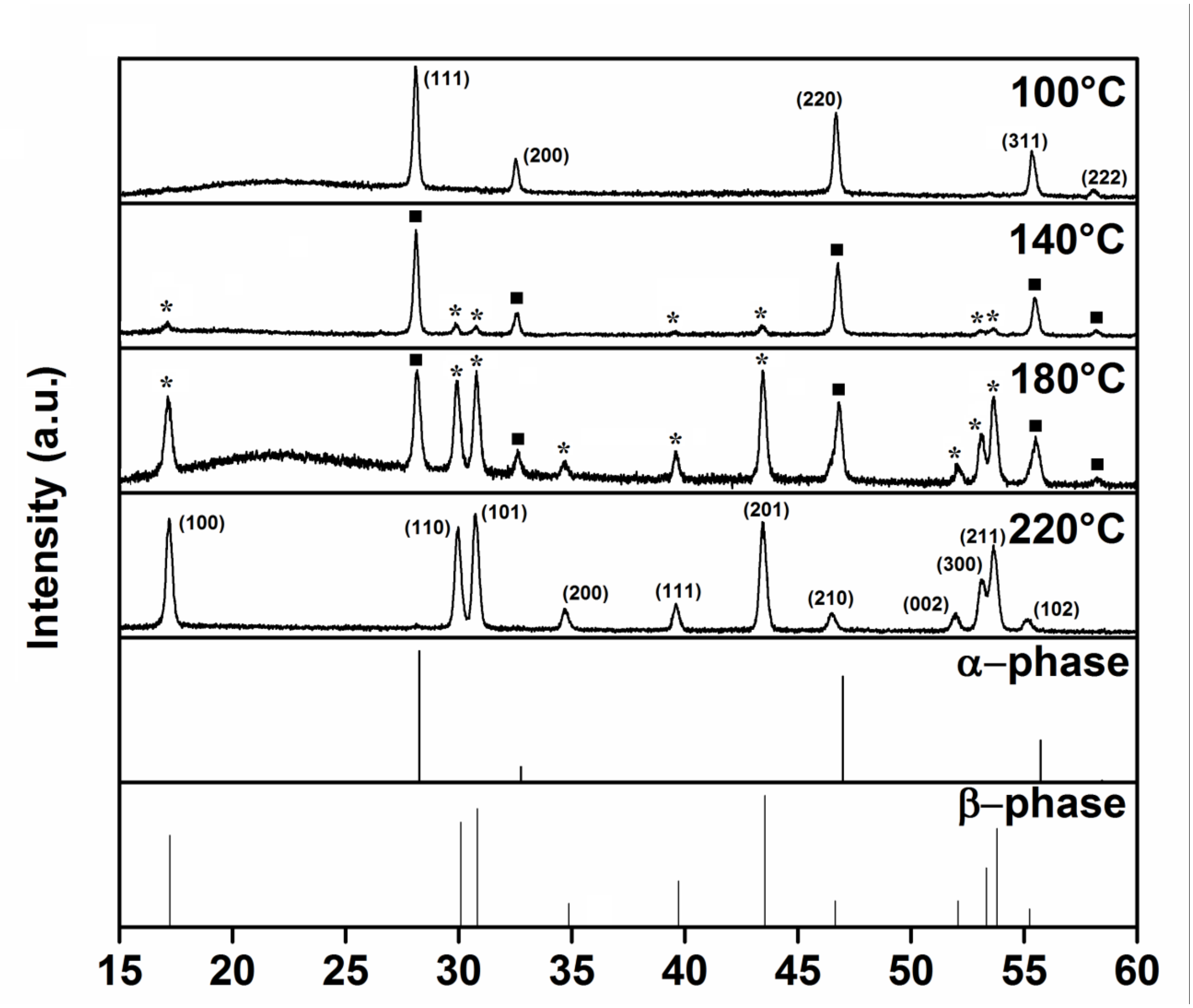

Figure 6.3. XRD patterns of as-prepared $NaYF_4$ samples, generated with *reaction temperatures* of 100°C, 140°C, 180°C, and 220°C, respectively. The ‘stars’ designate hexagonal-related facets, while the ‘squares’ correlate with cubic-related facets. The reaction time has been fixed at 2 h, while the ammonia concentration has been set at 0.2 M, for all four samples processed herein.

Moreover, as the reaction temperature was increased from 100 to 220°C, the morphology evolved from small particles (measuring ~150 nm average diameter) to one-dimensional nanorods (with dimensions of ~1 μm in diameter and ~5 μm in length) and ultimately onwards to chromosomal-shaped, micron-sized structures, with mixtures of these aforementioned shapes apparent in sample aliquots isolated between these two temperature intervals (Figure 6.4, panels A through D).

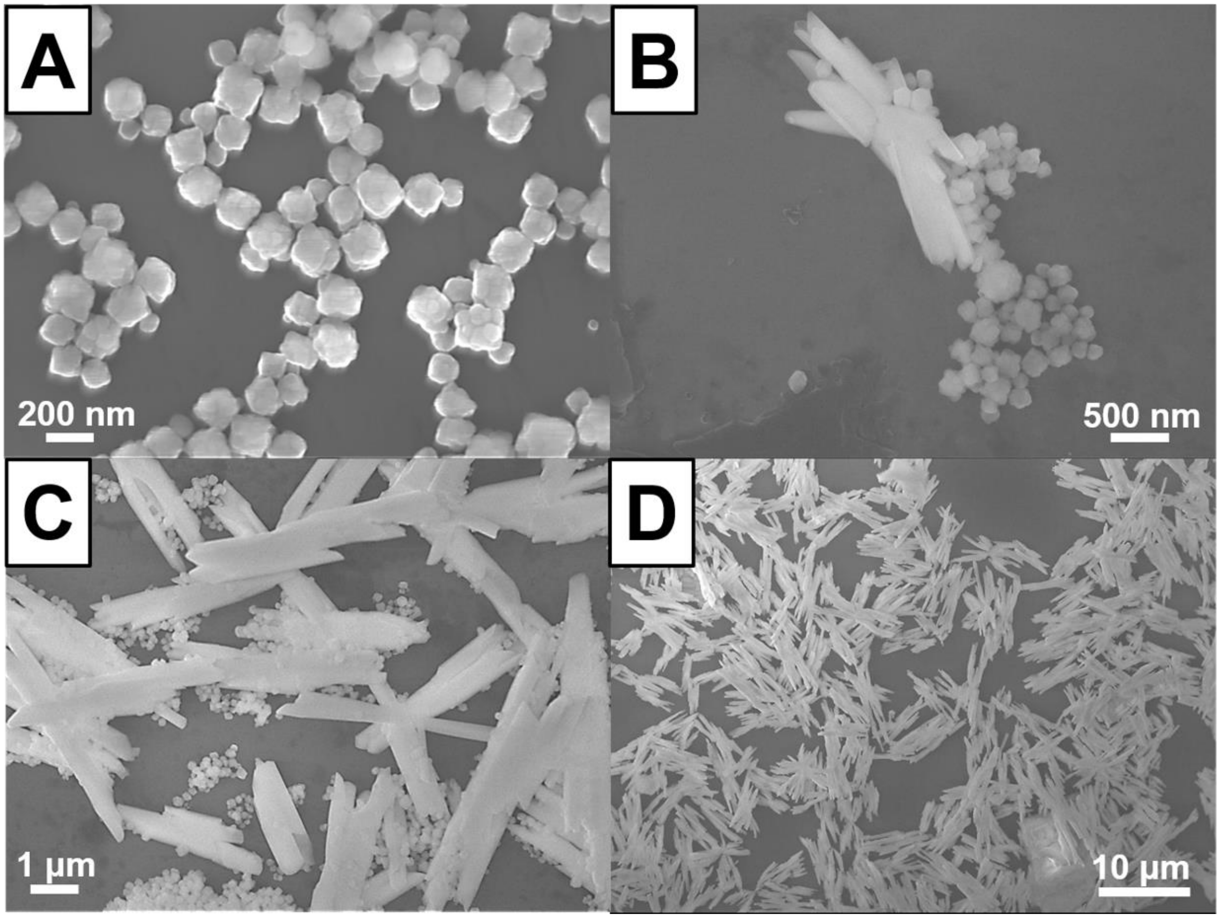

Figure 6.4. SEM images of as-prepared $NaYF_4$ samples, created with *reaction temperatures* of 100°C, 140°C, 180°C, and 220°C, respectively. The reaction time has been fixed at 2 h, while the ammonia concentration has remained constant at 0.2 M, for all four samples shown herein.

Therefore, with respect to both reaction time and reaction temperature, an increase in either parameter can correspond to an elevated input of thermal energy, thereby favoring the formation of the β-phase, which happens to be the most thermodynamically stable phase, as opposed to the α-phase,[32] an observation consistent with other previous reports.[33, 34] However, our synthetic conditions for the formation of β-phase herein are significantly milder (i.e. lower reaction temperature and shorter reaction time) as compared with other reports, a reality possibly attributable to the presence of ammonia. Detailed explanations concerning the precise role of ammonia will be discussed later.

6.2.1.2. Effect of the concentration of $NH_3 \cdot H_2O$

For these sets of experiments, the reaction temperature was set at 100°C with a reaction time of 2 h, in order to further examine the effect of the addition of ammonia. The reason that we chose these two experimental parameters is that we are expecting a transition from α-phase to β-phase, as we vary ammonia concentration. Hence, we prefer, for our starting point, a set of experimental synthesis conditions that favor the formation of the α-phase.

According to the XRD results (Figure 6.5), the use of a relatively larger concentration of ammonia (i.e. 0.4 M & 0.8 M, respectively), as opposed to comparatively lower concentrations (i.e. 0 M and 0.2 M, respectively), appears to bolster the formation of the β-phase.

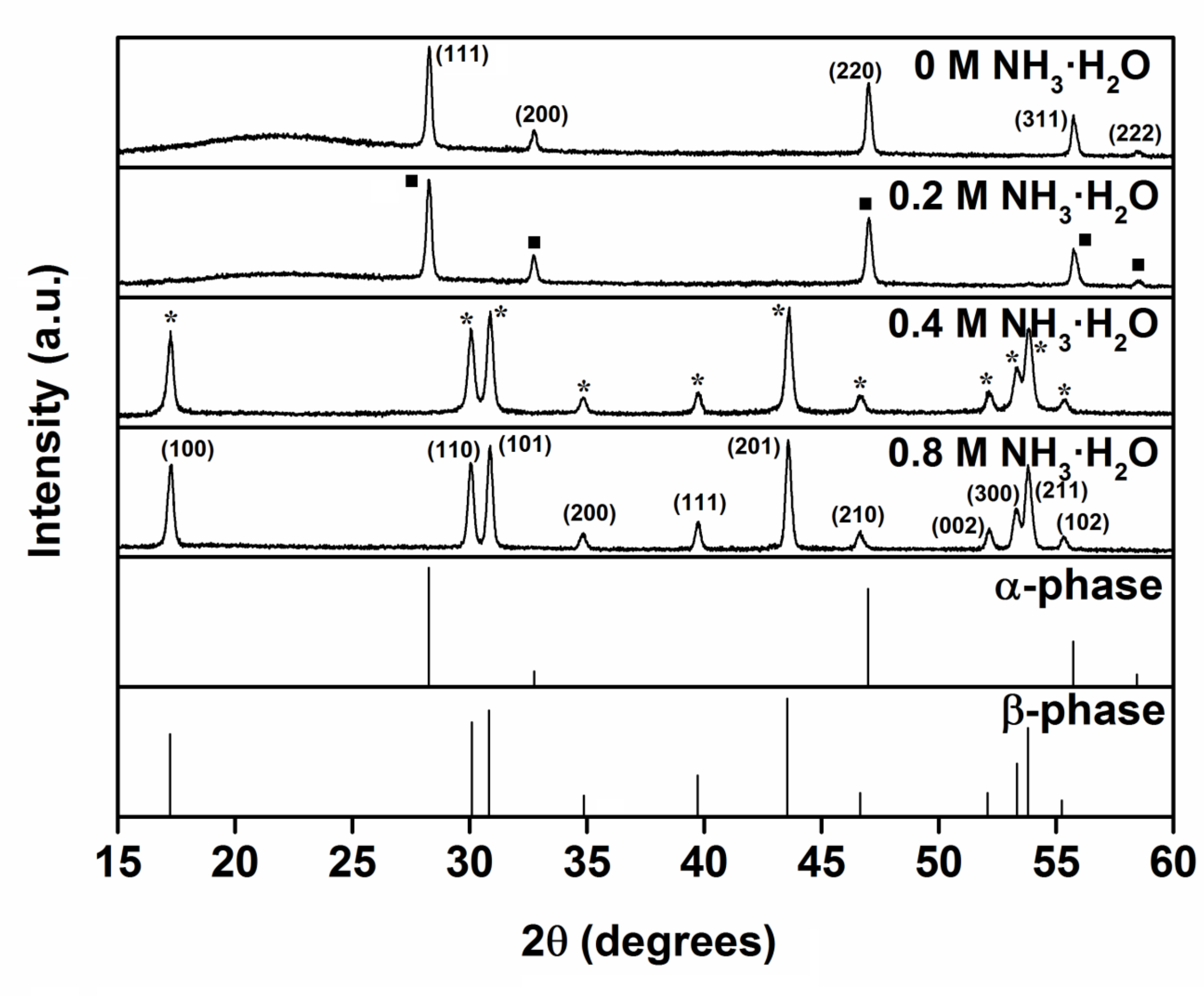

Figure 6.5. XRD patterns of as-prepared NaYF$_4$ samples, produced with *ammonia concentrations* of 0 M, 0.2 M, 0.4 M, and 0.8 M, respectively. The 'stars' designate hexagonal-related facets, while the 'squares' correlate with cubic-related facets. The reaction time has been fixed at 2 h, while the reaction temperature has been set at 100°C, for all four samples processed herein.

Meanwhile, the evolution of morphology is demonstrated in Figure 6.6. Specifically, when the concentration of ammonia was increased to 0.8 M, the morphology evolved into nanowire bundles, with overall dimensions of ~1.5 μm in diameter and ~5 μm in length, composed of constituent, ultrathin (d ~ 5 nm), micron-long one-dimensional subunits, as shown in Figure 6.6D.

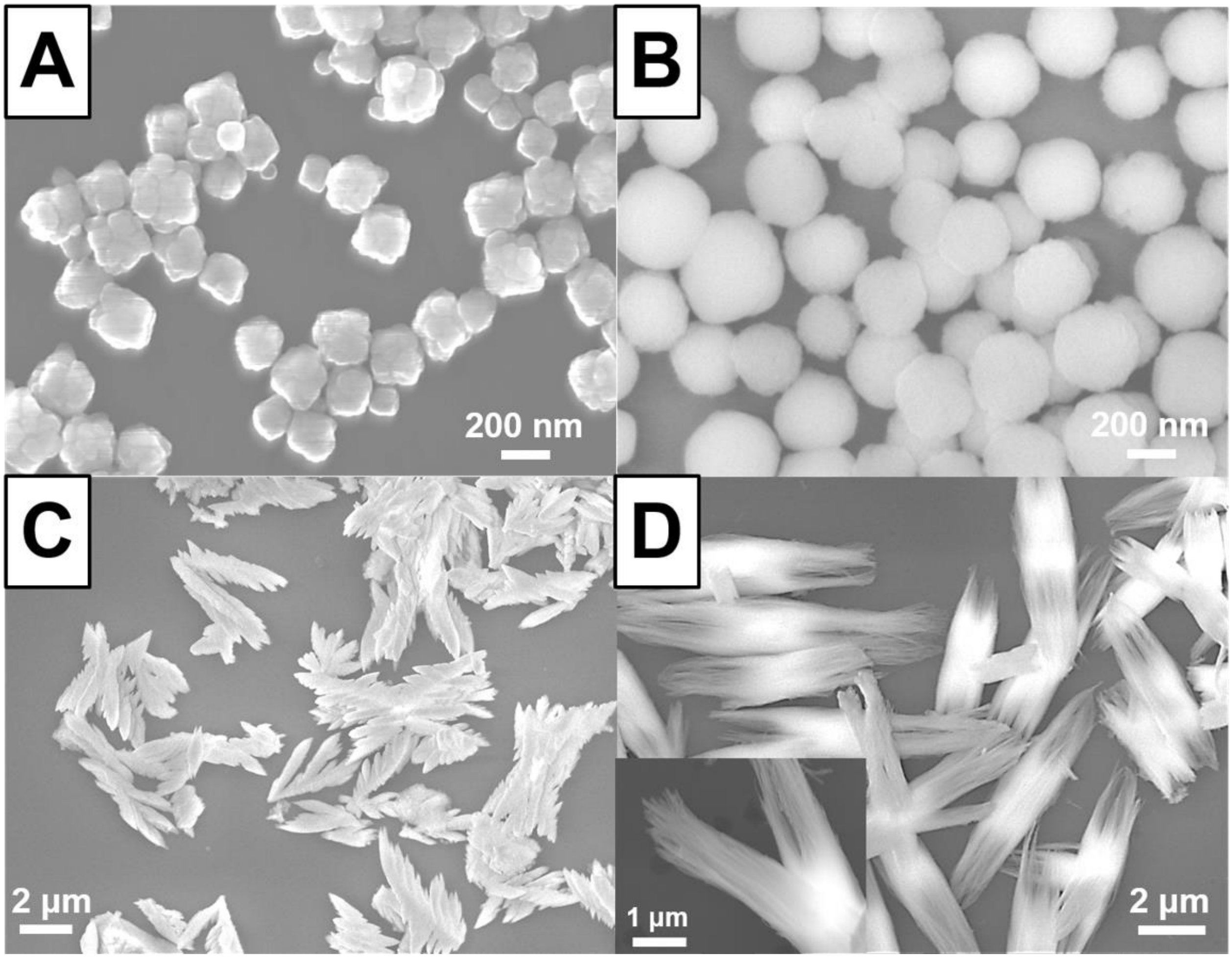

Figure 6.6. Representative SEM images of as-prepared $NaYF_4$ samples, created with *ammonia concentrations* of 0 M, 0.2 M, 0.4 M, and 0.8 M, respectively. The reaction time has been fixed at 2 h, while the reaction temperature has been set at 100°C, for all four samples herein.

We emphasize that these specific motifs have rarely if ever been observed with fluorides using similar synthesis approaches. In essence, we believe that the effect of ammonia concentration is superior to that of either reaction time or reaction temperature, as it gives rise to a hexagonal phase even under reaction time (2 h) and reaction temperature (100°C) conditions that appear to largely facilitate the formation of the cubic phase. Interestingly, the crystalline domain size calculated using the Debye-Scherrer equation can be computed to be 32.1 nm, 30.7 nm, 31.3 nm, and 30.5 nm for the various 0 M, 0.2 M, 0.4 M, and 0.8 M samples, respectively. In other words, despite their distinctive phases and shapes detected at a macroscopic level, the sizes of their constituent subunits are rather strikingly similar. This observation may imply that the growth mechanism for all of these samples may actually be governed by the same underlying regime, and that these samples may therefore represent distinctive and unique growth stages, not only associated with a specific growth mechanism but also accessible by varying the amount of ammonia present.

6.2.1.3. Detailed Structure and Crystallinity

We have carefully examined both the representative isotropic (nanospheres) and anisotropic (nanowire bundles) structures we have generated by means of high resolution TEM, as shown in Figure 6.7.

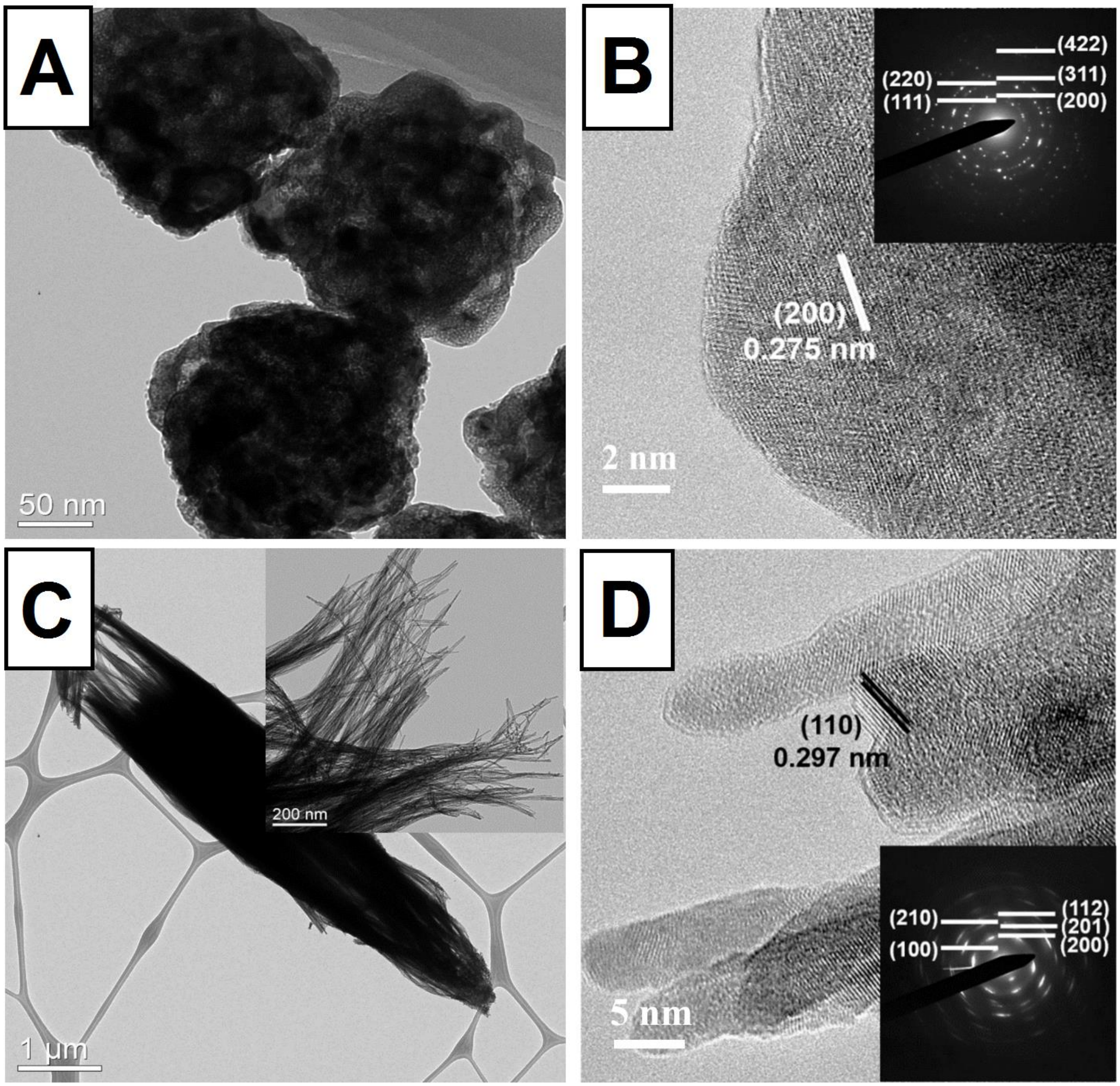

Figure 6.7. Representative (A) TEM image and (B) corresponding high-resolution TEM image of **α-phase** nanoparticles. Typical (C) TEM images and (D) coupled high-resolution TEM image of **β-phase** nanowire bundles. The insets to (B) and (D) are associated SAED patterns of these respective regions of the sample.

First, depending on the concentration of ammonia used (i.e. 0 versus 0.2 M), the diameters of the spheres may vary from ~150 nm to ~300 nm. The measured *d*-spacing of 0.275 nm can be ascribed to the (200) plane of cubic $NaYF_4$, which is consistent with a standard XRD pattern (i.e. JCPDS #77-2042). Moreover, the SAED pattern can be indexed to the (111), (200), (220), (311), and (422) planes, respectively, of cubic $NaYF_4$, as well. Overall, the electron microscopy results confirmed the nature of the observed crystal structure, which corresponds perfectly well with that of a highly crystalline cubic phase of $NaYF_4$.

On the other hand, we isolated a truly unique and novel morphological motif, i.e. nanowire bundles (synthesized with 0.8 M ammonia), possessing overall lengths of ~5 µm and widths of ~1.5 µm, whose crystal structure was consistent with that of a β-phase. We found these nanowire bundles to be composed of constituent component sub-units of long, ultrathin (~5 nm) nanowires with overall lengths of several microns. In this case, the measured *d*-spacing of 0.297 nm can be ascribed to the (110) plane of hexagonal $NaYF_4$, and is consistent with a standard XRD pattern (JCPDS #16-0334). In addition, the SAED pattern can be indexed to the (100), (200), (201), (210), and (112) planes, respectively, of hexagonal $NaYF_4$, as well. In effect, the electron microscopy data substantiated and verified the proposed crystal structure, corresponding perfectly well with that of a highly crystalline hexagonal phase of $NaYF_4$.

6.2.1.4. Discussion of reaction mechanism

Herein, we have experimentally and independently probed the effects of (1) reaction time, (2) reaction temperature, and (3) ammonia concentration upon the resulting morphology and chemical composition of as-prepared $NaYF_4$ nanocrystals.

As discussed in previous sections, it is not surprising that longer reaction times as well as higher reaction temperatures appear to induce a phase conversion, i.e. from α-phase to β-phase since the α-phase is the kinetic product whereas the β-phase represents the more stable, thermodynamic product.[32] In addition, there are many prior reports on this issue, claiming that a minimum of 10-12 h of reaction time as well as reaction temperatures higher than 200°C are necessary in order to generate the β-phase.[16, 35, 36]

Interestingly, with the use of ammonia, we are able to produce samples with a predominant β-phase at temperatures as low as 100°C and with reaction times as short as 2 hours. To the best of our knowledge, this desirable reaction parameter space has scarcely been reported, even with similar systems that utilize either hydrothermal or solvothermal synthesis.

Under the present experimental conditions, we observed that ammonia (hydroxide ions) concentration yields two major effects in terms of not only determining crystal structure but also lowering the reaction temperature and time needed to synthesize β-phase $NaYF_4$. As we have previously discussed in Section 6.2.1.2, the formation of all of these structures may be governed by an identical growth mechanism. We have indeed proposed a plausible path of morphological evolution, summarized in Figure 6.8, wherein the as-prepared nanowires bundles represent the final achievable end product.

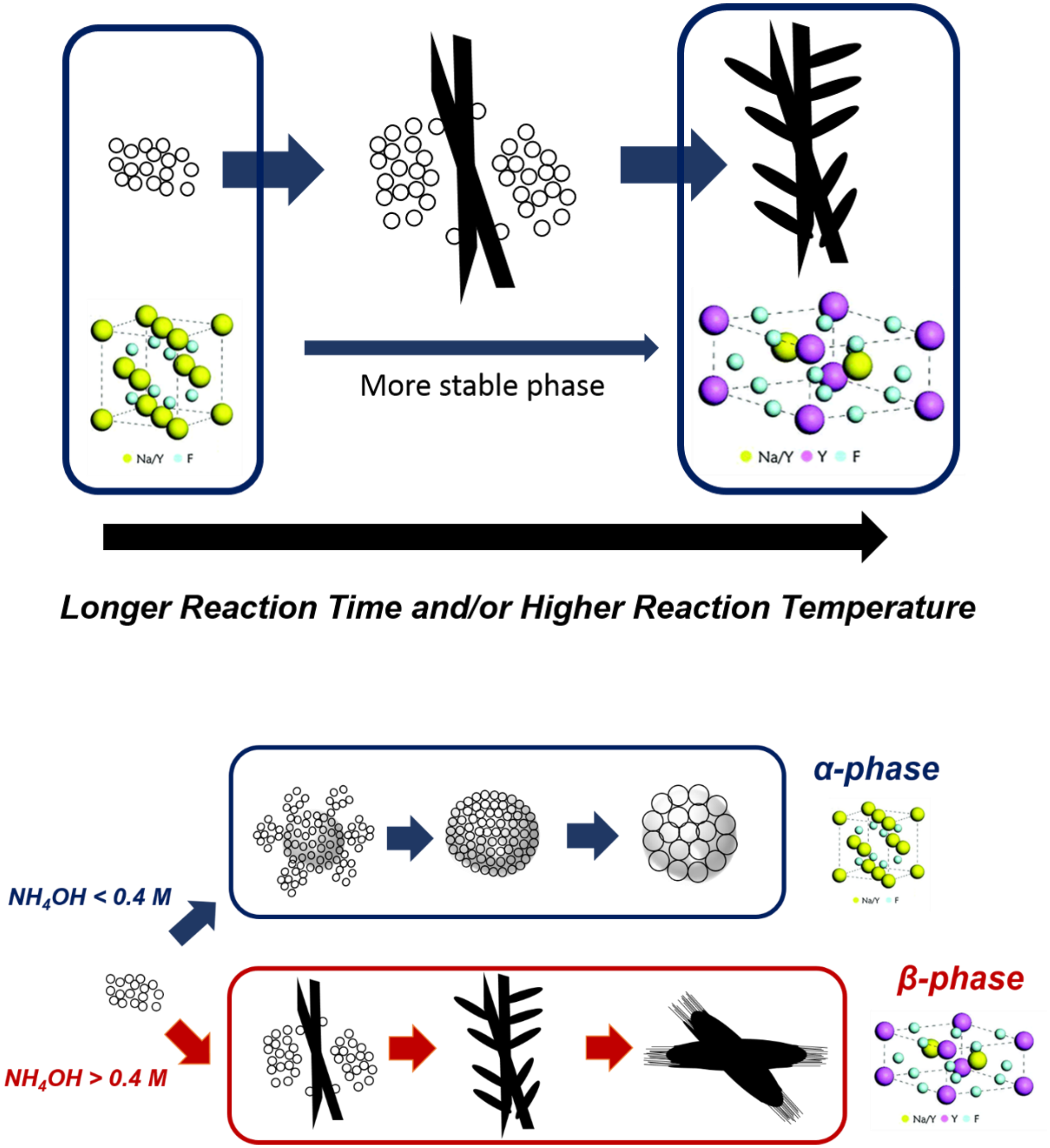

Figure 6.8. Top: Schematic representation of the effect of reaction time/reaction temperature upon the growth mechanism of as-prepared $NaYF_4$ nanocrystals. **Bottom:** Schematic representation of the effect of the concentration of $NH_3 \cdot H_2O$ upon the growth mechanism of as-prepared $NaYF_4$ nanocrystals.

First, we observed that the reaction temperature and time needed to synthesize β-phase of $NaYF_4$ is considerably lower and shorter, respectively, as compared with previous reports. Hypothetically, in the presence of an excess of hydroxide ions in the reaction, $Y(OH)_3$ can be easily generated as an intermediate species prior to the ion exchange process needed to form $NaYF_4$, a scenario which can facilitate the formation of hexagonal β-$NaYF_4$, because as-generated $Y(OH)_3$ compounds possess the same crystal structure and space group as that of the β-phase of $NaYF_4$.[15] In other words, the presence of $Y(OH)_3$ due to an excess quantity of hydroxide ions during the synthesis of $NaYF_4$ can selectively favor the creation and production of the β-phase composition as opposed to the analogous α-phase one.

A second key finding, consistent with previous reports, is that OH^- ions can be preferentially absorbed onto the (0001) surface of $NaYF_4$ and can subsequently inhibit the nucleation and crystal growth along the (0001) orientation in the absence of any ligands/surfactant,[37, 38] thereby yielding the hexagonal phase of $NaYF_4$ especially at higher ammonia concentrations. This scenario is consistent with the explanation of the morphological evolution of 1D hexagonal Zn_2SiO_4 structure in the presence of hydroxide ions.[39] Hence, when the concentration of ammonia is higher than the so-called ‘tipping point’ (> 0.4 M ammonia in our case, i.e. pH > 10) within our growth mechanism, growth of the (0001) surface is more significantly hindered. Therefore, under these higher pH conditions, the prospect of isotropic crystal growth (i.e., marked by blue arrows in the bottom schematic in Figure 6.8), which would have resulted in the formation of α-phase crystals possessing a spherical morphology, is suppressed. That is, through the controlled adsorption of OH^-, the nuclei of $NaYF_4$ likely form with a β-phase composition, and subsequently grow into anisotropic 1D-like motifs (i.e., marked by red arrows in the bottom schematic in Figure 6.8).

As a separate and corollary issue, we have also observed an inherent morphological preference associated with both phases. Specifically, the α-phase tends to be consistently associated with an isotropic morphology (i.e., small nanoparticles or aggregated spheres), whereas the β-phase is characterized by the presence of anisotropic structures (i.e., chromosomal-shaped motifs in addition to nanowire bundles). We attribute this phenomenon to the inherent crystal structures involved with each of these phases, as has been investigated in previous reports.[40] Specifically, isotropic growth of particles was induced by the presence of cubic $NaYF_4$ seeds which possess an isotropic unit cell structure, in order to minimize the surface energy of crystal facets. Conversely, the production of anisotropic structures, i.e. either chromosomal or nanowire bundles, is a consequence of selective growth along crystallographically reactive directions (i.e. the *c*-axis) of hexagonal $NaYF_4$ seeds, which are associated with the analogous formation of anisotropic unit cell structures.

6.2.2. Upconversion Properties of $NaYF_4$ nanostructures

The UC properties of our as-prepared samples have been examined. Significantly, all of the four lanthanide-co-doped $NaYF_4$ nanostructured samples synthesized under different conditions, specifically with different ammonia concentrations, maintain UC capabilities. Figure 6.9 depicted the corresponding spectra, where there are basically three emission bands located at 525, 539, and 653 nm, respectively.

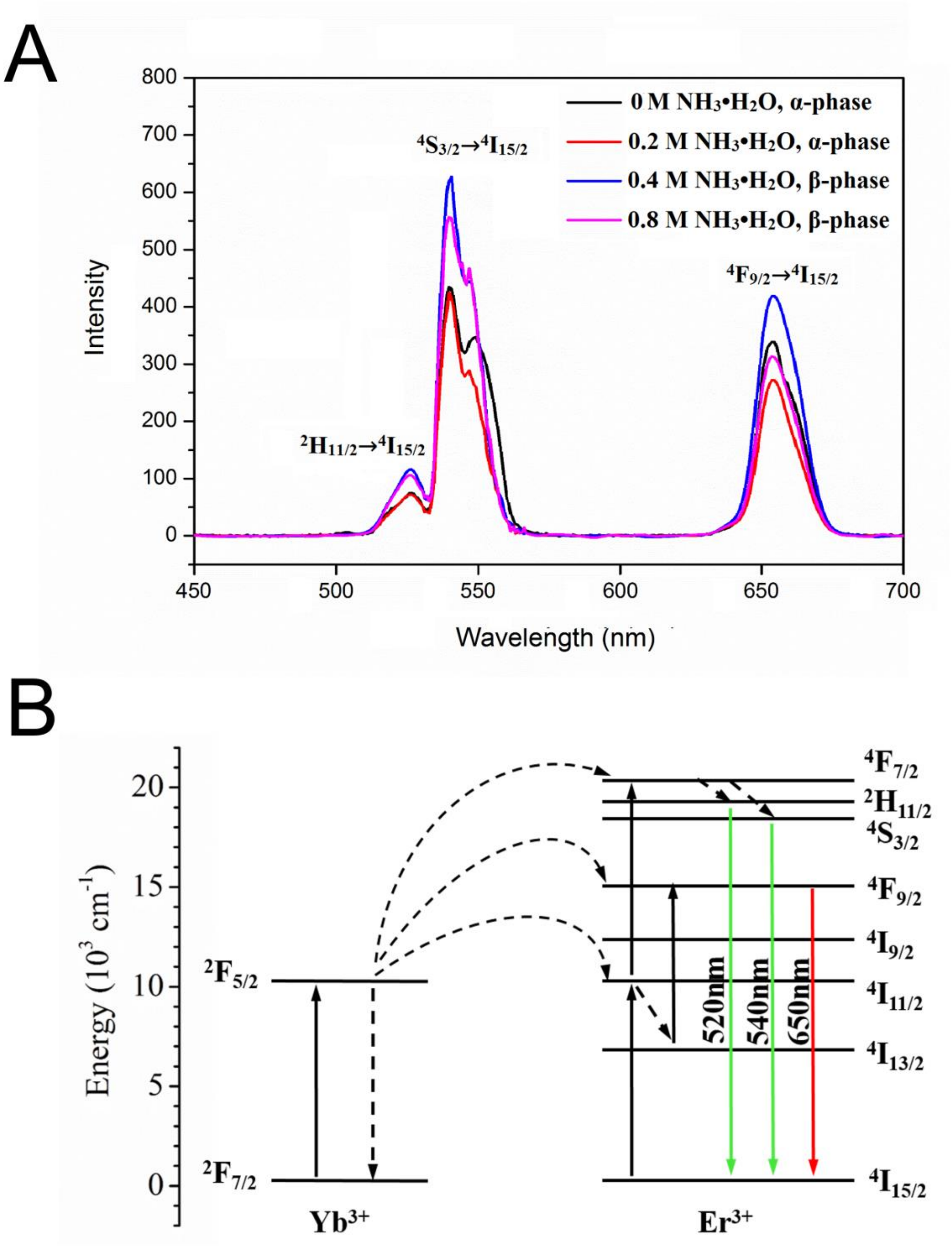

Figure 6.9. (A) Upconversion PL emission spectra of $NaYF_4$: Ln^{3+} nanocrystals excited by a 980 nm laser. Four different curves represent samples synthesized with 0 M ammonia, i.e. nanoparticles (black); samples generated with 0.2 M ammonia, i.e. aggregated nanospheres (red); sample produced with 0.4 M ammonia, i.e. chromosomal-shaped motifs (blue); and samples fabricated with 0.8 M ammonia (pink), respectively. (B) The corresponding energy diagram is

presented, highlighting all of the relevant transitions.

According to the energy diagram in Figure 6.9B, the observed peaks correlate with multi-phonon relaxation behavior from the excited states of $^2H_{11/2}$, $^4S_{3/2}$, and $^4F_{9/2}$ to the ground state of $^4I_{15/2}$, respectively. The peak positions are in agreement with analogous data from literature associated with the UC luminescence of Er and Yb co-activated $NaYF_4$.[38, 41, 42] It is also possible that a portion of the incident photon energy may have been dissipated through non-radiative relaxation processes, associated with the $^4I_{11/2}$ to $^4I_{13/2}$, $^4F_{7/2}$ to $^2H_{11/2}$, and $^4F_{7/2}$ to $^4S_{3/2}$ transitions, respectively.[43, 44]

Amongst these samples, the α-phase, characterized by a spherical morphology with average diameters of ~ 150 nm and ~300 nm, that had been prepared both in the absence of ammonia and with 0.2 M ammonia concentrations, respectively, yielded a lower spectral peak intensity as compared with the β-phase products, the latter of which were typified by either chromosomal or nanowire bundle-shaped motifs which had been generated with either 0.4 M or 0.8 M ammonia concentrations, respectively. These observations are not surprising, since the former two possessed an α-phase, whereas the latter two were characterized by a β-phase, which are intrinsically different in terms of UC efficiency.

The origin behind this observation lies in the differential amounts of non-harmonic phonons within the cubic and hexagonal lattices.[45] Specifically, by comparison with the highly-ordered cation distribution within the hexagonal lattice, it has been hypothesized that in the cubic phase, Na^+ and lanthanide cations randomly substitute with each other in the lattice, thereby leading to the production of additional non-harmonic phonon modes.[46] Moreover, between the two β-phase samples, we noted that the chromosomal-shaped sample appeared to give rise to a slightly higher emission intensity as compared with that of the nanowire bundles.

One possible reason for the relatively higher UC luminescence intensity associated with the chromosomal-shaped sample relative to that of the nanowire bundles is that the actual crystalline domain sizes may be different for these two disparate structures. From the X-ray diffraction pattern, it is evident that they possessed rather similar crystallinity with comparable crystalline domain sizes of around 30 nm. However, both HRTEM images and the corresponding SAED pattern strongly indicate that towards the end of the "tips" of nanowire bundles, the domain size is actually dramatically reduced to several nanometers.

If we consider this idea in more detail and compare the SAED pattern in Figure 6.7D, which is representative of the area near the "tips", with the corresponding SAED pattern in Figure 6.7B, which was collected on a region of nanoparticles, we find that the former consists of a pattern of 'smeared lines' as opposed to 'discrete and isolated points' for the nanoparticles. These results imply that the crystallite sizes at the tips appear to be much smaller than those near the "center" section of the nanowire bundles themselves. Therefore, it is entirely possible that there are localized structural discrepancies within the nanowire bundle itself. In other words, the center of the bundles might possess locally greater crystallinity as compared with the "tip" region.

In general, photoluminescent properties can be significantly affected by both particle size as well as crystallite domain size, and the PL intensity (i.e. quantum yield) typically increases with increasing constituent particle and crystallite size.[47, 48] Nonetheless, our nanowire bundles appear to encompass heterogeneity that is associated with the simultaneous presence of at least two different crystalline size regimes. Although it is not within the scope of this paper, we believe that the presence of increased surface defects due to lower crystallite size at the "tips" of our nanowire bundles can act as luminescent quenching sites, thereby inducing poorer PL performance, especially in the context of lower intensity ratios associated with the ${}^4S_{3/2}$–${}^4I_{15/2}$

(near 545 nm) to $^4F_{9/2}$–$^4I_{15/2}$ (near 650 nm) transition. Hence, these nanowire bundles, relative to the larger chromosomal-shaped sample, which also possessed a β phase, maintained not only a homogeneous structure but also a monodisperse crystalline size distribution, all of which likely induce advantageous optical behavior.

6.2.3. Structure-Dependent Optical Properties of $NaYF_4$-CdSe QD heterostructures

As an extension of prior studies used to further explore the possible interplay between the $NaYF_4$ phosphor and other types of light-emitting materials, we have synthesized and characterized a series of $NaYF_4$-CdSe QD heterostructures, incorporating as-prepared CdSe QDs as well as crystalline $NaYF_4$ nanocrystals, possessing various types of as-prepared morphologies, i.e., 0D, 1D, and 3D motifs, as described earlier. Specifically, the relevant synthetic protocols for all of the constituent components as well as of the heterostructures are discussed in the Experimental section. We believe the interaction responsible for the formation of the heterostructures does not necessarily involve the creation of a formal bond. Rather, an electrostatic attraction between oleic acid-capped $NaYF_4$ and hexadecylamine-capped CdSe QDs is likely involved, due to the presence of opposite and complementary charges on the surfaces of these two constituent nanostructures induced by the presence of the different capping agents, according to a previous report.[20]

Optical characterization results for as-prepared CdSe QDs have been included in Figure 6.10.

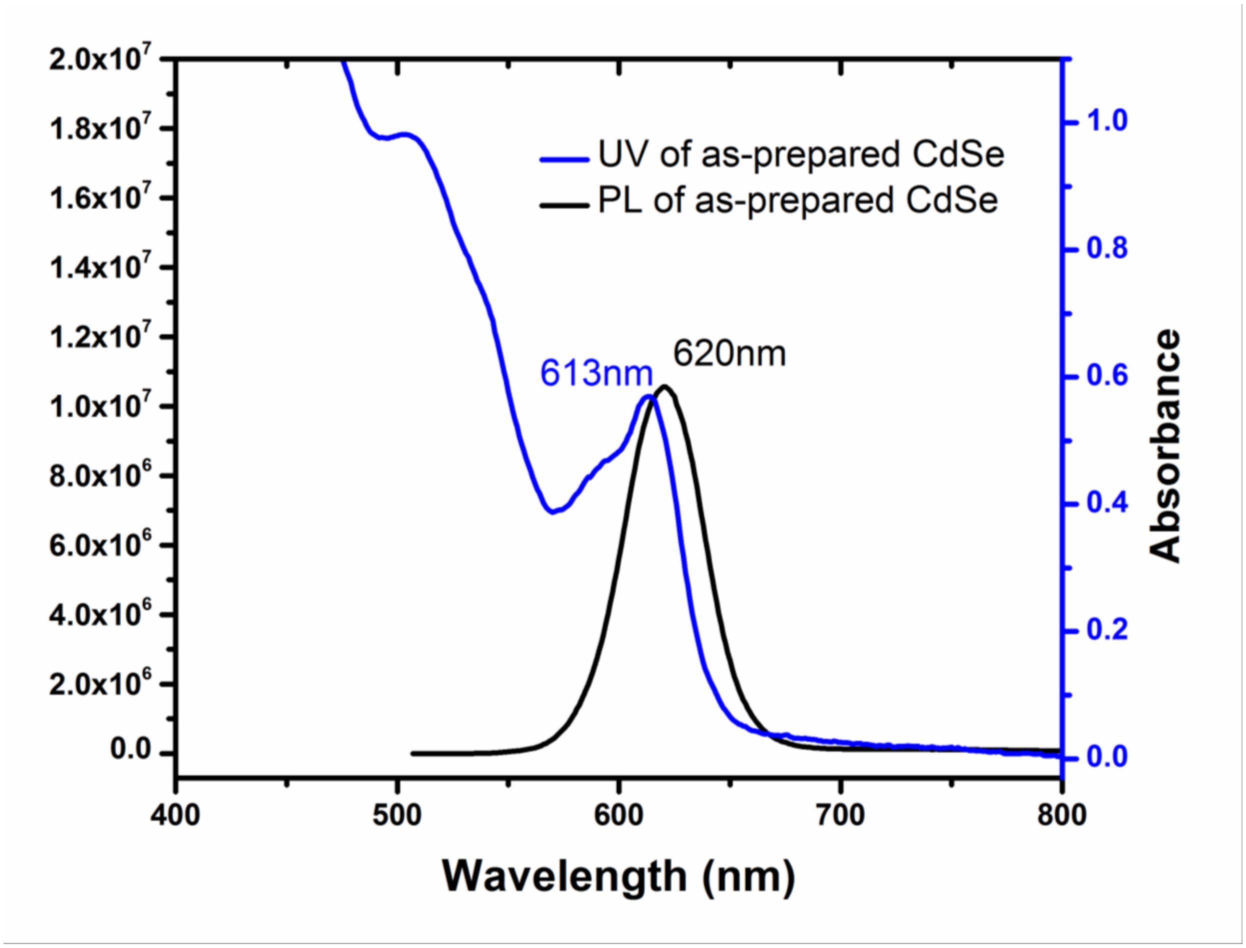

Figure 6.10. UV-visible and corresponding photoluminescent spectra of as-synthesized CdSe quantum dots. The calculated size of the QDs is 5.1 nm.

The data indicate that the QDs possess a high photoluminescent output, i.e. a high quantum yield, as well as a narrow, monodisperse size distribution, centered at 5.1 nm.

First, we have characterized the relevant morphologies and chemical compositions of as-prepared heterostructures, utilizing TEM and EDAX spectra, as depicted in Figures 6.11 and Figure 6.12, respectively.

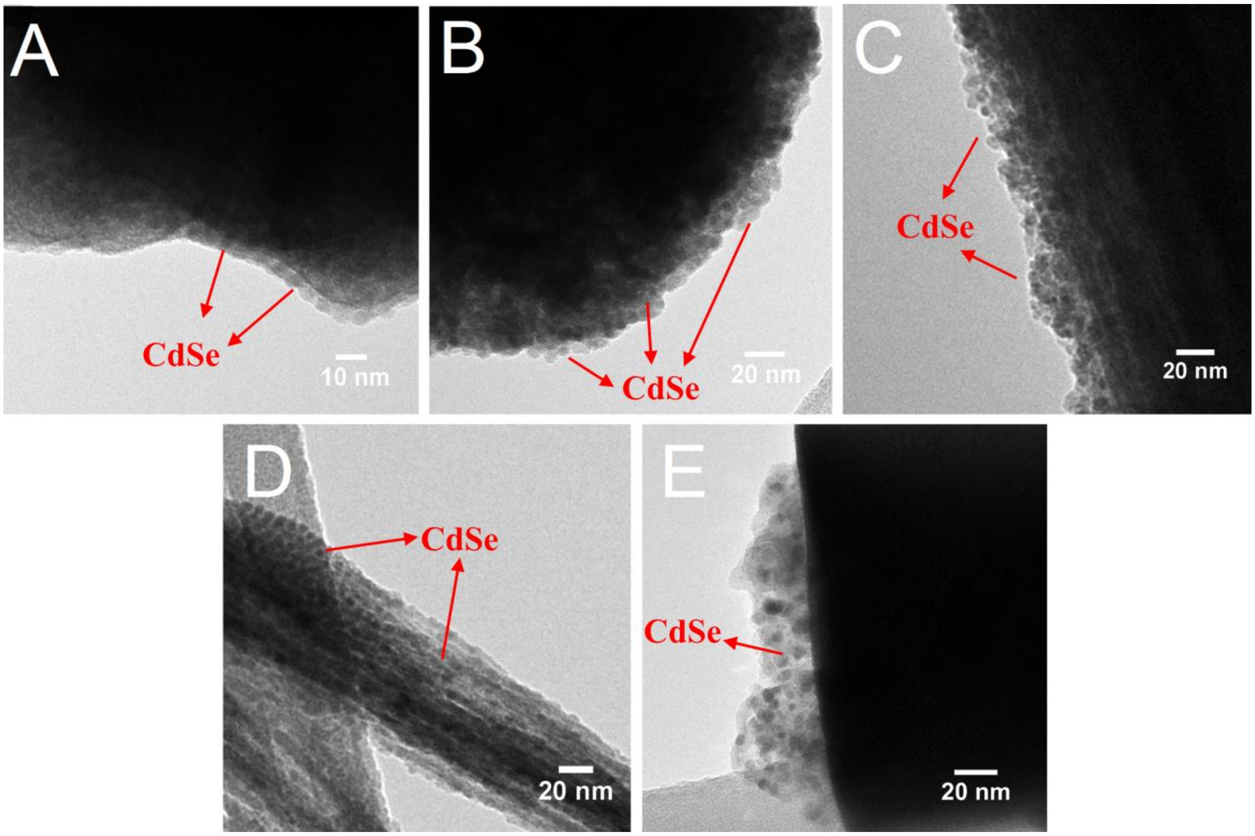

Figure 6.11. Representative TEM images of heterostructures composed of (i) CdSe quantum dots attached to (ii) 0D and (iii) 3D $NaYF_4$ nanostructures, which had been synthesized with (A) 0 M ammonia, (B) 0.2 M ammonia, (C) 0.4 M ammonia, and (D) 0.8 M ammonia, respectively, as well as of (iv) separately-prepared (E) 1D $NaYF_4$ nanorods, respectively.

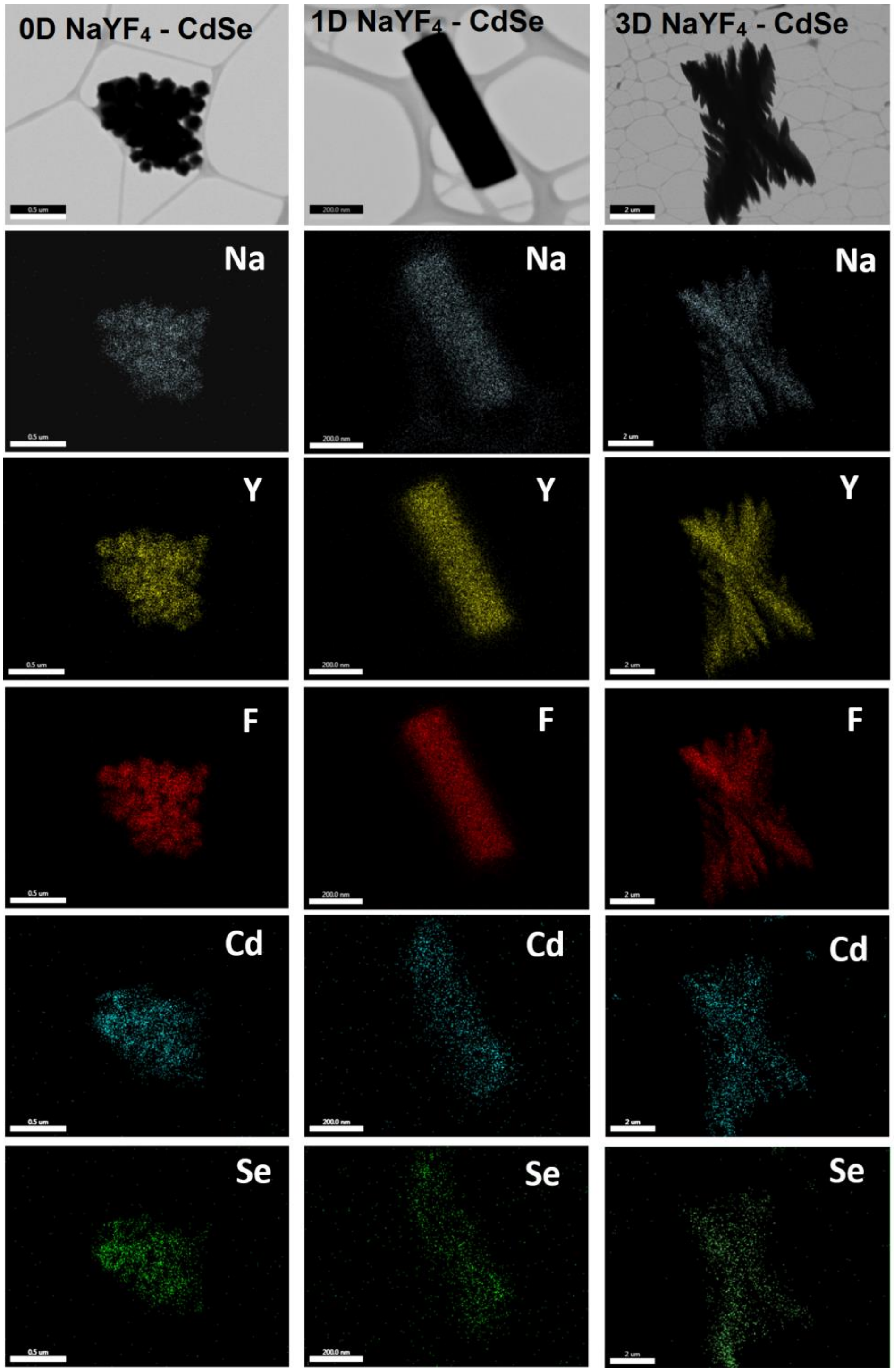

Figure 6.12. Representative STEM images as well as elemental mapping data associated with heterostructures composed of CdSe QDs coupled with 0D $NaYF_4$ (leftmost column), 1D $NaYF_4$ (middle column), and 3D $NaYF_4$ (right-side column), respectively. Scale bars for the three columns are 0.5 µm, 200 nm, and 2 µm, respectively.

Based upon the original literature, the average dimensions of the 1D nanorods should be ~100 to 200 nm in diameter with lengths of ~1 µm,[41] an assertion corroborated by the corresponding STEM image in Figure 6.12. Representative TEM images have demonstrated that the CdSe QDs possessing an average diameter of ~5 nm have been successfully attached onto the external surfaces of as-generated $NaYF_4$ nanocrystals. The corresponding 0D and 3D $NaYF_4$ depicted in Figure 6.12 denote samples synthesized under conditions of either 0 M (i.e. nanoparticles with average diameters of ~150 nm) or 0.4 M (i.e. chromosomally-shaped structures) of ammonia, respectively. Similar elemental mapping images of the heterostructures, implying a uniform and well-dispersed distribution of QDs onto the underlying $NaYF_4$ motifs, created using either 0.2 M (i.e. nanoparticles with average diameters of ~300 nm) or 0.8 M (i.e. nanowire bundles) of ammonia, were highlighted in Figures 6.13 and Figure 6.14, respectively.

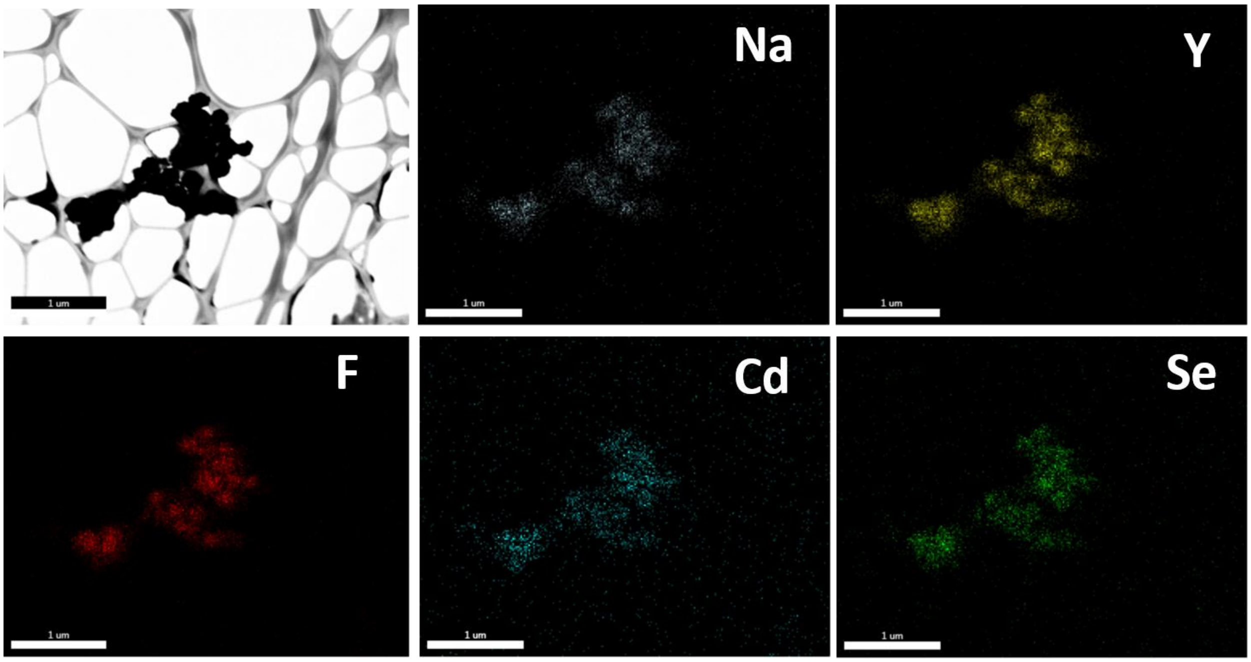

Figure 6.13. Representative elemental mapping images of 0D-0D $NaYF_4$-CdSe QD heterostructures, created using a nanoparticulate $NaYF_4$ sample (synthesized with 0.2 M ammonia), coupled to as-prepared CdSe quantum dots.

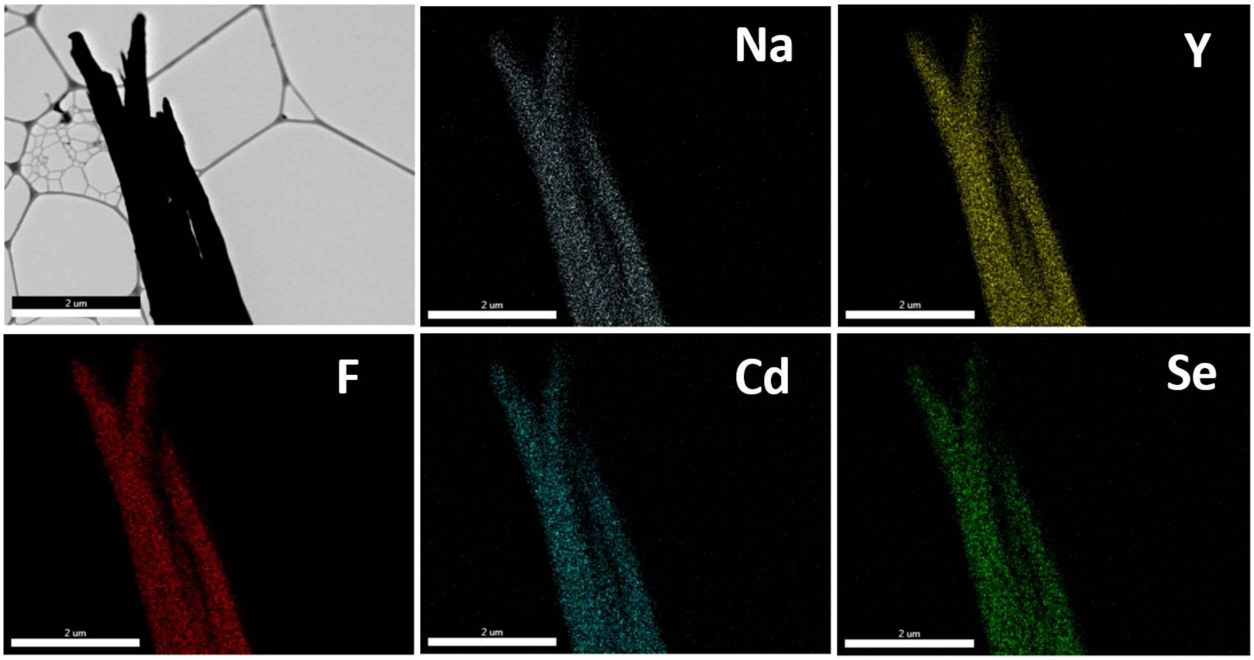

Figure 6.14. Representative elemental mapping images of 3D-0D $NaYF_4$-CdSe QD heterostructures, created from "nanowire bundles" of $NaYF_4$ (that had been synthesized with 0.8 M ammonia) coupled with as-prepared CdSe quantum dots.

We should note, however, that as compared with 0D and 3D $NaYF_4$-based heterostructures, the extent of QD aggregation is markedly much higher than that noted with their 1D $NaYF_4$ counterparts. This observation was confirmed in both TEM and EDAX images, a finding which we would prefer to attribute to the prolonged heat treatment (i.e. 60°C overnight) required for the synthesis process of the 1D $NaYF_4$-CdSe QD heterostructures. Moreover, the relative loading of QDs onto variously prepared $NaYF_4$, as noted by both EDAX and BET data, is summarized in Table 6.1.

Sample Preparation conditions, phase, and crystallinity	**Morphology and Dimensions**	**Surface Area (m^2/g)**	**QD loading within resulting heterostructures (CdSe: $NaYF_4$ molar ratio)**	**Estimated number of QDs per 10^6 nm^3 of the underlying $NaYF_4$ motif**	**FRET efficiencies (Percentage)**
0 M ammonia $NaYF_4$, α-phase, polycrystalline	0D Nanoparticles: average diameters of ~ 150 nm	13.9	0.32	3160	51%
0.2 M ammonia $NaYF_4$, α-phase, polycrystalline	Porous 0D Nanoparticles: average diameters of ~ 300 nm	21.7	0.68	6720	73%
0.4 M ammonia $NaYF_4$, β-phase, polycrystalline	3D Micron-sized chromosomal motifs: Overall average diameters of ~2 µm with lengths of ~ 5-8 µm	11.7	0.21	2340	48%
0.8 M ammonia $NaYF_4$, β-phase, polycrystalline	3D Micron-sized nanowire bundles: Overall average diameters of ~1.5 µm with lengths of ~ 5 µm	14.9	0.29	3240	57%
1D $NaYF_4$, β-phase, single crystalline	1D Nanorods: Average diameters of ~ 100-200 nm with lengths of ~ 1 µm	5.8	0.11	1230	27%

Table 6.1. Summary of the physical surface area data, calculated from BET results, the relevant quantum dot loading values and estimated numbers of quantum dots onto variously as-prepared heterostructures, as well as the energy transfer efficiencies of these heterostructures.

6.2.3.1. Role of QD Loading on Energy Transfer and Optical Behavior

Indeed, we have quantitatively analyzed the QD loadings in terms of approximate numbers of CdSe particles immobilized onto certain specific spatial volumes of the underlying $NaYF_4$ substrates possessing various morphologies. In particular, upon normalization to identical volumes (i.e. 10^6 nm^3) for all of the 0D, 1D, and 3D $NaYF_4$ structures systematically probed, we noted markedly differential CdSe nanocrystal coverages, ranging from 1000 to over 6000 CdSe QDs deposited onto the fluorides beneath (i.e. Table 6.1). In fact, these data suggest that the numbers of CdSe QDs are likely to be from 2 to 6 times more prevalent on the outer surfaces of 0D and 3D structures as compared with their 1D nanowire counterparts.

Significantly, with important implications for optical performance, the trend in the physical surface area correlates perfectly well with that of QD loading onto the underlying fluoride motifs. Moreover, we are aware of the additional key nuance associated with the structural porosity and surface roughness of the $NaYF_4$ nanoparticulate motifs, as implied by the TEM images in Figure 6.11B, which account for the higher surface area-to-volume ratios of our larger $NaYF_4$ motifs. In other words, we have been able to demonstrate that the density of QDs on the surface of $NaYF_4$ can be readily tuned by simply varying both the morphological and surface area characteristics of our as-prepared nanostructures, the capability of which, to the best of our knowledge, has not previously been reported.

As shown in Figure 6.15, after the deposition of CdSe QDs, we found that (a) the upconversion signal associated with $NaYF_4$ has been effectively quenched in all of our heterostructures, coupled with (b) a corresponding increase in the CdSe signal, suggestive of a plausible energy transfer from $NaYF_4$ to CdSe QDs, as evinced by the prior literature.[20]

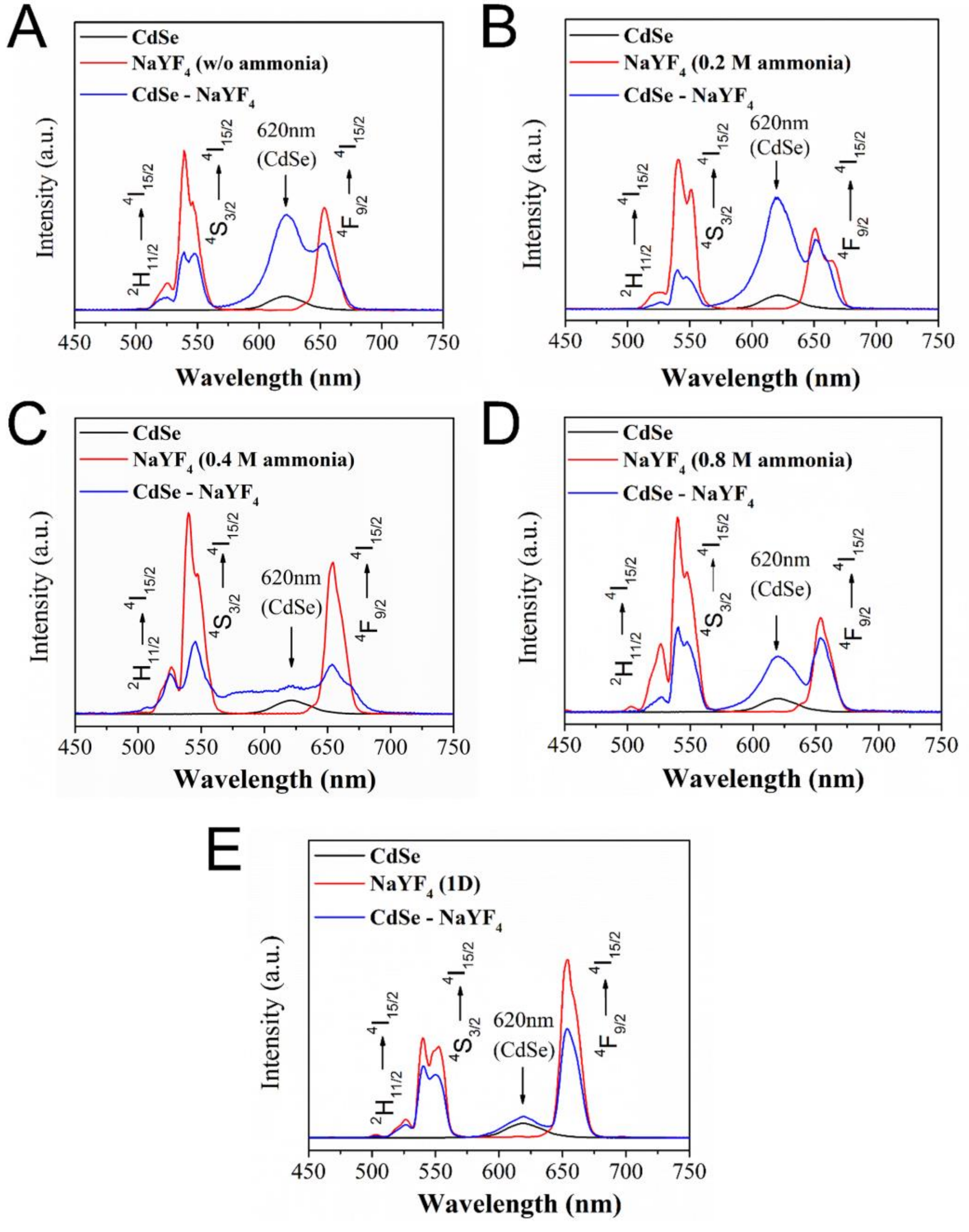

Figure 6.15. Upconversion data associated with heterostructures composed of (i) CdSe QDs attached to (ii) 0D and (iii) 3D NaYF$_4$ samples, which had been synthesized with (A) 0 M ammonia, (B) 0.2 M ammonia, (C) 0.4 M ammonia, and (D) 0.8 M ammonia, respectively, as well as onto (iv) separately prepared 1D NaYF$_4$ nanorods (E), respectively.

The corresponding energy diagram highlighting all of the relevant excitation, relaxation, and emission processes is shown in Figure 6.16.

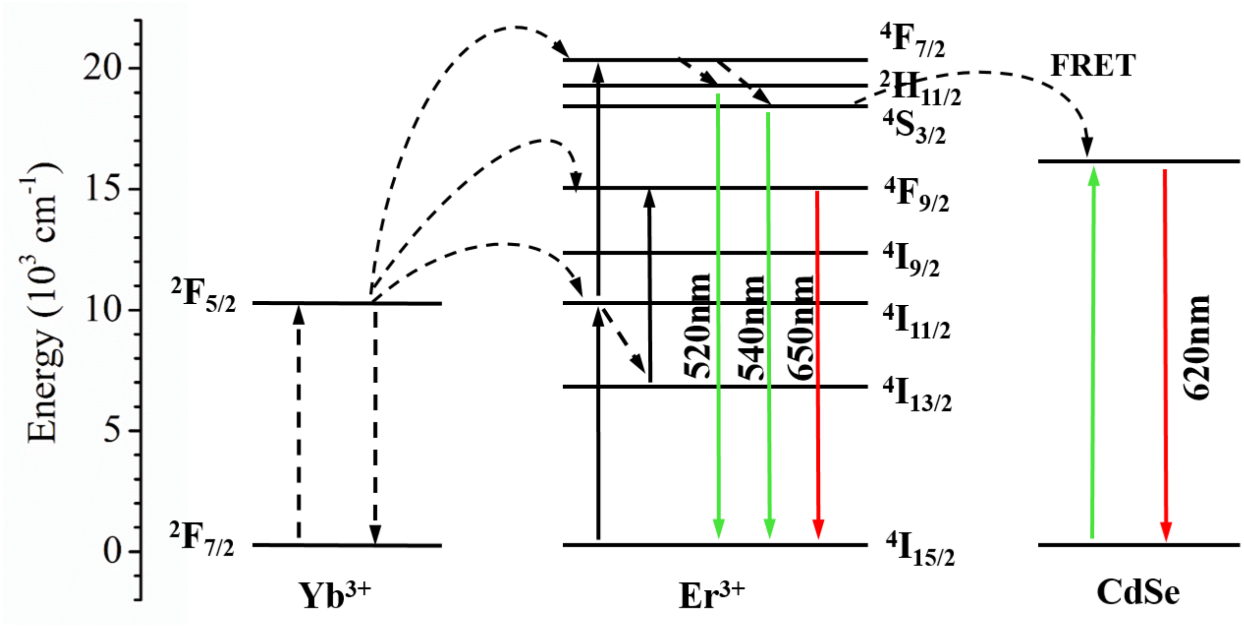

Figure 6.16. Energy diagram, highlighting all of the expected relevant transitions within as-prepared CdSe-NaYF$_4$ heterostructures.

We note that QDs serve as a valid reference point and control experiment for better understanding the resulting upconversion signal enhancement of as-generated CdSe QD-NaYF$_4$ heterostructures. As such, we find that although the excitation wavelength herein, i.e. 980 nm, is well below the energy of the conventional excitation range of CdSe QDs (i.e. 300-600 nm), the QDs still exhibited a pronounced upconversion signal upon excitation. Our data are not surprising, since CdSe QDs have been previously shown to give rise to a “two-photon” excitation behavior,[49] wherein CdSe QDs can be excited by two separate photons, each characterized by a 980 nm wavelength, and which collectively are functionally equivalent to the energy of a single photon, i.e. at ~490 nm.

The extent of the PL signal increase, however, is rather different and distinctive for all five as-generated heterostructures. For example, the heterostructures comprising the two differently-sized 0D NaYF$_4$ samples yielded a greater intensity as compared with the analogous composites, possessing the variously-sized 3D $NaYF_4$ motifs, a finding which implies the significance of more available active surface area and porosity which in turn enable greater QD loading for the 0D-based composites and hence help to dictate the observed optical performance.

By contrast, heterostructures incorporating 1D $NaYF_4$ yielded essentially a negligible change in PL behavior in spite of the ‘reasonable’ surface area associated with the 1D $NaYF_4$ motifs. To explain this phenomenon, as we noted in the Experimental section, the formation of robust 1D-based heterostructures necessitated a slightly more demanding preparative protocol involving a prolonged heat treatment under an argon atmosphere to ensure the reliable attachment of QDs onto the underlying 1D $NaYF_4$ nanorods. This experimental reality highlights the crucial importance of the surface chemistry of the constituent $NaYF_4$ motifs in addition to physical surface area and porosity considerations in the observed QD loading and hence, optical behavior of the resulting heterostructures.

In terms of a more quantitative evaluation of such distinctive, structure-dependent optical behaviors, we have calculated the corresponding energy transfer efficiencies (η_T) with the following expression, Equation 6.1, assuming that the PL quenching of $NaYF_4$ can be completely attributed to energy transfer to CdSe QDs.

$$\eta_T = 1 - \frac{E_S}{E_{SO}} \tag{6.1}$$

wherein E_{SO} and E_S denote the emission output (i.e., peak area) of $NaYF_4$ before and after CdSe QD attachment, respectively. Herein, we have focused on both the $^2H_{11/2} \rightarrow {}^4I_{15/2}$ and $^4S_{3/2} \rightarrow {}^4I_{15/2}$ transitions (near 525 nm and 545 nm, respectively) as the main peaks upon which to base our calculations, as the upconversion spectra in Figure 6.15 implied that energy transfer mainly occurs between doped $NaYF_4$ and CdSe QDs at these two specific energy levels.

As a consequence, the calculated η_T values for heterostructures incorporating 0D and 3D-based $NaYF_4$ synthesized using ammonia concentrations of (a) 0 M, (b) 0.2 M, (c) 0.4 M, and (d) 0.8 M, respectively, as well as of (e) 1D $NaYF_4$ were computed to be (a) 51%, (b) 73%, (c) 48%, (d) 57%, and (e) 27%, in that order. This trend in energy transfer efficiency correlates quite well with the corresponding QD loading within these heterostructures (Table 1), thereby implying that the efficiency of FRET is directly impacted and affected by the amount and number of quantum dots immobilized onto the external surfaces of the underlying host materials.

6.2.3.2. Role of Surface Chemistry on Energy Transfer and Optical Behavior

To gain insights into the surface chemistry of our $NaYF_4$ nanocrystalline samples, IR spectra were collected and analyzed. As described in the Experimental section, we should note that the IR spectra were taken on oleic acid-capped $NaYF_4$ samples as opposed to bare $NaYF_4$, in order to directly gauge possible peak shifts attributable to the attachment of QDs.

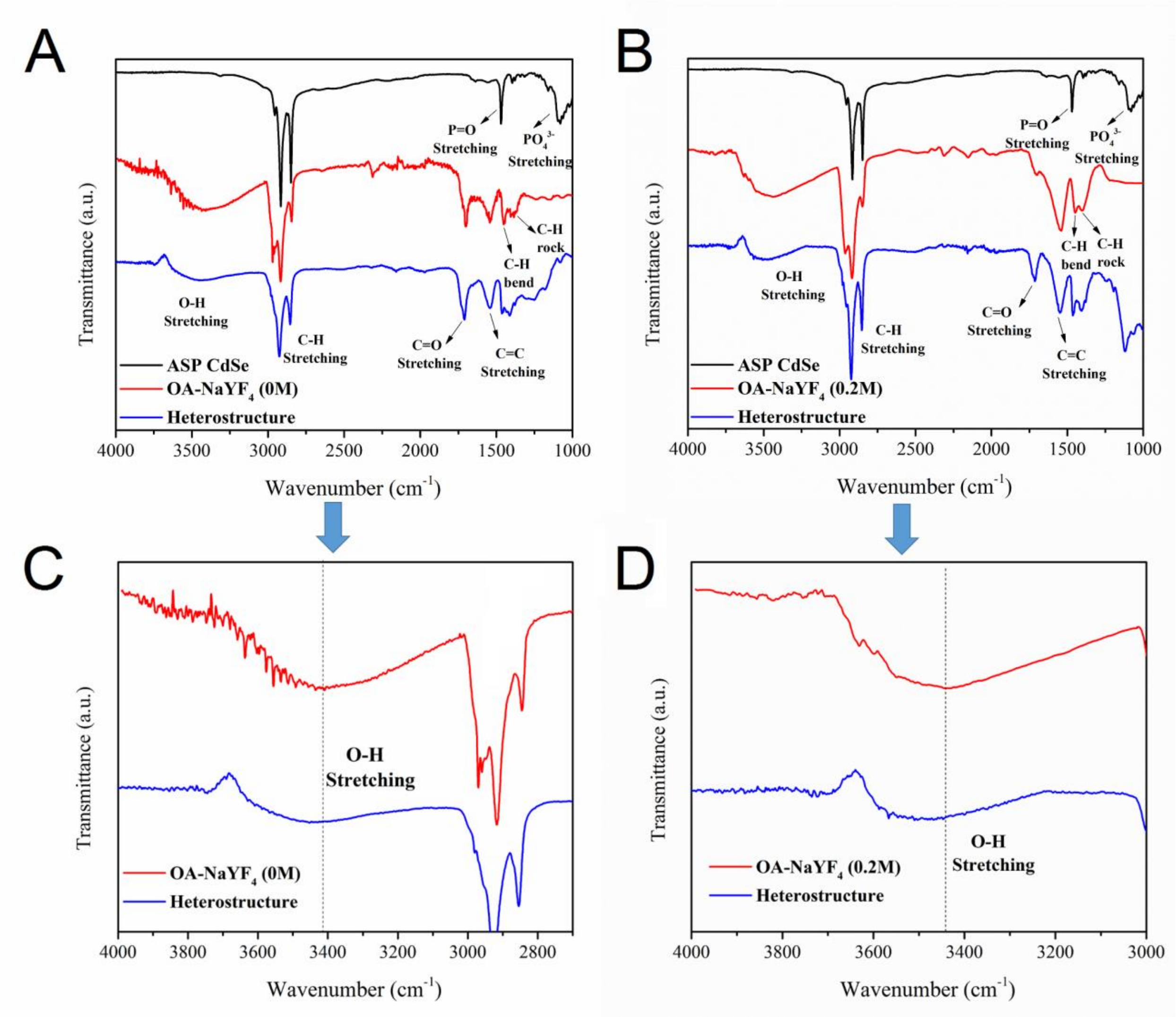

Figure 6.17. Representative IR spectra of as-prepared CdSe QDs, oleic acid-capped $NaYF_4$ nanoparticles, and the corresponding CdSe QD-$NaYF_4$ heterostructures (A and B). The $NaYF_4$ samples in panel A and B were prepared with 0 M and 0.2 M ammonia, respectively. A magnified view is presented in the range of the O-H stretching mode region (C and D).

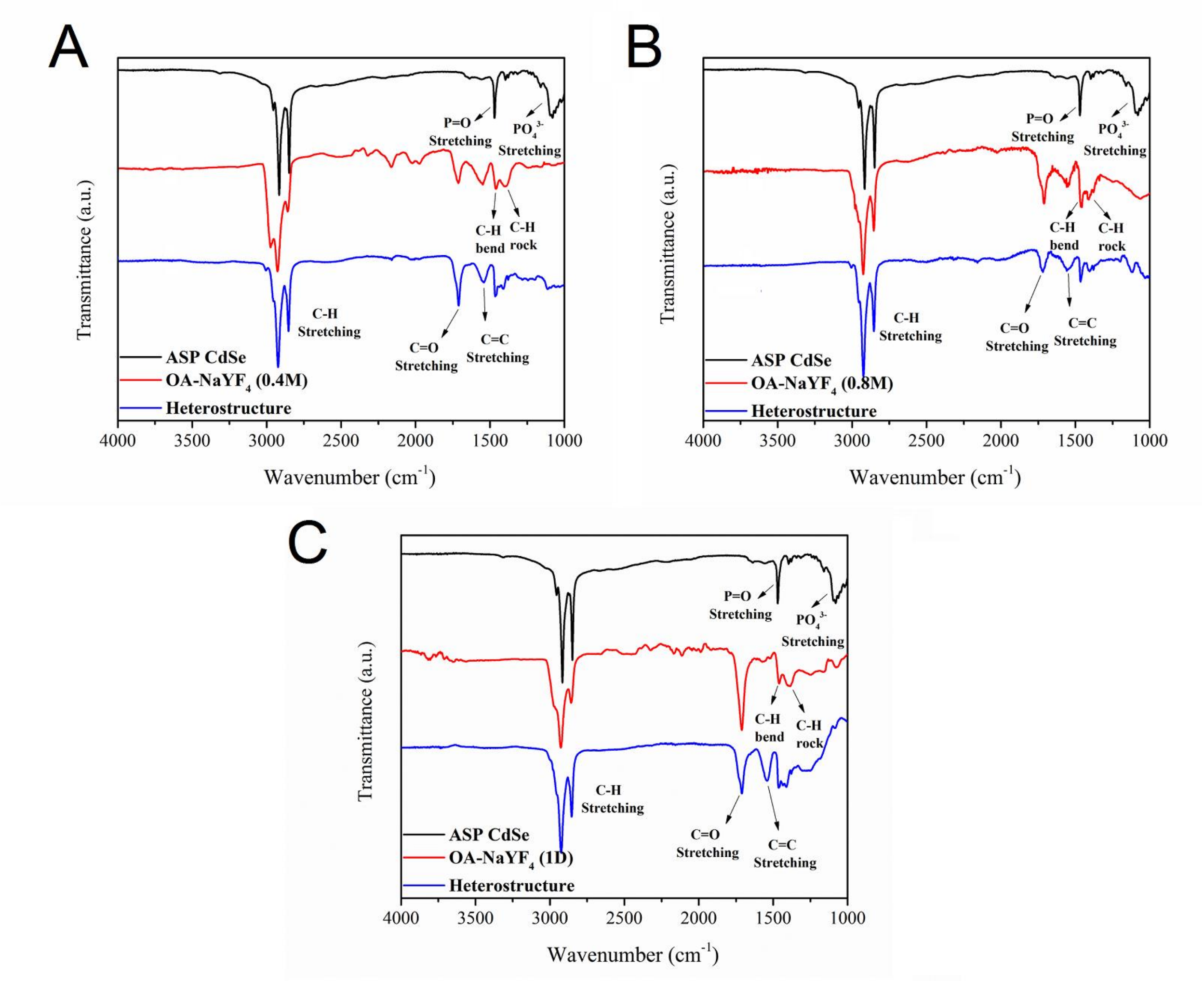

Figure 6.18. Representative IR spectra of as-prepared CdSe QDs, oleic acid-capped nanoscale motifs of $NaYF_4$ including both (A and B) 3D and (C) 1D morphologies, and the corresponding CdSe QD - $NaYF_4$ heterostructures. The $NaYF_4$ samples in panel A and B were prepared with 0.4 M and 0.8 M ammonia, respectively.

As shown in Figure 6.17 and Figure 6.18, the peaks at 1390 cm^{-1}, 1463 cm^{-1}, 1560 cm^{-1}, 1720 cm^{-1}, as well as 2850-3000 cm^{-1} can be assigned to various well-defined and expected vibrational modes, associated with the oleic acid capping agent.[50] In the spectrum of as-prepared (ASP) CdSe QDs, characteristic peaks that can be ascribed to P=O stretching (at 1469 cm^{-1}) as well as C-N stretching (at 1086 cm^{-1}) modes were present, associated with TOPO and HDA capping agents, respectively. As expected, in general, all of our CdSe QD - $NaYF_4$ heterostructures possessed peaks associated with both of these two constituent component species.

Interestingly, unlike either the 3D or 1D systems (Figure 6.18), we noted that all of the 0D $NaYF_4$ and corresponding heterostructured samples were characterized by a broad peak situated at 3300-3500 cm^{-1} (Figure 6.17), suggestive of an O-H stretching mode associated with hydrogen bonding. It is unlikely that an O-H stretching peak located at such a high wavenumber (> 3400 cm^{-1}) can be ascribed to oleic acid alone.[51] On the other hand, prior work suggests that OH functional groups may exist on the surfaces of $NaYF_4$ nanocrystals that had been fabricated in either an aqueous or water-containing environment.[46, 52, 53] In addition, after formation of the 0D-based heterostructures, the OH stretching peak position appeared to have shifted to higher wavenumbers. According to a previous study of analogous CdSe QD-$CaWO_4$ heterostructures, such a shift in the O-H stretching peak mode may be indicative of a hydrogen bonding interaction between the H atoms and the P=O moiety within residual TOPO capping agents coating the CdSe QDs.[54] We thereby hypothesize that the presence of these hydroxyl groups located on the external surfaces of our 0D $NaYF_4$ motifs may have served as "anchoring" sites for the subsequent attachment of CdSe QDs, and that these groups could have thereby facilitated and assisted in QD immobilization in creating the desired heterostructures.[55-57]

Nevertheless, it is clear that regardless of the precise role of hydroxyl 'anchoring sites', it is likely a less important effect. In fact, the primary determinant for QD loading onto the resulting heterostructures is the corresponding surface areas of the various 0D, 1D, and 3D $NaYF_4$ motifs (Table 6.1), as there is a direct and significant correlation between these two parameters. In this light, it is not surprising that a more rigorous and prolonged heat treatment was required to generate 1D $NaYF_4$-based heterostructures, as our data show that 1D $NaYF_4$ nanowires possess neither surface hydroxyl groups nor a large active surface area for reaction.

Therefore, it is likely that a fortuitous combination of available morphology-driven physical surface area coupled with beneficial surface chemistry served to increase the amount of CdSe QD loading onto the underlying 0D and 3D $NaYF_4$ nanostructures as compared with their 1D $NaYF_4$ analogues. This synergistic effect yielded noticeably greater energy transfer efficiencies for these 0D and 3D-based motifs as compared with their 1D counterparts. Moreover, increased QD loading and porosity in particular primarily accounted for the overall superior performance of the 0D $NaYF_4$-based heterostructures as compared with their 3D analogues.

6.3. Conclusions

We have highlighted herein the ability to control the size, shape, morphology, and phase of $NaYF_4$. Of particular significance, we are the first to reproducibly produce and hence observe complex chromosomal-shaped, micron-sized structures pertaining to $NaYF_4$ as a unique motif.

In the process, we have demonstrated structure-optical property correlations within heterostructures incorporating chemically pure, crystalline, phase-defined, morphologically distinctive, and relatively size monodisperse distributions of these particular fluoride motifs. As an initial set of experiments, in this report, we have synthesized both cubic (α-) and hexagonal (β-) phases of $NaYF_4$ nanocrystals using a facile hydrothermal synthetic approach. Specifically, we have deliberately isolated samples with an exclusive crystalline phase, possessing distinctive morphologies in the absence of surfactant, merely by carefully varying reaction parameters, including reaction temperature, reaction time, and the concentration of added ammonium hydroxide. According to our results, the alteration of these reaction conditions affects not only the shape but also the phase of as-generated $NaYF_4$ nanocrystals. For instance, under our relevant reaction conditions, the β-phase could be readily produced with longer reaction times and higher reaction temperatures. The critical inflection point is associated with reaction conditions of 2 hours and 140°C, respectively.

Moreover, most importantly, by changing the concentration of ammonia used, the growth mechanism can be readily controlled. In other words, spherical aggregates of the α-phase can often be readily formed at low ammonia concentrations, whereas bundles of nanowires of the β-phase, composed of constituent ultrathin wires, are frequently isolated at high ammonia concentrations. In terms of optical properties, we have been focusing on the effects of both phase and shape, and we have confirmed that the presence of the β-phase as well as of the larger overall crystalline domain sizes can lead to the measurement of improved UC efficiencies.

Furthermore, we have probed the fundamental structure-dependent energy transfer behavior of $NaYF_4$-CdSe QD heterostructures. Specifically, we have demonstrated that the nanoporous 0D particles, characterized by a relatively higher surface area coupled with surface “anchoring” hydroxyl groups for optimal QD loading, represent an excellent energy donating species towards CdSe QDs. We believe that our studies associated with the synthesis of a family of morphology-driven CdSe-$NaYF_4$ heterostructures with largely enhanced overall upconversion emission can enable us to rationally utilize these composites for photovoltaic applications.

In fact, the optoelectronic properties of the 0D-0D, 0D-1D, and 0D-3D CdSe QD-$NaYF_4$ nanocomposites, respectively, are measurably different, and are affected to a large extent by differential QD coverage densities on the underlying fluoride motifs. Therefore, we believe that our work has provided an experimental basis for optimizing analogous upconversion material -

QD-based hybrid systems, which represent promising candidates as functional components for the next generation of QD-sensitized solar cell configurations.

6.4. References

1. Wang, G.; Qin, W.; Zhang, J.; Wang, L.; Wei, G.; Zhu, P.; Kim, R. *Journal of Alloys and Compounds* **2009,** 475, (1–2), 452-455.
2. Auzel, F. *Chemical Reviews* **2004,** 104, (1), 139-174.
3. Sivakumar, S.; van Veggel, F. C. J. M.; Raudsepp, M. *Journal of the American Chemical Society* **2005,** 127, (36), 12464-12465.
4. Heer, S.; Kompe, K.; Gudel, H. U.; Haase, M. *Adv Mater* **2004,** 16, (23-24), 2102-+.
5. Dong, H.; Sun, L. D.; Yan, C. H. *Chem Soc Rev* **2015,** 44, (6), 1608-1634.
6. Zhang, F.; Li, J.; Shan, J.; Xu, L.; Zhao, D. Y. *Chem-Eur J* **2009,** 15, (41), 11010-11019.
7. Singh, L. P.; Srivastava, K.; Mishra, R.; Ningthoujam, R. S. *J Phys Chem C* **2014,** 118, (31), 18087-18096.
8. Bender, C. M.; Burlitch, J. M.; Barber, D.; Pollock, C. *Chem Mater* **2000,** 12, (7), 1969-1976.
9. Jackson, S. D. *Opt Lett* **2003,** 28, (22), 2192-2194.
10. Di Bartolo, B.; Powell, R. C., *Crystal symmetry, lattice vibrations and optical spectroscopy of solids : a group theoretical approach*. World Scientific: Hackensack New Jersey, 2014; p xviii, 515 pages.
11. Kramer, K. W.; Biner, D.; Frei, G.; Gudel, H. U.; Hehlen, M. P.; Luthi, S. R. *Chem Mater* **2004,** 16, (7), 1244-1251.
12. Boyer, J. C.; van Veggel, F. C. J. M. *Nanoscale* **2010,** 2, (8), 1417-1419.
13. Xu, C. T.; Zhan, Q. Q.; Liu, H. C.; Somesfalean, G.; Qian, J.; He, S. L.; Andersson-Engels, S. *Laser Photonics Rev* **2013,** 7, (5), 663-697.
14. Sun, Y. J.; Chen, Y.; Tian, L. J.; Yu, Y.; Kong, X. G.; Zhao, J. W.; Zhang, H. *Nanotechnology* **2007,** 18, (27).
15. Zhuang, J.; Yang, X.; Fu, J.; Liang, C.; Wu, M.; Wang, J.; Su, Q. *Crystal Growth & Design* **2013,** 13, (6), 2292-2297.
16. Yin, B. D.; Zhou, W. L.; Long, Q.; Li, C. Z.; Zhang, Y. Y.; Yao, S. Z. *Crystengcomm* **2014,** 16, (36), 8348-8355.
17. Yi, G. S.; Chow, G. M. *Adv Funct Mater* **2006,** 16, (18), 2324-2329.
18. Bednarkiewicz, A.; Nyk, M.; Samoc, M.; Strek, W. *J Phys Chem C* **2010,** 114, (41), 17535-17541.
19. Jeong, S.; Won, N.; Lee, J.; Bang, J.; Yoo, J.; Kim, S. G.; Chang, J. A.; Kim, J.; Kim, S. *Chem Commun* **2011,** 47, (28), 8022-8024.
20. Yan, C.; Dadvand, A.; Rosei, F.; Perepichka, D. F. *Journal of the American Chemical Society* **2010,** 132, (26), 8868-+.
21. Zhu, G.; Wang, H. Y.; Zhang, Q. X.; Zhang, L. *J Colloid Interf Sci* **2015,** 451, 15-20.
22. Klampaftis, E.; Ross, D.; McIntosh, K. R.; Richards, B. S. *Sol Energ Mat Sol C* **2009,** 93, (8), 1182-1194.
23. de Wild, J.; Meijerink, A.; Rath, J. K.; van Sark, W. G. J. H. M.; Schropp, R. E. I. *Energ Environ Sci* **2011,** 4, (12), 4835-4848.
24. Shan, G. B.; Assaaoudi, H.; Demopoulos, G. P. *Acs Appl Mater Inter* **2011,** 3, (9), 3239-3243.
25. Wang, K. F.; Jiang, J. Q.; Wan, S. J.; Zhai, J. *Electrochim Acta* **2015,** 155, 357-363.
26. Li, C. H.; Wang, F.; Zhu, J. A.; Yu, J. C. *Appl Catal B-Environ* **2010,** 100, (3-4), 433-439.

27. Zhou, Z. Y.; Wang, J. H.; Nan, F.; Bu, C. H.; Yu, Z. H.; Liu, W.; Guo, S. S.; Hu, H.; Zhao, X. Z. *Nanoscale* **2014,** 6, (4), 2052-2055.
28. Luoshan, M. D.; Li, M. Y.; Liu, X. L.; Guo, K. M.; Bai, L. H.; Zhu, Y. D.; Sun, B. L.; Zhao, X. Z. *J Power Sources* **2015,** 287, 231-236.
29. Han, J. K.; Wang, L.; Wong, S. S. *Rsc Adv* **2014,** 4, (66), 34963-34980.
30. Erdem, T.; Ibrahimova, V.; Jeon, D. W.; Lee, I. H.; Tuncel, D.; Demir, H. V. *J Phys Chem C* **2013,** 117, (36), 18613-18619.
31. Stevens, A. L.; Kaeser, A.; Schenning, A. P. H. J.; Herz, L. M. *Acs Nano* **2012,** 6, (6), 4777-4787.
32. Sui, Y. Q.; Tao, K.; Tian, Q.; Sun, K. *J Phys Chem C* **2012,** 116, (2), 1732-1739.
33. Lin, M.; Zhao, Y.; Liu, M.; Qiu, M. S.; Dong, Y. Q.; Duan, Z. F.; Li, Y. H.; Pingguan-Murphy, B.; Lu, T. J.; Xu, F. *J Mater Chem C* **2014,** 2, (19), 3671-3676.
34. Ma, D. K.; Yang, D. P.; Jiang, J. L.; Cai, P.; Huang, S. M. *Crystengcomm* **2010,** 12, (5), 1650-1658.
35. Wang, Y. H.; Cai, R. X.; Liu, Z. H. *Crystengcomm* **2011,** 13, (6), 1772-1774.
36. Kwon, S. H.; Lee, J. S.; Kim, Y. J. *J Nanosci Nanotechno* **2012,** 12, (11), 8845-8850.
37. Wu, S. L.; Liu, Y.; Chang, J.; Ning, Y. H.; Zhang, S. F. *Laser Photonics Rev* **2014,** 8, (4), 575-582.
38. Zhang, F.; Wan, Y.; Yu, T.; Zhang, F. Q.; Shi, Y. F.; Xie, S. H.; Li, Y. G.; Xu, L.; Tu, B.; Zhao, D. Y. *Angew Chem Int Edit* **2007,** 46, (42), 7976-7979.
39. An, J. S.; Noh, J. H.; Cho, I. S.; Roh, H. S.; Kim, J. Y.; Han, H. S.; Hong, K. S. *J Phys Chem C* **2010,** 114, (23), 10330-10335.
40. Li, C.; Yang, J.; Quan, Z.; Yang, P.; Kong, D.; Lin, J. *Chem Mater* **2007,** 19, (20), 4933-4942.
41. Yang, L. W.; Han, H. L.; Zhang, Y. Y.; Zhong, J. X. *J Phys Chem C* **2009,** 113, (44), 18995-18999.
42. Tao, F.; Pan, F.; Wang, Z. J.; Cai, W. L.; Yao, L. Z. *Crystengcomm* **2010,** 12, (12), 4263-4267.
43. Lin, C. K.; Berry, M. T.; Anderson, R.; Smith, S.; May, P. S. *Chem Mater* **2009,** 21, (14), 3406-3413.
44. Ding, M. Y.; Chen, D. Q.; Yin, S. L.; Ji, Z. G.; Zhong, J. S.; Ni, Y. R.; Lu, C. H.; Xu, Z. Z. *Sci Rep-Uk* **2015,** 5.
45. Wang, F.; Han, Y.; Lim, C. S.; Lu, Y. H.; Wang, J.; Xu, J.; Chen, H. Y.; Zhang, C.; Hong, M. H.; Liu, X. G. *Nature* **2010,** 463, (7284), 1061-1065.
46. Wang, L. M.; Li, X. Y.; Li, Z. Q.; Chu, W. S.; Li, R. F.; Lin, K.; Qian, H. S.; Wang, Y.; Wu, C. F.; Li, J.; Tu, D. T.; Zhang, Q.; Song, L.; Jiang, J.; Chen, X. Y.; Luo, Y.; Xie, Y.; Xiong, Y. J. *Adv Mater* **2015,** 27, (37), 5528-5533.
47. Han, J. K.; Hannah, M. E.; Piquette, A.; Talbot, J. B.; Mishra, K. C.; McKittrick, J. *Ecs J Solid State Sc* **2012,** 1, (3), R98-R102.
48. Jung, K. Y.; Lee, C. H.; Kang, Y. C. *Mater Lett* **2005,** 59, (19-20), 2451-2456.
49. Makarov, N. S.; Lau, P. C.; Olson, C.; Velizhanin, K. A.; Solntsev, K. M.; Kieu, K.; Kilina, S.; Tretiak, S.; Norwood, R. A.; Peyghambarian, N.; Perry, J. W. *Acs Nano* **2014,** 8, (12), 12572-12586.
50. Craver, C. D.; Coblentz Society., *The Coblentz Society desk book of infrared spectra*. 2nd ed.; The Society: Kirkwood, MO (P.O. Box 9952, Kirkwood 63122), 1982; p iii, 538 p.

51. Chen, C. J.; Lai, H. Y.; Lin, C. C.; Wang, J. S.; Chiang, R. K. *Nanoscale Res Lett* **2009,** 4, (11), 1343-1350.
52. Yang, X. J.; Xiao, Q. Q.; Niu, C. X.; Jin, N.; Ouyang, J.; Xiao, X. Y.; He, D. C. *J Mater Chem B* **2013,** 1, (21), 2757-2763.
53. Wang, C. Y.; Cheng, X. H. *Rsc Adv* **2015,** 5, (115), 94980-94985.
54. Han, J.; Wang, L.; Wong, S. S. *J Phys Chem C* **2014,** 118, (11), 5671-5682.
55. Panda, G. C.; Das, S. K.; Guha, A. K. *Colloid Surface B* **2008,** 62, (2), 173-179.
56. Li, R. F.; Lee, J.; Yang, B. C.; Horspool, D. N.; Aindow, M.; Papadimitrakopoulos, F. *Journal of the American Chemical Society* **2005,** 127, (8), 2524-2532.
57. Mata, Y. N.; Blazquez, M. L.; Ballester, A.; Gonzalez, F.; Munoz, J. A. *J Hazard Mater* **2008,** 158, (2-3), 316-323.

Chapter 7. Concluding Remarks and Future Directions

7.1. Conclusions

In this thesis, we have synthesized various types of high-quality nanomaterials, including metal alloys, noble metal-based core-shell structures, and lanthanum-doped fluorides with well-defined shapes as well as controlled chemical compositions, in order to demonstrate morphology-dependent and composition-dependent correlations between nanostructures and either electrochemical or photophysical properties.

In Chapters 3 and 4, we were able to fabricate a series of one-dimensional (1D) ultrathin $Pd_{1-x}Ni_x$ and $Pd_{1-x}Cu_x$ nanowires (average diameter ~ 2 nm) towards electrocatalysis protocols associated with the oxygen reduction reaction (ORR) and the formic acid oxidation (FAOR), respectively. Interestingly, both of these two series of nanowires evinced a volcano-shaped relationship between their chemical composition and corresponding electrocatalytic performance, which peaked at chemical compositions of Pd_9Ni and Pd_9Cu, respectively. These trends could be attributed to their optimized affinity towards reaction intermediates, namely hydroxide groups (-OH) in ORR and carbon monoxide (CO) in FAOR, which were probed through utilization of techniques including cyclic voltammetry, CO stripping, and so forth.

Moreover, after deposition of Pt monolayers (Pt_{ML}) on top of these ultrathin nanowires, the resulting $Pt\sim Pd_9Ni$ were shown to yield promising catalytic activities towards ORR, representing over a 3-fold increase over state-of-the-art Pt commercial nanoparticles (NPs). By analogous, the $Pt\sim Pd_{1-x}Cu_x$ series have exhibited outstanding electrocatalytic performances towards both methanol oxidation reaction (MOR) and ethanol oxidation reaction (EOR) in alkaline solution, yielding up to 3-fold and 4-fold enhancement as compared with commercial Pt

NPs, respectively. All of these results have demonstrated that the combination of 1D ultrathin motifs coupled with a Pt-monolayer shell, Pd-alloy core architecture is of particular interest and could potentially be a very promising electrocatalytic design for the future.

As a follow-up topic, an accurate understanding of the structure of individual catalysts is key to optimization of their performance. In a system that incorporate three or more metal elements, local restructuring is usually expected, yet rarely probed with demonstrable precision and accuracy. Hence, in Chapter 5, we have combined theoretical calculations, spectroscopic techniques (i.e., X-ray Absorption Spectroscopy) and electrochemical results, in order to assess the true active sites as well as the spatial distribution of different elements within a Pt_{ML}~Pd_9Au core-shell 1D ultrathin nanowire system, which has been proven to be an outstanding ORR catalyst candidate. Specifically, due to the extremely similar physical properties between Pt and Au atoms, conventional electron microscopy-based techniques were insufficient to truly investigate the actual structural configuration of this core-shell architecture, such as the exact spatial distribution of Au atoms. On the other hand, the DFT results associated with three different models describing varying extents of Au surface segregation have provided key structural insight into the desired, electrocatalytically active structure. Therefore, through utilization of Extended X-ray Absorption Fine Structure (EXAFS) spectroscopy, we successfully observed an Au surface segregation phenomenon, a finding further supported by the collective results from both DFT modelling and electrochemistry.

In terms of solar cells, the incorporation of upconversion materials such as lanthanum element doped $NaYF_4$ has become one of the approaches to harness a broader range of the solar spectrum, thereby improving the overall efficiency observed. In Chapter 6, we report on a straightforward hydrothermal synthesis, in the absence of any surfactant, to readily synthesize

$NaYF_4$ nanocrystals with various shapes, including 0D (nanoparticles), 1D (nanorods), and 3D (nanowire-bundles). Upon formation of a class of $NaYF_4$-CdSe quantum dot (QD, utilized as light absorber) heterostructures incorporating all of these distinctive nanomaterial components, we have observed tunable, structure-dependent energy transfer behavior. Specifically, the trend in energy transfer efficiency correlates very well with the corresponding QD loading within these heterostructures, thereby implying that the efficiency of FRET is directly affected by the amount of QDs immobilized onto the external surfaces of the underlying fluoride host materials.

7.2. Future Directions

7.2.1. Cathodic Materials Associated with Oxygen Reduction Reaction (ORR)

In terms of cathodic materials, namely electrocatalysts for ORR, Pt-based catalysts still represent the most widely used catalysts for applications in PEMFCs, due to their high activity. In fact, the highest electrochemical activity reported to date has been obtained by deliberately tuning the morphology of Pt-based bimetallic nanostructures. In so doing, activities of over a magnitude higher than state-of-the-art commercial Pt catalysts have been achieved.[1] However, there have been several issues associated with ORR catalysts, that require further exploration and/or improvement.

First, a reliable and scalable synthetic approach is lacking for the production of electrocatalysts with well-defined morphologies. We have demonstrated in this Dissertation that ultrathin nanowires can give rise to outstanding ORR electrocatalytic performance, due to both the (1) surface contraction owing to reduced dimensions as well as the (2) presence of extended and highly active facets due to its anisotropic motif. Other reports have described structures with only the highest electrochemically active facets exposed to electrolytes. This strategy so far has yielded the highest activity reported to date of 6.98 A mg^{-1}, i.e. a 35-fold enhancement over commercial Pt nanoparticles obtained with a Mo-doped Pt_3Ni octahedral structure.[2]

These examples have demonstrated that morphological variation is the key to designing futuristic ORR catalysts. However, these nanostructures generally still rely on relatively complex, milligram (mg) quantity syntheses. Therefore, one of the major challenges is to scale up synthesis without compromising effective control over size, shape, and morphology, especially in the case of a well-defined, high surface-area structure, such as either complex hierarchical or porous materials, which are particularly preferable as ORR catalysts.

Second, for the Pt- and Pd-based nanostructures we have highlighted herein, it is reasonable to assume that high activity is a necessary but potentially insufficient criterion for an effective ORR catalyst. Therefore, a high and uniform dispersion of these nanostructures on a substrate (typically Vulcan carbon) are also essential and crucial.[3] Nonetheless, there is a very limited fundamental understanding of the nucleation and growth pathways of Pt (including alloys) deposited onto support. For instance, Yao *et al.* have probed the growth direction of Pt nanowires on porous carbon matrix using high-resolution TEM.[4] However, analogous work has seldom been performed on either any alloys or core-shell structures. In addition, a fundamental understanding of the nucleation and growth pathways of Pt-based nanocrystals on these underlying substrates, such as the interaction of Pt precursors with the carbon support, through utilization of techniques such as *operando* electron spectroscopy, would be beneficial for the rational improvement of catalyst activity and durability.[5]

Third, under realistic fuel cell operating conditions, ORR catalysts, especially bimetallic Pt-M nanoparticles, suffer from considerable losses in performance, as a result of degradation issues including but not limited to (1) the agglomeration of nanoparticles; (2) the dissolution of either Pt or the transition metal itself; (3) the detachment and re-deposition of dissolved Pt; as well as (4) carbon corrosion.[6, 7] Unfortunately, it is still unclear as to the precise function and degradation mechanisms involved for many of these catalyst, Hence, a fundamental understanding about the dominant factors that control catalyst activity and durability remains limited. Advanced characterization tools, such as in situ electron microscopy, in situ X-ray microscopy in combination with computer simulation and modeling, may be helpful for tracking the structure and morphological evolution of catalysts and supports under realistic operational conditions and these efforts should guide the rational design of durable catalyst systems.

Meanwhile, from a broader perspective, a significant amount of work and effort has been expended towards achieving active non-precious-metal and metal-free catalysts. It has unequivocally been demonstrated that carbon-based nanostructures possessing doping elements, such as either N or transition metals, can be competitive with Pt-based ORR catalysts in terms of yielding outstanding ORR performance, especially with alkaline-media fuel cells, which can presumably be further tuned and optimized by controllably altering the physical and electronic structure of these materials. The real opportunity here will be to create an alternative, cost-effective pathway towards commercialization of portable and stationary fuel cell devices as well as of fuel cell vehicles (FCVs).

7.2.2. Anodic Materials Associated with Small Molecule Electro-oxidations

As for the anodic materials, namely the catalysts for reactions including the FAOR, MOR, and EOR, a better understanding of the intrinsic nature of the reaction mechanism on each individual type of material as well as the origins for possible electrocatalytic enhancement will inevitably be the focus.

The main issue that exists for both FAOR and MOR is the insufficient capability to remove the carbon monoxide intermediate. As a result, most of the catalysts are inclined to undergo poisoning by strong adsorption of CO. Hence, there is a need to either functionalize or modify the surfaces of existing noble metal-based systems. The enhancement of noble metal nanoparticles can be achieved through the formation of either bimetallic or trimetallic alloyed systems (e.g. PtRu, PtSn, PdCu, PtSnRu and so on), characterized by specific interactions between components, distinctive electronic properties, and often unique morphology.[8] Nonetheless, while is it clear that the "bifunctional" mechanism explained in Chapter 1 accounts for the excellent CO-resistance capabilities in PtRu system[9, 10], there have been conflicting reports as well as on-going debate associated with other Pt- and Pd-based alloy systems in terms of the origin behind their lowered CO-poisoning effects.[11-13] Essentially, using in situ X-ray absorption spectroscopy or similar types of techniques, which directly probe the electronic configuration of these catalysts, will be required to provide for additional guidance in order to achieve a better understanding of such phenomenon.

Meanwhile, it has been shown that certain inorganic oxides (e.g. WO_3, MoO_3, TiO_2, ZrO_2, V_2O_5, and CeO_2)[14-17] and polyoxometallates of molybdenum or tungsten[18, 19] may influence the nature of supported metal centers in ways other than simple dispersion over an electrode area.

Evidence has been presented that the support can modify the electrochemical activity (presumably the electronic nature) of catalytic metal nanoparticles, thereby affecting their chemisorptive and catalytic properties. Among the useful characteristics of metal oxides and related systems are the following: (1) they are able to generate -OH groups at low potentials that induce oxidation of passivating CO adsorbates (e.g. on Pt), much like the "bifunctional" mechanism in PtRu alloys; and (2) they can potentially break C-H bonds (for instance, by forming hydrogen tungsten oxide bronzes[15]). There have been a number of reports in this area, but further research is still necessary to elucidate the exact enhancement mechanisms that are responsible for the observed data. To classify metal oxides with respect to their reactivity and their ability to enhance activity of dispersed noble metal centers, systematic studies are needed with the aim of better understanding the ability of oxides to not only switch between different valence states but also undergo outer-sphere or inner-sphere electron transfers. Moreover, other structural parameters including morphology, porosity, stability, degree of crystallinity, nonstoichiometry, acidity, hydrophobicity, and hydrophilicity[20] are also important.

Regarding EOR, several fundamental issues of catalysts remain to be addressed. From a fundamental point of view, the EOR mechanism is far from established, as a number of key aspects need to be clarified. These include finding the key factors for determining whether EOR occurs through either the C1 pathway (2 electrons) or the C2 pathway (12 electrons); identifying intermediates during the C-C cleavage step in the C1 pathway; and understanding the nature of the as-formed intermediates, especially their adsorption mode on Pt and Pd surfaces.[21] Until these issues are satisfactorily addressed, the rational design of high performance catalysts for direct ethanol fuel cells (DEFCs) will remain preliminary. From a practical point of view, the reported methods for synthesizing high-performance catalysts are not suitable for large scale commercial production. We believe that efforts in these various directions are essential for the further development and deployment of commercially viable DEFCs.

7.2.3 Upconversion Material Based Solar Cells

In terms of solar cells, as discussed in Chapter 1, one of the major challenges affecting efficiencies is the spectral mismatch between the incident solar spectrum and the semiconductor used. Most of the sub-bandgap photons are not absorbed by the semiconductor and are instead transmitted. Spectral converters, such as the $NaYF_4$ upconversion (UC) nanomaterials discussed in this Dissertation, which can convert NIR light into visible light, have shown a promising potential to reduce transparency losses in large bandgap semiconductor solar cells. However, the efficiency of upconversion nanomaterials used for solar cells is generally low (~ 1%), which is one of the most significant factors, that limit the practical applicability of upconverters for solar cell configurations.

There have been different methods available to improve the UC efficiency, such as impurity doping,[22] the use of plasmonic structures,[23] and the construction of core-shell UC nanomaterials.[24, 25] (1) Regarding impurity doping, one of the most successful impurity ions is Li^+. Indeed, due to its small ionic radius, Li^+ ions can be easily doped into the host lattice either substitutionally or interstitially. This will result in the alteration of the crystal field around the rare-earth ions, thereby leading to an enhanced upconversion PL intensity.[26] For example, recent reports have shown that the use of Li^+ could give rise to an up to 20-fold enhancement in the visible UC emissions in $NaYF_4$:Yb,Er/Tm host materials.[27]

(2) Meanwhile, localized surface plasmon resonance (LSPR) from noble metal nanostructures can be used to enhance upconversion luminescence. Typically, upconversion nanoparticles are deposited onto metallic nanostructure films, such as gold films. In fact, Zhang *et al.* observed a five-fold overall enhancement of upconversion emission in $NaYF_4$:Yb,Er nanocrystals, when coupled with gold island films.[23] Regarding this type of configuration, the upconversion enhancement is highly dependent upon the distance between the upconverters and the metallic structures.[28] (3) In terms of core-shell structures, the shell enhances the photoluminescence by protecting the luminescent ions in the core from non-radiative decay, caused by the surface defects, as well as from vibrational deactivation ascribed to solvent molecules and ligands absorbed onto the surfaces of the upconversion materials.[29]

Yi *et al.* have reported that the visible UC emission in hexagonal-phase $NaYF_4$:Yb,Er and $NaYF_4$:Yb,Tm were enhanced by 7.4 times and 29.6 times, respectively, by growth of a thin layer of $NaYF_4$ (2 nm).[30] Among these approaches, the impurity doping strategy has currently exhibited great potential as a simple and efficient method to improve upon UC emission. Nonetheless, all of the techniques mentioned are still far from perfect and will require more thorough study and optimization. The incorporation of highly-efficient UC materials with tunable emission range should hopefully advance the development of upconversion solar cells.

7.3. References

1. Scofield, M. E.; Liu, H. Q.; Wong, S. S. *Chem Soc Rev* **2015,** 44, (16), 5836-5860.
2. Huang, X. Q.; Zhao, Z. P.; Cao, L.; Chen, Y.; Zhu, E. B.; Lin, Z. Y.; Li, M. F.; Yan, A. M.; Zettl, A.; Wang, Y. M.; Duan, X. F.; Mueller, T.; Huang, Y. *Science* **2015,** 348, (6240), 1230-1234.
3. Stephens, I. E. L.; Bondarenko, A. S.; Gronbjerg, U.; Rossmeisl, J.; Chorkendorff, I. *Energ Environ Sci* **2012,** 5, (5), 6744-6762.
4. Yao, X. Y.; Su, K. H.; Sui, S.; Mao, L. W.; He, A.; Zhang, J. L.; Du, S. F. *Int J Hydrogen Energ* **2013,** 38, (28), 12374-12378.
5. Shao, Y. Y.; Cheng, Y. W.; Duan, W. T.; Wang, W.; Lin, Y. H.; Wang, Y.; Liu, J. *Acs Catal* **2015,** 5, (12), 7288-7298.
6. Wu, J. B.; Yang, H. *Acc. Chem. Res.* **2013,** 46, (8), 1848-1857.
7. Meier, J. C.; Galeano, C.; Katsounaros, I.; Topalov, A. A.; Kostka, A.; Schuth, F.; Mayrhofer, K. J. J. *Acs Catal* **2012,** 2, (5), 832-843.
8. Kulesza, P. J.; Pieta, I. S.; Rutkowska, I. A.; Wadas, A.; Marks, D.; Klak, K.; Stobinski, L.; Cox, J. A. *Electrochim Acta* **2013,** 110, 474-483.
9. Xu, W. L.; Lu, T. H.; Liu, C. P.; Xing, W. *J Phys Chem B* **2005,** 109, (30), 14325-14330.
10. Lee, M. J.; Kang, J. S.; Kang, Y. S.; Chung, D. Y.; Shin, H.; Ahn, C. Y.; Park, S.; Kim, M. J.; Kim, S.; Lee, K. S.; Sung, Y. E. *Acs Catal* **2016,** 6, (4), 2398-2407.
11. Wang, H. S.; Alden, L. R.; DiSalvo, F. J.; Abruna, H. D. *Langmuir* **2009,** 25, (13), 7725-7735.
12. Almeida, T. S.; Kokoh, K. B.; De Andrade, A. R. *Int J Hydrogen Energ* **2011,** 36, (6), 3803-3810.
13. Barranco, J.; Pierna, A. R. *J Non-Cryst Solids* **2008,** 354, (47-51), 5153-5155.
14. Wang, H. J.; Wang, X. H.; Zheng, J. D.; Peng, F.; Yu, H. *Chinese J Catal* **2014,** 35, (10), 1687-1694.
15. Rutkowska, I. A.; Sek, J. P.; Marks, E.; Zelenay, P.; Kulesza, P. J. *Meeting Abstracts* **2015,** MA2015-01, (27), 1645.
16. Huang, H.; Li, W. Z.; Liu, H. C. *Catal Today* **2012,** 183, (1), 58-64.
17. Maiyalagan, T.; Khan, F. N. *Catal Commun* **2009,** 10, (5), 433-436.
18. Joo, J. B.; Kim, J.; Kim, P.; Yi, J. *J Nanosci Nanotechno* **2010,** 10, (5), 3397-3401.
19. Yuan, J. H.; Chen, Y. X.; Han, D. X.; Zhang, Y. J.; Shen, Y. F.; Wang, Z. J.; Niu, L. *Nanotechnology* **2006,** 17, (18), 4689-4694.
20. Trasatti, S., Interfacial electrochemistry of conductive oxides for electrocatalysis. In *Interfacial Electrochemistry: Theory, Experiment, and Applications*, Taylor & Francis 1999.
21. Wang, Y.; Zou, S. Z.; Cai, W. B. *Catalysts* **2015,** 5, (3), 1507-1534.
22. Chen, D. Q.; Wang, Y. S. *Nanoscale* **2013,** 5, (11), 4621-4637.
23. Zhang, H.; Xu, D.; Huang, Y.; Duan, X. F. *Chem Commun* **2011,** 47, (3), 979-981.
24. Xu, C. T.; Svenmarker, P.; Liu, H. C.; Wu, X.; Messing, M. E.; Wallenberg, L. R.; Andersson-Engels, S. *Acs Nano* **2012,** 6, (6), 4788-4795.
25. Zeng, Q. H.; Xue, B.; Zhang, Y. L.; Wang, D.; Liu, X. M.; Tu, L. P.; Zhao, H. F.; Kong, X. G.; Zhang, H. *Crystengcomm* **2013,** 15, (23), 4765-4772.
26. Chen, G. Y.; Liu, H. C.; Liang, H. J.; Somesfalean, G.; Zhang, Z. G. *J Phys Chem C* **2008,** 112, (31), 12030-12036.

27. Yang, D.; Dai, Y.; Ma, P. a.; Kang, X.; Shang, M.; Cheng, Z.; Li, C.; Lin, J. *J Mater Chem* **2012,** 22, (38), 20618-20625.

28. Saboktakin, M.; Ye, X. C.; Oh, S. J.; Hong, S. H.; Fafarman, A. T.; Chettiar, U. K.; Engheta, N.; Murray, C. B.; Kagan, C. R. *Acs Nano* **2012,** 6, (10), 8758-8766.

29. Xue, M.; Zhu, X.; Qiu, X.; Gu, Y.; Feng, W.; Li, F. *Acs Appl Mater Inter* **2016**.

30. Yi, G. S.; Chow, G. M. *Chem Mater* **2007,** 19, (3), 341-343.

Chapter 8. References

In Order of Appearance

1. Klaine, S. J.; Alvarez, P. J. J.; Batley, G. E.; Fernandes, T. F.; Handy, R. D.; Lyon, D. Y.; Mahendra, S.; McLaughlin, M. J.; Lead, J. R. *Environ Toxicol Chem* **2012,** 31, (12), 2893-2893.
2. *Chem Eng News* **2007,** 85, (16), 24-24.
3. *Anti-Corros Method M* **2014,** 61, (6), 450-451.
4. Freedonia Group., World nanomaterials. In *Industry study*, Freedonia Group: Cleveland, Ohio, p v.
5. Alivisatos, A. P. *Science* **1996,** 271, (5251), 933-937.
6. Sardar, R.; Funston, A. M.; Mulvaney, P.; Murray, R. W. *Langmuir* **2009,** 25, (24), 13840-13851.
7. Guczi, L.; Beck, A.; Frey, K. *Gold Bull* **2009,** 42, (1), 5-12.
8. Sajanlal, P. R.; Sreeprasad, T. S.; Samal, A. K.; Pradeep, T. *Nano Rev* **2011,** 2.
9. Daniel, M. C.; Astruc, D. *Chem Rev* **2004,** 104, (1), 293-346.
10. El-Sayed, M. A. *Accounts Chem Res* **2004,** 37, (5), 326-333.
11. Iijima, S. *Nature* **1991,** 354, (6348), 56-58.
12. Perez-Juste, J.; Pastoriza-Santos, I.; Liz-Marzan, L. M.; Mulvaney, P. *Coordin Chem Rev* **2005,** 249, (17-18), 1870-1901.
13. Busbee, B. D.; Obare, S. O.; Murphy, C. J. *Adv Mater* **2003,** 15, (5), 414-+.
14. Xia, Y. N.; Yang, P. D.; Sun, Y. G.; Wu, Y. Y.; Mayers, B.; Gates, B.; Yin, Y. D.; Kim, F.; Yan, Y. Q. *Adv Mater* **2003,** 15, (5), 353-389.
15. Wang, F.; Dong, A.; Buhro, W. E. *Chem Rev* **2016**.
16. Chen, J. Y.; Wiley, B. J.; Xia, Y. N. *Langmuir* **2007,** 23, (8), 4120-4129.
17. Hu, J. T.; Odom, T. W.; Lieber, C. M. *Accounts Chem Res* **1999,** 32, (5), 435-445.
18. Millstone, J. E.; Park, S.; Shuford, K. L.; Qin, L. D.; Schatz, G. C.; Mirkin, C. A. *Journal of the American Chemical Society* **2005,** 127, (15), 5312-5313.
19. Jin, R. C.; Cao, Y. W.; Mirkin, C. A.; Kelly, K. L.; Schatz, G. C.; Zheng, J. G. *Science* **2001,** 294, (5548), 1901-1903.
20. Scarabelli, L.; Coronado-Puchau, M.; Giner-Casares, J. J.; Langer, J.; Liz-Marzan, L. M. *Acs Nano* **2014,** 8, (6), 5833-5842.
21. Tan, C. L.; Zhang, H. *Chem Soc Rev* **2015,** 44, (9), 2713-2731.
22. Fan, Z. X.; Huang, X.; Tan, C. L.; Zhang, H. *Chem Sci* **2015,** 6, (1), 95-111.
23. Dutta, S.; Pati, S. K. *J Mater Chem* **2010,** 20, (38), 8207-8223.
24. Henzie, J.; Kwak, E. S.; Odom, T. W. *Nano Lett* **2005,** 5, (7), 1199-1202.
25. Lee, J.; Hasan, W.; Stender, C. L.; Odom, T. W. *Accounts Chem Res* **2008,** 41, (12), 1762-1771.
26. Burt, J. L.; Elechiguerra, J. L.; Reyes-Gasga, J.; Montejano-Carrizales, J. M.; Jose-Yacaman, M. *J Cryst Growth* **2005,** 285, (4), 681-691.
27. Wang, L.; Zhang, Y. M.; Scofield, M. E.; Yue, S. Y.; McBean, C.; Marschilok, A. C.; Takeuchi, K. J.; Takeuchi, E. S.; Wong, S. S. *Chemsuschem* **2015,** 8, (19), 3304-3313.
28. Jena, B. K.; Raj, C. R. *Langmuir* **2007,** 23, (7), 4064-4070.
29. Kharisov, B. I. *Recent Pat Nanotech* **2008,** 2, (3), 190-200.

30. O'Dwyer, C.; Navas, D.; Lavayen, V.; Benavente, E.; Santa Ana, M. A.; Gonzalez, G.; Newcomb, S. B.; Torres, C. M. S. *Chem Mater* **2006,** 18, (13), 3016-3022.
31. Hu, J. Q.; Zhang, Y.; Liu, B.; Liu, J. X.; Zhou, H. H.; Xu, Y. F.; Jiang, Y. X.; Yang, Z. L.; Tian, Z. Q. *Journal of the American Chemical Society* **2004,** 126, (31), 9470-9471.
32. Xia, X. H.; Xia, Y. N. *Front Phys-Beijing* **2014,** 9, (3), 378-384.
33. Sutter, E.; Jungjohann, K.; Bliznakov, S.; Courty, A.; Maisonhaute, E.; Tenney, S.; Sutter, P. *Nat Commun* **2014,** 5.
34. Wang, H.; Brandl, D. W.; Le, F.; Nordlander, P.; Halas, N. J. *Nano Lett* **2006,** 6, (4), 827-832.
35. Teranishi, T.; Inoue, Y.; Nakaya, M.; Oumi, Y.; Sano, T. *Journal of the American Chemical Society* **2004,** 126, (32), 9914-9915.
36. Yun, S.; Lee, Y. C.; Park, H. S. *Sci Rep-Uk* **2016,** 6.
37. Ma, C. M.; Zhang, R. F.; Liaw, J. W.; Cheng, J. C. *Appl Phys a-Mater* **2014,** 115, (1), 31-37.
38. Lin, X.; Chu, D. W.; Younis, A.; Li, S.; Dang, F. *Curr Org Chem* **2013,** 17, (15), 1666-1679.
39. Métraux, G. S.; Cao, Y. C.; Jin, R.; Mirkin, C. A. *Nano Lett* **2003,** 3, (4), 519-522.
40. Yu, H.; Chen, M.; Rice, P. M.; Wang, S. X.; White, R. L.; Sun, S. H. *Nano Lett* **2005,** 5, (2), 379-382.
41. Cahen, D.; Hodes, G.; Gratzel, M.; Guillemoles, J. F.; Riess, I. *J Phys Chem B* **2000,** 104, (9), 2053-2059.
42. Wan, J. Y.; Song, T.; Flox, C.; Yang, J. Y.; Yang, Q. H.; Han, X. G. *J Nanomater* **2015**.
43. Robertson, N. *Angew Chem Int Edit* **2006,** 45, (15), 2338-2345.
44. Weber, J.; Singhal, R.; Zekri, S.; Kumar, A. *Int Mater Rev* **2008,** 53, (4), 235-255.
45. Wang, N.; Cai, Y.; Zhang, R. Q. *Mat Sci Eng R* **2008,** 60, (1-6), 1-51.
46. Cademartiri, L.; Ozin, G. A. *Adv Mater* **2009,** 21, (9), 1013-1020.
47. Lim, B.; Jiang, M. J.; Camargo, P. H. C.; Cho, E. C.; Tao, J.; Lu, X. M.; Zhu, Y. M.; Xia, Y. N. *Science* **2009,** 324, (5932), 1302-1305.
48. Du, S. F.; Lin, K. J.; Malladi, S. K.; Lu, Y. X.; Sun, S. H.; Xu, Q.; Steinberger-Wilckens, R.; Dong, H. S. *Sci Rep-Uk* **2014,** 4.
49. Foley, J. M.; Price, M. J.; Feldblyum, J. I.; Maldonado, S. *Energ Environ Sci* **2012,** 5, (1), 5203-5220.
50. Larminie, J.; Dicks, A., *Fuel cell systems explained*. 2nd ed.; J. Wiley: Chichester, West Sussex, 2003; p xxii, 406 p.
51. Wang, Y.; Chen, K. S.; Mishler, J.; Cho, S. C.; Adroher, X. C. *Appl Energ* **2011,** 88, (4), 981-1007.
52. Lucia, U. *Renew Sust Energ Rev* **2014,** 30, 164-169.
53. Vielstich, W.; Lamm, A.; Gasteiger, H. A., *Handbook of fuel cells : fundamentals, technology, and applications*. Wiley: Chichester, England ; Hoboken, N.J., 2003; p 4 v.
54. Grubb, W. T.; Niedrach, L. W. *J Electrochem Soc* **1960,** 107, (2), 131-135.
55. Merle, G.; Wessling, M.; Nijmeijer, K. *J Membrane Sci* **2011,** 377, (1-2), 1-35.
56. Behling, N. H., *Fuel cells : current technology challenges and future research needs*. 1st ed.; Elsevier: Amsterdam ; Boston, 2013; p xiv, 685 p.
57. Anahara, R. *Int J Hydrogen Energ* **1992,** 17, (5), 375-379.
58. Choudhury, S. R., Phosphoric Acid Fuel Cell Technology. In *Recent Trends in Fuel Cell Science and Technology*, Basu, S., Ed. Springer New York: New York, NY, 2007; pp 188-216.

59. Plomp, L.; Veldhuis, J. B. J.; Sitters, E. F.; Vandermolen, S. B. *J Power Sources* **1992,** 39, (3), 369-373.
60. Leo, T. *Comprehensive Renewable Energy, Vol 4: Fuel Cells and Hydrogen Technology* **2012**, 247-259.
61. Stambouli, A. B.; Traversa, E. *Renew Sust Energ Rev* **2002,** 6, (5), 433-455.
62. Adams, T. A.; Nease, J.; Tucker, D.; Barton, P. I. *Ind Eng Chem Res* **2013,** 52, (9), 3089-3111.
63. Jiang, Z. Q.; Jiang, Z. J. *Carbon Nanotubes - Growth and Applications* **2011**, 567-604.
64. Kim, G.; Eom, K.; Kim, M.; Yoo, S. J.; Jang, J. H.; Kim, H. J.; Cho, E. *Acs Appl Mater Inter* **2015,** 7, (50), 27581-27585.
65. Pilatowsky, I.; Romero, R. J.; Isaza, C. A.; Gamboa, S. A.; Sebastian, P. J.; Rivera, W. *Green Energy Technol* **2011**, 25-36.
66. *Fuel Cell Catalysis: A Surface Science Approach*. John Wiley and Sons: Hoboken, NJ, 2009; p 1-632.
67. Murthi, V. S.; Urian, R. C.; Mukerjee, S. *J Phys Chem B* **2004,** 108, (30), 11011-11023.
68. Xu, Y.; Zhang, B. *Chem Soc Rev* **2014,** 43, (8), 2439-2450.
69. *Fuel Cell Technologies: Multi-Year Research, Development, and Demonstration Plan*; U.S. Department of Energy: 2012; pp 3.4-1 - 3.4-49.
70. Greeley, J.; Stephens, I. E. L.; Bondarenko, A. S.; Johansson, T. P.; Hansen, H. A.; Jaramillo, T. F.; Rossmeisl, J.; Chorkendorff, I.; Norskov, J. K. *Nat Chem* **2009,** 1, (7), 552-556.
71. Kitchin, J. R.; Norskov, J. K.; Barteau, M. A.; Chen, J. G. *Phys Rev Lett* **2004,** 93, (15), 156801/1-156801/4.
72. Han, L.; Liu, H.; Cui, P. L.; Peng, Z. J.; Zhang, S. J.; Yang, J. *Sci Rep-Uk* **2014,** 4.
73. Choi, S. I.; Xie, S. F.; Shao, M. H.; Odell, J. H.; Lu, N.; Peng, H. C.; Protsailo, L.; Guerrero, S.; Park, J. H.; Xia, X. H.; Wang, J. G.; Kim, M. J.; Xia, Y. N. *Nano Lett* **2013,** 13, (7), 3420-3425.
74. Oezaslan, M.; Hasche, F.; Strasser, P. *Journal of Physical Chemistry Letters* **2013,** 4, (19), 3273-3291.
75. Kang, Y.; Snyder, J.; Chi, M.; Li, D.; More, K. L.; Markovic, N. M.; Stamenkovic, V. R. *Nano Lett* **2014,** 14, (11), 6361-6367.
76. Adzic, R. R.; Zhang, J.; Sasaki, K.; Vukmirovic, M. B.; Shao, M.; Wang, J. X.; Nilekar, A. U.; Mavrikakis, M.; Valerio, J. A.; Uribe, F. *Top Catal* **2007,** 46, (3-4), 249-262.
77. Koenigsmann, C.; Scofield, M. E.; Liu, H. Q.; Wong, S. S. *J Phys Chem Lett* **2012,** 3, (22), 3385-3398.
78. Koenigsmann, C.; Sutter, E.; Adzic, R. R.; Wong, S. S. *J Phys Chem C* **2012,** 116, (29), 15297-15306.
79. Capon, A.; Parson, R. *Journal of Electroanalytical Chemistry and Interfacial Electrochemistry* **1973,** 44, (1), 1-7.
80. Capon, A.; Parsons, R. *Journal of Electroanalytical Chemistry and Interfacial Electrochemistry* **1973,** 44, (2), 239-254.
81. Capon, A.; Parsons, R. *Journal of Electroanalytical Chemistry and Interfacial Electrochemistry* **1973,** 45, (2), 205-231.
82. Jeong, K. J.; Miesse, C. A.; Choi, J. H.; Lee, J.; Han, J.; Yoon, S. P.; Nam, S. W.; Lim, T. H.; Lee, T. G. *J Power Sources* **2007,** 168, (1), 119-125.
83. Yu, X. W.; Pickup, P. G. *J Power Sources* **2008,** 182, (1), 124-132.
84. Uhm, S.; Lee, H. J.; Lee, J. *Phys Chem Chem Phys* **2009,** 11, (41), 9326-9336.

85. Jiang, K.; Zhang, H. X.; Zou, S. Z.; Cai, W. B. *Phys Chem Chem Phys* **2014,** 16, (38), 20360-20376.
86. Rice, C.; Ha, R. I.; Masel, R. I.; Waszczuk, P.; Wieckowski, A.; Barnard, T. *J Power Sources* **2002,** 111, (1), 83-89.
87. Zhou, W. P.; Lewera, A.; Larsen, R.; Masel, R. I.; Bagus, P. S.; Wieckowski, A. *J Phys Chem B* **2006,** 110, (27), 13393-13398.
88. Zhou, W. J.; Lee, J. Y. *J Phys Chem C* **2008,** 112, (10), 3789-3793.
89. Ojani, R.; Abkar, Z.; Hasheminejad, E.; Raoof, J. B. *Int J Hydrogen Energ* **2014,** 39, (15), 7788-7797.
90. Xu, C. X.; Liu, Y. Q.; Wang, J. P.; Geng, H. R.; Qiu, H. J. *J Power Sources* **2012,** 199, 124-131.
91. Antolini, E.; Gonzalez, E. R. *J Power Sources* **2010,** 195, (11), 3431-3450.
92. McLean, G. F.; Niet, T.; Prince-Richard, S.; Djilali, N. *Int J Hydrogen Energ* **2002,** 27, (5), 507-526.
93. Ramaswamy, N.; Mukerjee, S. *Advances in Physical Chemistry* **2012,** 2012, 17.
94. Lai, S. C. S.; Koper, M. T. M. *Phys Chem Chem Phys* **2009,** 11, (44), 10446-10456.
95. Kimble, M. C.; White, R. E. *J Electrochem Soc* **1991,** 138, (11), 3370-3382.
96. Jasinski, R. *Nature* **1964,** 201, (4925), 1212-1213.
97. Jeon, I. Y.; Choi, H. J.; Choi, M.; Seo, J. M.; Jung, S. M.; Kim, M. J.; Zhang, S.; Zhang, L. P.; Xia, Z. H.; Dai, L. M.; Park, N.; Baek, J. B. *Sci Rep-Uk* **2013,** 3.
98. Wu, G.; More, K. L.; Johnston, C. M.; Zelenay, P. *Science* **2011,** 332, (6028), 443-447.
99. Sun, X. J.; Zhang, Y. W.; Song, P.; Pan, J.; Zhuang, L.; Xu, W. L.; Xing, W. *Acs Catal* **2013,** 3, (8), 1726-1729.
100. Oh, H. S.; Kim, H. *J Power Sources* **2012,** 212, 220-225.
101. Chen, Z. W.; Higgins, D.; Yu, A. P.; Zhang, L.; Zhang, J. J. *Energ Environ Sci* **2011,** 4, (9), 3167-3192.
102. Jaouen, F.; Proietti, E.; Lefevre, M.; Chenitz, R.; Dodelet, J. P.; Wu, G.; Chung, H. T.; Johnston, C. M.; Zelenay, P. *Energ Environ Sci* **2011,** 4, (1), 114-130.
103. Xiang, Z. H.; Xue, Y. H.; Cao, D. P.; Huang, L.; Chen, J. F.; Dai, L. M. *Angew Chem Int Edit* **2014,** 53, (9), 2433-2437.
104. Koslowski, U. I.; Abs-Wurmbach, I.; Fiechter, S.; Bogdanoff, P. *J Phys Chem C* **2008,** 112, (39), 15356-15366.
105. Bouwkamp-Wijnoltz, A. L.; Visscher, W.; van Veen, J. A. R.; Boellaard, E.; van der Kraan, A. M.; Tang, S. C. *J Phys Chem B* **2002,** 106, (50), 12993-13001.
106. Rigsby, M. L.; Wasylenko, D. J.; Pegis, M. L.; Mayer, J. M. *Journal of the American Chemical Society* **2015,** 137, (13), 4296-4299.
107. Liu, H. S.; Shi, Z.; Zhang, J. L.; Zhang, L.; Zhang, J. J. *J Mater Chem* **2009,** 19, (4), 468-470.
108. Choi, J. Y.; Hsu, R. S.; Chen, Z. W. *J Phys Chem C* **2010,** 114, (17), 8048-8053.
109. Hsu, R. S.; Chen, Z. W. *Electrode Processes Relevant to Fuel Cell Technology* **2010,** 28, (23), 39-46.
110. Ye, S. Y.; Vijh, A. K. *Electrochem Commun* **2003,** 5, (3), 272-275.
111. Tian, J.; Morozan, A.; Sougrati, M. T.; Lefevre, M.; Chenitz, R.; Dodelet, J. P.; Jones, D.; Jaouen, F. *Angew Chem Int Edit* **2013,** 52, (27), 6867-6870.
112. Wang, M. Q.; Yang, W. H.; Wang, H. H.; Chen, C.; Zhou, Z. Y.; Sun, S. G. *Acs Catal* **2014,** 4, (11), 3928-3936.

113. Liu, J.; Sun, X. J.; Song, P.; Zhang, Y. W.; Xing, W.; Xu, W. L. *Adv Mater* **2013,** 25, (47), 6879-6883.
114. Xiao, M. L.; Zhu, J. B.; Feng, L. G.; Liu, C. P.; Xing, W. *Adv Mater* **2015,** 27, (15), 2521-2527.
115. Niu, W. H.; Li, L. G.; Liu, X. J.; Wang, N.; Liu, J.; Zhou, W. J.; Tang, Z. H.; Chen, S. W. *Journal of the American Chemical Society* **2015,** 137, (16), 5555-5562.
116. Ge, X. M.; Sumboja, A.; Wuu, D.; An, T.; Li, B.; Goh, F. W. T.; Hor, T. S. A.; Zong, Y.; Liu, Z. L. *Acs Catal* **2015,** 5, (8), 4643-4667.
117. Liu, J.; Li, E. L.; Ruan, M. B.; Song, P.; Xu, W. L. *Catalysts* **2015,** 5, (3), 1167-1192.
118. Morozan, A.; Jousselme, B.; Palacin, S. *Energ Environ Sci* **2011,** 4, (4), 1238-1254.
119. Varcoe, J. R.; Slade, R. C. T. *Electrochem Commun* **2006,** 8, (5), 839-843.
120. Sylwan, C. L. *Energ Convers* **1977,** 17, (2-3), 67-72.
121. Cairns, E. J.; Bartosik, D. C. *J Electrochem Soc* **1964,** 111, (3), C78-C78.
122. Jayashree, R. S.; Egas, D.; Spendelow, J. S.; Natarajan, D.; Markoski, L. J.; Kenis, P. J. A. *Electrochem Solid St* **2006,** 9, (5), A252-A256.
123. Choban, E. R.; Spendelow, J. S.; Gancs, L.; Wieckowski, A.; Kenis, P. J. A. *Electrochim Acta* **2005,** 50, (27), 5390-5398.
124. Yu, E. H.; Scott, K. *J Appl Electrochem* **2005,** 35, (1), 91-96.
125. Matsuoka, K.; Iriyama, Y.; Abe, T.; Matsuoka, M.; Ogumi, Z. *J Power Sources* **2005,** 150, 27-31.
126. Huang, A. B.; Xia, C. Y.; Xiao, C. B.; Zhuang, L. *J Appl Polym Sci* **2006,** 100, (3), 2248-2251.
127. Morallon, E.; Rodes, A.; Vazquez, J. L.; Perez, J. M. *J Electroanal Chem* **1995,** 391, (1-2), 149-157.
128. Matsuoka, K.; Iriyama, Y.; Abe, T.; Matsuoka, M.; Ogumi, Z. *Electrochim Acta* **2005,** 51, (6), 1085-1090.
129. Bagotzky, V. S.; Vassilyev, Y. B. *Electrochim Acta* **1967,** 12, (9), 1323-1343.
130. Spendelow, J. S.; Goodpaster, J. D.; Kenis, P. J. A.; Wieckowski, A. *Langmuir* **2006,** 22, (25), 10457-10464.
131. Tripkovic, A. V.; Popovic, K. D.; Grgur, B. N.; Blizanac, B.; Ross, P. N.; Markovic, N. M. *Electrochim Acta* **2002,** 47, (22-23), 3707-3714.
132. Spendelow, J. S.; Wieckowski, A. *Phys Chem Chem Phys* **2007,** 9, (21), 2654-2675.
133. Lu, C.; Rice, C.; Masel, R. I.; Babu, P. K.; Waszczuk, P.; Kim, H. S.; Oldfield, E.; Wieckowski, A. *J Phys Chem B* **2002,** 106, (37), 9581-9589.
134. Ishikawa, Y.; Liao, M. S.; Cabrera, C. R. *Surf Sci* **2000,** 463, (1), 66-80.
135. Liu, P.; Logadottir, A.; Nørskov, J. K. *Electrochim Acta* **2003,** 48, (25–26), 3731-3742.
136. Rolison, D. R.; Hagans, P. L.; Swider, K. E.; Long, J. W. *Langmuir* **1999,** 15, (3), 774-779.
137. Davies, J. C.; Bonde, J.; Logadottir, A.; Norskov, J. K.; Chorkendorff, I. *Fuel Cells* **2005,** 5, (4), 429-435.
138. Roth, C.; Papworth, A. J.; Hussain, I.; Nichols, R. J.; Schiffrin, D. J. *J Electroanal Chem* **2005,** 581, (1), 79-85.
139. Meng, H.; Zeng, D. R.; Xie, F. Y. *Catalysts* **2015,** 5, (3), 1221-1274.
140. Rodriguez, J. A.; Goodman, D. W. *Accounts Chem Res* **1995,** 28, (12), 477-478.
141. Zhou, W. P.; Lewera, A.; Bagus, P. S.; Wieckowski, A. *J Phys Chem C* **2007,** 111, (36), 13490-13496.

142. Kitchin, J. R.; Norskov, J. K.; Barteau, M. A.; Chen, J. G. *Phys Rev Lett* **2004,** 93, (15).

143. Greeley, J.; Mavrikakis, M. *Nat Mater* **2004,** 3, (11), 810-815.

144. Xu, Y.; Ruban, A. V.; Mavrikakis, M. *Journal of the American Chemical Society* **2004,** 126, (14), 4717-4725.

145. Mahapatra, S. S.; Datta, J. *International Journal of Electrochemistry* **2011,** 2011, 16.

146. Prabhuram, J.; Manoharan, R. *J Power Sources* **1998,** 74, (1), 54-61.

147. Manoharan, R.; Prabhuram, J. *J Power Sources* **2001,** 96, (1), 220-225.

148. Lamy, C.; Lima, A.; LeRhun, V.; Delime, F.; Coutanceau, C.; Leger, J. M. *J Power Sources* **2002,** 105, (2), 283-296.

149. Li, M.; Kowal, A.; Sasaki, K.; Marinkovic, N.; Su, D.; Korach, E.; Liu, P.; Adzic, R. R. *Electrochim Acta* **2010,** 55, (14), 4331-4338.

150. Demirci, U. B. *J Power Sources* **2007,** 173, (1), 11-18.

151. Kamarudin, M. Z. F.; Kamarudin, S. K.; Masdar, M. S.; Daud, W. R. W. *Int J Hydrogen Energ* **2013,** 38, (22), 9438-9453.

152. Shao, M. H.; Adzic, R. R. *Electrochim Acta* **2005,** 50, (12), 2415-2422.

153. Liang, Z. X.; Zhao, T. S.; Xu, J. B.; Zhu, L. D. *Electrochim Acta* **2009,** 54, (8), 2203-2208.

154. Hammer, B.; Norskov, J. K. *Adv Catal* **2000,** 45, 71-129.

155. Lai, S. C. S.; Kleijn, S. E. F.; Ozturk, F. T. Z.; Vellinga, V. C. V.; Koning, J.; Rodriguez, P.; Koper, M. T. M. *Catal Today* **2010,** 154, (1-2), 92-104.

156. Hitmi, H.; Belgsir, E. M.; Leger, J. M.; Lamy, C.; Lezna, R. O. *Electrochim Acta* **1994,** 39, (3), 407-415.

157. Vigier, F.; Coutanceau, C.; Hahn, F.; Belgsir, E. M.; Lamy, C. *J Electroanal Chem* **2004,** 563, (1), 81-89.

158. Rasko, J.; Domok, A.; Baan, K.; Erdohelyi, A. *Appl Catal a-Gen* **2006,** 299, 202-211.

159. Christensen, P. A.; Jones, S. W. M.; Hamnett, A. *J Phys Chem C* **2012,** 116, (46), 24681-24689.

160. Yang, Y. Y.; Ren, J.; Li, Q. X.; Zhou, Z. Y.; Sun, S. G.; Cai, W. B. *Acs Catal* **2014,** 4, (3), 798-803.

161. Iwasita, T.; Pastor, E. *Electrochim Acta* **1994,** 39, (4), 531-537.

162. Wang, H.; Jusys, Z.; Behm, R. J. *Fuel Cells* **2004,** 4, (1-2), 113-125.

163. Wang, H.; Jusys, Z.; Behm, R. J. *J Power Sources* **2006,** 154, (2), 351-359.

164. Wang, Q.; Sun, G. Q.; Jiang, L. H.; Xin, Q.; Sun, S. G.; Jiang, Y. X.; Chen, S. P.; Jusys, Z.; Behm, R. J. *Phys Chem Chem Phys* **2007,** 9, (21), 2686-2696.

165. Belgsir, E. M.; Bouhier, E.; Yei, H. E.; Kokoh, K. B.; Beden, B.; Huser, H.; Leger, J. M.; Lamy, C. *Electrochim Acta* **1991,** 36, (7), 1157-1164.

166. Tarnowski, D. J.; Korzeniewski, C. *J Phys Chem B* **1997,** 101, (2), 253-258.

167. Wang, H. F.; Liu, Z. P. *Journal of the American Chemical Society* **2008,** 130, (33), 10996-11004.

168. Kavanagh, R.; Cao, X. M.; Lin, W. F.; Hardacre, C.; Hu, P. *Angew Chem Int Edit* **2012,** 51, (7), 1572-1575.

169. Asiri, H. A.; Anderson, A. B. *J Electrochem Soc* **2015,** 162, (1), F115-F122.

170. Leung, L. W. H.; Chang, S. C.; Weaver, M. J. *J Electroanal Chem* **1989,** 266, (2), 317-336.

171. Leung, L. W. H.; Weaver, M. J. *J Phys Chem-Us* **1988,** 92, (14), 4019-4022.

172. Gao, P.; Chang, S. C.; Zhou, Z. H.; Weaver, M. J. *J Electroanal Chem* **1989,** 272, (1-2), 161-178.
173. Fang, X.; Wang, L. Q.; Shen, P. K.; Cui, G. F.; Bianchini, C. *J Power Sources* **2010,** 195, (5), 1375-1378.
174. Ma, L.; Chu, D.; Chen, R. R. *Int J Hydrogen Energ* **2012,** 37, (15), 11185-11194.
175. Sheikh, A. M.; Silva, E. L.; Moares, L.; Antonini, L. M.; Abellah, M. Y.; Malfatti, C. F. *American Journal of Mining and Metallurgy* **2014,** 2, (4), 64-69.
176. Zhu, L. D.; Zhao, T. S.; Xu, J. B.; Liang, Z. X. *J Power Sources* **2009,** 187, (1), 80-84.
177. Wang, H.; Xu, C. W.; Cheng, F. L.; Jiang, S. P. *Electrochem Commun* **2007,** 9, (5), 1212-1216.
178. Dutta, A.; Datta, J. *J Phys Chem C* **2012,** 116, (49), 25677-25688.
179. Bahemmat, S.; Ghassemzadeh, M.; Afsharpour, M.; Harms, K. *Polyhedron* **2015,** 89, 196-202.
180. Wang, K. W.; Kang, W. D.; Wei, Y. C.; Liu, C. W.; Su, P. C.; Chen, H. S.; Chung, S. R. *Chemcatchem* **2012,** 4, (8), 1154-1161.
181. Zhao, X.; Zhang, J.; Wang, L. J.; Liu, Z. L.; Chen, W. *J Mater Chem A* **2014,** 2, (48), 20933-20938.
182. Du, W. X.; Mackenzie, K. E.; Milano, D. F.; Deskins, N. A.; Su, D.; Teng, X. W. *Acs Catal* **2012,** 2, (2), 287-297.
183. Mao, H. M.; Wang, L. L.; Zhu, P. P.; Xu, Q. J.; Li, Q. X. *Int J Hydrogen Energ* **2014,** 39, (31), 17583-17588.
184. da Silva, S. G.; Assumpcao, M. H. M. T.; Silva, J. C. M.; De Souza, R. F. B.; Spinace, E. V.; Neto, A. O.; Buzzo, G. S. *Int J Electrochem Sc* **2014,** 9, (10), 5416-5424.
185. Carmo, M.; Sekol, R. C.; Ding, S. Y.; Kumar, G.; Schroers, J.; Taylor, A. D. *Acs Nano* **2011,** 5, (4), 2979-2983.
186. Takeguchi, T.; Anzai, Y.; Kikuchi, R.; Eguchi, K.; Ueda, W. *J Electrochem Soc* **2007,** 154, (11), B1132-B1137.
187. Shen, P. K.; Xu, C. W. *Electrochem Commun* **2006,** 8, (1), 184-188.
188. Wang, L. Q.; Lavacchi, A.; Bevilacqua, M.; Bellini, M.; Fornasiero, P.; Filippi, J.; Innocenti, M.; Marchionni, A.; Miller, H. A.; Vizza, F. *Chemcatchem* **2015,** 7, (14), 2214-2221.
189. Hu, C. G.; Cheng, H. H.; Zhao, Y.; Hu, Y.; Liu, Y.; Dai, L. M.; Qu, L. T. *Adv Mater* **2012,** 24, (40), 5493-5498.
190. Zhu, F. C.; Ma, G. S.; Bai, Z. C.; Hang, R. Q.; Tang, B.; Zhang, Z. H.; Wang, X. G. *J Power Sources* **2013,** 242, 610-620.
191. Wang, H.; Jusys, Z.; Behm, R. J. *J Phys Chem B* **2004,** 108, (50), 19413-19424.
192. Wang, Y.; Zou, S. Z.; Cai, W. B. *Catalysts* **2015,** 5, (3), 1507-1534.
193. Li, M.; Liu, P.; Adzic, R. R. *J Phys Chem Lett* **2012,** 3, (23), 3480-3485.
194. Wenham, S. R., *Applied photovoltaics*. 3rd ed.; Earthscan: London ; New York, 2012.
195. Mathew, S.; Yella, A.; Gao, P.; Humphry-Baker, R.; Curchod, B. F. E.; Ashari-Astani, N.; Tavernelli, I.; Rothlisberger, U.; Nazeeruddin, M. K.; Gratzel, M. *Nat Chem* **2014,** 6, (3), 242-247.
196. Kamat, P. V. *J Phys Chem C* **2008,** 112, (48), 18737-18753.
197. Sambur, J. B.; Novet, T.; Parkinson, B. A. *Science* **2010,** 330, (6000), 63-66.
198. Nozik, A. J.; Beard, M. C.; Luther, J. M.; Law, M.; Ellingson, R. J.; Johnson, J. C. *Chem Rev* **2010,** 110, (11), 6873-6890.

199. Duan, J. L.; Zhang, H. H.; Tang, Q. W.; He, B. L.; Yu, L. M. *J Mater Chem A* **2015,** 3, (34), 17497-17510.
200. Kouhnavard, M.; Ikeda, S.; Ludin, N. A.; Khairudin, N. B. A.; Ghaffari, B. V.; Mat-Teridi, M. A.; Ibrahim, M. A.; Sepeai, S.; Sopian, K. *Renew Sust Energ Rev* **2014,** 37, 397-407.
201. Singh, L. P.; Srivastava, K.; Mishra, R.; Ningthoujam, R. S. *J Phys Chem C* **2014,** 118, (31), 18087-18096.
202. Bender, C. M.; Burlitch, J. M.; Barber, D.; Pollock, C. *Chem Mater* **2000,** 12, (7), 1969-1976.
203. Jackson, S. D. *Opt Lett* **2003,** 28, (22), 2192-2194.
204. Di Bartolo, B.; Powell, R. C., *Crystal symmetry, lattice vibrations and optical spectroscopy of solids : a group theoretical approach*. World Scientific: Hackensack New Jersey, 2014; p xviii, 515 pages.
205. Trupke, T.; Green, M. A.; Wurfel, P. *J Appl Phys* **2002,** 92, (7), 4117-4122.
206. Zhou, Z. Y.; Wang, J. H.; Nan, F.; Bu, C. H.; Yu, Z. H.; Liu, W.; Guo, S. S.; Hu, H.; Zhao, X. Z. *Nanoscale* **2014,** 6, (4), 2052-2055.
207. Zhu, G.; Wang, H. Y.; Zhang, Q. X.; Zhang, L. *J Colloid Interf Sci* **2015,** 451, 15-20.
208. Luoshan, M. D.; Li, M. Y.; Liu, X. L.; Guo, K. M.; Bai, L. H.; Zhu, Y. D.; Sun, B. L.; Zhao, X. Z. *J Power Sources* **2015,** 287, 231-236.
209. Wang, K. F.; Jiang, J. Q.; Wan, S. J.; Zhai, J. *Electrochim Acta* **2015,** 155, 357-363.
210. Liu, H. Q.; Li, L. Y.; Scofield, M. E.; Wong, S. S. *Apl Mater* **2015,** 3, (8).
211. Johnson, S. A.; Khushalani, D.; Coombs, N.; Mallouk, T. E.; Ozin, G. A. *J Mater Chem* **1998,** 8, (1), 13-14.
212. Volosskiy, B.; Niwa, K.; Chen, Y.; Zhao, Z. P.; Weiss, N. O.; Zhong, X.; Ding, M. N.; Lee, C.; Huang, Y.; Duan, X. F. *Acs Nano* **2015,** 9, (3), 3044-3049.
213. Ruan, L. Y.; Zhu, E. B.; Chen, Y.; Lin, Z. Y.; Huang, X. Q.; Duan, X. F.; Huang, Y. *Angew Chem Int Edit* **2013,** 52, (48), 12577-12581.
214. Qian, Z. X.; Park, S. J. *Chem Mater* **2014,** 26, (21), 6172-6177.
215. Liu, H.; Cao, X. M.; Yang, J. M.; Gong, X. Q.; Shi, X. Y. *Sci Rep-Uk* **2013,** 3.
216. Morita, C.; Tanuma, H.; Kawai, C.; Ito, Y.; Imura, Y.; Kawai, T. *Langmuir* **2013,** 29, (5), 1669-1675.
217. Morita, C.; Kawai, C.; Tsujimoto, K.; Kasai, K.; Ogue, Y.; Imura, Y.; Kawai, T. *J Oleo Sci* **2013,** 62, (2), 81-87.
218. Shi, L. H.; Wang, A. Q.; Huang, Y. Q.; Chen, X. W.; Delgado, J. J.; Zhang, T. *Eur J Inorg Chem* **2012**, (16), 2700-2706.
219. Koenigsmann, C.; Santulli, A. C.; Gong, K. P.; Vukmirovic, M. B.; Zhou, W. P.; Sutter, E.; Wong, S. S.; Adzic, R. R. *J Am Chem Soc* **2011,** 133, (25), 9783-9795.
220. Koenigsmann, C.; Sutter, E.; Adzic, R. R.; Wong, S. S. *The Journal of Physical Chemistry C* **2012,** 116, (29), 15297-15306.
221. Teng, X. W.; Han, W. Q.; Ku, W.; Hucker, M. *Angew Chem Int Edit* **2008,** 47, (11), 2055-2058.
222. Koenigsmann, C.; Zhou, W. P.; Adzic, R. R.; Sutter, E.; Wong, S. S. *Nano Lett* **2010,** 10, (8), 2806-2811.
223. Liu, H. Q.; Koenigsmann, C.; Adzic, R. R.; Wong, S. S. *Acs Catal* **2014,** 4, (8), 2544-2555.
224. Liu, H. Q.; Adzic, R. R.; Wong, S. S. *Acs Appl Mater Inter* **2015,** 7, (47), 26145-26157.

225. Liu, H. Q.; An, W.; Li, Y. Y.; Frenkel, A. I.; Sasaki, K.; Koenigsmann, C.; Su, D.; Anderson, R. M.; Crooks, R. M.; Adzic, R. R.; Liu, P.; Wong, S. S. *Journal of the American Chemical Society* **2015,** 137, (39), 12597-12609.
226. Brankovic, S. R.; Wang, J. X.; Adzic, R. R. *Surf Sci* **2001,** 474, (1-3), L173-L179.
227. Wang, J. X.; Inada, H.; Wu, L.; Zhu, Y.; Choi, Y.; Liu, P.; Zhou, W.-P.; Adzic, R. R. *J Am Chem Soc* **2009,** 131, (47), 17298-17302.
228. Vukmirovic, M. B.; Bliznakov, S. T.; Sasaki, K.; Wang, J. X.; Adzic, R. R. *Electrochem. Soc. Interface* **2011,** 20, (2), 33-40.
229. Zhou, W. P.; Sasaki, K.; Su, D.; Zhu, Y. M.; Wang, J. X.; Adzic, R. R. *J Phys Chem C* **2010,** 114, (19), 8950-8957.
230. Wang, D. L.; Xin, H. L. L.; Hovden, R.; Wang, H. S.; Yu, Y. C.; Muller, D. A.; DiSalvo, F. J.; Abruna, H. D. *Nat Mater* **2013,** 12, (1), 81-87.
231. Mazumder, V.; Chi, M. F.; More, K. L.; Sun, S. H. *Journal of the American Chemical Society* **2010,** 132, (23), 7848-+.
232. Gong, K. P.; Su, D.; Adzic, R. R. *Journal of the American Chemical Society* **2010,** 132, (41), 14364-14366.
233. Chen, D.; Li, Y. X.; Liao, S. J.; Su, D.; Song, H. Y.; Li, Y. W.; Yang, L. J.; Li, C. *Sci Rep-Uk* **2015,** 5.
234. Feng, S. H.; Xu, R. R. *Accounts Chem Res* **2001,** 34, (3), 239-247.
235. Cundy, C. S.; Cox, P. A. *Chem Rev* **2003,** 103, (3), 663-701.
236. Byrappa, K.; Yoshimura, M., *Handbook of hydrothermal technology : a technology for crystal growth and materials processing*. Noyes Publications: Norwich, N.Y., 2001.
237. Lobachev, A. N., *Hydrothermal synthesis of crystals*. Consultants Bureau: New York,, 1971; p xiii, 153 p.
238. Einarsrud, M. A.; Grande, T. *Chem Soc Rev* **2014,** 43, (7), 2187-2199.
239. Yang, L. W.; Zhang, Y. Y.; Li, J. J.; Li, Y.; Zhong, J. X.; Chu, P. K. *Nanoscale* **2010,** 2, (12), 2805-2810.
240. Yang, L. W.; Han, H. L.; Zhang, Y. Y.; Zhong, J. X. *J Phys Chem C* **2009,** 113, (44), 18995-18999.
241. *Chemsuschem* **2010,** 3, (9), 1006-1006.
242. Kresse, G.; Furthmuller, J. *Phys. Rev. B* **1996,** 54, (16), 11169-11186.
243. Kresse, G.; Hafner, J. *Phys. Rev. B* **1993,** 47, (1), 558-561.
244. Perdew, J. P.; Chevary, J. A.; Vosko, S. H.; Jackson, K. A.; Pederson, M. R.; Singh, D. J.; Fiolhais, C. *Physical Review B* **1992,** 46, (11), 6671-6687.
245. Blochl, P. E. *Phys. Rev. B* **1994,** 50, (24), 17953-17979.
246. Monkhorst, H. J.; Pack, J. D. *Physical Review B* **1976,** 13, (12), 5188-5192.
247. Koenigsmann, C.; Sutter, E.; Chiesa, T. A.; Adzic, R. R.; Wong, S. S. *Nano Lett* **2012,** 12, (4), 2013-2020.
248. Norskov, J. K.; Rossmeisl, J.; Logadottir, A.; Lindqvist, L.; Kitchin, J. R.; Bligaard, T.; Jonsson, H. *J Phys Chem B* **2004,** 108, (46), 17886-17892.
249. Stamenkovic, V.; Mun, B. S.; Mayrhofer, K. J. J.; Ross, P. N.; Markovic, N. M.; Rossmeisl, J.; Greeley, J.; Norskov, J. K. *Angew Chem Int Edit* **2006,** 45, (18), 2897-2901.
250. Shao, M.; Liu, P.; Adzic, R. R. *J. Phys. Chem. B* **2007,** 111, 6772-6775.
251. Wang, J. X.; Inada, H.; Wu, L. J.; Zhu, Y. M.; Choi, Y. M.; Liu, P.; Zhou, W. P.; Adzic, R. R. *J Am Chem Soc* **2009,** 131, (47), 17298-17302.
252. Zhang, J.; Yang, H. Z.; Fang, J. Y.; Zou, S. Z. *Nano Lett* **2010,** 10, (2), 638-644.

253. An, W.; Liu, P. *J Phys Chem C* **2013,** 117, (31), 16144-16149.
254. Wolfers, F. *Cr Hebd Acad Sci* **1923,** 177, 759-762.
255. Barer, R.; Cosslett, V. E., Advances in optical and electron microscopy. Academic Press: London, New York,, 1966; p 14 volumes.
256. Hawkes, P. W., *The Beginnings of electron microscopy*. Academic Press: Orlando, 1985; p xix, 633 p.
257. Egerton, R. F., *Physical principles of electron microscopy : an introduction to TEM, SEM, and AEM*. Springer: New York, NY, 2005; p xii, 202 p.
258. Fultz, B.; Howe, J. M., *Transmission electron microscopy and diffractometry of materials*. 4th ed.; Springer: Heidelberg ; New York, 2013; p xx, 761 p.
259. Ke, X. X.; Bittencourt, C.; Van Tendeloo, G. *Beilstein J Nanotech* **2015,** 6, 1541-1557.
260. Thomas, G.; Goringe, M. J., *Transmission electron microscopy of materials*. Wiley: New York, 1979; p xiv, 388 p.
261. Williams, D. B.; Carter, C. B., *Transmission electron microscopy : a textbook for materials science*. Plenum Press: New York, 1996; p xxvii, 729 p.
262. McMullan, D. *Adv Imag Elect Phys* **2004,** 133, 59-91.
263. Danilatos, G. D. *J Microsc-Oxford* **1986,** 142, 317-325.
264. Goldstein, J., *Scanning electron microscopy and x-ray microanalysis*. 3rd ed.; Kluwer Academic/Plenum Publishers: New York, 2003; p xix, 689 p.
265. Teo, B. K., *EXAFS : basic principles and data analysis*. Springer-Verlag: Berlin ; New York, 1986; p xviii, 349 p.
266. Teo, B. K.; Joy, D. C.; Materials Research Society., *EXAFS spectroscopy, techniques and applications*. Plenum Press: New York, 1981; p viii, 275 p.
267. Das, N. C.; Bhabha Atomic Research Centre., *Optical and mechanical design of the extended x-ray absorption fine structure (EXAFS) beam-line at Indus-II synchrotron source*. Bhabha Atomic Research Centre: Mumbai, 2002; p 28 p.
268. Als-Nielsen, J.; McMorrow, D., *Elements of modern X-ray physics*. 2nd ed.; Wiley: Hoboken, 2011; p xii, 419 p.
269. Newville, M. *Rev Mineral Geochem* **2014,** 78, 33-74.
270. Frenkel, A. I. *Chem Soc Rev* **2012,** 41, (24), 8163-8178.
271. Gadaleta, S. J.; Mendelsohn, R.; Paschalis, E. L.; Camacho, N. P.; Betts, F.; Boskey, A. L. *Mineral Scale Formation and Inhibition* **1995**, 283-294.
272. Tan, T. L.; Lau, S. Y.; Ong, P. P.; Goh, K. L.; Teo, H. H. *J Mol Spectrosc* **2000,** 203, (2), 310-313.
273. Toyran, N. *Turk Klin Tip Bilim* **2008,** 28, (5), 704-714.
274. Burkholder, J. B.; Sinha, A.; Hammer, P. D.; Howard, C. J. *J Mol Spectrosc* **1987,** 126, (1), 72-77.
275. Masel, R. I., *Principles of adsorption and reaction on solid surfaces*. Wiley: New York, 1996; p xiv, 804 p.
276. Carr, D. O. *Abstr Pap Am Chem S* **1982,** 184, (Sep), 76-&.
277. Heer, S.; Kompe, K.; Gudel, H. U.; Haase, M. *Adv Mater* **2004,** 16, (23-24), 2102-+.
278. Pokhrel, M.; Gangadharan, A. K.; Sardar, D. K. *Mater Lett* **2013,** 99, 86-89.
279. Berry, M. T.; May, P. S. *J Phys Chem A* **2015,** 119, (38), 9805-9811.
280. Rodriguez, J. M. D.; Melian, J. A. H.; Pena, J. P. *J Chem Educ* **2000,** 77, (9), 1195-1197.
281. Shain, I. *J Electrochem Soc* **1970,** 117, (3), C119-&.
282. Millar, J.; Barnett, T. G. *J Neurosci Meth* **1988,** 25, (2), 91-95.

283. *Zeitschrift für Elektrochemie und angewandte physikalische Chemie* **1951,** 55, (4), 336-336.
284. Ginley, D. S.; Kahen, D. i., *Fundamentals of materials for energy and environmental sustainability*. Cambridge University Press: Cambridge ; New York, 2012; p xvi, 753 p.
285. Wu, J.; Zhang, J.; Peng, Z.; Yang, S.; Wagner, F. T.; Yang, H. *J Am Chem Soc* **2010,** 132, (14), 4984-4985.
286. Vidakovic, T.; Christov, M.; Sundmacher, K. *Electrochim Acta* **2007,** 52, (18), 5606-5613.
287. Garsany, Y.; Baturina, O. A.; Swider-Lyons, K. E.; Kocha, S. S. *Anal Chem* **2010,** 82, (15), 6321-6328.
288. *Fuel Cell Technologies Office Multi-Year Research, Development, and Demonstration Plan*; Department of Energy, 2012.
289. Koenigsmann, C.; Wong, S. S. *Energy & Environmental Science* **2011,** 4, (4), 1161-1176.
290. Koenigsmann, C.; Scofield, M. E.; Liu, H.; Wong, S. S. *The Journal of Physical Chemistry Letters* **2012,** 3, (22), 3385-3398.
291. Savadogo, O.; Lee, K.; Oishi, K.; Mitsushima, S.; Kamiya, N.; Ota, K. I. *Electrochem Commun* **2004,** 6, (2), 105-109.
292. Savadogo, O.; Lee, K.; Mitsushima, S.; Kamiya, N.; Ota, K. I. *J New Mat Electr Sys* **2004,** 7, (2), 77-83.
293. Løvvik, O. M. *Surface Science* **2005,** 583, (1), 100-106.
294. Greeley, J.; Norskov, J. K. *Surf Sci* **2005,** 592, (1-3), 104-111.
295. Li, B.; Prakash, J. *Electrochem Commun* **2009,** 11, (6), 1162-1165.
296. Li, B.; Amiruddin, S.; Prakash, J. *ECS Transactions* **2008,** 6, (25), 139-144.
297. Zhao, J.; Sarkar, A.; Manthiram, A. *Electrochimica Acta* **2010,** 55, (5), 1756-1765.
298. Liu, L.; Samjeske, G.; Nagamatsu, S.-i.; Sekizawa, O.; Nagasawa, K.; Takao, S.; Imaizumi, Y.; Yamamoto, T.; Uruga, T.; Iwasawa, Y. *Top Catal* **2013**, 1-12.
299. Ramos-Sanchez, G.; Bruno, M. M.; Thomas, Y. R. J.; Corti, H. R.; Solorza-Feria, O. *Int J Hydrogen Energ* **2012,** 37, (1), 31-40.
300. Ramos-Sanchez, G.; Yee-Madeira, H.; Solorza-Feria, O. *Int J Hydrogen Energ* **2008,** 33, (13), 3596-3600.
301. Wang, R. F.; Li, H.; Ji, S.; Wang, H.; Lei, Z. Q. *Electrochimica Acta* **2010,** 55, (5), 1519-1522.
302. Shao, M. H.; Smith, B. H.; Guerrero, S.; Protsailo, L.; Su, D.; Kaneko, K.; Odell, J. H.; Humbert, M. P.; Sasaki, K.; Marzullo, J.; Darling, R. M. *Phys Chem Chem Phys* **2013,** 15, (36), 15078-15090.
303. Tarasevich, M. R.; Zhutaeva, G. V.; Bogdanovskaya, V. A.; Radina, M. V.; Ehrenburg, M. R.; Chalykh, A. E. *Electrochimica Acta* **2007,** 52, (15), 5108-5118.
304. Alia, S. M.; Larsen, B. A.; Pylypenko, S.; Cullen, D. A.; Diercks, D. R.; Neyerlin, K. C.; Kocha, S. S.; Pivovar, B. S. *Acs Catal* **2014,** 4, (4), 1114-1119.
305. Calculated Ni-Pd phase diagram. National Physical Laboratory of the United Kingdom: http://resource.npl.co.uk/mtdata/phdiagrams/nipd.htm, 2000.
306. Lee, K.; Savadogo, O.; Ishihara, A.; Mitsushima, S.; Kamiya, N.; Ota, K.-i. *Journal of The Electrochemical Society* **2006,** 153, (1), A20.
307. Ham, D. J.; Pak, C.; Bae, G. H.; Han, S.; Kwon, K.; Jin, S. A.; Chang, H.; Choi, S. H.; Lee, J. S. *Chem Commun (Cambridge)* **2011,** 47, (20), 5792-4.

308. Bozzolo, G.; Noebe, R. D.; Khalil, J.; Morse, J. *Applied Surface Science* **2003,** 219, (1-2), 149-157.
309. Zhang, J.; Vukmirovic, M. B.; Sasaki, K.; Nilekar, A. U.; Mavrikakis, M.; Adzic, R. R. *J. Am. Chem. Soc.* **2005,** 127, 12480-12481.
310. Lima, F. H. B.; Lizcano-Valbuena, W. H.; Texeira-Neto, E.; Nart, F. C.; Gonzalez, E. R.; Ticianelli, E. A. *Electrochimica Acta* **2006,** 52, 385-393.
311. Hsu, S.-P.; Liu, C.-W.; Chen, H.-S.; Chen, T.-Y.; Lai, C.-M.; Lee, C.-H.; Lee, J.-F.; Chan, T.-S.; Tsai, L.-D.; Wang, K.-W. *Electrochimica Acta* **2013,** 105, 180-187.
312. Xing, Y.; Cai, Y.; Vukmirovic, M. B.; Zhou, W.-P.; Karan, H.; Wang, J. X.; Adzic, R. R. *The Journal of Physical Chemistry Letters* **2010,** 1, (21), 3238-3242.
313. Sasaki, K.; Naohara, H.; Cai, Y.; Choi, Y. M.; Liu, P.; Vukmirovic, M. B.; Wang, J. X.; Adzic, R. R. *Angewandte Chemie International Edition* **2010,** 49, (46), 8602-8607.
314. Holton, O. T.; Stevenson, J. W. *Platin Met Rev* **2013,** 57, (4), 259-271.
315. Antolini, E. *Energ Environ Sci* **2009,** 2, (9), 915-931.
316. Liu, H. S.; Song, C. J.; Zhang, L.; Zhang, J. J.; Wang, H. J.; Wilkinson, D. P. *J Power Sources* **2006,** 155, (2), 95-110.
317. Brouzgou, A.; Song, S. Q.; Tsiakaras, P. *Appl Catal B-Environ* **2012,** 127, 371-388.
318. Antolini, E.; Salgado, J. R. C.; Gonzalez, E. R. *Appl Catal B-Environ* **2006,** 63, (1-2), 137-149.
319. Bligaard, T.; Norskov, J. K. *Electrochim Acta* **2007,** 52, (18), 5512-5516.
320. Xu, C. X.; Liu, A. H.; Qiu, H. J.; Liu, Y. Q. *Electrochem Commun* **2011,** 13, (8), 766-769.
321. Jiang, K.; Cai, W.-B. *Applied Catalysis B: Environmental* **2014,** 147, 185-192.
322. Yin, J.; Shan, S. Y.; Ng, M. S.; Yang, L. F.; Mott, D.; Fang, W. Q.; Kang, N.; Luo, J.; Zhong, C. J. *Langmuir* **2013,** 29, (29), 9249-9258.
323. Hu, C. G.; Zhai, X. Q.; Zhao, Y.; Bian, K.; Zhang, J.; Qu, L. T.; Zhang, H. M.; Luo, H. X. *Nanoscale* **2014,** 6, (5), 2768-2775.
324. Dong, Q.; Zhao, Y.; Han, X.; Wang, Y.; Liu, M. C.; Li, Y. *Int J Hydrogen Energ* **2014,** 39, (27), 14669-14679.
325. Shih, Z. Y.; Wang, C. W.; Xu, G. B.; Chang, H. T. *J Mater Chem A* **2013,** 1, (15), 4773-4778.
326. Hsieh, M. W.; Whang, T. J. *Appl Surf Sci* **2013,** 270, 252-259.
327. Wang, R. F.; Zhang, Z.; Wang, H.; Lei, Z. Q. *Electrochem Commun* **2009,** 11, (5), 1089-1091.
328. Wang, H.; Ji, S.; Wang, W.; Wang, R. F. *S Afr J Chem-S-Afr T* **2013,** 66, 17-20.
329. Wen, D.; Guo, S. J.; Dong, S. J.; Wang, E. K. *Biosens Bioelectron* **2010,** 26, (3), 1056-1061.
330. Zhu, C. Z.; Guo, S. J.; Dong, S. J. *J Mater Chem* **2012,** 22, (30), 14851-14855.
331. Xiao, M. L.; Li, S. T.; Zhao, X.; Zhu, J. B.; Yin, M.; Liu, C. P.; Xing, W. *Chemcatchem* **2014,** 6, (10), 2825-2831.
332. Xia, B. Y.; Wu, H. B.; Li, N.; Yan, Y.; Lou, X. W.; Wang, X. *Angewandte Chemie International Edition* **2015,** 54, (12), 3797-3801.
333. Scofield, M. E.; Koenigsmann, C.; Wang, L.; Liu, H. Q.; Wong, S. S. *Energ Environ Sci* **2015,** 8, (1), 350-363.
334. Yu, Y.; Lim, K. H.; Wang, J. Y.; Wang, X. *The Journal of Physical Chemistry C* **2012,** 116, (5), 3851-3856.
335. Wang, Y. Y.; Qi, Y. Y.; Zhang, D. J. *Comput Theor Chem* **2014,** 1049, 51-54.

336. Mazumder, V.; Sun, S. H. *J Am Chem Soc* **2009,** 131, (13), 4588-+.
337. Zhang, H.-X.; Wang, S.-H.; Jiang, K.; André, T.; Cai, W.-B. *J Power Sources* **2012,** 199, 165-169.
338. Jiang, K.; Xu, K.; Zou, S.; Cai, W.-B. *J Am Chem Soc* **2014,** 136, (13), 4861-4864.
339. Wang, L.; Zhai, J. J.; Jiang, K.; Wang, J. Q.; Cai, W. B. *Int J Hydrogen Energ* **2015,** 40, (4), 1726-1734.
340. Noakes, T. C. Q.; Bailey, P.; Laroze, S.; Bloxham, L. H.; Raval, R.; Baddeley, C. J. *Surf Interface Anal* **2000,** 30, (1), 81-84.
341. Adzic, R. *Electrocatalysis-Us* **2012,** 3, (3-4), 163-169.
342. Zhang, Y.; Hsieh, Y. C.; Volkov, V.; Su, D.; An, W.; Si, R.; Zhu, Y. M.; Liu, P.; Wang, J. X.; Adzic, R. R. *Acs Catal* **2014,** 4, (3), 738-742.
343. Kang, Y. J.; Qi, L.; Li, M.; Diaz, R. E.; Su, D.; Adzic, R. R.; Stach, E.; Li, J.; Murray, C. B. *Acs Nano* **2012,** 6, (3), 2818-2825.
344. Hong, W.; Wang, J.; Wang, E. *Nano Res.* **2015**, 1-9.
345. Cuong, N. T.; Fujiwara, A.; Mitani, T.; Chi, D. H. *Comp Mater Sci* **2008,** 44, (1), 163-166.
346. Kim, G.; Jhi, S. H. *Acs Nano* **2011,** 5, (2), 805-810.
347. Zhou, X. J.; Qiao, J. L.; Yang, L.; Zhang, J. J. *Adv Energy Mater* **2014,** 4, (8).
348. Koenigsmann, C.; Tan, Z.; Peng, H.; Sutter, E.; Jacobskind, J.; Wong, S. S. *Israel Journal of Chemistry* **2012,** 52, (11-12), 1090-1103.
349. Strasser, P.; Koh, S.; Anniyev, T.; Greeley, J.; More, K.; Yu, C. F.; Liu, Z. C.; Kaya, S.; Nordlund, D.; Ogasawara, H.; Toney, M. F.; Nilsson, A. *Nat Chem* **2010,** 2, (6), 454-460.
350. Matanovic, I.; Kent, P. R. C.; Garzon, F. H.; Henson, N. J. *J Electrochem Soc* **2013,** 160, (6), F548-F553.
351. Russell, A. E.; Tessier, B. C.; Wise, A. M.; Rose, A.; Price, S. W. T.; Richardson, P. W.; Ball, S. C.; Theobald, B.; Thompsett, D.; Crabb, E. M. *Ecs Transactions* **2011,** 41, (1), 55-67.
352. Rettew, R. E.; Allam, N. K.; Alamgir, F. M. *Acs Appl Mater Inter* **2011,** 3, (2), 147-151.
353. Cheon, J. Y.; Kim, T.; Choi, Y.; Jeong, H. Y.; Kim, M. G.; Sa, Y. J.; Kim, J.; Lee, Z.; Yang, T. H.; Kwon, K.; Terasaki, O.; Park, G. G.; Adzic, R. R.; Joo, S. H. *Sci Rep-Uk* **2013,** 3.
354. Gao, J.; Zhong, J.; Bai, L. L.; Liu, J. Y.; Zhao, G. Q.; Sun, X. H. *Sci Rep-Uk* **2014,** 4.
355. Nashner, M. S.; Frenkel, A. I.; Adler, D. L.; Shapley, J. R.; Nuzzo, R. G. *J Am Chem Soc* **1997,** 119, (33), 7760-7771.
356. Frenkel, A. I. *J Synchrotron Radiat* **1999,** 6, 293-295.
357. Frenkel, A. I.; Hills, C. W.; Nuzzo, R. G. *J Phys Chem B* **2001,** 105, (51), 12689-12703.
358. Alayoglu, S.; Zavalij, P.; Eichhorn, B.; Wang, Q.; Frenkel, A. I.; Chupas, P. *Acs Nano* **2009,** 3, (10), 3127-3137.
359. Jung, U.; Elsen, A.; Li, Y.; Smith, J. G.; Small, M. W.; Stach, E. A.; Frenkel, A. I.; Nuzzo, R. G. *Acs Catal* **2015**, 1539-1551.
360. Dutta, I.; Carpenter, M. K.; Balogh, M. P.; Ziegelbauer, J. M.; Moylan, T. E.; Atwan, M. H.; Irish, N. P. *J Phys Chem C* **2010,** 114, (39), 16309-16320.
361. Sasaki, K.; Naohara, H.; Choi, Y. M.; Cai, Y.; Chen, W. F.; Liu, P.; Adzic, R. R. *Nat Commun* **2012,** 3.
362. Kuttiyiel, K. A.; Sasaki, K.; Su, D.; Vukmirovic, M. B.; Marinkovic, N. S.; Adzic, R. R. *Electrochim Acta* **2013,** 110, 267-272.
363. Anderson, R. M.; Zhang, L.; Loussaert, J. A.; Frenkel, A. I.; Henkelman, G.; Crooks, R. M. *Acs Nano* **2013,** 7, (10), 9345-9353.

364. Nashner, M. S.; Frenkel, A. I.; Somerville, D.; Hills, C. W.; Shapley, J. R.; Nuzzo, R. G. *J Am Chem Soc* **1998,** 120, (32), 8093-8101.
365. Knecht, M. R.; Weir, M. G.; Frenkel, A. I.; Crooks, R. M. *Chemistry of Materials* **2007,** 20, (3), 1019-1028.
366. Shu, Y. Y.; Murillo, L. E.; Bosco, J. P.; Huang, W.; Frenkel, A. I.; Chen, J. G. *Appl Catal a-Gen* **2008,** 339, (2), 169-179.
367. Teng, X. W.; Han, W. Q.; Wang, Q.; Li, L.; Frenkel, A. I.; Yang, J. C. *J Phys Chem C* **2008,** 112, (38), 14696-14701.
368. Teng, X. W.; Wang, Q.; Liu, P.; Han, W.; Frenkel, A.; Wen, W.; Marinkovic, N.; Hanson, J. C.; Rodriguez, J. A. *J Am Chem Soc* **2008,** 130, (3), 1093-1101.
369. Dowben, P.; Miller, A.; Vook, R. *Gold Bull* **1987,** 20, (3), 54-65.
370. Deng, L.; Hu, W. Y.; Deng, H. Q.; Xiao, S. F.; Tang, J. F. *J Phys Chem C* **2011,** 115, (23), 11355-11363.
371. Carino, E. V.; Kim, H. Y.; Henkelman, G.; Crooks, R. M. *J Am Chem Soc* **2012,** 134, (9), 4153-4162.
372. Ramirez-Caballero, G. E.; Ma, Y. G.; Callejas-Tovar, R.; Balbuena, P. B. *Phys Chem Chem Phys* **2010,** 12, (9), 2209-2218.
373. Herron, J. A.; Mavrikakis, M. *Catal Commun* **2014,** 52, 65-71.
374. Hammer, B.; Norskov, J. K. *Nature* **1995,** 376, (6537), 238-240.
375. Rodriguez, P.; Garcia-Araez, N.; Koper, M. T. M. *Phys Chem Chem Phys* **2010,** 12, (32), 9373-9380.
376. Ruban, A. V.; Skriver, H. L. *Computational Materials Science* **1999,** 15, (2), 119-143.
377. Ruban, A. V.; Skriver, H. L.; Norskov, J. K. *Physical Review B* **1999,** 59, (24), 15990-16000.
378. Mavrikakis, M.; Hammer, B.; Nørskov, J. K. *Phys Rev Lett* **1998,** 81, (13), 2819-2822.
379. Tripkovic, V.; Skúlason, E.; Siahrostami, S.; Nørskov, J. K.; Rossmeisl, J. *Electrochim Acta* **2010,** 55, (27), 7975-7981.
380. Grgur, B. N.; Marković, N. M.; Ross, P. N. *Canadian Journal of Chemistry* **1997,** 75, (11), 1465-1471.
381. Xing, Y. C.; Cai, Y.; Vukmirovic, M. B.; Zhou, W. P.; Karan, H.; Wang, J. X.; Adzic, R. R. *J Phys Chem Lett* **2010,** 1, (21), 3238-3242.
382. Kang, Y. J.; Snyder, J.; Chi, M. F.; Li, D. G.; More, K. L.; Markovic, N. M.; Stamenkovic, V. R. *Nano Lett* **2014,** 14, (11), 6361-6367.
383. Mayrhofer, K. J. J.; Juhart, V.; Hartl, K.; Hanzlik, M.; Arenz, M. *Angew Chem Int Edit* **2009,** 48, (19), 3529-3531.
384. Volker, E.; Williams, F. J.; Calvo, E. J.; Jacob, T.; Schiffrin, D. J. *Phys Chem Chem Phys* **2012,** 14, (20), 7448-7455.
385. Jirkovsky, J. S.; Panas, I.; Romani, S.; Ahlberg, E.; Schiffrin, D. J. *J Phys Chem Lett* **2012,** 3, (3), 315-321.
386. Kwon, G.; Ferguson, G. A.; Heard, C. J.; Tyo, E. C.; Yin, C. R.; DeBartolo, J.; Seifert, S.; Winans, R. E.; Kropf, A. J.; Greeley, J.; Johnston, R. L.; Curtiss, L. A.; Pellin, M. J.; Vajda, S. *Acs Nano* **2013,** 7, (7), 5808-5817.
387. Shao, M. H.; Huang, T.; Liu, P.; Zhang, J.; Sasaki, K.; Vukmirovic, M. B.; Adzic, R. R. *Langmuir* **2006,** 22, (25), 10409-10415.
388. Wang, G.; Qin, W.; Zhang, J.; Wang, L.; Wei, G.; Zhu, P.; Kim, R. *Journal of Alloys and Compounds* **2009,** 475, (1–2), 452-455.

389. Auzel, F. *Chemical Reviews* **2004,** 104, (1), 139-174.
390. Sivakumar, S.; van Veggel, F. C. J. M.; Raudsepp, M. *Journal of the American Chemical Society* **2005,** 127, (36), 12464-12465.
391. Dong, H.; Sun, L. D.; Yan, C. H. *Chem Soc Rev* **2015,** 44, (6), 1608-1634.
392. Zhang, F.; Li, J.; Shan, J.; Xu, L.; Zhao, D. Y. *Chem-Eur J* **2009,** 15, (41), 11010-11019.
393. Kramer, K. W.; Biner, D.; Frei, G.; Gudel, H. U.; Hehlen, M. P.; Luthi, S. R. *Chem Mater* **2004,** 16, (7), 1244-1251.
394. Boyer, J. C.; van Veggel, F. C. J. M. *Nanoscale* **2010,** 2, (8), 1417-1419.
395. Xu, C. T.; Zhan, Q. Q.; Liu, H. C.; Somesfalean, G.; Qian, J.; He, S. L.; Andersson-Engels, S. *Laser Photonics Rev* **2013,** 7, (5), 663-697.
396. Sun, Y. J.; Chen, Y.; Tian, L. J.; Yu, Y.; Kong, X. G.; Zhao, J. W.; Zhang, H. *Nanotechnology* **2007,** 18, (27).
397. Zhuang, J.; Yang, X.; Fu, J.; Liang, C.; Wu, M.; Wang, J.; Su, Q. *Crystal Growth & Design* **2013,** 13, (6), 2292-2297.
398. Yin, B. D.; Zhou, W. L.; Long, Q.; Li, C. Z.; Zhang, Y. Y.; Yao, S. Z. *Crystengcomm* **2014,** 16, (36), 8348-8355.
399. Yi, G. S.; Chow, G. M. *Adv Funct Mater* **2006,** 16, (18), 2324-2329.
400. Bednarkiewicz, A.; Nyk, M.; Samoc, M.; Strek, W. *J Phys Chem C* **2010,** 114, (41), 17535-17541.
401. Jeong, S.; Won, N.; Lee, J.; Bang, J.; Yoo, J.; Kim, S. G.; Chang, J. A.; Kim, J.; Kim, S. *Chem Commun* **2011,** 47, (28), 8022-8024.
402. Yan, C.; Dadvand, A.; Rosei, F.; Perepichka, D. F. *Journal of the American Chemical Society* **2010,** 132, (26), 8868-+.
403. Klampaftis, E.; Ross, D.; McIntosh, K. R.; Richards, B. S. *Sol Energ Mat Sol C* **2009,** 93, (8), 1182-1194.
404. de Wild, J.; Meijerink, A.; Rath, J. K.; van Sark, W. G. J. H. M.; Schropp, R. E. I. *Energ Environ Sci* **2011,** 4, (12), 4835-4848.
405. Shan, G. B.; Assaaoudi, H.; Demopoulos, G. P. *Acs Appl Mater Inter* **2011,** 3, (9), 3239-3243.
406. Li, C. H.; Wang, F.; Zhu, J. A.; Yu, J. C. *Appl Catal B-Environ* **2010,** 100, (3-4), 433-439.
407. Han, J. K.; Wang, L.; Wong, S. S. *Rsc Adv* **2014,** 4, (66), 34963-34980.
408. Erdem, T.; Ibrahimova, V.; Jeon, D. W.; Lee, I. H.; Tuncel, D.; Demir, H. V. *J Phys Chem C* **2013,** 117, (36), 18613-18619.
409. Stevens, A. L.; Kaeser, A.; Schenning, A. P. H. J.; Herz, L. M. *Acs Nano* **2012,** 6, (6), 4777-4787.
410. Sui, Y. Q.; Tao, K.; Tian, Q.; Sun, K. *J Phys Chem C* **2012,** 116, (2), 1732-1739.
411. Lin, M.; Zhao, Y.; Liu, M.; Qiu, M. S.; Dong, Y. Q.; Duan, Z. F.; Li, Y. H.; Pingguan-Murphy, B.; Lu, T. J.; Xu, F. *J Mater Chem C* **2014,** 2, (19), 3671-3676.
412. Ma, D. K.; Yang, D. P.; Jiang, J. L.; Cai, P.; Huang, S. M. *Crystengcomm* **2010,** 12, (5), 1650-1658.
413. Wang, Y. H.; Cai, R. X.; Liu, Z. H. *Crystengcomm* **2011,** 13, (6), 1772-1774.
414. Kwon, S. H.; Lee, J. S.; Kim, Y. J. *J Nanosci Nanotechno* **2012,** 12, (11), 8845-8850.
415. Wu, S. L.; Liu, Y.; Chang, J.; Ning, Y. H.; Zhang, S. F. *Laser Photonics Rev* **2014,** 8, (4), 575-582.
416. Zhang, F.; Wan, Y.; Yu, T.; Zhang, F. Q.; Shi, Y. F.; Xie, S. H.; Li, Y. G.; Xu, L.; Tu, B.; Zhao, D. Y. *Angew Chem Int Edit* **2007,** 46, (42), 7976-7979.

417. An, J. S.; Noh, J. H.; Cho, I. S.; Roh, H. S.; Kim, J. Y.; Han, H. S.; Hong, K. S. *J Phys Chem C* **2010,** 114, (23), 10330-10335.
418. Li, C.; Yang, J.; Quan, Z.; Yang, P.; Kong, D.; Lin, J. *Chem Mater* **2007,** 19, (20), 4933-4942.
419. Tao, F.; Pan, F.; Wang, Z. J.; Cai, W. L.; Yao, L. Z. *Crystengcomm* **2010,** 12, (12), 4263-4267.
420. Lin, C. K.; Berry, M. T.; Anderson, R.; Smith, S.; May, P. S. *Chem Mater* **2009,** 21, (14), 3406-3413.
421. Ding, M. Y.; Chen, D. Q.; Yin, S. L.; Ji, Z. G.; Zhong, J. S.; Ni, Y. R.; Lu, C. H.; Xu, Z. Z. *Sci Rep-Uk* **2015,** 5.
422. Wang, F.; Han, Y.; Lim, C. S.; Lu, Y. H.; Wang, J.; Xu, J.; Chen, H. Y.; Zhang, C.; Hong, M. H.; Liu, X. G. *Nature* **2010,** 463, (7284), 1061-1065.
423. Wang, L. M.; Li, X. Y.; Li, Z. Q.; Chu, W. S.; Li, R. F.; Lin, K.; Qian, H. S.; Wang, Y.; Wu, C. F.; Li, J.; Tu, D. T.; Zhang, Q.; Song, L.; Jiang, J.; Chen, X. Y.; Luo, Y.; Xie, Y.; Xiong, Y. J. *Adv Mater* **2015,** 27, (37), 5528-5533.
424. Han, J. K.; Hannah, M. E.; Piquette, A.; Talbot, J. B.; Mishra, K. C.; McKittrick, J. *Ecs J Solid State Sc* **2012,** 1, (3), R98-R102.
425. Jung, K. Y.; Lee, C. H.; Kang, Y. C. *Mater Lett* **2005,** 59, (19-20), 2451-2456.
426. Makarov, N. S.; Lau, P. C.; Olson, C.; Velizhanin, K. A.; Solntsev, K. M.; Kieu, K.; Kilina, S.; Tretiak, S.; Norwood, R. A.; Peyghambarian, N.; Perry, J. W. *Acs Nano* **2014,** 8, (12), 12572-12586.
427. Craver, C. D.; Coblentz Society., *The Coblentz Society desk book of infrared spectra*. 2nd ed.; The Society: Kirkwood, MO (P.O. Box 9952, Kirkwood 63122), 1982; p iii, 538 p.
428. Chen, C. J.; Lai, H. Y.; Lin, C. C.; Wang, J. S.; Chiang, R. K. *Nanoscale Res Lett* **2009,** 4, (11), 1343-1350.
429. Yang, X. J.; Xiao, Q. Q.; Niu, C. X.; Jin, N.; Ouyang, J.; Xiao, X. Y.; He, D. C. *J Mater Chem B* **2013,** 1, (21), 2757-2763.
430. Wang, C. Y.; Cheng, X. H. *Rsc Adv* **2015,** 5, (115), 94980-94985.
431. Han, J.; Wang, L.; Wong, S. S. *J Phys Chem C* **2014,** 118, (11), 5671-5682.
432. Panda, G. C.; Das, S. K.; Guha, A. K. *Colloid Surface B* **2008,** 62, (2), 173-179.
433. Li, R. F.; Lee, J.; Yang, B. C.; Horspool, D. N.; Aindow, M.; Papadimitrakopoulos, F. *Journal of the American Chemical Society* **2005,** 127, (8), 2524-2532.
434. Mata, Y. N.; Blazquez, M. L.; Ballester, A.; Gonzalez, F.; Munoz, J. A. *J Hazard Mater* **2008,** 158, (2-3), 316-323.
435. Scofield, M. E.; Liu, H. Q.; Wong, S. S. *Chem Soc Rev* **2015,** 44, (16), 5836-5860.
436. Huang, X. Q.; Zhao, Z. P.; Cao, L.; Chen, Y.; Zhu, E. B.; Lin, Z. Y.; Li, M. F.; Yan, A. M.; Zettl, A.; Wang, Y. M.; Duan, X. F.; Mueller, T.; Huang, Y. *Science* **2015,** 348, (6240), 1230-1234.
437. Stephens, I. E. L.; Bondarenko, A. S.; Gronbjerg, U.; Rossmeisl, J.; Chorkendorff, I. *Energ Environ Sci* **2012,** 5, (5), 6744-6762.
438. Yao, X. Y.; Su, K. H.; Sui, S.; Mao, L. W.; He, A.; Zhang, J. L.; Du, S. F. *Int J Hydrogen Energ* **2013,** 38, (28), 12374-12378.
439. Shao, Y. Y.; Cheng, Y. W.; Duan, W. T.; Wang, W.; Lin, Y. H.; Wang, Y.; Liu, J. *Acs Catal* **2015,** 5, (12), 7288-7298.
440. Wu, J. B.; Yang, H. *Acc. Chem. Res.* **2013,** 46, (8), 1848-1857.

441. Meier, J. C.; Galeano, C.; Katsounaros, I.; Topalov, A. A.; Kostka, A.; Schuth, F.; Mayrhofer, K. J. J. *Acs Catal* **2012,** 2, (5), 832-843.
442. Kulesza, P. J.; Pieta, I. S.; Rutkowska, I. A.; Wadas, A.; Marks, D.; Klak, K.; Stobinski, L.; Cox, J. A. *Electrochim Acta* **2013,** 110, 474-483.
443. Xu, W. L.; Lu, T. H.; Liu, C. P.; Xing, W. *J Phys Chem B* **2005,** 109, (30), 14325-14330.
444. Lee, M. J.; Kang, J. S.; Kang, Y. S.; Chung, D. Y.; Shin, H.; Ahn, C. Y.; Park, S.; Kim, M. J.; Kim, S.; Lee, K. S.; Sung, Y. E. *Acs Catal* **2016,** 6, (4), 2398-2407.
445. Wang, H. S.; Alden, L. R.; DiSalvo, F. J.; Abruna, H. D. *Langmuir* **2009,** 25, (13), 7725-7735.
446. Almeida, T. S.; Kokoh, K. B.; De Andrade, A. R. *Int J Hydrogen Energ* **2011,** 36, (6), 3803-3810.
447. Barranco, J.; Pierna, A. R. *J Non-Cryst Solids* **2008,** 354, (47-51), 5153-5155.
448. Wang, H. J.; Wang, X. H.; Zheng, J. D.; Peng, F.; Yu, H. *Chinese J Catal* **2014,** 35, (10), 1687-1694.
449. Rutkowska, I. A.; Sek, J. P.; Marks, E.; Zelenay, P.; Kulesza, P. J. *Meeting Abstracts* **2015,** MA2015-01, (27), 1645.
450. Huang, H.; Li, W. Z.; Liu, H. C. *Catal Today* **2012,** 183, (1), 58-64.
451. Maiyalagan, T.; Khan, F. N. *Catal Commun* **2009,** 10, (5), 433-436.
452. Joo, J. B.; Kim, J.; Kim, P.; Yi, J. *J Nanosci Nanotechno* **2010,** 10, (5), 3397-3401.
453. Yuan, J. H.; Chen, Y. X.; Han, D. X.; Zhang, Y. J.; Shen, Y. F.; Wang, Z. J.; Niu, L. *Nanotechnology* **2006,** 17, (18), 4689-4694.
454. Trasatti, S., Interfacial electrochemistry of conductive oxides for electrocatalysis. In *Interfacial Electrochemistry: Theory, Experiment, and Applications*, Taylor & Francis 1999.
455. Chen, D. Q.; Wang, Y. S. *Nanoscale* **2013,** 5, (11), 4621-4637.
456. Zhang, H.; Xu, D.; Huang, Y.; Duan, X. F. *Chem Commun* **2011,** 47, (3), 979-981.
457. Xu, C. T.; Svenmarker, P.; Liu, H. C.; Wu, X.; Messing, M. E.; Wallenberg, L. R.; Andersson-Engels, S. *Acs Nano* **2012,** 6, (6), 4788-4795.
458. Zeng, Q. H.; Xue, B.; Zhang, Y. L.; Wang, D.; Liu, X. M.; Tu, L. P.; Zhao, H. F.; Kong, X. G.; Zhang, H. *Crystengcomm* **2013,** 15, (23), 4765-4772.
459. Chen, G. Y.; Liu, H. C.; Liang, H. J.; Somesfalean, G.; Zhang, Z. G. *J Phys Chem C* **2008,** 112, (31), 12030-12036.
460. Yang, D.; Dai, Y.; Ma, P. a.; Kang, X.; Shang, M.; Cheng, Z.; Li, C.; Lin, J. *J Mater Chem* **2012,** 22, (38), 20618-20625.
461. Saboktakin, M.; Ye, X. C.; Oh, S. J.; Hong, S. H.; Fafarman, A. T.; Chettiar, U. K.; Engheta, N.; Murray, C. B.; Kagan, C. R. *Acs Nano* **2012,** 6, (10), 8758-8766.
462. Xue, M.; Zhu, X.; Qiu, X.; Gu, Y.; Feng, W.; Li, F. *Acs Appl Mater Inter* **2016**.
463. Yi, G. S.; Chow, G. M. *Chem Mater* **2007,** 19, (3), 341-343.